



# Jordan Journal of P H Y S I C S

An International Peer-Reviewed Research Journal

---

Volume 12, No. 1, April 2019, Shaban 1440 H

---

**Jordan Journal of Physics (JJP):** An International Peer-Reviewed Research Journal funded by the Scientific Research Support Fund, Jordan, and published biannually by the Deanship of Research and Graduate Studies, Yarmouk University, Irbid, Jordan.

**EDITOR-IN-CHIEF:**

**Ibrahim O. Abu Al-Jarayesh**

*Department of Physics, Yarmouk University, Irbid, Jordan.*

*[ijaraysh@yu.edu.jo](mailto:ijaraysh@yu.edu.jo)*

**EDITORIAL BOARD:**

**Prof. Dia-Eddin M. Arafah**

*Department of Physics, University of Jordan, Amman, Jordan.*

*[darafah@ju.edu.jo](mailto:darafah@ju.edu.jo)*

**Prof. Nabil Y. Ayoub**

*President, American University of Madaba, Madaba, Jordan.*

*[nabil.ayoub@giu.edu.jo](mailto:nabil.ayoub@giu.edu.jo)*

**Prof. Jamil M. Khalifeh**

*Department of Physics, University of Jordan, Amman, Jordan.*

*[jkalifa@ju.edu.jo](mailto:jkalifa@ju.edu.jo)*

**Prof. Sami H. Mahmood**

*Department of Physics, University of Jordan, Amman, Jordan.*

*[s.mahmood@ju.edu.jo](mailto:s.mahmood@ju.edu.jo)*

**Prof. Nihad A. Yusuf**

*Department of Physics, Yarmouk University, Irbid, Jordan.*

*[nihadyusuf@yu.edu.jo](mailto:nihadyusuf@yu.edu.jo)*

**Prof. Marwan S. Mousa**

*Department of Physics, Mu'tah University, Al-Karak, Jordan.*

*[mmousa@mutah.edu.jo](mailto:mmousa@mutah.edu.jo)*

**Prof. Akram A. Rousan**

*Department of Applied Physical Sciences, Jordan University Of Science and Technology, Irbid, Jordan.*

*[akram@just.edu.jo](mailto:akram@just.edu.jo)*

**Prof. Mohammad Al-Sugheir**

*Department of Physics, The Hashemite University, Zarqa, Jordan.*

*[msugh@hu.edu.jo](mailto:msugh@hu.edu.jo)*

**ASSOCIATE EDITORIAL BOARD**

**Prof. Mark Hagmann**

*Desert Electronics Research Corporation, 762 Lacey Way, North Salt Lake 84064, Utah, U. S. A.*

*[MHagmann@NewPathResearch.Com](mailto:MHagmann@NewPathResearch.Com)*

**Dr. Richard G. Forbes**

*Dept. of Electrical and Electronic Engineering, University of Surrey, Advanced Technology Institute and Guildford, Surrey GU2 7XH, UK.*

*[r.forbes@surrey.ac.uk](mailto:r.forbes@surrey.ac.uk)*

**Prof. Roy Chantrell**

*Physics Department, The University of York, York, YO10 5DD, UK.*

*[roy.chantrell@york.ac.uk](mailto:roy.chantrell@york.ac.uk)*

**Prof. Susamu Taketomi**

*2-35-8 Higashisakamoto, Kagoshima City, 892-0861, Japan.*

*[staketomi@hotmail.com](mailto:staketomi@hotmail.com)*

**Editorial Secretary:** Majdi Al-Shannaq.

**Languages Editor:** Haider Al-Momani

**Manuscripts should be submitted to:**

Prof. Ibrahim O. Abu Al-Jarayesh  
Editor-in-Chief, Jordan Journal of Physics  
Deanship of Research and Graduate Studies  
Yarmouk University-Irbid-Jordan  
Tel. 00 962 2 7211111 Ext. 2075  
E-mail: [jjp@yu.edu.jo](mailto:jjp@yu.edu.jo)  
Website: <http://Journals.yu.edu.jo/jjp>

# Jordan Journal of PHYSICS

An International Peer-Reviewed Research Journal

---

Volume 12, No. 1, April 2019, Shaban 1440 H

---

## INTERNATIONAL ADVISORY BOARD

**Prof. Dr. Ahmad Saleh**

Department of Physics, Yarmouk University, Irbid, Jordan.  
[salema@yu.edu.jo](mailto:salema@yu.edu.jo)

**Prof. Dr. Aurore Savoy-Navarro**

LPNHE Université de Paris 6/IN2P3-CNRS, Tour 33, RdC 4,  
Place Jussieu, F 75252, Paris Cedex 05, France.  
[auore@lpnhep.in2p3.fr](mailto:auore@lpnhep.in2p3.fr)

**Prof. Dr. Bernard Barbara**

Laboratoire Louis Neel, Salle/Room: D 108, 25, Avenue des  
Martyrs BP 166, 38042-Grenoble Cedex 9, France.  
[Barbara@grenoble.cnrs.fr](mailto:Barbara@grenoble.cnrs.fr)

**Prof. Dr. Bruno Guiderdoni**

Observatoire Astronomique de Lyon, g, avenue Ch. Antre-F-69561,  
Saint Genis Laval Cedex, France.  
[Bruno.guiderdoni@olos.univ-lyon1.fr](mailto:Bruno.guiderdoni@olos.univ-lyon1.fr)

**Prof. Dr. Buford Price**

Physics Department, University of California, Berkeley, CA 94720,  
U. S. A.  
[bprice@berkeley.edu](mailto:bprice@berkeley.edu)

**Prof. Dr. Colin Cough**

School of Physics and Astronomy, University of Birmingham, B15  
2TT, U. K.  
[c.cough@bham.ac.uk](mailto:c.cough@bham.ac.uk)

**Prof. Dr. Desmond Cook**

Department of Physics, Condensed Matter and Materials Physics  
Research Group, Old Dominion University, Norfolk, Virginia  
23529, U. S. A.  
[Dcook@physics.odu.edu](mailto:Dcook@physics.odu.edu)

**Prof. Dr. Evgeny Sheshin**

MIPT, Institutskij per. 9, Dogoprudnyi 141700, Russia.  
[sheshin@lafaet.mipt.ru](mailto:sheshin@lafaet.mipt.ru)

**Prof. Dr. Hans Ott**

Laboratorium fuer Festkorperphysik, ETH Honggerberg, CH-  
8093 Zurich, Switzerland.  
[ott@solid.phys.ethz.ch](mailto:ott@solid.phys.ethz.ch)

**Prof. Dr. Herwig Schopper**

President SESAME Council, Chairman Scientific Board UNESCO  
IBSP Programme, CERN, 1211 Geneva, Switzerland.  
[Herwig.Schopper@cern.ch](mailto:Herwig.Schopper@cern.ch)

**Prof. Dr. Humam Ghassib**

Department of Physics, The University of Jordan, Amman 11942,  
Jordan.  
[humamg@ju.edu.jo](mailto:humamg@ju.edu.jo)

**Prof. Dr. Khalid Touqan**

Chairman of Jordan Atomic Energy Commission, Amman, Jordan.

**Prof. Dr. Nasr Zubeidev**

President: Al-Zaytoonah University of Jordan, Amman, Jordan.  
[President@alzaytoonah.edu.jo](mailto:President@alzaytoonah.edu.jo)

**Prof. Dr. Patrick Roudeau**

Laboratoire de l'Accelérateur, Lineaire (LAL), Université Paris-  
Sud 11, Batiment 200, 91898 Orsay Cedex, France.  
[roudeau@mail.cern.ch](mailto:roudeau@mail.cern.ch)

**Prof. Dr. Paul Chu**

Department of Physics, University of Houston, Houston, Texas  
77204-5005, U. S. A.  
[Ching-Wu.Chu@mail.uh.edu](mailto:Ching-Wu.Chu@mail.uh.edu)

**Prof. Dr. Peter Dowben**

Nebraska Center for Materials and Nanoscience, Department of  
Physics and Astronomy, 255 Behlen Laboratory (10th and R  
Streets), 116 Brace Lab., P. O. Box 880111, Lincoln, NE 68588-  
0111, U. S. A.  
[pdowben@unl.edu](mailto:pdowben@unl.edu)

**Prof. Dr. Peter Mulser**

Institute fuer Physik, T.U. Darmstadt, Hochschulstr. 4a, 64289  
Darmstadt, Germany.  
[Peter.mulser@physik.tu-darmstadt.de](mailto:Peter.mulser@physik.tu-darmstadt.de)

**Prof. Dr. Rasheed Azzam**

Department of Electrical Engineering, University of New Orleans  
New Orleans, Louisiana 70148, U. S. A.  
[razzam@uno.edu](mailto:razzam@uno.edu)

**Prof. Dr. Shawqi Al-Dallal**

Department of Physics, Faculty of Science, University of Bahrain,  
Manamah, Kingdom of Bahrain.

**Prof. Dr. Wolfgang Nolting**

Institute of Physics / Chair: Solid State Theory, Humboldt-  
University at Berlin, Newtonstr. 15 D-12489 Berlin, Germany  
[Wolfgang.nolting@physik.hu-berlin.de](mailto:Wolfgang.nolting@physik.hu-berlin.de)

**Prof. Dr. Ingo Hofmann**

GSI Darmstadt, Planckstr. 1, 64291, Darmstadt, Germany.  
[i.hofmann@gsi.de](mailto:i.hofmann@gsi.de)

**Prof. Dr. Jozef Lipka**

Department of Nuclear Physics and Technology, Slovak University  
of Technology, Bratislava, Ilkovicova 3, 812 19 Bratislava,  
Slovakia.  
[Lipka@elf.stuba.sk](mailto:Lipka@elf.stuba.sk)







The Hashemite Kingdom of Jordan



Yarmouk University

Jordan Journal of  
**PHYSICS**

An International Peer-Reviewed Research Journal  
Funded by the Scientific Research Support Fund

**Special Issue**

**Volume 12, No. 1, April 2019, Shaban 1440 H**



## Instructions to Authors

Instructions to authors concerning manuscript organization and format apply to hardcopy submission by mail, and also to electronic online submission via the Journal homepage website (<http://jjp.yu.edu.jo>).

## Manuscript Submission

1- **E-mail to :** [jjp@yu.edu.jo](mailto:jjp@yu.edu.jo)

2- **Online:** Follow the instructions at the journal homepage website.

Original *Research Articles*, *Communications* and *Technical Notes* are subject to critical review by minimum of two competent referees. Authors are encouraged to suggest names of competent reviewers. *Feature Articles* in active Physics research fields, in which the author's own contribution and its relationship to other work in the field constitute the main body of the article, appear as a result of an invitation from the Editorial Board, and will be so designated. The author of a *Feature Article* will be asked to provide a clear, concise and critical status report of the field as an introduction to the article. *Review Articles* on active and rapidly changing Physics research fields will also be published. Authors of *Review Articles* are encouraged to submit two-page proposals to the Editor-in-Chief for approval. Manuscripts submitted in *Arabic* should be accompanied by an Abstract and Keywords in English.

## Organization of the Manuscript

Manuscripts should be typed double spaced on one side of A4 sheets (21.6 x 27.9 cm) with 3.71 cm margins, using Microsoft Word 2000 or a later version thereof. The author should adhere to the following order of presentation: Article Title, Author(s), Full Address and E-mail, Abstract, PACS and Keywords, Main Text, Acknowledgment. Only the first letters of words in the Title, Headings and Subheadings are capitalized. Headings should be in **bold** while subheadings in *italic* fonts.

**Title Page:** Includes the title of the article, authors' first names, middle initials and surnames and affiliations. The affiliation should comprise the department, institution (university or company), city, zip code and state and should be typed as a footnote to the author's name. The name and complete mailing address, telephone and fax numbers, and e-mail address of the author responsible for correspondence (designated with an asterisk) should also be included for official use. The title should be carefully, concisely and clearly constructed to highlight the emphasis and content of the manuscript, which is very important for information retrieval.

**Abstract:** A one paragraph abstract not exceeding 200 words is required, which should be arranged to highlight the purpose, methods used, results and major findings.

**Keywords:** A list of 4-6 keywords, which expresses the precise content of the manuscript for indexing purposes, should follow the abstract.

**PACS:** Authors should supply one or more relevant PACS-2006 classification codes, (available at <http://www.aip.org/pacs/pacs06/pacs06-toc.html>)

**Introduction:** Should present the purpose of the submitted work and its relationship to earlier work in the field, but it should not be an extensive review of the literature (e.g., should not exceed 1 ½ typed pages).

**Experimental Methods:** Should be sufficiently informative to allow competent reproduction of the experimental procedures presented; yet concise enough not to be repetitive of earlier published procedures.

**Results:** should present the results clearly and concisely.

**Discussion:** Should be concise and focus on the interpretation of the results.

**Conclusion:** Should be a brief account of the major findings of the study not exceeding one typed page.

**Acknowledgments:** Including those for grant and financial support if any, should be typed in one paragraph directly preceding the References.

**References:** References should be typed double spaced and numbered sequentially in the order in which they are cited in the text. References should be cited in the text by the appropriate Arabic numerals, enclosed in square brackets. Titles of journals are abbreviated according to list of scientific periodicals. The style and punctuation should conform to the following examples:

**1. Journal Article:**

- a) Heisenberg, W., Z. Phys. 49 (1928) 619.
- b) Bednorz, J. G. and Müller, K. A., Z. Phys. B64 (1986) 189
- c) Bardeen, J., Cooper, L.N. and Schrieffer, J. R., Phys. Rev. 106 (1957) 162.
- d) Asad, J. H., Hijjawi, R. S., Sakaji, A. and Khalifeh, J. M., Int. J. Theor. Phys. 44(4) (2005), 3977.

**2. Books with Authors, but no Editors:**

- a) Kittel, C., "Introduction to Solid State Physics", 8<sup>th</sup> Ed. (John Wiley and Sons, New York, 2005), chapter 16.
- b) Chikazumi, S., C. D. Graham, JR, "Physics of Ferromagnetism", 2<sup>nd</sup> Ed. (Oxford University Press, Oxford, 1997).

**3. Books with Authors and Editors:**

- a) Allen, P. B. "Dynamical Properties of Solids", Ed. (1), G. K. Horton and A. A. Maradudin (North-Holland, Amsterdam, 1980), p137.
- b) Chantrell, R. W. and O'Grady, K., "Magnetic Properties of Fine Particles" Eds. J. L. Dormann and D. Fiorani (North-Holland, Amsterdam, 1992), p103.

**4. Technical Report:**

Purcell, J. "The Superconducting Magnet System for the 12-Foot Bubble Chamber", report ANL/HEP6813, Argonne Natl. Lab., Argonne, III, (1968).

**5. Patent:**

Bigham, C. B., Schneider, H. R., US patent 3 925 676 (1975).

**6. Thesis:**

Mahmood, S. H., Ph.D. Thesis, Michigan State University, (1986), USA (Unpublished).

**7. Conference or Symposium Proceedings:**

Blandin, A. and Lederer, P. Proc. Intern. Conf. on Magnetism, Nottingham (1964), P.71.

**8. Internet Source:**

Should include authors' names (if any), title, internet website, URL, and date of access.

**9. Prepublication online articles (already accepted for publication):**

Should include authors' names (if any), title of digital database, database website, URL, and date of access.

For other types of referenced works, provide sufficient information to enable readers to access them.

**Tables:** Tables should be numbered with Arabic numerals and referred to by number in the Text (e.g., Table 1). Each table should be typed on a separate page with the legend above the table, while explanatory footnotes, which are indicated by superscript lowercase letters, should be typed below the table.

**Illustrations:** Figures, drawings, diagrams, charts and photographs are to be numbered in a consecutive series of Arabic numerals in the order in which they are cited in the text. Computer-generated illustrations and good-quality digital photographic prints are accepted. They should be black and white originals (not photocopies) provided on separate pages and identified with their corresponding numbers. Actual size graphics should be provided, which need no further manipulation, with lettering (Arial or Helvetica) not smaller than 8 points, lines no thinner than 0.5 point, and each of uniform density. All colors should be removed from graphics except for those graphics to be considered for publication in color. If graphics are to be submitted digitally, they should conform to the following minimum resolution requirements: 1200 dpi for black and white line art, 600 dpi for grayscale art, and 300 dpi for color art. All graphic files must be saved as TIFF images, and all illustrations must be submitted in the actual size at which they should appear in the journal. Note that good quality hardcopy original illustrations are required for both online and mail submissions of manuscripts.

**Text Footnotes:** The use of text footnotes is to be avoided. When their use is absolutely necessary, they should be typed at the bottom of the page to which they refer, and should be cited in the text by a superscript asterisk or multiples thereof. Place a line above the footnote, so that it is set off from the text.

**Supplementary Material:** Authors are encouraged to provide all supplementary materials that may facilitate the review process, including any detailed mathematical derivations that may not appear in whole in the manuscript.

### **Revised Manuscript and Computer Disks**

Following the acceptance of a manuscript for publication and the incorporation of all required revisions, authors should submit an original and one more copy of the final disk containing the complete manuscript typed double spaced in Microsoft Word for Windows 2000 or a later version thereof. All graphic files must be saved as PDF, JPG, or TIFF images.

Allen, P.B., “.....”, in: Horton, G.K., and Muradudin, A. A., (eds.), “Dynamical.....”, (North.....), pp....

### **Reprints**

Twenty (20) reprints free of charge are provided to the corresponding author. For orders of more reprints, a reprint order form and prices will be sent with the article proofs, which should be returned directly to the Editor for processing.

### **Copyright**



Submission is an admission by the authors that the manuscript has neither been previously published nor is being considered for publication elsewhere. A statement transferring copyright from the authors to Yarmouk University is required before the manuscript can be accepted for publication. The necessary form for such transfer is supplied by the Editor-in-Chief. Reproduction of any part of the contents of a published work is forbidden without a written permission by the Editor-in-Chief.

### **Disclaimer**

Opinions expressed in this Journal are those of the authors and neither necessarily reflects the opinions of the Editorial Board or the University, nor the policy of the Higher Scientific Research Committee or the Ministry of Higher Education and Scientific Research. The publisher shoulders no responsibility or liability whatsoever for the use or misuse of the information published by JJP.

### **Indexing**

JJP is currently indexing in:

	<b>Emerging Sources Citation Index (ESCI)</b>	
---	---	---



Jordan Journal of  
P H Y S I C S

An International Peer-Reviewed Research Journal

---

Volume 12, No. 1, April 2019, Shaban 1440 H

---

**Editorial Preface**

This special issue of Jordan Journal of Physics (JJP) presents 8 selected papers presented at the international conference that was held Under the Patronage of His Royal Highness Prince Hamzah Bin Al Hussein between 10-12/4/2018 in the campus of Jordan University of Science and Technology, Irbid, Jordan under the title: "International Conference on Current Nanotechnology and its Application (ICCNA2018)". These papers were subjected to standard refereeing of JJP.





# Jordan Journal of P H Y S I C S

An International Peer-Reviewed Research Journal

---

Volume 12, No. 1, April 2019, Shaban 1440 H

---

## **International Conference on Current Nanotechnology and its Application (ICCNA2018)**

**10<sup>th</sup> to 12<sup>th</sup> April 2018**

**Jordan University of Science and Technology, Irbid, Jordan.**

### **Guest Editor Preface**

The conference "International Conference on Current Nanotechnology and its Application" (ICCNA2018) was held from Tuesday 10<sup>th</sup> to Thursday 12<sup>th</sup> April 2018 on the beautiful campus of The Jordan University of Science and Technology, Irbid, Jordan.

The generous support of the Scientific Research Support Fund (SRSF), Jordan University of Science and Technology, Bruker, and Hijaz for Electronic and Scientific Supplies Est., among other local organizations, played an important role in the success of this Conference.

The main goal of the conference is to bring together experts in Advance Nanomaterials with its applications and to provide a platform for researchers, engineers, academicians as well as industrial professionals from all over the world to present their research results and development activities. This conference provides a venue for the delegates to exchange new ideas and experiences with up to date and state-of-art technology in advanced materials; furthermore, the conference provides an opportunity to establish research relations and to find global partners for future collaboration.

The conference covered the following themes and specific research areas in current advanced nanotechnology and its application:

- Nanotechnology and Functional Materials for Energy
- Nanotechnology for Environment and Sustainable Development.
- Nanotechnology and Biomaterials
- Nanostructured Materials for Functional Applications
- Nanotechnology and Electronic and Magnetic Materials
- Nanotechnology and Manufacturing and Processing for Materials Performance.
- Enhancement (thin film, surface, nanostructuring, interface)
- Structural Materials (including steels, light alloys, bulk metallic glasses, high-temperature materials, ceramics, polymer composites, and hybrid materials)
- Nanotechnology and Sensors: (Bio, chemical and physical)
- Nanotechnology and Materials for imaging and diagnostics
- Nanotechnology and tissue engineering
- Nanotechnology drug targeting
- Nanotoxicology

The Conference was one of the most successful academic activities in the field of nanotechnology in the Middle East. More than 200 participants attended the Conference, and 63 papers were presented in ten sessions. Only fourteen papers out of 63 were selected and approved by the conference scientific committee to be submitted to *The Jordan Journal of Physics*. These selected papers were submitted to the rigorous standards of the Journal regulations and only eight papers were finally approved by the Guest editor and the Journal editorial board after a two blind peer review by the reviewers.

These eight high quality papers that appeared in this special issue give a clear sign of the strong commitment of Jordan University of Science and Technology as well as the *Jordan Journal of Physics* to be in the front line in the Middle East. Accordingly, *The Jordan Journal of Physics* is proud to take this initiative and publish a special issue in current advance nanotechnology as a conference proceeding.

This Special Issue aims to document the recent advances in nanomaterials with its applications and to provide a platform for researchers, engineers, academicians as well as industrial professionals. This special issue of the conference proceedings provides opportunities with up to date and state-of-art technology in advanced nanomaterials. Moreover, interesting topics covered with their potential applications, should be valuable subjects for the readers.

*Guest Editor*

**Prof. Dr. M-Ali AL-Akhras (AL-Omari)**

*Vice Dean Faculty of Science and Arts*

*Department of Physics*

*Jordan University of Science and Technology(JUST)*

*P.O.ox (3030) Irbid 22110 Jordan*

Tel.: 00962-779-488104

Fax.: 00 962-2-7201071

# Jordan Journal of P H Y S I C S

An International Peer-Reviewed Research Journal

---

Volume 12, No. 1, April 2019, Shaban 1440 H

---

## **International Conference on Current Nanotechnology and its Application (ICCNA2018) 10<sup>th</sup> to 12<sup>th</sup> April 2018 Jordan University of Science and Technology, Irbid, Jordan.**

### **Organizing Committee**

Prof. Mohammad-Ali Al-Omari (Chair)

Dr. Mohamed Al-Fandi (Chair)

Dr. Nusaiba Al-Nemrawi (Co-chair)

Prof. Abeer Al-Bawab, Director General of the Scientific Research Support Fund, The University of Jordan  
Prof. Dr. Hanan Malkawi, Vice President for Science Engagement Royal Scientific Society  
Prof. Qutaibah T. Khatatbeh, Dean Faculty of Science and Arts  
Prof. Rami Oweis, Nanotechnology Institute  
Prof. Marwan Mousa, Mutah University and Chairman of JPS, Jordan  
Prof. Rabi Rabady, Nanotechnology Institute  
Dr. Yahia Makableh, Nanotechnology Institute  
Dr. Ahmed Hijazi, Department of Chemistry, JUST  
Prof. Dr. Eqab M. Rabei, Al al-Bayt University  
Dr. Husam El-Nasser, Physics Department, Al al-Bayt University  
Dr. Yahya Al Khatatbeh, Princess Sumaya University for Technology, Jordan  
Prof. Dr. Mahmoud Al-Hussein, Jordan University, Jordan  
Prof. Dr. Jebreel Khoshman, Al-Hussein Bin Talal University, Jordan  
Dr. Areen M. Khattabi, Applied Science University, Amman, Jordan  
Prof. Zaid Ahmed Amber, Al-Balqa Applied University, Jordan  
Dr. Nid'A H. Alshraiedeh, Faculty of Pharmacy, JUST  
Prof. Dr. Ahmad Omari, Department of Physics, JUST  
Dr. Rami Alkhatib, Department of Biology, JUST  
Dr. Jood Mohammad Ali Hashem, Applied Medical Sciences. JUST  
Dr. Jumana Mahmoud Abu-Khalaf, German Jordanian University  
Prof. Ala'aldeen Tawfeek Al-Halhouli, German Jordanian University  
Dr. yazan Hussien Akkam, Pharmacy, Yarmouk University  
Dr. Kaled AL-Heuseen, Ajloun University College, Al-Balqa Applied University, Jordan  
Dr. Inshad. Jum'h, German Jordanian University, Amman, Jordan  
Dr. Hussein Al-Taani, German Jordanian University, Amman, Jordan  
Dr. Muna Abu-Dalo, Department of Chemistry, JUST  
Dr. Yousef Al-Abdallat, The National Program for linkage Academic Institutions with industrial sector  
Program Manager. The University of Jordan  
Dr. Majed M. Masadeh, Dept. of Pharmaceutical Technology, JUST  
Prof. Dr. Ahmad Alsaad, Department of Physics, JUST  
Dr. Alaa A Aljabali, Faculty of Pharmacy, Yarmouk University  
Dr. Gassem Alzoubi, Department of Physics, The Hashemite University, Jordan  
Dr. Moath Aldahoun, Amman Arab University, Amman, Jordan  
Dr. Moaz Altarawneh, Mutah University, Jordan  
Dr. Suhaila Al-Sheboul, Department of Lab Sciences, Jordan University of Science and Technology, Jordan  
Dr. Riad Salem Ababneh, Yarmouk University  
Dr. Abeer Al Bsoul, Chemical Engineering, Al-Balqa Applied University  
Conference Secretary Mrs: Bayan Mohammad ALshoha

### **International Advisory Board**

Prof. Brian S. Sorg, National Cancer Institute, USA  
Prof. Mohamad Suhaimi Jaafar, Universiti Sains Malaysia, Malaysia  
Prof. Syed Ismat Shah, University of Delaware, USA  
Prof. Isabel C. Escobar, The University of Toledo, USA  
Prof. Nabil Y. Ayoub, president of the American University of Madaba, Jordan  
Prof. Ihab M. Obaidat, University of UAE. UAE  
Prof. Martin Kordesch, Ohio University, USA  
Dr. Renat Sabirianov, University of Nebraska-Omaha, USA  
Dr. Ahmad Telfah, Senior Scientist, Bunsen-Kirchhoff-Straße 11, Dortmund, Germany  
Dr. Khaled Saoud, Professor of Physics, Virginia Commonwealth University in Qatar  
Prof. Dr. Şule ERTEN-ELA, Ege University, Solar Energy Institute, Turkey  
Prof. Isabel C. Escobar, PhD, Professor of Chemical and Materials Engineering, University of Kentucky, USA  
Prof. Vinka Oyanedel-Craver, Department of Civil and Environmental Engineering, University of Rhode Island  
Prof. N.J. Ianno, Milton E. Mohr Professor. NCMNS, Dept. of Elec. Eng. University of Nebraska-Lincoln, USA  
Dr. Kostiantyn V. Shportko. Senior research fellow at V.E. Lashkaryov Institute for Semiconductor Physics of NAS of Ukraine  
Prof. Mohamed Henini. Nottingham Nanotechnology and Nanoscience Centre, University of Nottingham, Nottingham UK  
Prof. Richard Partch, Research Group Center for Advanced Materials Processing Clarkson University, USA  
Prof. M. Alper Şahiner, Chair and Professor of Physics, Seton Hall University, NJ, USA  
Prof. Raed Hashaiekh, Professor, Chemical Engineering Department, Abu Dhabi, UAE  
Prof. Mark J. Hagmann, President and CTO, NewPath Research L.L.C. Salt Lake City, Utah, USA  
Prof. Nathir A.F. Al-Rawashdeh, Dean of Higher Colleges of Technology, UAE  
Prof. Dr. A. Abdelghani, National Institute of Applied Science and Technology (INSAT, Tunisia)  
Prof. Dr.-Ing. Dr. Olfa Kanoun, Technische Universität Chemnitz, Dept. of Elec. Eng. and Information Technology, Germany  
Prof. Dr. Alexandre MAYER, University of Namur , Laboratoire de Physique du Solide Richard Partch, Belgium  
Prof. Dr. Majda Sekkal, Faculty of Exact Sciences. University Djillali Liabes of Sidi Bel-Abbes. 22000 Sidi Bel-Abbès, Algeria  
Prof. Dr. Sameer Makki, University of Baghdad-College of Education for Pure Science, Iraq  
Dr. Dr. Richard Forbes, University of Surrey, United Kingdom  
Dr. Azeez A. Barzinjy, Salahaddin University-Erbil, Ishik University, Erbil, Kurdistan-region, Iraq

Jordan Journal of  
P H Y S I C S

An International Peer-Reviewed Research Journal

---

Volume 12, No. 1, April 2019, Shaban 1440 H

---

Table of Contents:

<b>English Articles</b>	<b>Pages</b>
<b>New Software Simulating the Full Operation of a Scanning Tunneling Microscope and Its Application to an FPGA-Based Instrument</b>	1-5
Mark J. Hagmann, Gregory R. Spencer, Jeremy Wiedemeier and Marwan S. Mousa	
<b>Comparative Study of Field Electron Emission from Single-Walled Carbon Nanotube and Multi-Walled Carbon Nanotube Mounted on Tungsten</b>	7-15
Marwan S. Mousa, Samer I. Daradkeh and Emad S. Bani Ali	
<b>A Genetic Algorithm for Addressing Computationally Expensive Optimization Problems in Optical Engineering</b>	17-36
A. Mayer and Michaël Lobet	
<b>Monte Carlo Computation of the Influence of Carbon Contamination Layer on the Energy Distribution of Backscattered Electrons Emerging from Al and Au</b>	37-44
A. M. D. Assa'd	
<b>Ionic Liquids: Sustainable Media for Nanoparticles</b>	45-62
Azeez A. Barzinjy, Samir M. Hamad and Ashna F. Arkawazi	
<b>Numerical Testing by a Transfer-Matrix Technique of Simmons' Equation for the Local Current Density in Metal-Vacuum-Metal Junctions</b>	63-77
Alexandre Mayer, Marwan S. Mousa, Mark J. Hagmann and Richard G. Forbes	
<b>Preparation and Preliminary Characterization of Hybrid Alginate – Carrageenan Aerogel: Effect of Gelation Methods</b>	79-86
M. Alnaief, B. Mohammad, Mohannad Aljarrah and R. M. Obaidat	
<b>Effect of Relaxation and Cooling Process on Field Electron Emission from Single-Walled Carbon Nanotubes Embedded in Glass</b>	87-96
Marwan S. Mousa and Samer I. Daradkeh	



# Jordan Journal of Physics

## ARTICLE

---

### New Software Simulating the Full Operation of a Scanning Tunneling Microscope and Its Application to an FPGA-Based Instrument

Mark J. Hagmann<sup>a</sup>, Gregory R. Spencer<sup>a</sup>, Jeremy Wiedemeier<sup>a</sup> and Marwan S. Mousa<sup>b</sup>

<sup>a</sup> *NewPath Research L.L.C., Salt Lake City, Utah 84115, USA.*

<sup>b</sup> *Department of Physics, Mu'tah University, Al-Karak 61710, Jordan.*

---

*Received on: 2/7/2018;*

*Accepted on: 22/10/2018*

---

**Abstract:** The scanning tunneling microscope is an essential tool in nanoscience and nanotechnology, because it enables imaging surfaces at the atomic level with sub-nanometer resolution. We have written a LabVIEW-based virtual instrument to simulate the operation of an STM and made it available as a free-download at our company website. This is an executable version to be run on a Windows operating system without requiring other software. We have also constructed an STM that implements the same algorithms with a field-programmable gate array (FPGA) to provide deterministic real-time control of multiple tasks.

**Keywords:** Scanning Tunneling Microscope, Field-Programmable Gate Array, Nanoscience, Nanotechnology.

## Introduction

The scanning tunneling microscope (STM), invented by Gerd Binnig and Heinrich Rohrer at IBM Zurich in 1986 [1], is an essential tool in nanoscience and nanotechnology. In an STM, a nanoscale metal tip electrode is brought within several tenths of a nanometer of an electrically-conductive sample and a DC bias voltage is applied to cause an electrical current to flow through this junction by quantum tunneling. Typically, a piezoelectric actuator is used to move the tip to adjust its distance from the sample as the tip is scanned to create images of the sample surface. The exponential sensitivity of the tunneling current to the tip-sample distance enables sub-nanometer resolution for images at the atomic level.

Others have written software to simulate the operation of an STM for classroom demonstrations [2] or created a simulator that may be downloaded for a trial period to demonstrate their products for imaging with an STM [3]. We have developed a LabVIEW

Virtual Instrument (VI) which simulates the full operation of an STM that may be downloaded from our company website for permanent use without registration, cost or time limits [4]. Documentation for the software and a narrated video showing typical operation of our simulator are also available at the website. The documentation includes figures, equations and definitions of the terminology. We hope that this VI will be useful for educational and training purposes. It was compiled using the LabVIEW Application Builder which allows stand alone applications to be bundled with the LabVIEW Run-Time Engine as an installer so the download does not require the installation of any other software. Our application was compiled to run on a Windows operating system, but if requested, we will modify the STM simulator VI so that it may be used on Mac operating systems as well. Fig. 1 shows the main display screen of the VI when imaging unreconstructed silicon (100).

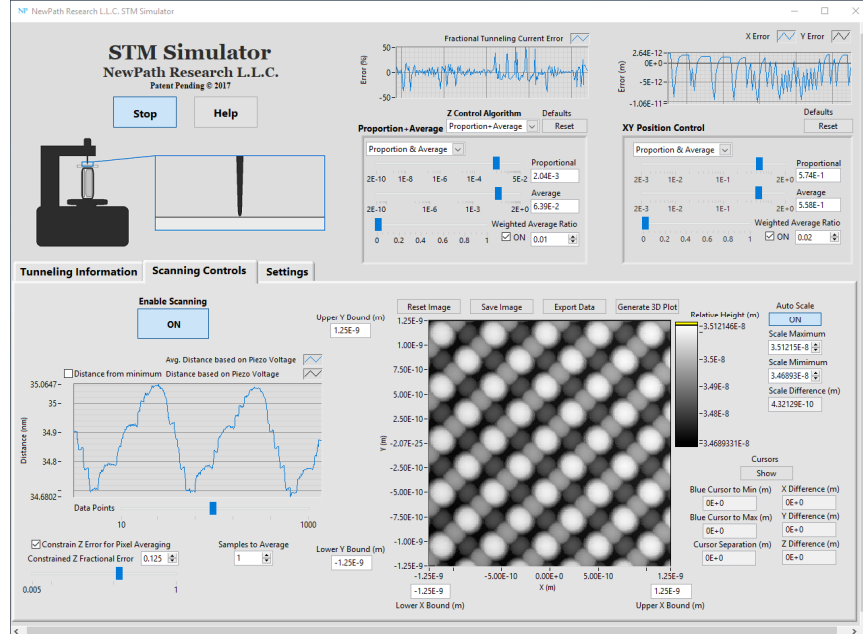


FIG. 1. Main display screen of the new STM simulator VI during operation, showing the unreconstructed surface of silicon (100). Image width = 2.5 nm.

## Materials and Methods

### Modeling of Non-Ideal Phenomena

To our knowledge, this is the first STM simulator to include the effects of noise in the tunneling current. Noise in the voltages controlling the x-, y- and z-motions of the piezoelectric actuator is modeled by introducing white Gaussian noise to the measured tunneling current. Stochastic slow-drift in the vertical position of the tip electrode which would be caused by vibration and temperature changes is modeled by gradually adjusting the tip-sample distance according to a random walk. The effects of the voltage drop on the series resistance, such as the spreading resistance in the sample at the tunneling junction, are also included. The adverse effects of blunted tips can be seen by adjusting the related parameters (such as the tip radius). We do not, however, model the effects of tips having unusual shapes such as double-pointed tips. Bounds for these non-ideal behaviors may be set by the user to determine their effects on measurements and imaging. We understand that other factors such as  $1/f$  noise, Johnson noise and generation-recombination noise may also have an effect on measurements [5]; however, these phenomena are yet included.

The software is written in a modular format to facilitate upgrading different parts to better

meet our needs and also to follow the suggestions from those who have downloaded this simulator VI. For example, we could model the resonances, nonlinearities and hysteresis in the response of the piezoelectric actuator which is used for fine-positioning of the tip electrode and may also provide different approximations to calculate the tunneling current including expressions for semiconductor samples.

### Four Methods for Feedback Control

Feedback control is used to adjust the tip-sample distance in an STM when initiating quantum tunneling and then to minimize the error in the tunneling current which is given by  $e(t) = I(t) - I_{sp}$ , where  $I(t)$  is the current at time  $t$  and  $I_{sp}$  is the chosen value for the set-point current. Simply making a change in the voltage  $\Delta V$  to the piezoelectric actuator that is proportional to the error is insufficient, because this would cause the tunneling current to oscillate about the set-point value.

PI (Proportion + Integral) feedback control, where the change in the voltage that is applied to the piezoelectric actuator is proportional to the sum of the error and the integral of the error, as shown in Eq. (1), is frequently used in scanning tunneling microscopy.

$$\Delta V = K_p e(t) + K_i \int_0^t e(t') dt' \quad (1)$$



Simulations made with the STM simulator VI show that PI feedback control is only stable over a specific range for the two coefficients  $K_p$  and  $K_I$  (see Fig. 2). The size and location of the stable region for these two coefficients depend on the properties of the tip and the tip-sample distance. Large oscillations in the tunneling

current, including the possibility of tip-crash failure or loss of tunneling, occur when one (or both) of these coefficients is outside the region for stability. It is inconvenient to have to estimate the value for both coefficients before the measurements.

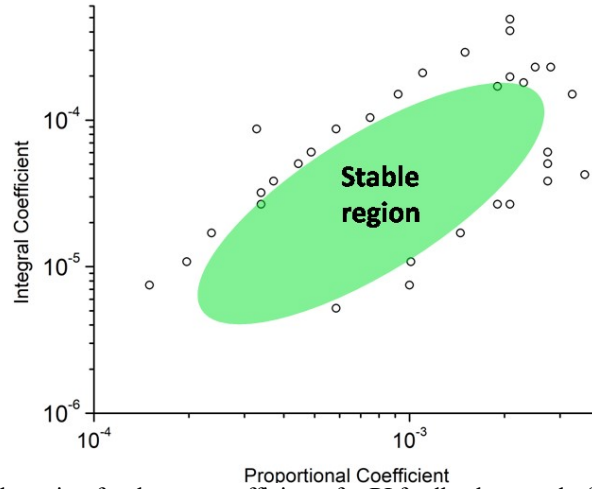


FIG. 2. Stable region for the two coefficients for PI feedback control of the tunneling current.

The control algorithms included in the VI are: (1) Unmodified PI as previously described, (2) D.A.S. (Digitally Adapted Steps) which adjusts the sizes of the steps of the piezoelectric actuator based on the tunneling current [6], (3) Modified Proportion in which the proportion coefficient is adjusted based on the tunneling current and (4) Proportion + Average which is similar to PI control but instead of integrating it takes the mean of the last few values of the error. Each of these algorithms is described in detail on our website.

The STM simulator VI may be used to compare the stability, response time and ease of use for feedback control of the current when using the four different algorithms with various values for their parameters.

### Stepper Motor and Piezoelectric Actuator

In order to obtain atomic resolution in imaging, the piezoelectric actuator must have a small range of motion (typically 60 nm). Thus, it is necessary to add a precision digital stepper motor for coarser positioning of the tip electrode in order to provide a greater range of motion in the system. The piezoelectric actuator is automatically decremented each time before the digital stepper motor is incremented to avoid missing specific tip-sample distances which

would be caused by the effects of the finite precision of the step motor.

### Simulation of Crystal Lattice Surfaces in Real-Time

Once the simulation shows that stable quantum tunneling has been achieved, it is possible to generate an image of highly ordered pyrolytic graphite (HOPG), graphene, unreconstructed silicon (100) or the reconstructed surface of silicon after it has been cleaved. The surfaces of these four materials were modeled by approximating the contours for the local density of states of electrons in the atoms as spheres with appropriate sizes. The images of the surfaces are created by scanning over the simulated surfaces while calculating the tunneling current based on the distance from the surface to the tip. Fig. 1 shows the main display screen when simulating the imaging of unreconstructed silicon (100). The graph at the lower left corner of this figure shows the relative height of the tip which is calculated from the voltage that is applied to the piezoelectric actuator. Oscillations in the height, which are seen in this graph, are caused by the tip electrode passing over several silicon atoms in the lattice.

At the upper left corner of Fig. 1, there is a sketch of the STM scan-head with an animated

diagram showing the vertical tip electrode above the horizontal sample. If the value calculated for the tip position is below the surface of the sample, indicating that a tip-crash has occurred, this cartoon shows that the tip is bent and the simulation has stopped. However, with an actual STM, it may not be obvious that a tip-crash has occurred, because images with high resolution are still possible. Thus, this feature enables the user to determine the optimum parameters to prevent tip-crash. Later, we will incorporate an algorithm to determine whether a tip-crash has occurred without relying on the simulated height of the tip. For example, a small increment in the voltage to the piezoelectric actuator would not change the current when the tip is in contact with the sample. This change would be necessary before the STM simulator VI software could be implemented in an actual STM.

In the constant current mode, feedback control of the tunneling current is enabled during scanning. In the constant height mode, feedback control is disabled during scanning so that the tip

is moved in a plane above the surface of the sample. This mode is prone to loss of tunneling or tip-crash unless it is used to image small areas or with samples having relatively flat surfaces.

## Results

Fig. 3 shows a graph of the simulated tunneling current over a specific time interval which is incremented throughout each session. This figure shows the effects of the noise in the tunneling current. A separate plot that is made over a much longer time interval is used to monitor the effects of feedback control on the tunneling current as well as the response to the simulated stochastic slow-drift.

After at least one line of a scan has been completed, a 3-D image of the sample may be generated as the data is collected for an image. Fig. 4 shows an example of a completed 3-D simulated image of unreconstructed silicon (100).

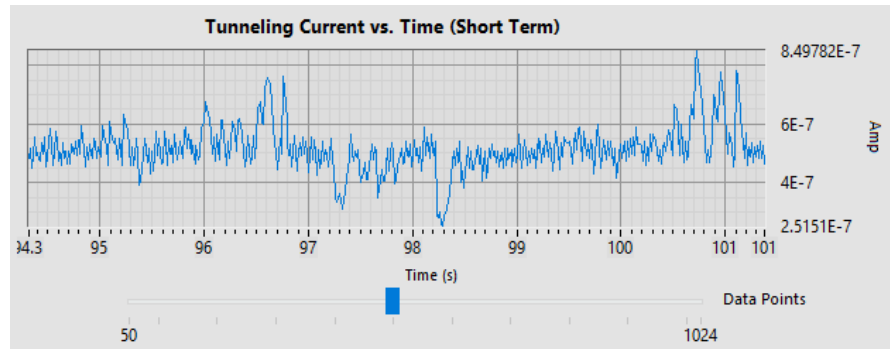


FIG. 3. Graph of the simulated tunneling current vs. time, showing the noise in the tunneling current.

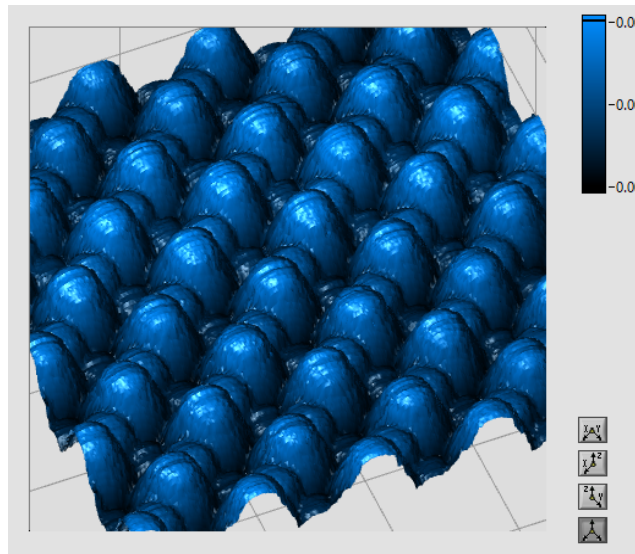


FIG. 4. Three-dimensional plot of a simulated image of unreconstructed silicon (100).

## Application of This Software to an FPGA-Based Instrument

Fig. 5 shows the scan-head of our portable in-house STM. This instrument has a reduced mechanical length for the C-shaped path between the tip and the sample with greater stiffness to provide unusually high stability. Thus, the tunneling typically continues automatically for a period of at least 72 hours. The software for the STM is written in

LabVIEW, input and output tools that are similar to those in the VI. There is also the same selection of algorithms for feedback control to increase the speed and accuracy of the measurements while reducing the probability of tip-crash. All of this is done using a field-programmable gate array (FPGA) to enable performing multiple deterministic tasks in real-time in addition to the feedback control of the tunneling current.

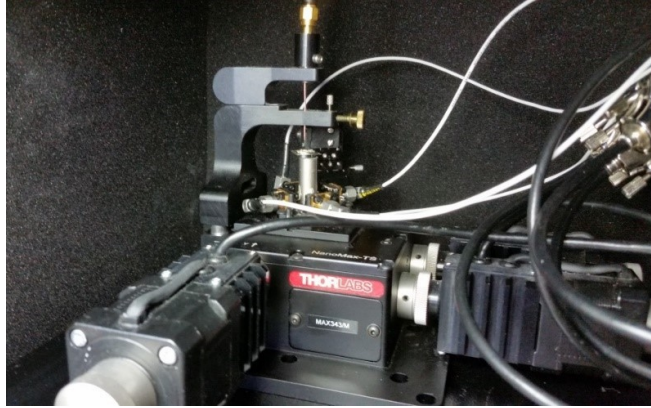


FIG. 5. Scan-head for our in-house STM.

This instrument was designed for experimental studies in which a microwave frequency comb is generated by focusing a mode-locked laser on the tunneling junction of an STM [7]. Thus, the tip electrode is attached to the center conductor of a semi-rigid coaxial cable to couple the microwave harmonics directly from the tunneling junction to a spectrum analyzer. A bias-T is attached to the SMA connector at the top end of this cable and its low-frequency port is connected to the low-noise STM preamplifier of the STM. The high-frequency port of the bias-T is connected to the spectrum analyzer or to an equivalent 50- $\Omega$  dummy load during calibration of the STM, in order to mitigate interference with the feedback control of the tunneling current.

## Conclusions

Our testing with this VI suggests that PID feedback control is effective after tunneling has been established. However, before there is a tunneling current, the history of zero current which is used as a criterion for the use of integration in feedback control delays the response when the current is first seen to potentiate the probability of tip-crash. Our results suggest that the method of D.A.S.

(Digitally Adapted Steps) simplifies the choice of the control parameters and provides fast response at the time when the tunneling current is first seen.

## Acknowledgment

This work is funded by the National Science Foundation under grant 164881.

## References

- [1] Binnig, G. and Rohrer, H., IBM J. Res. Dev., 30 (1986) 355.
- [2] Rebello, N.S. et al., Eur. J. Phys., 18 (1997) 456.
- [3] Specs Zurich GmbH, Zurich, [www.specs-zurich.com](http://www.specs-zurich.com).
- [4] NewPath Research L.L.C., Salt Lake City, Utah, [www.newpathresearch.com](http://www.newpathresearch.com).
- [5] Chen, C.J., "Introduction to Scanning Tunneling Microscopy", Oxford Series in Optical and Imaging Sciences, (1993), 252-253.
- [6] Hagmann, M.J., U.S. Patent 9, 885, 737 (2018).
- [7] Hagmann, M.J., Andrei, P., Pandey, S. and Nahata, A., J. Vac. Sci. Technol. B, 33(2015) 02B109.



### Comparative Study of Field Electron Emission from Single-Walled Carbon Nanotube and Multi-Walled Carbon Nanotube Mounted on Tungsten

Marwan S. Mousa, Samer I. Daradkeh and Emad S. Bani Ali

*Surface Physics and Materials Technology Lab., Department of Physics, Mutah University, Al-Karak 61710, Jordan.*

---

Received on: 2/7/2018;

Accepted on: 26/11/2018

---

**Abstract:** Field Electron Emission (FEE) from Single-Walled Carbon Nanotubes (SWCNTs) and Multi-Walled Carbon Nanotubes (MWCNTs) mounted on blunt tungsten tip has been investigated to make sure that FEE comes from the CNTs. The FEE properties were studied using Field Emission Microscope (FEM), where the distance between the emitter and screen was fixed at  $\sim 10$  mm and the system was evacuated to ( $\sim 10^{-9}$  mbar). The emitters were prepared during two stages, with the first one being electrolytically etching the tungsten (W) wire of (0.1 mm diameter) in 2 mol of NaOH, while the second stage involves fixing the CNTs on the etched tungsten. Current-voltage (I-V) measurements were recorded and presented in the most common way as (I-V) plot with its related Fowler-Nordheim (FN) plot. It has been found that SWCNT samples have several advantages over MWCNT samples, such as the field electron emission having been initiated at lower applied voltage values and maintaining emitting electrons at lower applied voltage values, but MWCNTs emitted higher current values compared to SWCNTs.

**Keywords:** Field Electron Emission, SWCNTs, MWCNTs.

## Introduction

Field electron emission (FEE) in solids occurs in intense electric field and is strongly dependent on the work function of the emitting material. In a parallel-plate arrangement, the macroscopic field  $E_{macro}$  between the plates is given by  $E_{macro} = V/d$ , where  $d$  is the plate separation and  $V$  is the applied voltage. If a sharp object is created on a plate, then the local field  $E_{local}$  at its apex is greater than  $E_{macro}$  and can be related to  $E_{macro}$  by [1]:

$$E_{local} = \gamma \times E_{macro}.$$

The parameter  $\gamma$  is called the field enhancement factor and is basically determined by the shape of the object [1]. FEE occurs when the applied electric field value is  $\sim 10^9$  V/m [2]. In order to achieve that high electric field at the

tip of a sample, the sample has been fabricated to have a high tip curvature [3].

Metals have been extensively used as field electron emitters until 1991, where Multi-Walled Carbon Nanotube (MWCNT) was discovered accidentally by Sumio Iijima [4] while studying the surfaces of graphite electrode used in electric arc discharge. Two years later, Single-Walled Carbon Nanotube (SWCNT) was discovered by the same scientist and his colleagues [5]. These materials have attracted much attention due to their features, so they can be used as field electron emitters [6].

Carbon materials exist in various forms, such as graphite, diamond, carbon fibers, fullerenes and carbon nanotubes. Carbon nanotubes show distinguished properties and their discovery had

a great impact on the development in the field of semiconductor science due to their unique properties [7]. Those tubes are considered to be the strongest and stiffest materials yet discovered in terms of tensile strength and elastic modulus, because of the covalent  $sp^2$  bonds formed between individual carbon atoms [8], electrical properties [9], mechanical strength and chemical strength [10]. The natural resonance (fundamental vibrational frequency) of a cantilevered single-wall nanotube of 1 micron length is shown to be about 12 MHz [11]. It is one of the best candidates to be used as field electron emitters because of the advantages it has over other metallic emitters, such as enhanced current stability, low threshold voltage, nano-size, high aspect ratio and long lifetime [12]. Due to these properties, CNTs are very widely used in technological and industrial fields, such as flat panel displays, cathode-ray-tube lighting elements and drug delivery systems [13].

Field emission behavior of a CNT strongly depends upon its morphology, diameter, alignment and the contact between the CNT and the substrate, as well as the condition of the CNT tip (defects, adsorption, doping, ... and so on) [14]. The FN theory can reveal some basic factors that have influence on the FE mechanism. The experimental data can reveal other factors, such as value of the enhancement factor and emitting area [15]. The best method to represent the experimental data is using the FN plot,  $\ln(I/V^2)$  vs.  $1/V$ , and the expected shape of the FN plot is a straight line according to the theory. However, experimentalists experienced a deviation from FN theory during testing the FE mechanism from CNTs, that could be as an effect of non-uniform field enhancement factor [16], or adsorbed molecules, influence of high apex curvature, space charge effect, localized electron state, contact resistance, among others [17]. The main aim of this article is to keep the ongoing research of seeking for optimum field emission (FE) cold cathodes by studying and comparing the two kinds of CNTs employed in this investigation. In previous research, FE differences between FEE from SWCNTs and MWCNTs have been investigated, where both emitters have been prepared using different preparation techniques from the preparation technique mentioned in [18]. Variation in results

was obtained due to these differences; so critical comparison between the results reported here and those previously found [19] will be carried out in the future. In this study, it can be noted that a SWCNT emitter can initiate electron emission at lower applied voltage values, but an MWCNT emitter produces a higher electron emission current than that from an SWCNT emitter [19].

## Materials and Methodology

This study uses SWCNTs produced by catalytic conversion of high-pressure Carbon Monoxide over Fe particles (HiPCO) processed at CNI, Houston, TX, where the length of individual SWCNT is approximately (1 - 3)  $\mu\text{m}$  and the mean diameter is (1 - 4) nm. The MWCNT Nanocly<sup>TM</sup> NC 7000 of a carbon purity of (90%) and an average tube diameter of (9.5 nm) with high aspect ratio ( $> 150$ ) has been tested. In the etching process, a tungsten wire of (0.1 mm) diameter and high purity (99.95 %) was used (Produced by Good Fellow Metals Company, UK).

The emitters were fabricated by mounting the CNTs over a blunt tungsten tip, to make sure that the tungsten (W) does not contribute to the field emission process. The mounting procedures consisted of two steps; the first step starts with preparing the tungsten substrate using electrolytic etching of a wire at the meniscus of a 2 mol/liter of NaOH solution; i.e., by same technique used for tungsten emitters [20-21]. Etching process starts with cutting  $\sim 3$  cm of tungsten wire, then attaching one of its ends inside a stainless steel tube. The tungsten wire has been etched using an electrochemical circuit, using a power supply (10 – 12 V), an ammeter and a graphite rod as a cathode. The process has been performed in Pyrex glass beakers that are connected by a separating glass pipe to prevent interfering of the produced hydrogen in the etching process [22]. By immersing about 0.3 cm of the W wire in the etching NaOH solution, the electrical etching process starts. This process ends by removing the tungsten from the NaOH solution, after the etching current suddenly drops. Fig. 1 shows a schematic diagram of the electrical etching circuit.

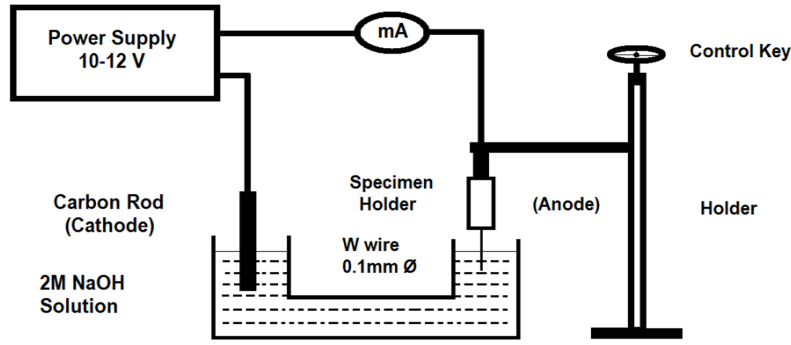


FIG. 1. Schematic diagram of electrical etching circuit.

After ultrasonic cleaning for ~8 min, we start with the second step which involves applying a thin layer of epoxylite resin; that is necessary to attach the CNT over the tungsten tip. The tungsten blunt tip was slowly and regularly dipped once into the epoxy resin, then very slowly pulled out to prevent the formation of bubbles [23]. Then, the CNTs were mechanically attached to the tungsten tip under observation of optical microscopy.

In the work reported here, various types of CNTs/W blunt emitters have been characterized using the conventional field electron microscope (FEM) with tip-screen separation standardized at 10 mm. The vacuum system was baked out at ~170 °C overnight having a pressure during the FEE tests of  $\sim 2 \times 10^{-9}$  mbar. The most common method of investigating the emitter behavior is recording the current-voltage (I-V) characteristics and presenting the data produced as I-V as well as FN plots [24].

Generally, Fowler-Nordheim (FN) theory has been employed to describe field emission behavior of metals. The theory is expressed by the following equation [25]:

$$I = \lambda A a \phi^{-1} F^2 \exp(-\mu b \phi^{3/2} / F)$$

where  $\phi$  and  $F$  are the local work function and the barrier field,  $a$  and  $b$  are the usual universal FN constants,  $A$  is the emission area and  $\lambda$  and  $\mu$  are the generalized correction factors.

## Results

Fig. 2 presents SEM images for both types of emitters, where the attached CNTs on the tungsten blunt tips are shown (SWCNTs on blunt W tip (left) and MWCNTs on blunt W tip (right)). Attaching CNTs on iron tip has been done by [26] and MWCNTs on tungsten tip by [26-27] in order to study the FEE from these CNTs. In this work, we will investigate the FEE mechanism from SWCNTs on blunt tip and MWCNTs on blunt tungsten tip.

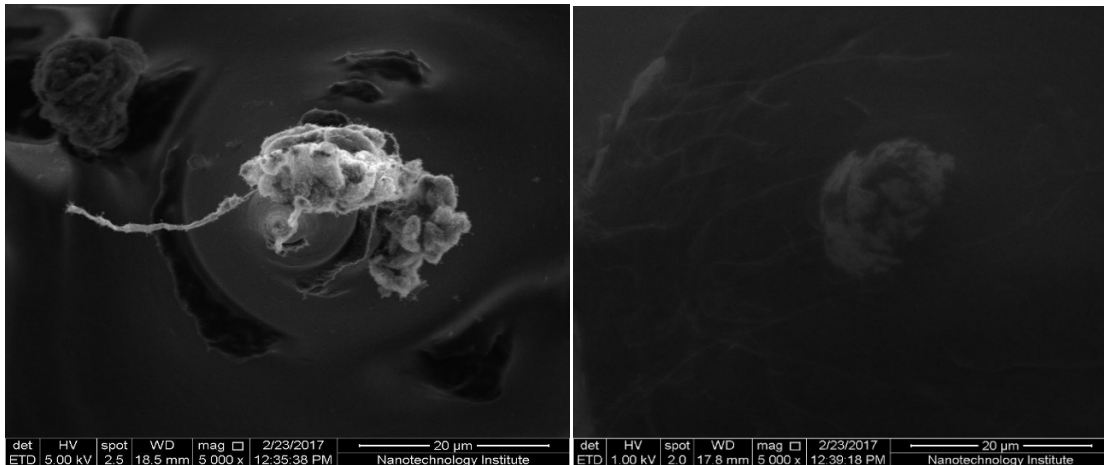


FIG. 2. SEM images for SWCNTs/W tip (left), MWCNTs/W tip (right), with a magnification of 5000 times.



As mentioned before, we attached the CNTs on blunt tungsten tip, in order to make sure that tungsten tip will not contribute to the FEE process.

We performed the tests on the two types of samples, (SWCNTs/W) and (MWCNTs/W), under the same conditions. The voltage applied to the SWCNTs/W tip was slowly increased with the I-V characteristics being recorded. The emission current initiated at 2 pA with the applied voltage at 450 V. The emission current increased linearly by increasing the applied voltage, thus indicating a constant-resistance regime. Then, the applied voltage has been increased until “switch-on” phenomenon occurs at ( $V_{SW}=1250$  V). The emission current was suddenly raised from nA range to  $\mu$ A range, where the emission current was ( $2.9 \mu$ A). By

further increasing the applied voltage, the emission current continued increasing, until (2850 V) was reached, where the recorded emission current was ( $17.9 \mu$ A). By decreasing the applied voltage, the linear region of the FN plot extends down to ( $V = 650$  V), with an emission current ( $I = 1.06 \mu$ A). By further voltage decreasing, the emission current vanishes at ( $V_{TH} = 400$  V), with an emission current ( $I_{TH} = 3$  pA). Fig. 3 shows the I-V characteristics and the related FN plots for (SWCNTs/W). The slope of both voltage cycles is pointed out in the FN plots (for low emission current value), where the slope of FN plot can reveal the value of some important parameters like field enhancement factor by calculating the slope and emission area through calculating the intercept [28].

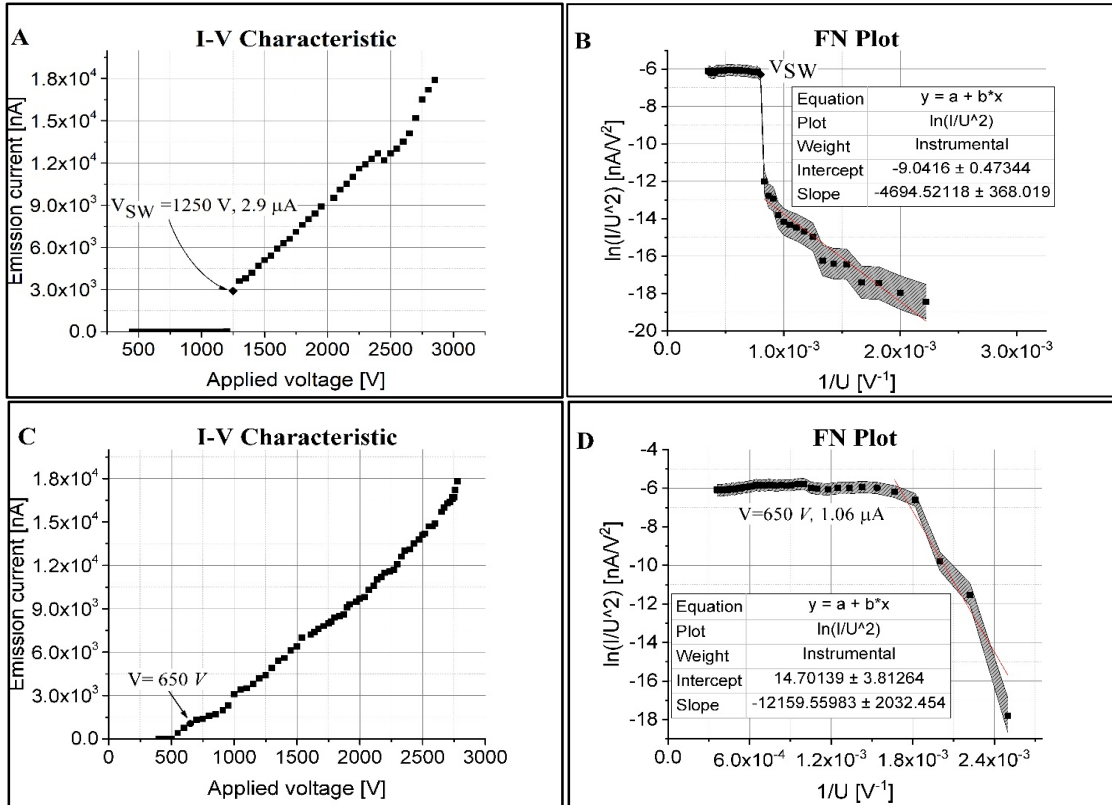


FIG. 3. (SWCNTs/W): at increasing voltage - (A) I-V characteristics and (B) FN plot. At decreasing voltage - (C) I-V characteristics and (D) FN plot.

As it appeared from Fig. (3-B and D), there are multi-linear segment FN plots, which can be divided into two linear segments. Such behavior could be attributed to the existence of constant resistance. The indication of the existence of constant resistance is the linear increase in the I-V plot in Fig. (3A). Additionally, the slope value

for the increasing cycle of the applied voltage is -4694.5 Np, while the decreasing voltage cycle gave a slope of -12159.5 Np.

For the (MWCNTs/W) emitter, at an applied voltage value of 750 V, the emission current with a value of 9.4 pA has been initiated. By further increasing the applied voltage, the



emission current increased until the applied voltage reached (3920 V), where “switch-on” phenomenon suddenly occurred with an emission current value of (22  $\mu$ A) recorded. It is to be noted that the emission current increased from 6.3 nA to 22  $\mu$ A. By decreasing the applied voltage, the emission current started to decrease, but it remained in the ( $\mu$ A) range until the applied voltage reached ( $V = 1000$  V), where the emission current was ( $I = 2.1$   $\mu$ A). As being noted from Fig. 4, the linear behavior appeared in the I-V characteristics of the MWCNTs, where it has the same indication, illustrating the existence of constant resistance. By further decreasing the applied voltage, the emission

current continues to decrease until it vanishes at ( $V_{TH} = 670$  V), ( $I_{TH} = 8.2$  pA). Fig. 4 shows the I-V characteristics and the related FN plot, with the slope shown by the FN plots (for low emission current). The FN plot that is related to FEE from MWCNTs shows a multi-linear segment as the FN plot of SWCNTs, which could be the same evidence for the existence of constant resistance. In addition, the FN plot shape bends downward at its left end which indicates an increasing field enhancement factor [29]. From the FN plots for FEE from MWCNTs (Fig. 4), the slope values at increasing and decreasing cycles of the applied voltage are -18204.4 Np and -18649.9 Np, respectively.

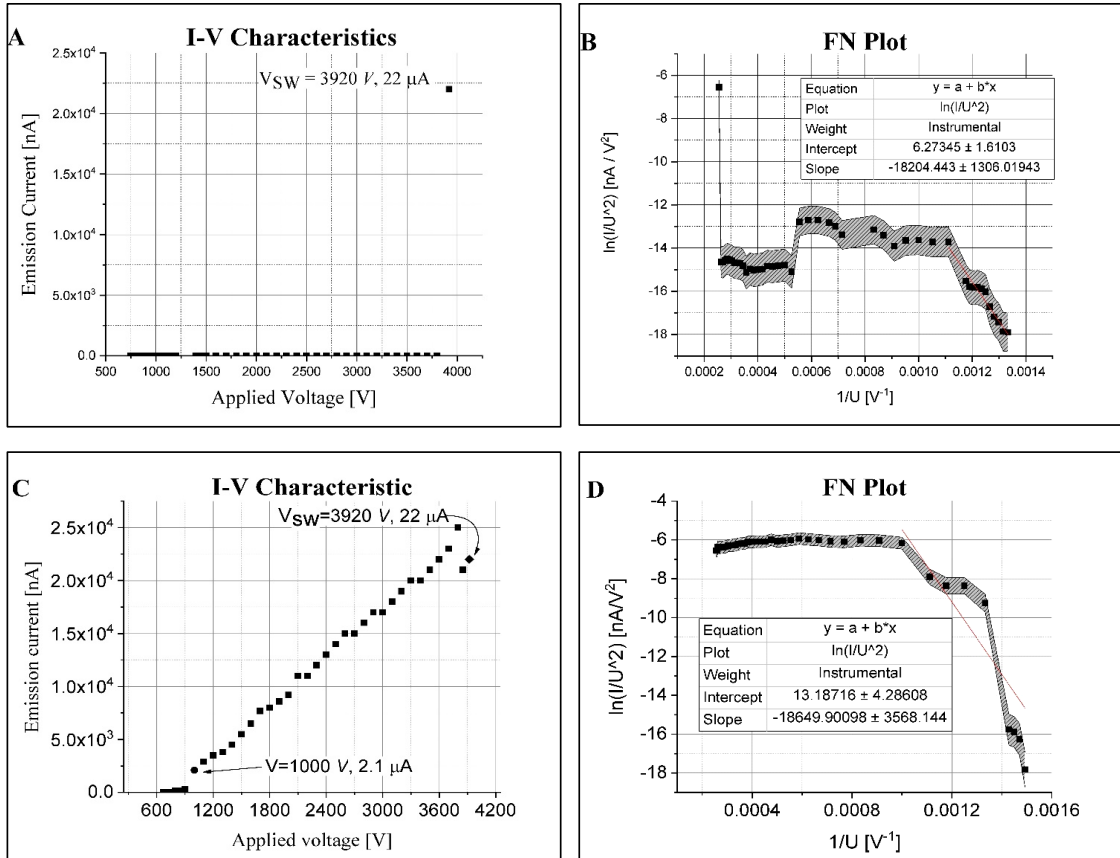


FIG. 4. (MWCNTs/W): at increasing voltage - (A) I-V characteristics and (B) FN plot. At decreasing voltage - (C) I-V characteristics and (D) FN plot.

The experiments were repeated under the same conditions. For the (SWCNTs/W) emitter, the applied voltage ranged between (550 V) and (1400 V), with an emission current of (9 pA) to (4.2  $\mu$ A) recorded, with the “switch-on” phenomenon occurring at ( $V_{SW} = 1000$  V), ( $I_{SW} = 1.3$   $\mu$ A). The emission current increased linearly at an applied voltage of (900 V) to (1400 V), then with starting to decrease the applied

voltage, the linear region extends from ( $V = 1350$  V), ( $I = 4.1$   $\mu$ A) to ( $V = 500$  V), ( $I = 70$  nA). By further decreasing the applied voltage, the emission current falls smoothly to ( $I_{TH} = 1$  pA), where the applied voltage value was ( $V_{TH} = 300$  V). Fig. 5 shows the I-V characteristics and related FN plot at increasing and decreasing voltage.

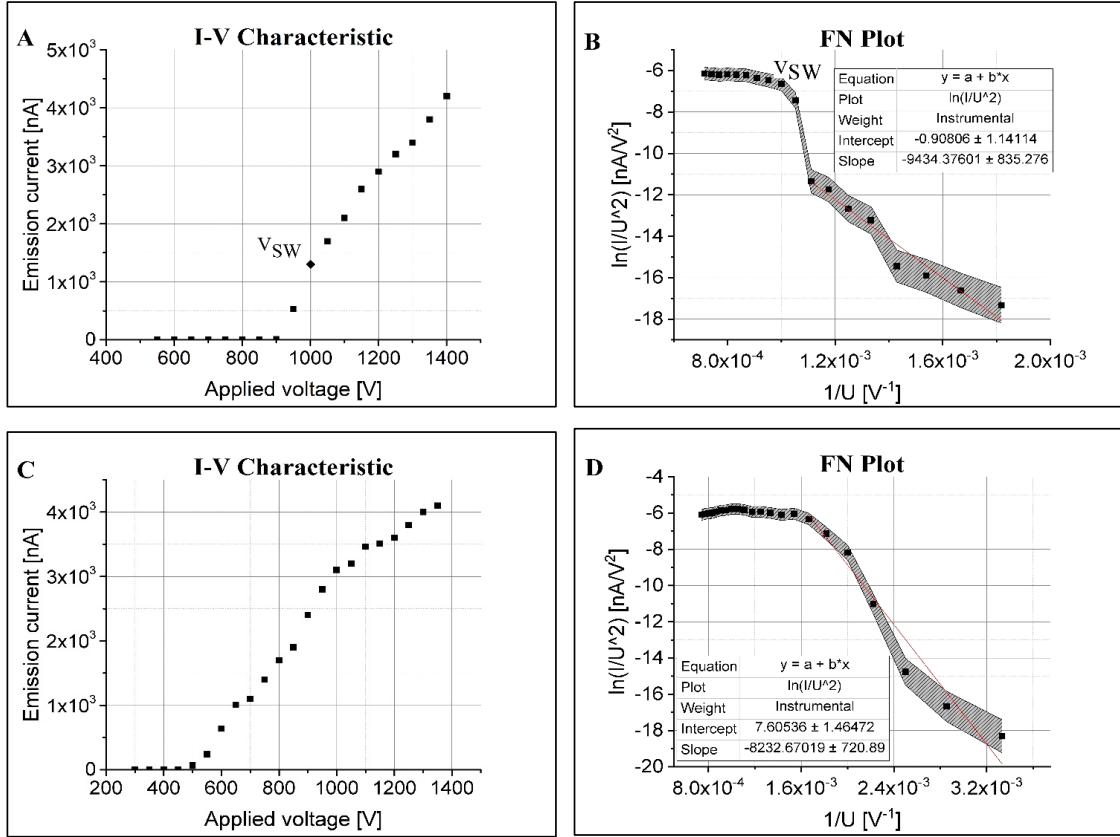


FIG. 5. For (SWCNTs/W). Cycle 2; at increasing voltage - (A) I-V characteristics and (B) FN plot. At decreasing voltage - (C) I-V characteristics and (D) FN plot.

In case of (MWCNTs/W) emitter, the applied voltage ranges from (800 V) to (1930 V), with an emission current ranging from (9 pA) to (6.1  $\mu$ A), where the “switch-on” phenomenon occurs at an applied voltage value of ( $V_{SW} = 1930$  V), with an emission current value of ( $I_{SW} = 6.1$   $\mu$ A). During the decreasing cycle ranging from (1930 V) to (560 V), with an emission current ranging from (6.1  $\mu$ A) to (7 pA), the saturation region extends down to ( $V_{SAT} = 1250$  V), with the emission current value ( $I_{SAT} = 1.1$   $\mu$ A) and by further decreasing the applied voltage, the emission current vanishes at ( $V_{TH} = 560$  V) with ( $I_{TH} = 7$  pA). Fig. 5 shows the I-V characteristics and related FN plot for the (SWCNTs/W) emitter, while Fig. 6 shows the I-V characteristics and related FN plot for the (MWCNTs/W) emitter. The slope values of the

FN plot that relates to SWCNT emitter at low emission current value during the increasing and decreasing voltage cycles are -9434.37 Np and -8232.67 Np, respectively. The slope values of FN plot that relates to MWCNT emitter at low emission current value at increasing and decreasing applied voltage are -1114.63 Np and -12643 Np, respectively. Fig. 7 shows a set of emission current images for (SWCNT/W) and (MWCNT/W).

From Fig. 7, it can be seen that the emission current image of the SWCNT emitter is more concentrated than the emission current image of the MWCNT emitter at  $V_{SW}$  value. Also, the emission current value at  $V_{SW}$  of MWCNT emitter is higher than that of SWCNT emitter.

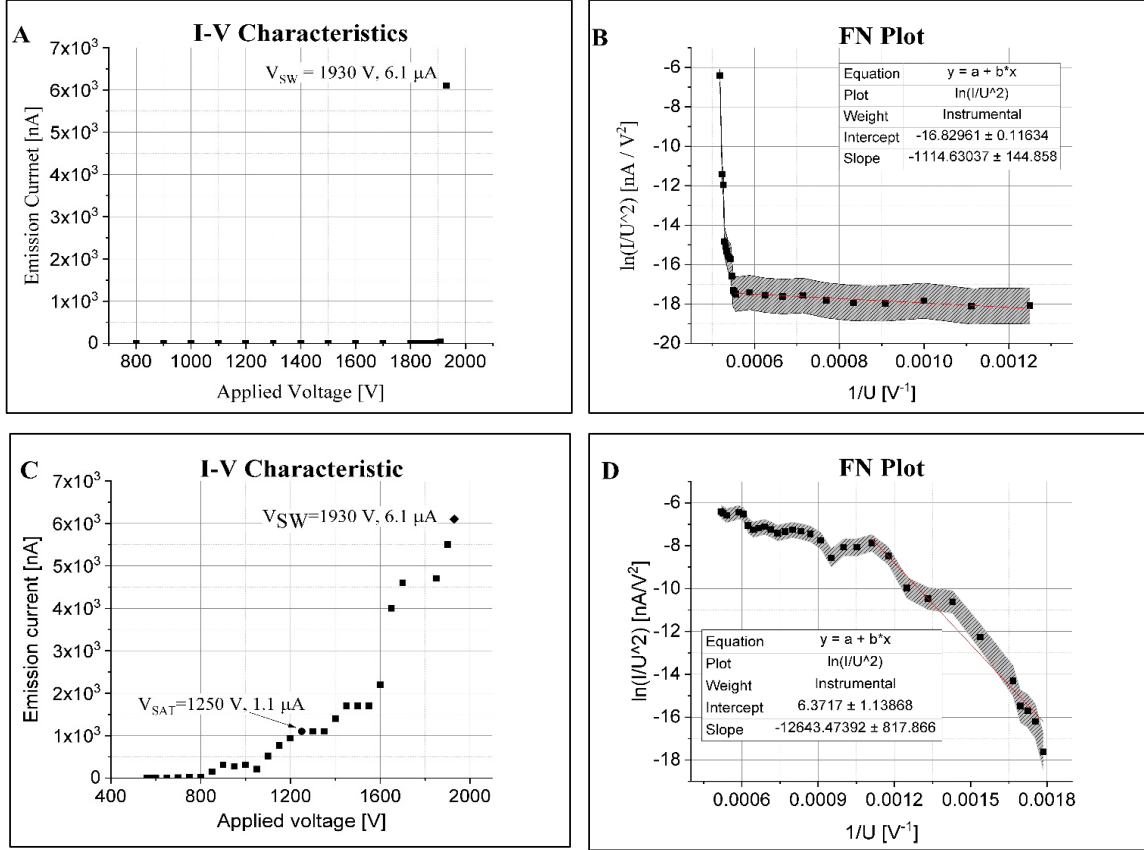


FIG. 6. For (MWCNTs/W). Cycle 2; at increasing voltage - (A) I-V characteristics and (B) FN plot. At decreasing voltage - (C) I-V characteristics and (D) FN plot.

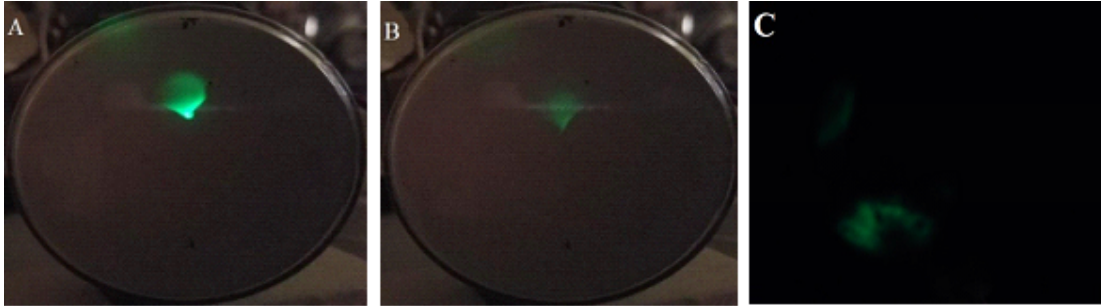


FIG. 7. Emission images at applied voltage (SWCNTs/W) (A)  $V_{SW} = 1250 \text{ V}$ ,  $I_{SW} = 2.9 \mu\text{A}$ . (B)  $V_{SAT} = 650 \text{ V}$ ,  $I_{SAT} = 1.06 \mu\text{A}$ . (MWCNTs/W) (C)  $V_{SW} = 1930 \text{ V}$ ,  $I_{SW} = 6.1 \mu\text{A}$ .

By comparing the slope value for the (SWCNTs/W) emitter with that of the (MWCNTs/W) emitter, according to [30], the slope value from the FN plot  $S$  is given as:

$$S = -6.44 \times 10^9 \times \phi^{3/2}(d/\gamma);$$

where  $S$  is the slope value from FN plot,  $\phi$  is the effective work function,  $d$  is the diameter of the CNT and  $\gamma$  is the field enhancement factor. According to the previous equation, it can be

found that the field enhancement factor value for (SWCNTs) is higher than that for (MWCNTs). This indicates that the field concentration at (SWCNT) emitter tip is higher than that in the case of (MWCNT) emitter. This can cause a reduction of the effective threshold voltage for emission [31].

It can be seen from the SEM images of (SWCNTs/W) and (MWCNTs/W) that the CNTs are not perfectly vertically aligned on the

tungsten tip. Vertically aligned CNTs are better than randomly aligned CNTs on tungsten tip, where the field enhancement factor in case of vertically aligned CNTs will be higher than for randomly aligned CNTs on tungsten tip [32]. The lower the number of CNTs mounted on tungsten tip, the higher the field enhancement factor value will be, because having a lower number of neighboring tubes will reduce the screening effect [33-34], but the emission current density will be lower due to lower active emission area.

## Conclusions

The emission current behavior has been recorded during increasing and decreasing cycles of the applied voltage on the emitter surface in order to obtain the FN plots. FN plots for both emitters have shown that the SWCNT emitter has a higher field enhancement factor, which is the reason behind the lower recorded value of the "switch-on" voltage, lower saturation region value and lower threshold voltage. For the SWCNT emitter, the "switch-on" phenomenon occurs at lower applied voltage value than that for the MWCNT emitter. Also, the saturation region extends down to lower voltage values in the case of SWCNT emitter than that in the

MWCNT emitter. But, the MWCNT emitter can emit a higher emission current than that emitted from the SWCNT emitter. From the I-V characteristics of the first cycle of increasing and decreasing of the applied voltage for both SWCNTs and MWCNTs (Figs. 3 and 4), it can be seen that the shape of I-V characteristics has a linear trend, that indicates the existence of a constant resistance somewhere at the CNT/substrate interface or along of the CNT.

In the future, a more accurate methodology will be used to mount the CNTs on the metallic base using nano-manipulator. This will enable to create more accurate uniformly aligned CNTs on metal substrates and create large-area field electron emitter (LAFE) of CNTs to compare its FEE characterization with that an individual CNT emitter. All of the above is for maintaining the ongoing research aiming at obtaining the optimum field electron emitter.

## Acknowledgments

The authors would like to thank the Deanship of Academic Research at Mu'tah University for supporting this work through research project number 241/19/120.

## References

- [1] Lan, Y., Wang, Y. and Ren, Z.F., *Advances in Physics*, 60 (4) (2011) 553.
- [2] Latham, R.V. and Mousa, M.S., *Journal of Physics D: Applied Physics*, 19 (4) (1986) 699.
- [3] Yunhan, L., Yonghai, S. and Yeow, J.T.W., *Nanotechnology*, 26 (24) (2015) 242001.
- [4] Iijima, S., *Nature*, 354 (6348) (1991) 56.
- [5] Iijima, S. and Ichihashi, T., *Nature*, 363 (6430) (1993) 603.
- [6] Heo, S., Ihsan, A., Yoo, S., Ali, G. and Cho, S., *Nanoscale Research Letters*, 5 (4) (2010) 720.
- [7] Nasir, S., Hussein, M.Z., Zainal, Z. and Yusof, N.A., *Materials*, 11 (2) (2018) 295.
- [8] Yu, M.-F., Lourie, O., Dyer, M.J., Moloni, K., Kelly, T.F. and Ruoff, R.S., *Science*, 287 (5453) (2000) 637.
- [9] Popov, V.N., *Materials Science and Engineering: R: Reports*, 43 (3) (2004) 61.
- [10] Peng, S., O'Keeffe, J., Wei, C., Cho, K., Kong, J., Chen, R., Franklin, N. and Dai, H., *Carbon Nanotube Chemical and Mechanical Sensors*. In: *International Workshop on Structural Health Monitoring*, (2001) 1-8.
- [11] Ruoff, R.S. and Lorents, D.C., *Carbon*, 33 (7) (1995) 925.
- [12] Hong, P.N., Thang, B.H., Hong, N.T., Lee, S. and Minh, P.N., *Journal of Physics: Conference Series*, 187 (2009) 012041.
- [13] Bianco, A., Kostarelos, K. and Prato, M., *Current Opinion in Chemical Biology*, 9 (6) (2005) 674.
- [14] Evtukh, A., Hartnagel, H., Yilmazoglu, O., Mimura, H. and Pavlidis, D., *"Vacuum Nanoelectronic Devices: Novel Electron Sources and Applications"*. (John Wiley and Sons, United Kingdom, 2015).

- [15] Liang, S.-D., "Quantum Tunneling and Field Electron Emission Theories". (World Scientific Publishing Co. Pte. Ltd., 2013) 1-387.
- [16] Lu, X., Yang, Q., Xiao, C. and Hirose, A., Journal of Physics D: Applied Physics, 39 (15) (2006) 3375.
- [17] Kleshch, V.I., Eremina, V.A., Serbun, P., Orekhov, A.S., Lützenkirchen-Hecht, D., Obraztsova, E.D. and Obraztsov, A.N., Physica Status Solidi (B), 255 (1) (2018) 1700268.
- [18] Bani-Ali, E. and Mousa, M.S., Applied Microscopy, 46 (2016) 244.
- [19] Mousa, M.S., IOP Conference Series: Materials Science and Engineering, 305 (1) (2018) 012025.
- [20] Müller, E.M., Zeitschrift für Physik, 106 (1937) 541.
- [21] Mousa, M.S., Surface Science, 266 (1-3) (1992) 110.
- [22] Revenikiotis, A., "Optimization of STM-Tip Preparation Methods". (Royal Institute of Technology (KTH), Stockholm, Sweden, 2010).
- [23] Mousa, M.S., Surface Science, 231 (1) (1990) 149.
- [24] Forbes, R., Deane, J., Fischer, A. and Mousa, M., Jordan J. Phy., 8 (2015) 125.
- [25] Forbes, R.G., Deane, J.H.B., Hamid, N. and Sim, H.S., Journal of Vacuum Science and Technology B: Microelectronics and Nanometer Structures Processing, Measurement and Phenomena, 22 (3) (2004) 1222.
- [26] Zhong, D.Y., Zhang, G.Y., Liu, S., Sakurai, T. and Wang, E.G., Applied Physics Letters, 80 (3) (2002) 506.
- [27] Pasquini, A., Picotto, G.B. and Pisani, M., Sensors and Actuators A: Physical, 123-124 (2005) 655.
- [28] Fischer, A., Mousa, M.S. and Forbes, R.G., Journal of Vacuum Science and Technology B, 31 (3) (2013) 032201.
- [29] Wang, W. and Li, Z., Mesoscale and Nanoscale Physics, 2012.
- [30] Cheng, T.C., Chen, P.Y. and Wu, S.Y., Nanoscale Research Letters, 7 (1) (2012) 125.
- [31] Peng, J., Li, Z., He, C., Deng, S., Xu, N., Zheng, X. and Chen, G., Physical Review B, 72 (23) (2005) 235106.
- [32] Cheng, Y. and Zhou, O., Comptes Rendus Physique, 4 (9) (2003) 1021.
- [33] Suh, J.S., Jeong, K.S., Lee, J.S. and Han, I., Applied Physics Letters, 80 (13) (2002) 2392.
- [34] Cai, D. and Liu, L., AIP Advances, 3 (12) (2013) 122103.



### A Genetic Algorithm for Addressing Computationally Expensive Optimization Problems in Optical Engineering

A. Mayer<sup>a</sup> and Michaël Lobet<sup>a,b</sup>

<sup>a</sup> *Department of Physics, University of Namur, Rue de Bruxelles 61, 5000 Namur, Belgium.*

<sup>b</sup> *John A. Paulson School of Engineering and Applied Sciences, Harvard University, 9 Oxford Street, 02138 Cambridge, MA, USA.*

---

*Received on: 2/7/2018;*

*Accepted on: 14/11/2018*

---

**Abstract:** We present a genetic algorithm that we developed in order to address computationally expensive optimization problems in optical engineering. The idea consists of working with a population of individuals representing possible solutions to the problem. The best individuals are selected. They generate new individuals for the next generation. Random mutations in the coding of parameters are introduced. This strategy is repeated from generation to generation until the algorithm converges to the global optimum of the problem considered. For computationally expensive problems, one can analyze the data collected by the algorithm in order to infer more rapidly the final solution. The use of a mutation operator that acts on randomly-shifted Gray codes helps the genetic algorithm escape local optima and enables a wider diversity of displacements. These techniques reduce the computational cost of optical engineering problems, where the design parameters have a finite resolution and are limited to a realistic range. We demonstrate the performance of this algorithm by considering a set of 22 benchmark problems in 5, 10 and 20 dimensions that reflect the conditions of these engineering problems. We finally show how these techniques accelerate the determination of optimal structures for the broadband absorption of electromagnetic radiations.

**Keywords:** Genetic Algorithm, Optical Engineering, Optimization, Quadratic Approximation, Gray Codes, Metamaterials.

**PACS:** 02.60.Pn, 42.15.Eq, 42.25.Bs, 78.67.Pt.

## Introduction

The design of optical devices requires at some point the search for optimal parameters in order to achieve maximal performances. With genetic algorithms (GAs), natural selection is mimicked in order to determine this set of optimal parameters. The idea consists of working with a virtual population of individuals representing possible solutions to the problem. The initial population consists of random individuals. The best individuals are then selected. They generate new individuals for the next generation. Random mutations in the coding of parameters are

finally introduced. When repeated from generation to generation, this strategy enables the determination of a globally optimal set of parameters [1-6].

Optical engineering problems are typically computationally expensive due to the numerous degrees of freedom and the CPU time involved by the numerical modeling. It is therefore desirable to solve the optimization problem ideally by a single run of the GA and with a reduced number of fitness evaluations. The fitness is defined as the objective function to be optimized. When the time required by

the fitness evaluations is largely superior to the time required by the GA itself, it makes sense to establish a record with all fitness evaluations in order to avoid any duplication of these calculations. The GA also gains at being organized in a way that enables all fitness calculations in a given generation to be addressed at the same time. This allows indeed a massive parallelization of these calculations on modern supercalculators. The genetic algorithm finally gains at being combined with a mathematical analysis of the collected data in order to accelerate convergence to the final solution. The objective is to determine the global optimum as quickly as possible (reduced number of generations) and with a reduced number of fitness evaluations.

One can guide the algorithm to promising directions and accelerate the refinement of the final solution by coupling the genetic algorithm with a local optimizer (memetic algorithm) [7-13]. A first approach consists of applying a local optimization procedure on the solutions established by the genetic algorithm, either regularly (starting from best-so-far solutions established at each generation by the GA) or after the GA has converged (starting from the final best solutions established by the GA) [5, 8]. This approach requires however an extra budget of fitness evaluations. Another approach consists of working on the data already collected by the genetic algorithm in order to avoid an increase in the number of fitness evaluations. An idea consists of establishing different approximations of the fitness (reduced models) in order to implement this local optimization [14-19], improve the genetic operators [20, 21], estimate the robustness of solutions [22] or avoid unnecessary evaluations of the fitness [23-25]. The data collected by the GA can actually be analyzed by a variety of mathematical methods. Methods based on the Singular Values Decomposition were used to estimate the evolution direction and increase the population diversity [26]. This technique was also used to qualify potential candidates for the next generation [27]. Recent papers finally considered training neural networks in order to guide the genetic algorithm [20, 28-31]. A neural network is then trained on the data collected by the GA in order to establish reduced models of the fitness and suggest promising solutions.

In optical engineering problems, the physical parameters to determine have a finite resolution due to physical or experimental limitations in the fabrication of a device [32-37]. The decision variables have therefore a finite number of possible values (typically of the order of 1000). A binary encoding of these decision variables offers the advantage to account for this discrete set of possible values at all stages of the algorithm. Optical engineering problems that rely on numerical simulations for the evaluation of the fitness have also as specificity the fact that the fitness is generally accurate to only three or four significant digits. Optimizing the fitness beyond this limited accuracy does not make any sense. The genetic algorithm on the contrary gains at being tuned to achieve a target accuracy that is both realistic and appropriate for these applications (typically  $\Delta f_{\text{target}} \sim 10^{-4}$ ).

We present in this article an algorithm that we developed in order to account for these different issues when addressing optical engineering problems. Our approach consists of establishing at each generation a quadratic approximation of the fitness in the close neighborhood of the best-so-far individual in order to infer more rapidly the global optimum. We also consider randomly-shifted Gray codes when applying mutations in order to improve exploration and escape local optima. These modifications of the well-known genetic algorithm reduce the computational cost of optical engineering problems, where the design parameters have a finite resolution and are limited to a realistic range. This article is organized as follows. The main lines of our algorithm are presented in the next section. Then, we apply our algorithm to typical benchmark problems in 5, 10 and 20 dimensions in order to demonstrate its performance. Then, we provide a real optical engineering application. Finally, we conclude this article.

## Description of the Genetic Algorithm

The genetic algorithm described in this section aims at determining the global optimum (depending on the application, it will be the global minimum or the global maximum) of an objective function  $f =$



$f(x_1, \dots, x_n)$ , where  $n$  is the number of decision variables.  $x_i \in [x_i^{\min}, x_i^{\max}]$ , with a discretization step  $\Delta x_i$ . The boundaries  $x_i^{\min}$  and  $x_i^{\max}$  must be specified at the beginning of the search.  $\Delta x_i$  accounts for the experimental resolution of each decision variable. The variables  $x_i$  are represented by sequences of binary digits (genes). We use the Gray code to interpret the bit content of these genes [5, 38]. The decision variables are then given by  $x_i = x_i^{\min} + \langle \text{gene } i \rangle \times \Delta_i$ , where  $\langle \text{gene } i \rangle \in [0, 2^{n_i} - 1]$  refers to the value of the gene. The bit length  $n_i$  of each gene is the first integer for which  $x_i^{\min} + (2^{n_i} - 1) \times \Delta_i \geq x_i^{\max}$ .  $n_{\text{bits}} = \sum_{i=1}^n n_i$  refers to the total number of bits in a DNA; i.e., the set of genes used for coding the  $n$  decision variables.

A detailed pseudocode of our algorithm can be found in Appendix A. We present here only the main ideas of this algorithm, which are as follows: We consider a population of  $n_{\text{pop}} = 50$  individuals. We start with a random population. We evaluate the fitness  $f(x_1, \dots, x_n)$  of each individual and sort the population from the best individual to the worst one. We save the computed  $\{\vec{x}, f(\vec{x})\}$  data in a record. We compute the genetic similarity  $s$  of the population;  $s$  corresponds to the fraction of bits in the population whose value is identical to the best individual [32, 38]. We then define a progress indicator  $p = |s - 0.5|/0.5$ , which takes values between 0 and 1. The worst  $n_{\text{rand}} = \text{even}[0.1 \times n_{\text{pop}} \times (1-p)]$  individuals of the population are then replaced by random individuals (even  $[\cdot]$  stands for the nearest even integer). These random individuals are transferred to the next generation. The remaining  $N = n_{\text{pop}} - n_{\text{rand}}$  individuals of the current population participate to the usual steps of selection, crossover and mutation. We hence select  $N$  parents in this subset of  $N$  individuals by a rank-based roulette wheel selection, noting that a given individual can be selected several times [5, 32]. For any pair of parents, we define two children for the next generation either (i) by a one-point crossover of the parents' DNA (probability of 70%) or (ii) by a simple replication of

the parents. The children obtained by crossover are subjected to a modified mutation operator that acts on randomly-shifted Gray codes (see Appendix B), using  $m = 0.95/n_{\text{bits}}$  as mutation rate for individual bit flips. We apply at this point a local optimization procedure on the  $\{\vec{x}, f(\vec{x})\}$  data collected so far by the genetic algorithm in order to guess the final solution (see Appendix C). If the result of this local optimization can be accepted, it replaces the last individual already scheduled for the next generation (a random individual if  $n_{\text{rand}} > 0$ ). Before evaluating the fitness of the individuals finally scheduled for the next generation, we check the records in order to avoid any duplication of these evaluations. We then evaluate the fitness of the individuals scheduled for the next generation for which no  $\{\vec{x}, f(\vec{x})\}$  data was found. We sort the new population and apply elitism in order to make sure that the best solution achieved so far is not lost when going from one generation to the next [5]. We apply these different steps from generation to generation until a termination criterion is met.

The organization of the algorithm ensures that all fitness calculations in a given generation can be evaluated in parallel, since there is only one round of fitness evaluations per generation. In this implementation, the parents are not transferred automatically to the next generation, since this leads to premature convergence to solutions that are not globally optimal. We found in previous, unpublished work that a crossover rate of 70% maintains a good balance between the conservation of good solutions (individuals transferred to the next generation without any modification) and the exploration of new solutions (individuals modified by the operators of crossover and mutation). The mutation rate  $m = 0.95/n_{\text{bits}}$  is settled automatically by the number of bits used for the representation of the decision variables. We found in previous work that the optimal mutation rate decreases with the dimension of the problem. Maintaining  $m \times n_{\text{bits}} < 1$  is also motivated by biological evidence [39]. This condition ensures

indeed that the best individuals in the population have a chance to be unaffected by mutations. We confirmed empirically that this improves in the long term the quality of the solutions established by the genetic algorithm. The use of a mutation operator that acts on randomly-shifted Gray codes helps the genetic algorithm escape local optima, since the displacements generated by this mutation operator have a wider diversity (see Appendix B). This improves also the exploration of the decision variable space. The local optimization procedure finally provides a useful guidance to the genetic algorithm by indicating, generation after generation, directions to consider based on collected data. The technical parameters of this algorithm were tuned on test problems in 5, 10 and 20 dimensions, for conditions that reflect those encountered in optical engineering problems [40]. We demonstrate the performance of this algorithm on an extended set of test problems in the next section.

### Application to Test Problems in 5, 10 and 20 Dimensions

In optical engineering problems that stimulated this work [32-34], the decision variables  $x_i$  must be determined only up to a precision  $\Delta x_i$  due to experimental limitations in the fabrication of a device. We will therefore consider in this section test problems for which  $\Delta x_i = (x_i^{\max} - x_i^{\min})/4096$  in order to reflect the conditions of these applications. This corresponds to  $n_i=12$  bits per gene, since  $2^{12} = 4096$ . We will also consider that the global minimum of the test problems considered in this section is found if the objective function is within a margin  $\Delta f_{\text{target}}$  of  $10^{-4}$  compared to the exact solution. This reflects again the accuracy with which solutions should be established in these optical engineering applications. Our objective was to determine the global minimum of this type of problems with a high chance of success in one run and with a reduced number of fitness evaluations (since we accept a margin  $\Delta f_{\text{target}}$  on the global minimum, technically we actually seek determining a "global  $\Delta f_{\text{target}}$ -optimal

solution". Since the algorithm is stochastic, there is of course no guarantee on optimality).

The 22 benchmark functions considered in this work are given in Table 1. The boundaries  $[x_i^{\min}, x_i^{\max}]$  considered for each function are provided as well as the number of bits  $n_i$  used for the representation of each decision variable ( $n_i=12$ , except for Schwefel 7, where  $n_i=16$ ) [41]. With this setting of the experiment, all gene values can be accepted and there is a point in the grid for which the target  $\Delta f_{\text{target}}$  of  $10^{-4}$  can actually be reached. In order to make sure that our results do not depend on a specific encoding of the decision variables and in order to break easy symmetries, we consider for each instance of the genetic algorithm a random shift of the domain  $[x_i^{\min}, x_i^{\max}]$  considered for each decision variable. This randomization of the boundaries is limited to integer multiples of  $\Delta x_i = (x_i^{\max} - x_i^{\min})/2^{n_i}$  in order to make sure that the point for which the target  $\Delta f_{\text{target}}$  of  $10^{-4}$  can actually be reached remains on the grid. The limits considered for this randomization of the boundaries are given in the fourth column of Table 1.

When running the genetic algorithm on a given function  $f(\vec{x})$  in order to determine its global minimum, we consider that the target  $\Delta f_{\text{target}}$  is reached if  $|f(\vec{x}_{\text{best}}) - f_{\text{opt}}^*| \leq \Delta f_{\text{target}}$ , where  $f(\vec{x}_{\text{best}})$  is the best-so-far solution found by the genetic algorithm and  $f_{\text{opt}}^*$  the exact global minimum. By running the genetic algorithm  $\# \text{run}$  times on each test function, we can measure the probability  $P(\Delta f_{\text{target}})$  with which the target  $\Delta f_{\text{target}}$  is reached by a given run of the algorithm. This quantity is calculated by  $P(\Delta f_{\text{target}}) = \# \text{success} / \# \text{run}$ , where  $\# \text{success}$  refers to the number of successful runs. We can also measure the average number of fitness evaluations required to reach  $\Delta f_{\text{target}}$ . This quantity is calculated by  $\langle n_{\text{eval}} \rangle = \# \text{eval}(\text{target not reached}) / \# \text{success}$ , where  $\# \text{eval}(\text{target not reached})$  is the number of fitness evaluations in all generations for which the target  $\Delta f_{\text{target}}$  was not reached

(summing over the #run executions of the GA) [11].  $\langle n_{\text{eval}} \rangle$  includes fitness evaluations in runs that failed to meet the target. Accounting for failed attempts makes sense, since they must be paid in real-world applications. They consume indeed CPU time and cause a delay in the resolution of a problem. Our efforts to tune the genetic algorithm therefore focusses on  $\langle n_{\text{eval}} \rangle$  as a measure for the computational cost associated with a given

target  $\Delta f_{\text{target}}$ . Another measure commonly used in the literature is  $\langle n_{\text{eval}}^* \rangle$ , the average number of fitness evaluations required to reach  $\Delta f_{\text{target}}$  when this target is actually reached.  $\langle n_{\text{eval}}^* \rangle$  does not account for failed attempts. Similarly,  $\langle n_{\text{gen}}^* \rangle$  measures the average number of generations required to reach a  $\Delta f_{\text{target}}$  for runs that actually reach this target.  $\langle n_{\text{gen}}^* \rangle$  is representative of how fast a solution is found, if found.

TABLE 1. List of test functions with the boundaries  $[x_i^{\min}, x_i^{\max}]$  considered for the decision variables and the number of bits  $n_i$  used for the representation of each gene. The fourth column indicates the limits considered for the randomization of the boundaries when running a given instance of the genetic algorithm. Names: Sphere (#1), Rotated Hyper-Ellipsoid (#2), Rosenbrock (#3), Modified Dixon-Price (#4), Mayer (#5), Schwefel 7 (#6), Levy (#7), Rastrigin (#8), Ackley (#9), Griewank (#10), Cosine Mixture (#11), Exponential (#12), Levy and Montalvo 1 (#13), Levy and Montalvo 2 (#14), Zakharov (#15), Schwefel 3 (#16), Brown 3 (#17), Cigar (#18), Sinusoidal (#19), Trigonometric 1 (#20), Pinter (#21) and Whitley (#22).

#	Formula	$[x_i^{\min}, x_i^{\max}]$	rand shift	$n_i$
1	$f(\vec{x}) = \sum_{i=1}^n x_i^2$	$[-5.12, 5.12]$	$[-0.5, 0.5]$	12
2	$f(\vec{x}) = \sum_{i=1}^n (\sum_{j=1}^i x_j)^2$	$[-65.5, 65.5]$	$[-5, 5]$	12
3	$f(\vec{x}) = \sum_{i=1}^{n-1} [100(x_{i+1} - x_i^2)^2 + (1 - x_i)^2]$	$[-2, 2]$	$[-0.2, 0.2]$	12
4	$f(\vec{x}) = n(x_1 - 1)^2 + \sum_{i=2}^n (2x_i^2 - x_{i-1})^2$	$[0, 10.24]$	$[0, 0.25]$	12
5	$f(\vec{x}) = -\prod_{i=1}^n \cos(x_i)^2 \exp(-x_i^2/10)$	$[-5, 5]$	$[-0.5, 0.5]$	12
6	$f(\vec{x}) = 418.98288727243 \times n - \sum_{i=1}^n x_i \sin(\sqrt{ x_i })$	$[-500, 500]$	$[-5, 10]$	16
7	$f(\vec{x}) = \sin^2(\pi w_1) + \sum_{i=1}^{n-1} (w_i - 1)^2 [1 + 10 \sin^2(\pi w_i + 1)] + (w_n - 1)^2 [1 + \sin^2(2\pi w_n)]$ , $w_i = 1 + (x_i - 1)/4$	$[-10.24, 10.24]$	$[-1, 1]$	12
8	$f(\vec{x}) = 10n + \sum_{i=1}^n (x_i^2 - 10 \cos(2\pi x_i))$	$[-5.12, 5.12]$	$[-0.5, 0.5]$	12
9	$f(\vec{x}) = -a \exp\left(-b \sqrt{\frac{1}{n} \sum_{i=1}^n x_i^2}\right) - \exp\left(\frac{1}{n} \sum_{i=1}^n \cos(cx_i)\right) + a + e$ , $a = 20, b = 0.2, c = 2\pi$	$[-32, 32]$	$[-3, 3]$	12
10	$f(\vec{x}) = 1 + \sum_{i=1}^n \frac{x_i^2}{4000} - \prod_{i=1}^n \cos(x_i/\sqrt{i})$	$[-600, 600]$	$[-50, 50]$	12
11	$f(\vec{x}) = 0.1 \times n + \sum_{i=1}^n x_i^2 - 0.1 \sum_{i=1}^n \cos(5\pi x_i)$	$[-1, 1]$	$[-0.1, 0.1]$	12
12	$f(\vec{x}) = 1 - \exp\left(-0.5 \sum_{i=1}^n x_i^2\right)$	$[-1, 1]$	$[-0.1, 0.1]$	12
13	$f(\vec{x}) = \frac{\pi}{n} (10 \sin^2(\pi w_1) + \sum_{i=1}^{n-1} (w_i - 1)^2 [1 + 10 \sin^2(\pi w_{i+1}) + (w_n - 1)^2])$ , $w_i = 1 + \frac{x_i + 1}{4}$	$[-10.24, 10.14]$	$[-1, 1]$	12
14	$f(\vec{x}) = 0.1 (\sin^2(3\pi x_1) + \sum_{i=1}^{n-1} (x_i - 1)^2 [1 + \sin^2(3\pi x_{i+1}) + (x_n - 1)^2 [1 + \sin^2(2\pi x_n)])]$	$[-5.12, 5.12]$	$[-0.5, 0.5]$	12
15	$f(\vec{x}) = \sum_{i=1}^n x_i^2 + (\frac{1}{2} \sum_{i=1}^n i x_i)^2 + (\frac{1}{2} \sum_{i=1}^n i x_i)^4$	$[-5.12, 5.12]$	$[-0.5, 0.5]$	12
16	$f(\vec{x}) = \sum_{i=1}^n  x_i  + \prod_{i=1}^n  x_i $	$[-10, 10]$	$[-1, 1]$	12
17	$f(\vec{x}) = \sum_{i=1}^{n-1} ((x_i^2)^{x_{i+1}^2+1} + (x_{i+1}^2)^{x_i^2+1})$	$[-1, 4]$	$[-0.1, 0.4]$	12
18	$f(\vec{x}) = x_1^2 + 100,000 \sum_{i=2}^n x_i^2$	$[-10, 10]$	$[-1, 1]$	12
19	$f(\vec{x}) = 3.5 - 2.5 \prod_{i=1}^n \sin(x_i - \frac{\pi}{6}) - \prod_{i=1}^n \sin(5(x_i - \frac{\pi}{6}))^2$	$[0, 3.1415]$	$[-0.1, 0.2]$	12
20	$f(\vec{x}) = \sum_{i=1}^n [n - \sum_{j=1}^n \cos x_j + i(1 - \cos x_i - \sin x_i)]^2$	$[0, 3.1415]$	$[-0.3, 0]$	12
21	$f(\vec{x}) = \sum_{i=1}^n i x_i^2 + \sum_{i=1}^n 20i \sin^2 A + \sum_{i=1}^n i \log_{10}(1 + i B^2)$ , $A = x_{i-1} \sin x_i + \sin x_{i+1}$ , $x_0 = x_n$ , $x_{n+1} = x_1$ , $B = x_{i-1}^2 - 2x_i + 3x_{i+1} - \cos x_i + 1$	$[-10, 10]$	$[-1, 1]$	12
22	$f(\vec{x}) = \sum_{i=1}^n \sum_{j=1}^n \left[ \frac{(100(x_i^2 - x_j)^2 + (1 - x_j)^2)^2}{4000} - \cos(100(x_i^2 - x_j)^2 + (1 - x_j)^2) + 1 \right]$	$[-10.24, 10.24]$	$[-1, 1]$	12

The results obtained with our algorithm, when considering the benchmark problems of Table 1 for  $n = 5$ , 10 and 20 dimensions, are summarized in Table 2. Tables 3, 4 and 5 provide the  $P(\Delta f_{\text{target}})$ ,  $\langle n_{\text{eval}} \rangle$ ,  $\langle n_{\text{eval}}^* \rangle$  and  $\langle n_{\text{gen}}^* \rangle$  values obtained for individual functions when considering a target  $\Delta f_{\text{target}}$  of  $10^{-4}$ . For these benchmark problems, we consider a maximum of  $30 \times n_{\text{bits}}$  generations for a given run of the algorithm. The algorithm is interrupted if (i) there is no improvement of the best fitness in the last  $1.5 \times n_{\text{bits}}$  generations, (ii) the mean value of the genetic similarity  $s$  over the last  $1.5 \times n_{\text{bits}}$  generations is higher than  $1-3m$ , (iii)  $s \geq 1-m$  or (iv) the number of fitness evaluations exceeds  $10000 \times n$ . The different columns of Table 2 show the results obtained when considering/not considering (i) local optimizations based on quadratic approximations of the fitness and (ii) a mutation operator that acts on randomly-shifted Gray codes. The table provides the probability of success in one run  $P(\Delta f_{\text{target}})$  and the average number of fitness evaluations  $\langle n_{\text{eval}} \rangle$  for different values of  $\Delta f_{\text{target}}$ . It also specifies the number of functions for which the target was reached at least once in ten runs. This comparison between different versions of our algorithm proves the advantage of using a mutation operator that acts on randomly-shifted Gray codes and a local optimization procedure that works on the data collected by the algorithm (see Appendix B and Appendix C).

By using the local optimization procedure and a mutation operator that acts on randomly-shifted Gray codes, we achieve a probability of success in one run  $P(\Delta f_{\text{target}})$  of 94.9% for  $n=5$  dimensions, 92.3% for  $n=10$  dimensions and 89.0% for  $n=20$  dimensions when considering a target  $\Delta f_{\text{target}}$  of  $10^{-4}$  (these values correspond to an average over the 22 benchmark problems; the values obtained for individual functions can be found in Tables 3, 4 and 5). The average number of fitness evaluations  $\langle n_{\text{eval}} \rangle$  required to reach this target is 1724 for  $n=5$  dimensions, 5104 for  $n=10$  dimensions and 19870 for  $n=20$  dimensions. This

corresponds to  $\langle n_{\text{eval}} \rangle / n$  ratios of 345 for  $n = 5$  dimensions, 510 for  $n = 10$  dimensions and 993 for  $n = 20$  dimensions. We meet therefore our objective to determine the global minimum of these test problems with a high probability of success in one run ( $P(\Delta f_{\text{target}}) = 89-95\%$ ), while keeping to a budget of fitness evaluations  $\langle n_{\text{eval}} \rangle$  of the order of  $\sim 1000 \times n$ . In contrast, when the techniques presented in the two Appendices are not used, the probability of success in one run  $P(\Delta f_{\text{target}})$  is reduced to 75.6% for  $n=5$  dimensions, 62.5% for  $n=10$  dimensions and 46.7% for  $n=20$  dimensions. The number of functions for which the global minimum is determined at least once in ten runs decreases rapidly with the dimension of the problem, going from 18 functions out of 22 for problems in 5 dimensions to only 15 functions out of 22 for problems in 20 dimensions. The average number of fitness evaluations required to reach a given target is also significantly higher.

The local optimization procedure improves significantly the ability of the genetic algorithm to determine the global minimum (a global  $\Delta f_{\text{target}}$ -optimal solution) of the functions considered (increase of  $P(\Delta f_{\text{target}})$ ). This conclusion was tested for statistical significance [42]. This technique also accelerates the algorithm by reducing the number of fitness evaluations (decrease of  $\langle n_{\text{eval}} \rangle$ ). Although originally intended to accelerate the refinement of the final solution, this technique actually provides a useful guidance to the genetic algorithm by indicating, generation after generation, directions to consider based on collected data. This is especially useful for functions that require displacements in preferential directions, like the function #3 (Rosenbrock). It is also useful for functions whose large-scale structure leads to the global minimum despite the presence of many local minima, like the function #10 (Griewank). For functions that have a single minimum, like the function #1 (Sphere) and the function #2 (Rotated Hyper-Ellipsoid), the procedure is actually able to finalize the

minimization as soon as a sufficient number of data points have been collected. Other functions, like the function #12 (Exponential), the function #17 (Brown 3)

and the function #18 (Cigar), have their global minimum also much more rapidly determined.

TABLE 2. Results obtained for test problems in 5, 10 and 20 dimensions. The different columns correspond to results obtained when considering/not considering (i) local optimizations based on quadratic approximations of the fitness and (ii) a mutation operator that acts on randomly-shifted Gray codes.  $P(\Delta f_{\text{target}})$  represents the probability to reach a target  $\Delta f_{\text{target}}$  by a single run of the GA.  $\langle n_{\text{eval}} \rangle$  is the average number of fitness evaluations required to reach this target, counting runs that fail to meet the target. #fct( $P \geq 10\%$ ) is the number of functions for which the target was reached at least once in ten runs. The last column provides for comparison the results obtained with CMA-ES when using the same population size of 50 individuals. These statistics were generated by running the genetic algorithm 100 times on each test function.

#### 5 dimensions

$\Delta f_{\text{target}}$	Local Optim.	no	no	yes	yes	CMA-ES
	Shifted Gray	no	yes	no	yes	
$10^{-4}$	$P(\Delta f_{\text{target}})$	75.6%	83.2%	87.0%	94.9%	83.7%
	$\langle n_{\text{eval}} \rangle$	9051	7867	1866	1724	3287
	#fct( $P \geq 10\%$ )	18/22	20/22	21/22	all	21/22
$10^{-3}$	$P(\Delta f_{\text{target}})$	75.8%	83.4%	87.1%	94.9%	83.7%
	$\langle n_{\text{eval}} \rangle$	8256	7153	1751	1622	3017
	#fct( $P \geq 10\%$ )	18/22	20/22	21/22	all	21/22
$10^{-2}$	$P(\Delta f_{\text{target}})$	78.8%	86.4%	87.2%	94.9%	85.4%
	$\langle n_{\text{eval}} \rangle$	7037	5990	1604	1488	2630
	#fct( $P \geq 10\%$ )	19/22	20/22	21/22	all	21/22
$10^{-1}$	$P(\Delta f_{\text{target}})$	83.5%	91.6%	88.5%	95.5%	87.4%
	$\langle n_{\text{eval}} \rangle$	5389	4436	1248	1173	2170
	#fct( $P \geq 10\%$ )	21/22	all	21/22	all	21/22

#### 10 dimensions

$\Delta f_{\text{target}}$	Local Optim.	no	no	yes	yes	CMA-ES
	Shifted Gray	no	yes	no	yes	
$10^{-4}$	$P(\Delta f_{\text{target}})$	62.5%	78.3%	77.8%	92.3%	81.7%
	$\langle n_{\text{eval}} \rangle$	30884	22981	5928	5104	6891
	#fct( $P \geq 10\%$ )	17/22	18/22	19/22	21/22	19/22
$10^{-3}$	$P(\Delta f_{\text{target}})$	63.4%	78.5%	78.1%	92.5%	81.7%
	$\langle n_{\text{eval}} \rangle$	28144	20834	5698	4892	6399
	#fct( $P \geq 10\%$ )	17/22	18/22	19/22	all	19/22
$10^{-2}$	$P(\Delta f_{\text{target}})$	67.0%	82.9%	78.5%	92.6%	81.9%
	$\langle n_{\text{eval}} \rangle$	24387	17323	5302	4541	5865
	#fct( $P \geq 10\%$ )	18/22	20/22	19/22	all	19/22
$10^{-1}$	$P(\Delta f_{\text{target}})$	71.8%	87.6%	79.2%	92.6%	82.0%
	$\langle n_{\text{eval}} \rangle$	19331	13371	4462	3896	5289
	#fct( $P \geq 10\%$ )	20/22	21/22	19/22	all	19/22

#### 20 dimensions

$\Delta f_{\text{target}}$	Local Optim.	no	no	yes	yes	CMA-ES
	Shifted Gray	no	yes	no	yes	
$10^{-4}$	$P(\Delta f_{\text{target}})$	46.7%	76.1%	62.2%	89.0%	72.0%
	$\langle n_{\text{eval}} \rangle$	108941	61676	29643	19870	16081
	#fct( $P \geq 10\%$ )	15/22	18/22	17/22	20/22	18/22
$10^{-3}$	$P(\Delta f_{\text{target}})$	48.4%	76.4%	62.7%	89.3%	72.0%
	$\langle n_{\text{eval}} \rangle$	98986	56276	27280	18325	15242
	#fct( $P \geq 10\%$ )	15/22	18/22	17/22	20/22	18/22
$10^{-2}$	$P(\Delta f_{\text{target}})$	50.1%	79.5%	63.1%	89.5%	72.0%
	$\langle n_{\text{eval}} \rangle$	90715	49375	25404	16989	14377
	#fct( $P \geq 10\%$ )	15/22	19/22	17/22	20/22	18/22
$10^{-1}$	$P(\Delta f_{\text{target}})$	59.4%	84.9%	64.9%	89.6%	72.0%
	$\langle n_{\text{eval}} \rangle$	68611	39038	22229	15133	13426
	#fct( $P \geq 10\%$ )	16/22	20/22	17/22	20/22	18/22

TABLE 3. Results obtained for each test function when considering a target  $\Delta f_{\text{target}}$  of  $10^{-4}$  for problems in 5 dimensions. The local optimization procedure as well as a mutation operator that acts on randomly-shifted Gray codes are used by the genetic algorithm. The quantities represented are the probability of success in one run ( $P(\Delta f_{\text{target}})$ ), the average number of fitness evaluations required to reach the target counting runs that fail to meet the target ( $\langle n_{\text{eval}} \rangle$ ), the average number of fitness evaluations required to reach the target counting only runs that reach the target ( $\langle n_{\text{eval}}^* \rangle$ ) and the average number of generations required to reach the target counting only runs that reach the target ( $\langle n_{\text{gen}}^* \rangle$ ).  $\langle n_{\text{gen}}^* \rangle$  corresponds to the number of generations beyond that associated with the initial population. The standard deviation (std) of  $\langle n_{\text{eval}} \rangle$ ,  $\langle n_{\text{eval}}^* \rangle$  and  $\langle n_{\text{gen}}^* \rangle$  is also indicated. These statistics were generated by running the genetic algorithm 100 times on each test function.

$n=5$ dimensions				
#	$P$	$\langle n_{\text{eval}} \rangle$	$\langle n_{\text{eval}}^* \rangle$	$\langle n_{\text{gen}}^* \rangle$
1	100%	$85 \pm 4$	$85 \pm 4$	$1 \pm 0$
2	100%	$86 \pm 5$	$86 \pm 5$	$1 \pm 0$
3	99%	$6250 \pm 1147$	$6156 \pm 1102$	$187 \pm 34$
4	100%	$1333 \pm 166$	$1333 \pm 166$	$38 \pm 5$
5	100%	$953 \pm 209$	$953 \pm 209$	$26 \pm 7$
6	100%	$1403 \pm 603$	$1403 \pm 603$	$42 \pm 22$
7	100%	$1235 \pm 213$	$1235 \pm 213$	$35 \pm 7$
8	95%	$2754 \pm 733$	$2565 \pm 694$	$85 \pm 27$
9	100%	$1823 \pm 343$	$1823 \pm 343$	$55 \pm 11$
10	95%	$1186 \pm 736$	$1004 \pm 474$	$30 \pm 17$
11	100%	$513 \pm 79$	$513 \pm 79$	$13 \pm 2$
12	100%	$270 \pm 55$	$270 \pm 55$	$6 \pm 2$
13	100%	$1040 \pm 215$	$1040 \pm 215$	$30 \pm 7$
14	100%	$1133 \pm 221$	$1133 \pm 221$	$33 \pm 7$
15	100%	$1893 \pm 392$	$1893 \pm 392$	$55 \pm 12$
16	100%	$1777 \pm 300$	$1777 \pm 300$	$54 \pm 10$
17	100%	$654 \pm 91$	$654 \pm 91$	$17 \pm 3$
18	100%	$1199 \pm 478$	$1199 \pm 478$	$41 \pm 18$
19	98%	$991 \pm 427$	$928 \pm 298$	$26 \pm 11$
20	87%	$2571 \pm 1392$	$1978 \pm 1152$	$60 \pm 42$
21	99%	$1341 \pm 669$	$1295 \pm 585$	$37 \pm 18$
22	14%	$43640 \pm 6590$	$2727 \pm 490$	$85 \pm 16$

The use of a mutation operator that acts on randomly-shifted Gray codes provides a further boost to our results. Table 2 reveals indeed that the probability to determine the global minimum (a global  $\Delta f_{\text{target}}$ -optimal solution) of the functions considered by a single run of the genetic algorithm is improved by this technique. This conclusion was also tested for statistical significance [43]. It applies whether the local optimization procedure is used or not. Table 2 reveals consistently that the number of fitness evaluations required to determine the global minimum of the functions considered is reduced by this technique. The use of randomly-shifted Gray codes when applying mutations helps the genetic algorithm

escape local minima, since the displacements generated by these mutations have a wider diversity (see Appendix A). This is especially useful for functions with many local minima, like the function #6 (Schwefel), the function #8 (Rastrigin), the function #11 (Cosine Mixture), the function #13 (Levy and Montalvo 1), the function #14 (Levy and Montalvo 2) and the function #21 (Pinter). The wider variety of displacements generated by the use of randomly-shifted Gray codes improves exploration of the decision variable space, which results in a higher probability to detect the global minimum of the functions considered. This technique represents a useful complement to the local optimization procedure used in this work.



TABLE 4. Results obtained for each test function when considering a target  $\Delta f_{\text{target}}$  of  $10^{-4}$  for problems in 10 dimensions. The local optimization procedure as well as a mutation operator that acts on randomly-shifted Gray codes are used by the genetic algorithm. The quantities represented are the probability of success in one run ( $P(\Delta f_{\text{target}})$ ), the average number of fitness evaluations required to reach the target counting runs that fail to meet the target ( $\langle n_{\text{eval}} \rangle$ ), the average number of fitness evaluations required to reach the target counting only runs that reach the target ( $\langle n_{\text{eval}}^* \rangle$ ) and the average number of generations required to reach the target counting only runs that reach the target ( $\langle n_{\text{gen}}^* \rangle$ ).  $\langle n_{\text{gen}}^* \rangle$  corresponds to the number of generations beyond that associated with the initial population. The standard deviation (std) of  $\langle n_{\text{eval}} \rangle$ ,  $\langle n_{\text{eval}}^* \rangle$  and  $\langle n_{\text{gen}}^* \rangle$  is also indicated. These statistics were generated by running the genetic algorithm 100 times on each test function.

#	$n=10$ dimensions			
	$P$	$\langle n_{\text{eval}} \rangle$	$\langle n_{\text{eval}}^* \rangle$	$\langle n_{\text{gen}}^* \rangle$
1	100%	121±6	121±6	2±0
2	100%	120±7	120±7	2±0
3	99%	16962±3162	16766±3151	522±102
4	100%	3016±341	3016±341	90±11
5	100%	2407±372	2407±372	72±12
6	99%	4298±1445	4214±1383	136±51
7	100%	3164±414	3164±414	95±13
8	94%	7800±1720	7264±1673	251±67
9	100%	4952±666	4952±666	155±22
10	100%	458±580	458±580	12±19
11	100%	1079±196	1079±196	30±6
12	100%	585±58	585±58	15±2
13	100%	2352±361	2352±361	70±11
14	100%	2598±567	2598±567	78±19
15	100%	11596±2080	11596±2080	356±65
16	100%	6067±1041	6067±1041	197±37
17	100%	1495±219	1495±219	43±7
18	100%	2063±878	2063±878	75±35
19	98%	2449±722	2315±396	68±12
20	34%	26531±4548	9785±3652	308±126
21	100%	3541±1105	3541±1105	108±35
22	7%	260736±24993	11907±5253	397±189

The genetic algorithm presented in this work generally achieves good results on the test problems considered. The functions #20 (Trigonometric 1) and #22 (Whitley) remain however challenging. It is interesting at this point to compare our results with those provided by the reference algorithm CMA-ES [44-46]. CMA-ES, for Covariance-Matrix Adaptation-Evolution Strategy, is a genetic algorithm that relies on a real-value encoding of the decision variables.

Mutations consist of random normally-distributed perturbations of the decision variables. The covariance matrix that actually controls the distribution of these mutations is adapted along the optimization. When applying CMA-ES to our test problems with the same population size of 50 individuals, it actually achieves a probability of success in one run  $P(\Delta f_{\text{target}} = 10^{-4})$  of 84.1% for  $n=5$  dimensions, 81.7% for  $n=10$  dimensions and 72.0% for  $n=20$

dimensions [47]. These results are included in Table 2. A detailed analysis of the results achieved with CMA-ES on individual test functions for  $n=20$  dimensions can be found in Table 6. The comparison with Table 5 shows that the algorithm presented in this work achieves respectable performances for the class of

problems considered. The use of a mutation operator that acts on randomly-shifted Gray codes enables indeed our genetic algorithm to escape local optima more easily. This improves its ability to determine the true global minimum of the multimodal functions considered in this work.

TABLE 5. Results obtained for each test function when considering a target  $\Delta f_{\text{target}}$  of  $10^{-4}$  for problems in 20 dimensions. The local optimization procedure as well as a mutation operator that acts on randomly-shifted Gray codes are used by the genetic algorithm. The quantities represented are the probability of success in one run ( $P(\Delta f_{\text{target}})$ ), the average number of fitness evaluations required to reach the target counting runs that fail to meet the target ( $\langle n_{\text{eval}} \rangle$ ), the average number of fitness evaluations required to reach the target counting only runs that reach the target ( $\langle n_{\text{eval}}^* \rangle$ ) and the average number of generations required to reach the target counting only runs that reach the target ( $\langle n_{\text{gen}}^* \rangle$ ).  $\langle n_{\text{gen}}^* \rangle$  corresponds to the number of generations beyond that associated with the initial population. The standard deviation (std) of  $\langle n_{\text{eval}} \rangle$ ,  $\langle n_{\text{eval}}^* \rangle$  and  $\langle n_{\text{gen}}^* \rangle$  is also indicated. These statistics were generated by running the genetic algorithm 100 times on each test function.

$n=20$ dimensions				
#	$P$	$\langle n_{\text{eval}} \rangle$	$\langle n_{\text{eval}}^* \rangle$	$\langle n_{\text{gen}}^* \rangle$
1	100%	284±11	284±11	6±0
2	100%	283±11	283±11	6±0
3	98%	74216±17673	72168±17207	2340±572
4	100%	9700±1271	9700±1271	303±41
5	100%	6313±757	6313±757	194±24
6	99%	11840±2766	11624±2586	377±98
7	100%	8380±818	8380±818	259±26
8	97%	18950±3498	18269±3430	631±138
9	100%	13833±1458	13833±1458	444±50
10	100%	623±1102	623±1102	18±37
11	100%	3893±759	3893±759	118±24
12	100%	2228±323	2228±323	65±10
13	100%	6264±809	6264±809	193±27
14	100%	8142±1519	8142±1519	255±56
15	95%	89761±11592	84907±11222	2707±367
16	100%	18387±2402	18387±2402	620±87
17	100%	3986±442	3986±442	120±14
18	100%	3715±1389	3715±1389	143±56
19	91%	7866±2975	6354±815	195±28
20	4%	677342±48424	49436±19695	1590±674
21	73%	40537±22437	24540±15579	799±526
22	1%	5108453	44272	1509



TABLE 6. Results obtained with CMA-ES for each test function when considering a target  $\Delta f_{\text{target}}$  of  $10^{-4}$  for problems in 20 dimensions. CMA-ES is used with a population size of 50 individuals. The quantities represented are the probability of success in one run ( $P(\Delta f_{\text{target}})$ ), the average number of fitness evaluations required to reach the target counting runs that fail to meet the target ( $\langle n_{\text{eval}} \rangle$ ), the average number of fitness evaluations required to reach the target counting only runs that reach the target ( $\langle n_{\text{eval}}^* \rangle$ ) and the average number of generations required to reach the target counting only runs that reach the target ( $\langle n_{\text{gen}}^* \rangle$ ).  $\langle n_{\text{gen}}^* \rangle$  corresponds to the number of generations beyond that associated with the initial population. The standard deviation (std) of  $\langle n_{\text{eval}} \rangle$ ,  $\langle n_{\text{eval}}^* \rangle$  and  $\langle n_{\text{gen}}^* \rangle$  is also indicated. These statistics were generated by running CMA-ES 100 times on each test function.

$n=20$ dimensions (CMA-ES)				
#	$P$	$\langle n_{\text{eval}} \rangle$	$\langle n_{\text{eval}}^* \rangle$	$\langle n_{\text{gen}}^* \rangle$
1	100%	4582±214	4582±214	92±4
2	100%	9000±314	9000±314	180±6
3	100%	34559±1151	34559±1151	691±23
4	100%	6662±310	6662±310	133±6
5	4%	22162±15607	5688±278	114±6
6	0%	/	/	/
7	100%	5704±263	5704±263	114±5
8	0%	/	/	/
9	96%	9261±1882	8622±378	172±8
10	100%	7250±293	7250±293	145±6
11	99%	4804±741	4685±211	94±4
12	100%	3399±191	3399±191	68±4
13	100%	5010±302	5010±302	100±6
14	100%	5022±316	5022±316	100±6
15	100%	8199±313	8199±313	164±6
16	100%	9232±341	9232±341	185±7
17	100%	5532±327	5532±327	111±7
18	100%	14186±451	14186±451	284±9
19	28%	104618±47707	6322±3318	126±66
20	23%	67967±3169	13818±1450	276±29
21	35%	39899±6176	9197±605	184±12
22	0%	/	/	/

## Application in Optical Engineering

In order to provide a real-world application in optical engineering, we consider the maximization of broadband absorption by a metamaterial. The structures considered in this work consist of 2-D periodic arrays of truncated square-based pyramids made of 3 stacks of titanium/poly (methyl methacrylate) (Ti/PMMA) layers (see Fig. 1). These pyramids stand on a flat support that consists of successive uniform layers of Au (60 nm), Cr (5 nm) and amorphous Si (1 micron). Previous work has shown that periodic arrays of truncated square-based

pyramids made of successive stacks of metal/dielectric layers can lead to the quasi-perfect absorption of electromagnetic radiations over a wide wavelength range. By considering pyramids made of 20 stacks of Au/Ge layers, Lobet et al. could indeed achieve an integrated absorptance of 98% of incident light over a 0.2-5.8  $\mu\text{m}$  wavelength range [48, 49]. This ultra-broadband absorption is essentially due to (i) an efficient anti-reflection property of these pyramidal structures [50, 51] and (ii) a well-designed coupling between the localized surface plasmons found at the metal/dielectric interfaces of each stack [52-55].

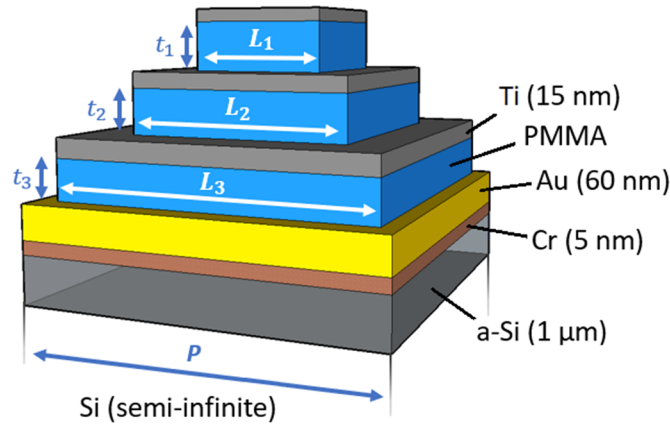


FIG. 1. Square-based pyramids made of 3 stacks of Ti/PMMA layers. The support of the pyramids consists of uniform layers of Au (60 nm), Cr (5 nm) and a-Si (1 micron). We assume an infinite substrate of Si ( $\epsilon=16$ ).

In order to reduce the difficulty of fabricating structures made of many different layers, we will consider in this work pyramids that consist of only three stacks of Ti/PMMA layers (see Fig. 1 again). Our objective is to maximize the absorption of incident radiations in the wavelength range 420-1600 nm by tuning the geometrical parameters of the system. The objective function (fitness) for this problem is therefore defined by  $\eta(\%) =$

$100 \times \frac{\int_{\lambda_{\min}}^{\lambda_{\max}} A(\lambda) d\lambda}{\lambda_{\max} - \lambda_{\min}}$ , where  $\lambda_{\min}=420$  nm and  $\lambda_{\max}=1600$  nm.  $A(\lambda)$  refers to the absorptance of normally incident radiations at the wavelength  $\lambda$ . It is calculated by a Rigorous Coupled Waves Analysis (RCWA) method [56, 57]. This method solves Maxwell's equations numerically in laterally periodic systems. We used this method with  $11 \times 11$  plane waves and reported values for the refractive indices [58-60]. The parameters to determine in order to maximize the figure of merit  $\eta$  are (i) the lateral period  $P$  of the system, (ii) the lateral dimensions  $L_1$ ,  $L_2$  and  $L_3$  of the three stacks of Ti/PMMA layers and (iii) the thicknesses  $t_1$ ,  $t_2$  and  $t_3$  of the three PMMA layers (the subscripts 1, 2 and 3 refer respectively to the top, medium and bottom stacks of the nanopylramids). The thickness of each Ti layer is fixed at 15 nm. In order to reduce the search to a realistic range, we actually consider  $P$  values between 50 and 500 nm,  $L_1$ ,  $L_2$  and  $L_3$  values between 50 and 500 nm and  $t_1$ ,  $t_2$ ,  $t_3$  values between 50 and 250 nm. We account for the experimental

resolution with which these structures can possibly be fabricated by considering a discretization step of 1 nm for these different quantities. In order to obtain pyramidal structures, we finally impose that the genetic algorithm only considers solutions for which  $L_1 < L_2 < L_3 \leq P$  [61]. With these specifications, we hence have seven decision variables to determine and  $1.3 \times 10^{16}$  possible parameter combinations! Each simulation takes approximately one hour of CPU time. We are therefore in conditions where it is impossible to test all parameter combinations. We are also in conditions where the time required by the fitness evaluations is largely superior to the time required for running the genetic algorithm.

In order to show the advantage of using the techniques developed in Appendix B and Appendix C, we represent in Fig. 2 the fitness (figure of merit  $\eta$ ) of the best individual as a function of the number of generations. When using a mutation operator that acts on randomly-shifted Gray codes (Appendix B) and a local optimization procedure that analyzes the collected data (Appendix C), the genetic algorithm determines after 167 generations and 4628 fitness evaluations the final solution (global optimum associated with a figure of merit  $\eta=99.757\%$ ; the parameters found by the GA are the following:  $L_1=155$  nm,  $t_1=124$  nm,  $L_2=285$  nm,  $t_2=126$  nm,  $L_3=416$  nm,  $t_3=98$  nm and  $P=416$  nm). If all fitness calculations in a given

generation run in parallel, this solution is actually obtained after 7 days. When the techniques described in Appendix B and Appendix C are not used, the genetic algorithm stops after 266 generations and 6275 fitness evaluations without finding the global optimum (the solution found in this case corresponds to a figure of merit  $\eta=99.726\%$ ; the parameters associated with this solution are the following:  $L_1=161$  nm,  $t_1=125$  nm,  $L_2=295$  nm,  $t_2=126$  nm,  $L_3=431$  nm,  $t_3=97$  nm and  $P=431$  nm). The GA stopped in this case, because the mean value of the genetic similarity  $s$  over the last  $1.5 \times n_{\text{bits}}$  generations was higher than  $1-3m$ , where the total number of bits  $n_{\text{bits}}$  is 60 and the

mutation rate  $m=0.95/n_{\text{bits}}$  is 1.6% for this application. If all fitness calculations in a given generation run in parallel, this sub-optimal solution is obtained after 11 days. As shown in the previous section, several runs are typically necessary on difficult problems when the techniques of Appendix B and Appendix C are not used. This would be the case here. Fig. 2 shows that the modified version of the genetic algorithm (techniques of Appendix B and Appendix C used) actually outperforms the classical version of the genetic algorithm (techniques of Appendix B and Appendix C not used) after only 50 generations.

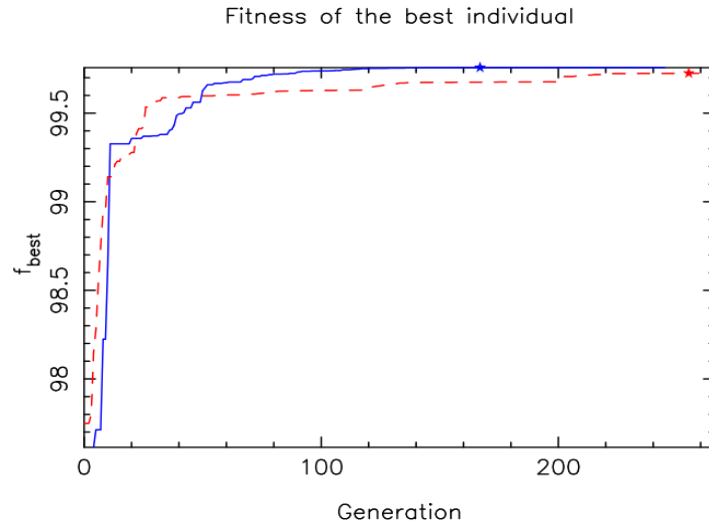


FIG. 2. Best fitness (figure of merit  $\eta$ ) when optimizing a structure made of three stacks of Ti/PMMA layers. Solid: the GA is used with a mutation operator that acts on randomly-shifted Gray codes (Appendix B) and a local optimization procedure (Appendix C). Dashed: the GA does not use the techniques developed in Appendix B and Appendix C. The stars indicate when the best solution is found.

## Conclusions

This article describes a genetic algorithm that we developed in order to address computationally expensive optimization problems in optical engineering. For these problems, the decision variables are characterized by a finite set of possible values due to experimental limitations in the fabrication of a device. A target accuracy of  $10^{-4}$  on the objective function is also sufficient for these applications. The technical parameters of our algorithm were tuned to address these conditions. The organization of the algorithm enables a massive

parallelization of the fitness calculations. The data collected by the genetic algorithm is analyzed by a local optimization procedure in order to infer more rapidly the final solution. This procedure, which relies on quadratic approximations of the fitness in the close neighborhood of the best-so-far solution, provides a useful guidance to the genetic algorithm by indicating, generation after generation, directions to consider based on these collected data. We also use a mutation operator that acts on randomly-shifted Gray codes. This helps the genetic algorithm escape local optima. It also improves the exploration of the decision

variable space by enabling a wider diversity of displacements. We applied this algorithm to a set of 22 benchmark problems in 5, 10 and 20 dimensions in order to demonstrate its performance. The results prove that the techniques presented in this work improve significantly the ability of the genetic algorithm to determine the global minimum of these problems. The average number of fitness evaluations required to determine these solutions is also significantly reduced. This algorithm was already applied successfully to a variety of computationally expensive optimization problems in optical engineering. We showed in this article how these techniques accelerate the optimization of square-based pyramidal structures for the broadband absorption of electromagnetic radiations.

## Appendix A: Pseudocode of the Genetic Algorithm

Initialize a Population of  $n_{\text{pop}}$  random individuals.  
 Compute the fitness  $f(\vec{x})$  of each individual in the Population.  
 Save the calculated  $\{\vec{x}, f(\vec{x})\}$  data in the Records.  
 Sort the Population from best to worst individuals.  
 Save  $\{\vec{x}_{\text{best}}, f_{\text{best}}\}$ =best-so-far solution.

For  $k$  ranging from 1 to  $n_{\text{gen}}$ :

  Compute genetic similarity  $s$  of the Population.  
  Set  $p = |s - 0.5|/0.5$ ,  
   $n_{\text{rand}} = \text{even}[0.1 \times n_{\text{pop}} \times (1-p)]$  and  $N = n_{\text{pop}} - n_{\text{rand}}$ .  
  Define, for the modified mutation operator, a random shift  $i \in [0, 2^{n_i} - 1]$  for each gene  $i \in [1, n]$ .

  Pool( $N+1:n_{\text{pop}}$ ) =  $n_{\text{rand}}$  random individuals.

  For  $i$  ranging from 1 to  $N/2$ :

    Select Parent<sub>1</sub> in Population(1: $N$ ) by a rank-based roulette wheel selection.

    Select Parent<sub>2</sub> in Population(1: $N$ ) by a rank-based roulette wheel selection.

    If  $\text{rnd} \leq 0.7$ :

      {Child<sub>1</sub>, Child<sub>2</sub>} = 1-point crossover between {Parent<sub>1</sub>, Parent<sub>2</sub>}.

      Apply\_Mutation=True.

    Else:

      {Child<sub>1</sub>, Child<sub>2</sub>} = {Parent<sub>1</sub>, Parent<sub>2</sub>}.

    Apply\_Mutation=False.

  If Apply\_Mutation:

    Apply modified mutation operator on Child<sub>1</sub> (see Appendix B).

    Apply modified mutation operator on Child<sub>2</sub> (see Appendix B).

    Pool( $1+(i-1)*2$ )=Child<sub>1</sub>.

    Pool( $2+(i-1)*2$ )=Child<sub>2</sub>.

    Guess=Local Optimization using  $\{\vec{x}, f(\vec{x})\}$  data in the Records (see Appendix C).

  If Guess can be accepted:

    Pool( $N$ )=Guess.

Check the Records to avoid any duplication in the fitness evaluations.

Compute the fitness  $f(\vec{x})$  of each new individual in the Pool.

Save the calculated  $\{\vec{x}, f(\vec{x})\}$  data in the Records.

Sort the Pool from best to worst individuals.

Set new Population=Pool.

If best individual in new Population not as good as previous  $\{\vec{x}_{\text{best}}, f_{\text{best}}\}$ :

  Choose random integer  $i \in [1, n_{\text{pop}}]$ .

  Population( $i$ ) =  $\vec{x}_{\text{best}}$ .

  Update sorting of Population.

  Save  $\{\vec{x}_{\text{best}}, f_{\text{best}}\}$ =best-so-far solution.

  Exit if a stopping criterion is met.

## Appendix B: Modified Mutation Operator Based on Randomly-Shifted Gray Codes

The decision variables are represented by  $x_i = x_i^{\min} + \langle \text{gene } i \rangle \times \Delta_i$ , where  $\langle \text{gene } i \rangle \in [0, 2^{n_i} - 1]$  stands for the value coded by the  $n_i$  binary digits of the gene. We use the Gray code to interpret the value of this gene [5, 39]. A Gray code is characterized by the fact that successive numbers differ only by one bit (see Table 7). It is therefore always possible to move from  $x_i$  to  $x_i + \Delta x_i$  by changing a single bit. This is an advantage compared to standard binary, where several bit changes are typically necessary [62]. The use of Gray codes enables thus mutations to perform a fine tuning of the decision variables. By changing the  $n_i-2$  other bits of the gene, mutations will generate wider displacements in the decision variable space. These wider displacements are important for exploration. The displacements generated by mutations depend however artificially on the coding considered and this is a limit to exploration.

TABLE 7. Comparison between decimal, standard binary, the original Gray code and a shifted version of the Gray code (circular permutation by 3 steps).

Decimal	Binary	Gray	Gray+3
0	000	000	010
1	001	001	110
2	010	011	111
3	011	010	101
4	100	110	100
5	101	111	000
6	110	101	001
7	111	100	011

The idea to improve the mutation operator is hence to apply this operator to the encoding obtained with shifted versions of the Gray code. It consists actually of a circular permutation of the original encoding; see last column of Table 7 [62-64]. At each generation, a random shift in the range  $[0, 2^{n_i} - 1]$  is attributed to each gene. This shift is specific to the gene. It is identical for all individuals of the current generation. Its value is reset at each generation. A possible implementation of the modified mutation operator is given in Table 8. This modified mutation operator receives genes that are expressed in the original Gray code. Before applying mutations, the original chain of binary

digits  $\langle \text{gene } i \rangle$  is translated from the original Gray code to the shifted Gray code (in Table 7, this comes to moving from column 3 to column 4 on the line associated with the original encoding). Mutations are then applied on the modified encoding. The result is finally translated back from the shifted Gray code to the original Gray code (in Table 7, this comes to moving back from column 4 to column 3 on the line associated with the modified version of the gene). Since the result of this modified mutation operator is expressed in the original Gray code (reference encoding used in the rest of the algorithm), adaptation related to this reference encoding can still take place.

TABLE 8. Possible implementation of the modified mutation operator. Operations 1, 2 and 3 transform  $\langle \text{gene } i \rangle$  from the original Gray code to the shifted Gray code. Operation 4 introduces mutations on the encoding obtained with this shifted Gray code. Operations 5, 6 and 7 transform the modified gene from the shifted Gray code to the original Gray code. The shift assigned to each gene is the same for all individuals in the population. It is reset randomly at each generation.

Input : $\langle \text{gene}_i \rangle$ (Gray code)
Operations:
1. Decode the gene : $\langle \text{gene}_i \rangle$ (Gray code) $\rightarrow$ integer
2. Apply the shift : integer $\rightarrow \text{mod}(\text{integer} + \text{shift}, 2^{n_i})$
3. Get Gray code representation : integer $\rightarrow$ Gray code
4. Apply bit-wise mutations
5. Decode the gene : Gray code $\rightarrow$ integer
6. Remove the shift : integer $\rightarrow \text{mod}(\text{integer} - \text{shift}, 2^{n_i})$
7. Recode the gene : integer $\rightarrow \langle \text{gene}_i \rangle$ (Gray code)
Output : $\langle \text{gene}_i \rangle$ (Gray code) with mutations



**Illustrative example:** Let us consider the number "3" (010 in the original Gray code; see third column of Table 7). Individual bit flips can lead to "2" (011), "4" (110) and "0" (000). This possible transition between "3" and "0" is specific to the original Gray code. There is no direct transition to the other entries of the table. If we consider a circular permutation by three steps of the original Gray code (last column of Table 7), the number "3" is now encoded by "101". Individual bit flips lead now to "2" (111), "4" (100) and "6" (001). There is a possible transition between "3" and "6" (instead of "3" and "0"). By changing the shift introduced in the Gray code at each generation, we reset the transitions generated by individual bit flips.

**Illustration with Rastrigin's function:** Rastrigin's function (fct#8 in Table 1) provides a good illustration for the benefit of using randomly-shifted Gray codes when applying mutations. This function has many local minima. The global minimum is for  $x_i=0$  ( $i=1, \dots, n$ ). When searching for the global minimum of Rastrigin's function in  $n=10$  dimensions, it turns out that the algorithm described in Sec. 2 fails

most of the times at finding this global minimum if the mutation operator does not shift the Gray code. The reason is that  $x_i=0$  is represented by 110000000000 in our case if we work in the original domain  $[-5.12, 5.12]$  (we have indeed  $x_i^{\min}=-5.12$  and  $\Delta x_i=0.0025$ ; a gene value of 2048 is represented by 110000000000 in the original Gray code). The closest local minimum is at  $x_i=0.995$ , which is represented by 110101001001. There is a difference of four bits between these two encodings and the genetic algorithm has a hard time finding the appropriate bit changes once trapped in this local minimum. Fig. 3 shows that there is a poor diversity in the displacements generated by mutations if no shifting of the Gray code is considered. By considering randomly-shifted versions of the Gray code when applying mutations, we increase the diversity of the displacements generated by these mutations. This helps the genetic algorithm escape the local minimum to eventually find the global minimum. The second part of Fig. 3 shows that there is indeed a wider diversity in the displacements generated by mutations when considering randomly-shifted Gray codes.

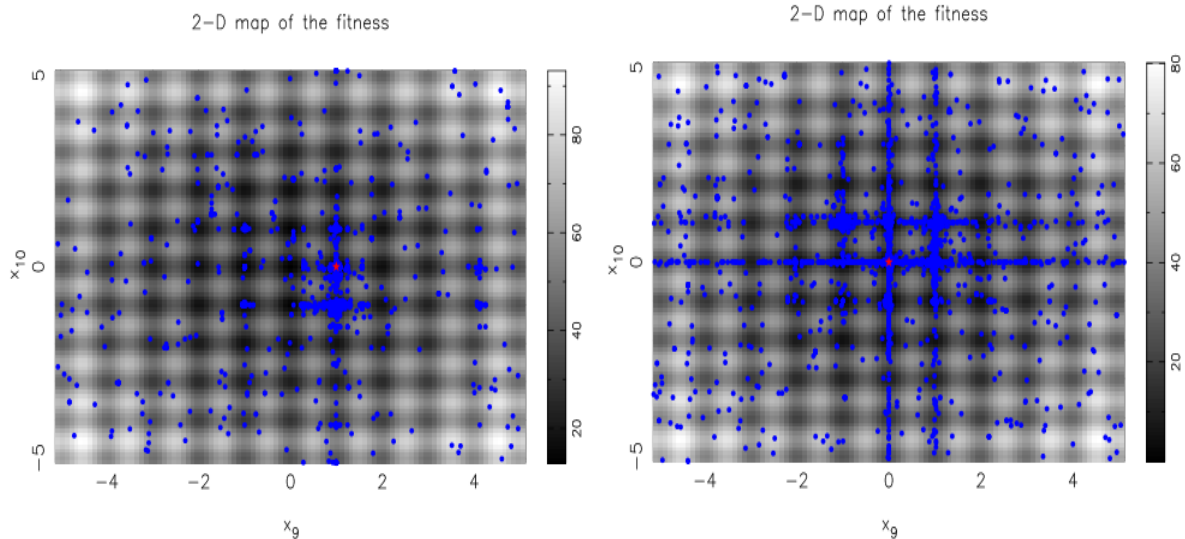


FIG. 3. Application of the genetic algorithm to Rastrigin's function in 10 dimensions. The blue dots represent individuals considered by the genetic algorithm. The star represents the best solution found by the algorithm. The algorithm was interrupted after 10000 evaluations of the fitness. Top: There is no shift of the Gray code when applying mutations; the genetic algorithm is trapped in a local minimum. Bottom: Mutations are applied to randomly-shifted versions of the Gray code; the algorithm finds the global minimum.

## Appendix C: Local Optimization Based on a Quadratic Approximation of the Fitness

The data collected by the genetic algorithm can be analyzed, generation after generation, in order to infer more rapidly the final solution. The idea consists of establishing a quadratic approximation of the fitness in the close neighborhood of the best-so-far solution. We then inject in the population an individual that corresponds to the optimum of this approximation [65]. We chose as reference point ( $\vec{x}_{\text{ref}}$ ) the best-so-far solution found by the genetic algorithm. In order to establish the quadratic approximation, we will use  $N_{\text{select}}$  distinct data points from the records established by the genetic algorithm. A data point  $\vec{x}$  is selected if  $\max_i \frac{|x_i - x_{i,\text{ref}}|}{\Delta x_i} \leq W$ , where  $W$  specifies the width of the selection, in units of  $\Delta x_i$ . We take  $W=5$  as initial value each time we start this procedure.

The expression to establish has the form:

$$f(\vec{x}) = a_0 + \vec{A}_1 \cdot \vec{X} + \frac{1}{2} \vec{X} \cdot A_2 \vec{X}, \quad (1)$$

where  $\vec{X} = \Delta^{-1}(\vec{x} - \vec{x}_{\text{ref}})$  with  $\Delta = \text{diag}[\Delta x_1, \dots, \Delta x_n] / \max_i \Delta x_i$  a diagonal matrix that contains appropriate scaling factors.  $a_0$  is a scalar,  $\vec{A}_1$  is a vector of size  $n$  and  $A_2$  is a symmetric matrix of size  $n \times n$ . Since  $A_2$  is symmetric, there is a total of  $N_{\text{coeff}} = 1 + n + n(n+1)/2$  coefficients to determine. We must ensure at this point that  $N_{\text{select}} \geq 2N_{\text{coeff}}$ , by increasing  $W$  if needed. To establish the quadratic approximation, we define a vector  $\vec{f}$  of size  $N_{\text{select}}$  that contains the  $f(\vec{x})$  values of the selected data points and a vector  $\vec{A}$  of size  $N_{\text{coeff}}$  that contains the unknown coefficients in  $a_0$ ,  $\vec{A}_1$  and  $A_2$ . The equation to solve can then be written as:  $\vec{f} = M\vec{A}$ , where  $M$  is an  $N_{\text{select}} \times N_{\text{coeff}}$  matrix with coefficients defined from Eq. (1). Since the system  $\vec{f} = M\vec{A}$  is overdetermined, we actually require that  $\|\vec{f} - M\vec{A}\|^2$  be minimized (by an appropriate choice of  $\vec{A}$ ). We compute for

this purpose the singular values decomposition (SVD) of the matrix  $M$  [66]. This gives  $M = U\Sigma V^t$ , where  $U$  is an orthonormal matrix of size  $N_{\text{select}} \times N_{\text{coeff}}$  and  $V$  is an orthonormal matrix of size  $N_{\text{coeff}} \times N_{\text{coeff}}$ .  $\Sigma$  is a diagonal matrix of size  $N_{\text{coeff}} \times N_{\text{coeff}}$  that contains the singular values  $\sigma_k$  of the matrix  $M$ . The solution of  $\min \|\vec{f} - M\vec{A}\|^2$  is then given by  $\vec{A} = V\Sigma^+ U^t \vec{f}$ , where  $\Sigma^+$  is a diagonal matrix of size  $N_{\text{coeff}} \times N_{\text{coeff}}$  whose diagonal elements are defined by  $\sigma_k^{-1}$  if  $\sigma_k \geq \varepsilon \times \sigma_{\text{max}}$  (with  $\sigma_{\text{max}} = \max_k \sigma_k$ ) and 0 otherwise.  $\varepsilon$  accounts for the relative accuracy of  $f(\vec{x})$ .

Once the quadratic approximation has been established, the solution of  $\vec{\nabla} f = 0$  is given formally by  $\vec{x}^* = \vec{x}_{\text{ref}} - \Delta A_2^{-1} \vec{A}_1$ . Since the matrix  $A_2$  may be non-invertible, we use an approach based on the spectral decomposition of  $A_2$ . Since the matrix  $A_2$  is symmetric, its eigensystem  $A_2 \vec{x}_k = \lambda_k \vec{x}_k$  is characterized by real eigenvalues  $\lambda_k$  and its eigenvectors  $\vec{x}_k$  form an orthonormal basis. It is useful at this point to define  $\lambda_{\text{max}} = \max_k |\lambda_k|$  and  $\lambda_{\text{min}} = \min_k |\lambda_k|$ . The solution of  $\vec{\nabla} f = 0$  can then be expressed as:

$$\vec{x}^* = \vec{x}_{\text{ref}} - \Delta \sum_k \frac{\vec{x}_k \cdot \vec{A}_1}{\lambda_k} \vec{x}_k, \quad (2)$$

where the sum is restricted to the eigenvalues  $\lambda_k$  that satisfy  $|\lambda_k| \geq \varepsilon_{\text{inv}} \times \lambda_{\text{max}}$  in order to avoid numerical instabilities. For analytical functions, we take  $\varepsilon = 10^{-10}$  and  $\varepsilon_{\text{inv}} = 10 \frac{\lambda_{\text{max}}}{\lambda_{\text{min}}} \varepsilon$ . For problems in which the fitness has an accuracy limited to three significant digits, we recommend using  $\varepsilon_{\text{inv}} = \varepsilon = 10^{-3}$ . If the solution  $\vec{x}^*$  provided by this approach can be accepted, it replaces the last individual scheduled for the next generation. We repeat otherwise this procedure up to three times by increasing the width of the selection ( $W \rightarrow W + 2$ ).

## Acknowledgments

Alexandre Mayer is funded by the Fund for Scientific Research (F.R.S.-FNRS) of Belgium. He is member of NaXys, Namur Institute for Complex Systems, University of Namur, Belgium. This work was performed

while Michaël Lobet was a recipient of a fellowship of the Belgian American Educational Foundation. The authors acknowledge Benoit Hackens, Nicolas Reckinger, Luc Henrard and Sarah Griesse-Nascimento for useful discussions on the nanopylramids. This research used resources of the “Plateforme Technologique de Calcul

Intensif (PTCI)” (<http://www.ptci.unamur.be>) located at the University of Namur, Belgium, which is supported by the F.R.S.-FNRS under the convention No. 2.5020.11. The PTCI is member of the “Consortium des Equipements de Calcul Intensif (CECI)” (<http://www.cec-hpc.be>).

## References

- [1] Holland, J., “Adaptation in Natural and Artificial Systems”, (University of Michigan Press, Ann Arbor, Mich., 1975).
- [2] De Jong, K., Ph.D. Thesis, University of Michigan, (1975), Ann Arbor, Mich.
- [3] Goldberg, D., “Genetic Algorithms in Search, Optimization and Machine Learning”, (Addison-Wesley, Reading, Mass., 1989).
- [4] Haupt, R. and Werner, D., “Genetic Algorithms in Electromagnetics”, (J. Wiley and Sons, Hoboken, NJ, 2007).
- [5] Eiben, A. and Smith, J., “Introduction to Evolutionary Computing”, 2<sup>nd</sup> Edn. (Springer-Verlag, Berlin, 2007).
- [6] Eiben, A. and Smith, J., *Nature*, 521 (2015) 476.
- [7] Hinton, G. and Nowlan, S., *Complex Systems*, 1 (1987) 495.
- [8] Krasnogor, N. and Smith, J., *IEEE T. Evolut. Comput.*, 9 (2005) 474.
- [9] Chen, X., Ong, Y.-S., Lim, M.-H. and Tan, K., *IEEE T. Evolut. Comput.*, 15 (2011) 591.
- [10] Neri, F., Cotta, C. and Moscato, P., “Handbook of Memetic Algorithms”, (Springer, Berlin, 2011).
- [11] Posik, P., Hoyer, W. and Pal, L., *Evol. Comput.*, 20 (2012) 509.
- [12] Sapin, E., De Jong, K. and Shehu, A., *Proceedings of the Genetic and Evolutionary Computation Conference, Denver (2016)*, 85.
- [13] Nguyen, P. and Sudholt, D., *Proceedings of the Genetic and Evolutionary Computation Conference, Kyoto (2018)*, 1071.
- [14] Powell, M., *Large-Scale Non-linear Optimization*, 83 (2006) 255.
- [15] Wanner, E., Guimaraes, F., Takahashi, R. and Fleming, P., *IEEE C. Evolut. Comput.*, (2007) 677.
- [16] Wanner, E., Guimaraes, F., Takahashi, R. and Fleming, P., *Evol. Comput.*, 16 (2008) 185.
- [17] Deep, K. and Das, K., *Appl. Math. Comput.*, 203 (2008) 86.
- [18] da Cruz, A., Wanner, E., Cardoso, R. and Takahashi, R., *IEEE C. Evolut. Comput.*, (2011) 1217.
- [19] Fonseca, C. and Wanner, E., *IEEE C. Evolut. Comput.*, (2016) 4911.
- [20] Rasheed, K., Ni, X. and Vattam, S., *Soft Comput.*, 9 (2005) 29.
- [21] Regis, R. and Shoemaker, C., *IEEE T. Evolut. Comput.*, 8 (2004) 490.
- [22] Paenke, I., Branke, J. and Jin, Y., *IEEE T. Evolut. Comput.*, 10 (2006) 405.
- [23] Jones, D.R., *J. Global Optim.*, 21 (2001) 345.
- [24] Jin, Y., *Swarm Evol. Comput.*, 1 (2011) 61.
- [25] Forrester, A., Sobester, A. and Keane, A., “Engineering Design *via* Surrogate Modelling: A Practical Guide”, (J. Wiley and Sons, Chichester, UK, 2008).
- [26] De Lucia, A., M., D.P., Oliveto, R. and Panichella, A., *Proceedings of the Genetic and Evolutionary Computation Conference, Philadelphia (2012)*, 617.
- [27] Martin, J. and Rasheed, K., *Proceedings of the 2003 Congress on Evolutionary Computation, Canberra (2003)*, 1612.
- [28] Marim, L., Lemes, M. and Dal Pino, A., *Phys. Rev. A*, 67 (2003) 033203.



- [29] Javadi, A., Farmani, R. and Tan, T., *Adv. Eng. Inform.*, 19 (2005) 255.
- [30] Patra, T., Meenakshisundaram, V., Hung, J.-H. and Simmons, D., *ACS Comb. Sci.*, 19 (2017) 96.
- [31] Garciarena, U., Santana, R. and Mendiburu, A., *Proceedings of the Genetic and Evolutionary Computation Conference, Kyoto (2018)*, 849.
- [32] Mayer, A. and Bay, A., *J. Opt.*, 17 (2015) 025002.
- [33] Mayer, A., Gaouyat, L., Nicolay, D., Carletti, T. and Deparis, O., *Opt. Express*, 22 (2014) A1641.
- [34] Mayer, A., Muller, J., Herman, A. and Deparis, O., *Proc. SPIE 9546, San Diego (2015)*, 95461N.
- [35] Lin, A. and Phillips, J., *Sol. Energ. Mat. Sol. C.*, 92 (2008) 1689.
- [36] Wang, C., Yu, S., Chen, W. and Sun, C., *Sci. Rep.*, 3 (2013) 1.
- [37] Yu, S., Wang, C., Sun, C. and Chen, W., *Struct. Multidisc. Optim.*, 50 (2014) 367.
- [38] Judson, R., *Reviews in Computational Chemistry*, 10 (1997) 1.
- [39] Smith, J., "Evolutionary Genetics", 2<sup>nd</sup> Edn., (Oxford University Press, 1998).
- [40] Mayer, A., *Proceedings of the Genetic and Evolutionary Computation Conference Companion, Berlin (2017)*, 195.
- [41] For Schwefel 7 (fct #6 in Table 1), we actually consider  $n_i=16$  bits per gene, since we can otherwise not get sufficiently close to the exact solution  $x_i=420.96874636$ .
- [42] The hypothesis  $H_0="P(\Delta f_{\text{target}})$  not improved by the local optimization procedure" is rejected at a confidence level  $\alpha=0.005$  by a right-tailed z-test, where  $\mu_0 = P(\Delta f_{\text{target}})$  for the reference model (no local optimization) and  $s_0^2 = \#run * \mu_0 * (1 - \mu_0)$ . We used  $\Delta f_{\text{target}}=10^{-4}$  and  $\#run=100$  in our numerical experiment. This confidence level holds for problems in 5, 10 and 20 dimensions and whether shifted Gray codes are used or not.
- [43] The hypothesis  $H_0="P(\Delta f_{\text{target}})$  not improved by shifted Gray codes" is rejected at a confidence level  $\alpha=0.05$  by a right-tailed z-test, where  $\mu_0 = P(\Delta f_{\text{target}})$  for the reference model (no shift of the Gray code) and  $s_0^2 = \#run * \mu_0 * (1 - \mu_0)$ . We used  $\Delta f_{\text{target}}=10^{-4}$  and  $\#run=100$  in our numerical experiment. This confidence level holds for problems in 5, 10 and 20 dimensions and whether the local optimization procedure was used or not.
- [44] Hansen, N. and Ostermeier, A., *Evol. Comput.*, 9 (2001) 159.
- [45] Hansen, N., "Towards a New Evolutionary Computation. Advances on Estimation of Distribution Algorithms", (Springer, Berlin, 2006), 75.
- [46] Hansen, N., *Proceedings of the Genetic and Evolutionary Computation Conference, Montreal (2009)*, 2389.
- [47] CMA-ES accounts for the boundaries  $[x_i^{\min}, x_i^{\max}]$  specified in Table 1. The starting point  $\langle \vec{x} \rangle_0$  used by CMA-ES is a random position in the search domain. We finally take  $\sigma^{(0)} = (x_i^{\max} - x_i^{\min})/3$  as recommended.
- [48] Lobet, M., Lard, M., Sarrazin, M., Deparis, O. and Henrard, L., *Opt. Express*, 22 (2014) 12678.
- [49] Lobet, M. and Henrard, L., 8<sup>th</sup> International Congress on Advanced Electromagnetic Materials in Microwaves and Optics, Copenhagen (2014), 190.
- [50] Clapham, P. and Hutley, M., *Nature*, 244 (1973) 281.
- [51] Deparis, O., Vigneron, J.-P., Agustsson, O. and Decroupet, D., *J. Appl. Phys.*, 106 (2009) 094505.
- [52] Prodan, E., Radlo, C., Halas, N. and Nordlander, P., *Science*, 302 (2003) 419.
- [53] Christ, A., Zentgraf, T., Tikhodeev, S., Gippius, N., Kuhl, J. and Giessen, H., *Phys. Rev. B*, 74 (2006) 155435.
- [54] Liu, N., Guo, H., Fu, L., Kaiser, S., Schweizer, H. and Giessen, H., *Adv. Mater.*, 19 (2007) 3628.

- [55] Pu, M., Feng, Q., Hu, C. and Luo, X., *Plasmonics*, 7 (2012) 733.
- [56] Moharam, M. and Gaylord, T., *J. Opt. Soc. Am. A*, 71 (1981) 811.
- [57] Lobet, M. and Deparis, O., *Proc. SPIE* 8425, Brussels (2012), 842509.
- [58] Johnson, P. and Christy, R., *Phys. Rev. B*, 9 (1974) 5056.
- [59] Ordal, M., Bell, R., Alexander, R., Newquist, L. and Querry, M., *Appl. Opt.*, 27 (1988) 1203.
- [60] Beadie, G., Brindza, M., Flynn, R., Rosenberg, A. and Shirk, J., *Appl. Optics*, 54 (2015) 139.
- [61] For applications with constraints on acceptable gene values, the genetic algorithm will only consider individuals that match these constraints. The crossover operator makes in this case  $n_{\text{bits}}-1$  attempts to generate children with acceptable gene values. If these attempts fail, children will be simple copies of the parents. The mutation operator is repeated from scratch on the input DNA until it generates a DNA with acceptable gene values.
- [62] Rowe, J., Whitley, D., Barbulescu, L. and Watson, J.-P., *Evol. Comput.*, 12 (2004) 47.
- [63] Barbulescu, L., Watson, J.-P. and Whitley, D., 17<sup>th</sup> National Conference on Artificial Intelligence, Austin (2000), 879.
- [64] Whitley, D., *Information and Software Technology*, 43 (2001) 817.
- [65] We use a quadratic approximation of the fitness, because establishing this approximation and its optimum is easily tractable for problems in up to 20 dimensions as in this work and because it is indeed appropriate to describe the local behavior of the fitness in the region of interest. Advanced methods are available for higher dimensions or for situations in which the time required by this analysis is no more negligible compared to that required for evaluating the fitness [14-16,19].
- [66] Golub, G. and Kahan, W., *J. Soc. Ind. Appl. Math. Ser. B Numer. Anal.*, 2 (1965) 205.

### Monte Carlo Computation of the Influence of Carbon Contamination Layer on the Energy Distribution of Backscattered Electrons Emerging from Al and Au

A. M. D. Assa'd

*Department of Basic Sciences Faculty of Arts and Sciences, Al-Ahliyya Amman University, Amman 19328, Jordan.*

---

*Received on: 2/7/2018;*

*Accepted on: 4/10/2018*

---

**Abstract:** The influence of carbon contamination layer (5nm) on the energy distribution of backscattered electrons (BSEs) emerging from the top of Al- and Au-substrates at a wide range of normal primary electron energies ( $E_p = 0.5\text{-}20\text{keV}$ ) has been theoretically examined. The study is based on using a CASINO Monte Carlo model. Generally, the results show a clear effect of the contamination on the backscattering coefficient and the energy distribution of backscattered electrons. This appeared as a reduction of the number of BSE emerging from the surface with energies close to the primary energy. For primary energy less than 5keV, the contamination effects are clearly seen in the reduction of the number of BSEs emerging with energy close to  $E_p$  and the increment of the number of BSEs with low energies. The backscattered electron spectrum starts with a wide peak at low energies and becomes sharper as the primary energy increases. For high primary electron energies (10-20keV), the influence of the carbon contamination layer is restricted on the energy distribution of the backscattered electrons with energies above 95% of the primary energy. The influence of the carbon contamination layer was observed more clearly for the Au-substrate than for the Al-substrate as a reduction of the number of backscattered electrons.

**Keywords:** Backscattered Electrons, Monte Carlo Model, CASINO, Backscattering Coefficient, Carbon Contamination, Energy Distribution.

## Introduction

Backscattered electrons (BSEs) are defined as those incident primary electrons (PEs) that exit the target surface with energy greater than 50eV after they penetrated the target surface and traveled through it. The backscattering coefficient ( $\eta$ ) is the ratio of the number of backscattered electrons (BSEs) to the number of primary electrons (PEs).  $\eta$  depends strongly on the primary electron energy ( $E_p$ ) and the average atomic number ( $Z_{avr}$ ) of the tested target. Therefore, it is useful in providing an atomic contrast mechanism in a Scanning Electron Microscope (SEM) [1]. However,  $\eta$  determination faces a lot of problems, both experimentally and theoretically. Experimentally, the first main problem is that of keeping the surface clean of contamination [2].

Another problem is having a stable incident beam current during the measurement [3]. El-Gomati *et al.* [2] measured  $\eta$  from 24 different elements at low primary electron beam energy (250-5000eV).  $\eta$  was measured for both clean and unclean surfaces under an ultra-high vacuum condition in order to protect the surface from any contamination that could happen during the experiment. The results showed an increment in  $\eta$  obtained from clean surface elements. Theoretically, the  $\eta$  calculation accuracy depends on having accurate elastic and stopping power formulae [4]. In the case of elastic scattering, there is a significant variation in the predication of the small angle elastic scattering between the provided formulae in the literature [5]. This variation reflects strongly on  $\eta$  calculation [6].

The importance of studying the behavior of backscattered electrons (BSEs) is due to their contribution to generating other signals, such as secondary electrons (SEs), Auger electrons (AEs) and X-ray, which are used in Scanning Electron Microscopy (SEM), Scanning Auger Microscopy (SAM) and X-ray microscopy, respectively. This can be exemplified in the case of SEs generation. The number of SE generated per BSE is greater by a factor of  $\beta > 1$  than the number generated per PE [1]. This is due to the reduction in the mean energy of BSEs and to the fact that BSEs pass the surface layer with a shallow exit angle relative to the surface normal. Therefore, any changes in the BSE behavior could reflect on the intensity of the other signals used to image the samples in the mentioned microscopes. BSE energy distribution should be also studied in parallel with the backscattering coefficient ( $\eta$ ). This will help to understand the behavior of incident primary electrons during their travel in the solid before being backscattered from the surface.

In this study, Monte Carlo simulation is used to examine theoretically the effect of a contamination layer (5-nm carbon layer) on  $\eta$  and on the energy distribution of backscattered electrons emerging from the Al- and Au-surface targeted at primary electron energy range (0.5-20 keV), where most of the modern SEMs are operated. The exact thickness of the C contamination is not known. So, in this work, a 5-nm C-layer thickness is chosen with the belief that qualitatively the same results would be found for a somewhat different thickness, higher or lower.

### Monte Carlo Model

For several decades, Monte Carlo simulation has been used as the main tool to investigate theoretically the electron solid interaction [7, 8, 9, 10]. An appropriate Monte Carlo model must operate for a wide range of primary electron energies and solid atomic numbers. In the present work, a free CASINO V2.51 (2017) Monte Carlo simulation model provided by the Université de Sherbrooke - Canada is used. The model can be downloaded from this link: <http://www.gel.usherbrooke.ca/casino/index.html> web page [11]. The model is based on the continuous slowing-down approximation (CSDA) method. A full description of the model can be found in reference [12]. For the elastic scattering cross-section, the model lists four

options that could be used. These are: the tabulated Mott cross-section provided by Mott and Massey [13], Gauvin and Drouin formula [14], Browning *et al.* equation [15] and the modified Rutherford cross-section equation proposed by Murata and Kyser [16]. The Gauvin and Drouin formula and the constants therein have been obtained from the values of the total elastic Mott cross-sections computed by Czyżewski *et al.* [17] using Thomas-Fermi-Dirac atomic potentials. The Browning *et al.* equation is an empirical form of cross-sections derived from trends in tabulated Mott scattering cross-sections. However, the model uses an equation proposed in Joy and Luo [18] in order to determine the primary electron energy loss due to inelastic scattering and the mean free path length between two scattering events. This equation is applicable for a wide range of primary electron energies, thus overcoming the weakness of the Bethe equation [19] at low energies.

In other studies, the use of the Browning *et al.* equation for the elastic scattering cross-section gave good agreement between the measured and the calculated  $\eta$  for Al and Au compared with the Mott tabulated cross-section [20, 21]. Therefore, Browning *et al.* equation is used in the present study.

### Results and Discussion

Fig. 1 shows the trend of backscattering coefficient ( $\eta$ ) for pure clean surfaces of C, Al, Au and for 5-nm C on top of Al- and Au-substrates (unclean target surface) as a function of normal incidence primary electron energy ( $E_p$ ). The results show the effect of the presence of 5-nm C on top of Al- and Au-substrates. It can be classified into three categories: 1) at  $E_p = 0.5$  keV,  $\eta$  is the same for both tested targets C/Al and C/Au. 2) For  $E_p > 0.5$  keV,  $\eta$  values increase toward the values of clean Al and Au. 3) The difference between the values of  $\eta$  for clean and unclean surfaces vanished at  $E_p \geq 5$  keV for Al, while for Au, it vanished at  $E_p = 10$  keV. By using the Kanaya and Okayama formula [22], the electron range at  $E_p = 0.5$  keV on a pure C target is 9 nm, while the BSE range is around 4.5 nm as calculated by Monte Carlo simulation, Table 1. This means that the BSEs did not reach the substrates and their behavior is controlled by the C top layer. As  $E_p$  increases, the BSE range ( $R_{BSE}$ ) increases, Table 1, and an increasing effect of the substrate atomic number on  $\eta$  values

can be noticed in Fig. 1. For a 5-nm C-layer on top of an Al-substrate, the  $\eta$  value increases as  $E_p$  increases until it becomes constant at  $E_p \geq 5$  keV and equal to those of clean Al target. However, for a 5-nm C-layer on top of an Au-substrate, the  $\eta$  value increases until it becomes constant at  $E_p \geq 10$  keV. The data of Table 1 shows that as  $E_p$  increases, the BSE range increases until it becomes as high as that of the

clean Al and Au targets at  $E_p \geq 5$  keV and 10 keV, respectively. For example, at  $E_p = 5$  keV, the BSE range ( $R_{BSE} = 195$  nm) for 5-nm C-layer on top of Al is close to that of the clean surface Al target  $R_{BSE} = 190$  nm. Also, for higher  $E_p$ ,  $R_{BSE}$  data of both targets is equal, Table 1. This means that the 5-nm C-layer has no more effect on  $\eta$  values. This is also applicable for Au substrate at  $E_p \geq 10$  keV.

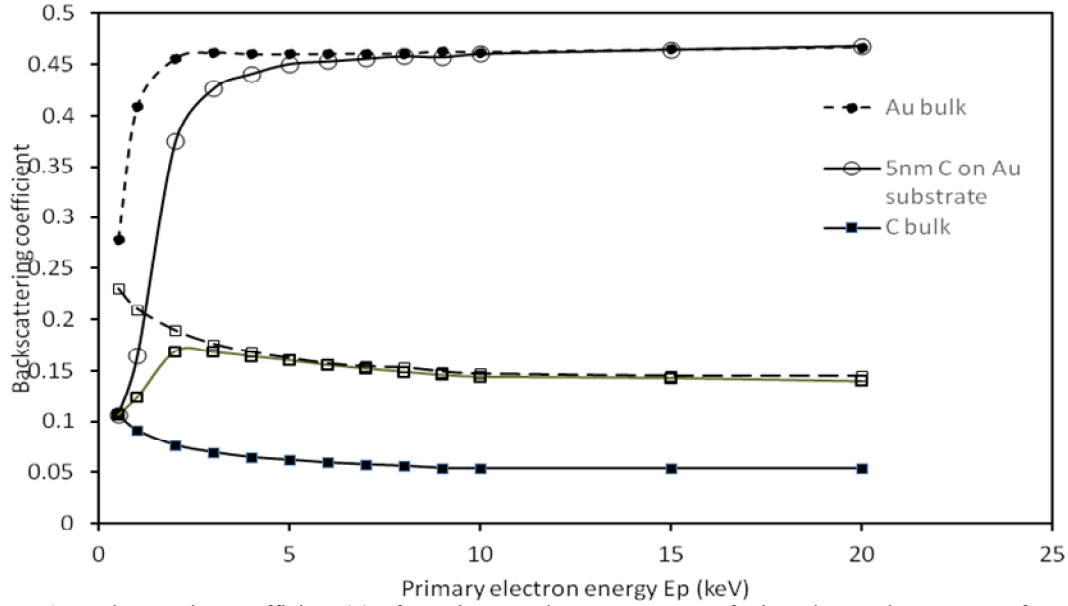


FIG. 1. Backscattering coefficient ( $\eta$ ) of C, Al, Au and 5-nm C on top of Al- and Au-substrates as a function of primary electron energy ( $E_p$ ).

TABLE 1. The maximum range of the primary ( $R_E$ ) and backscattered ( $R_{BSE}$ ) electrons as a function of primary energy ( $E_p$ ).  $R_E$  is calculated by Kanaya and Okayama formula [22], while  $R_{BSE}$  is calculated by the present Monte Carlo model.

	Carbon		Aluminum		5-nm C on Al-substrate	Gold		5-nm C on Au-substrate
( $E_p$ ) keV	$R_E$ (nm)	$R_{BSE}$ (nm)	$R_E$ (nm)	$R_{BSE}$ (nm)	$R_{BSE}$ (nm)	$R_E$ (nm)	$R_{BSE}$ (nm)	$R_{BSE}$ (nm)
0.5	9.19	4.5	8.85	5	4.5	2.65	3	4.5
1	29.23	9	28.15	15	13	5.24	6	8.5
2	93.01	40	89.58	41	40	16.67	15	17
3	183.06	67	176.32	80	85	32.82	25	28
4	295.97	110	285.06	130	140	53.06	33	37
5	429.62	159	413.79	190	200	77.02	43	50
6	582.53	220	561.06	270	270	104.43	58	65
7	753.57	280	725.79	340	340	135.09	71	85
8	941.82	370	907.11	460	460	168.84	91	92
9	1146.55	480	1104.29	490	490	205.54	110	115
10	1367.12	510	1316.74	640	640	245.08	135	140
15	2690.79	1200	2591.62	1300	1300	482.38	260	265
20	4350.39	1750	4190.05	2100	2100	779.90	450	450

FIG. 2 shows the backscattered electron energy distribution for pure C, Al and Au as the targets are bombarded by a 20 keV normal incidence beam of primary electrons. It is clear

that the shape of the spectrum depends on the atomic number of the target material as shown by different experimental results [23, 24].

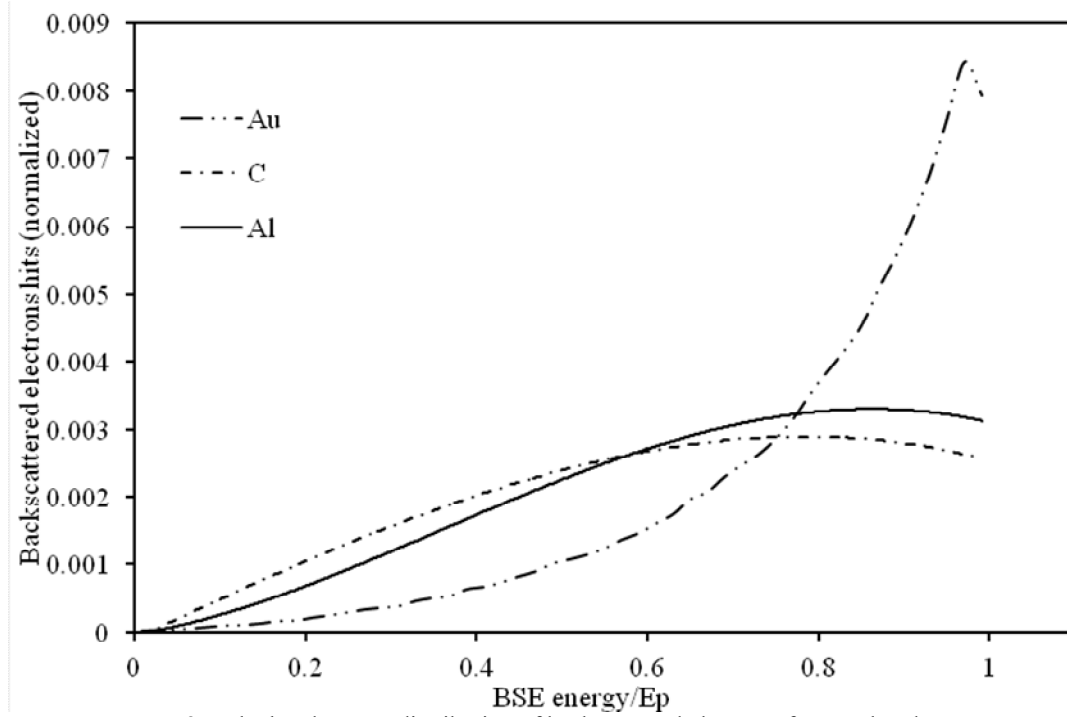


FIG. 2. Calculated energy distribution of backscattered electrons for C, Al and Au.

The dependence of the collected BSE spectrum on the primary electron energy ( $E_p$ ) for the clean surface Al and Au targets is shown in Figs. 3 and 4, respectively. As  $E_p$  increases, the peak of the spectrum becomes sharper, higher and closer to  $E_p$ . Moreover, a reduction in the spectra at backscattered energies below  $0.4 E_p$  for Al and  $0.75 E_p$  for Au is demonstrated as  $E_p$  increases. The probability of having elastic scattering increases as  $E_p$  increases, which makes the primary electrons backscatter with minimum loss of their energy. Those BSEs collected with energies close to  $E_p$  escaped after they penetrated a depth of a few nanometers below the surface and suffered more elastic scattering than inelastic scattering even without losing much of

their energy. So, as  $E_p$  increases, more BSEs with high energy escape from the surface. However, the peak sharpness depends on the target average atomic number. This is rather more clear in the case of Al, where the probability of having inelastic scattering increases compared to the case of Au. Therefore, the primary electrons will travel deeper in the target and suffer more energy loss before escaping from the surface with low energies. This makes the BSE spectrum look wider and not as sharp as in the case of Au. So, the behavior of high energetic BSEs is surface-sensitive and can be used to investigate the surface topography, since these have a small exit depth.

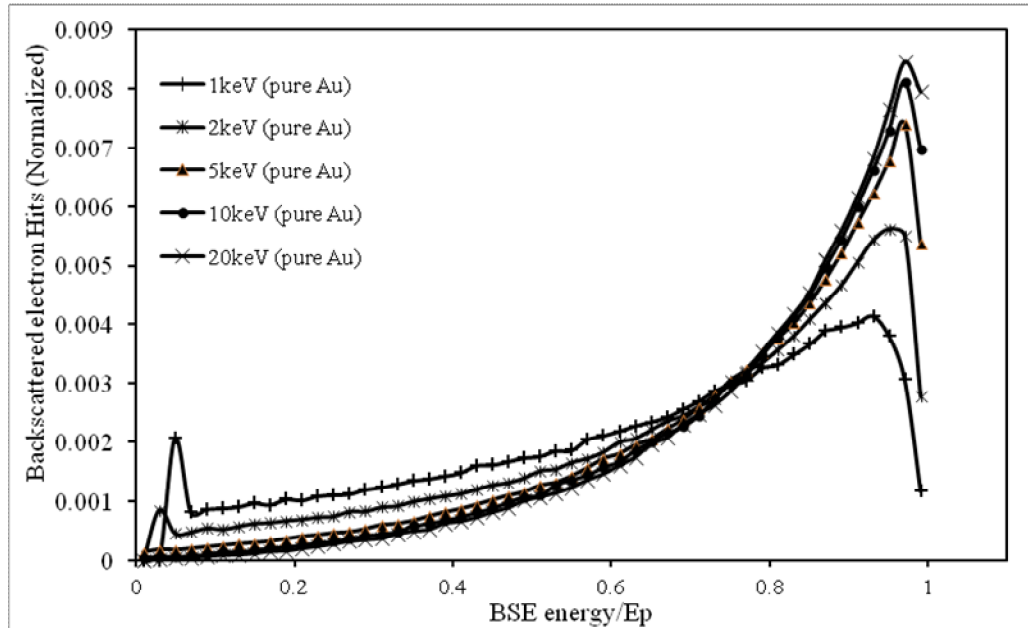


FIG. 3. Energy distribution of backscattered electrons for a pure Au target and primary electron energy range (1-20keV).

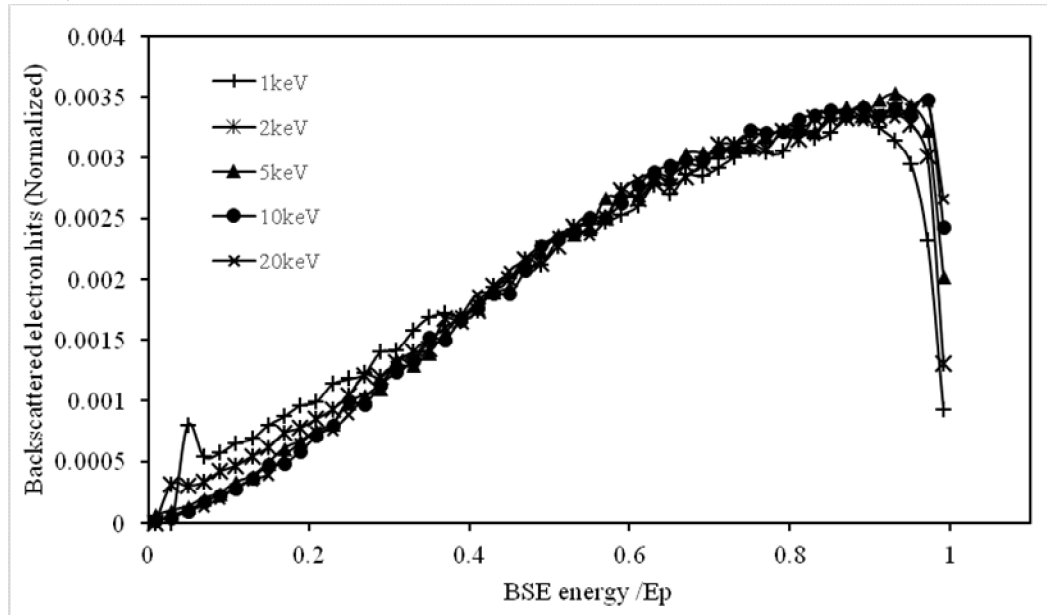


FIG. 4. Energy distribution of backscattered electrons for a pure Al target and primary electron energy range (1-20keV).

Figs. 5 and 6 show the energy distribution of the backscattered electrons as a function of  $E_p$  for a 5-nm C-layer deposited on Al- and Au-substrates, respectively. The BSE spectrum of primary electron energy  $E_p = 0.5\text{keV}$  is not shown, because it is similar to that of the pure C target. Figs. 5a and 6a show a comparison between the BSE spectra of clean Al- and Au-surfaces and those from 5-nm C-layers on top of

Al- and Au-substrates (unclean surfaces). The effect of the C top layer on the shape of BSE spectrum is clearly shown at low  $E_p$  and for high-energy BSEs ( $E_{BSE}$ ). The BSE spectrum shows a massive reduction of BSEs with energy close to  $E_p$  ( $E_{BSE} \geq 0.6E_p$ ) and an increase of BSEs with low energies ( $E_{BSE} < 0.6E_p$ ). This could make BSEs more effective in generating secondary and Auger electrons from C layer and X-ray from C-layer and from Al- and Au-

substrates at high  $E_p$ . More investigation could be done in the future to study the effect of BSEs on the other signals in the presence of contamination. The increase of the BSE spectrum at low  $E_{BSE}$  is due to the energy loss that BSEs suffered in the C top layer in their way back to surface. As  $E_p$  increases, the peak of BSE spectrum shifts toward  $E_p$  and  $\eta$  value increases toward the data of clean Al and Au targets, Figs. 5b and 6b. A greater number of BSEs escaped from the surface, particularly those with higher energies. The reason for this is the increase in the primary electron range ( $R_E$ ), which means having a larger depth of electron-solid interaction volume, Table 1. Hence, the

primary electron will suffer more scattering events in the substrate before coming back to the C top layer in its way back to the surface. As  $E_p$  increases, the interaction volume increases and the importance of the C top layer thickness on the interaction volume decreases. So the effect of the C top layer on the BSE spectrum will be minimized. The only effect of the C top layer on the BSE spectrum will remain on BSEs with energy above  $0.95E_p$ , Fig. 7. These electrons are backscattered from a small exit depth less than the C top surface thickness which has low backscattering coefficient compared to the substrate materials.

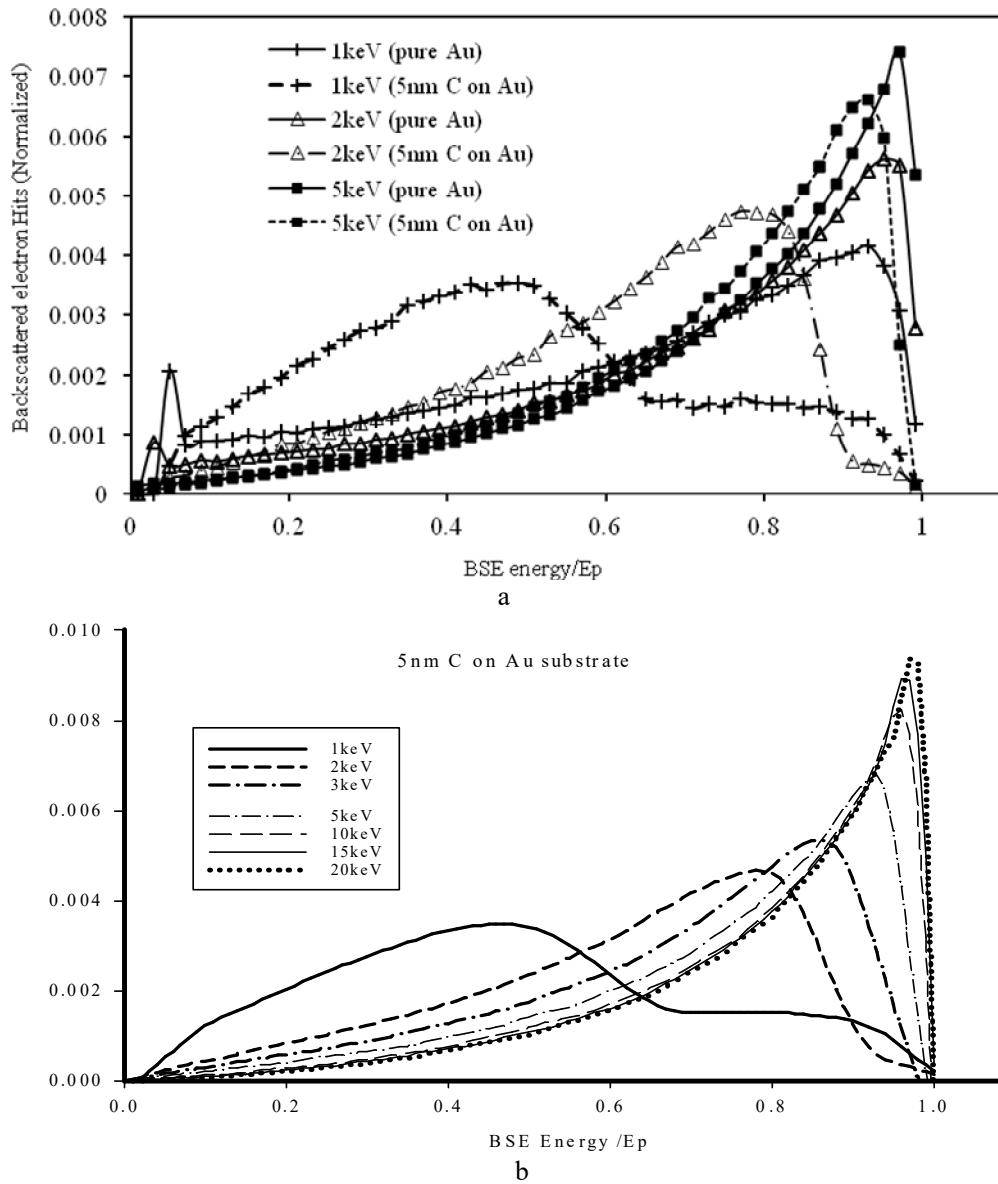
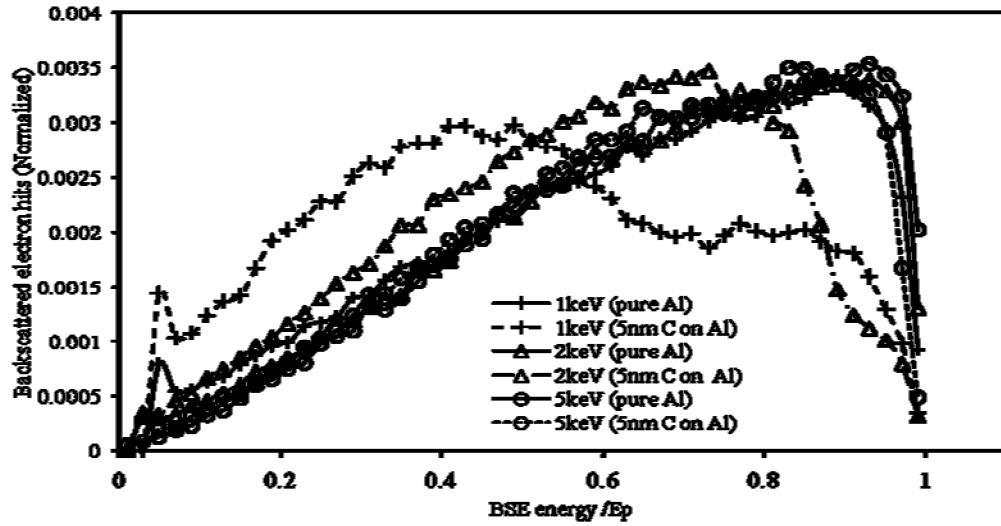
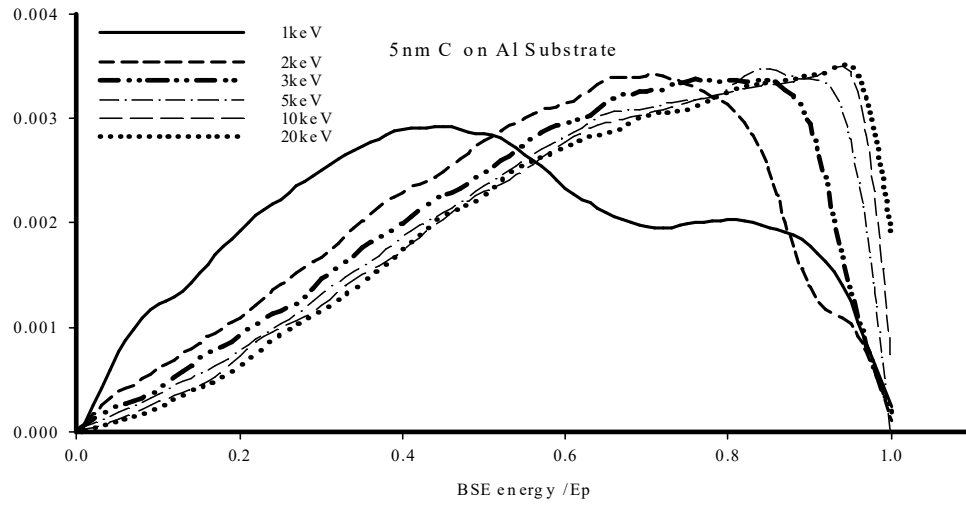


FIG. 5. Energy distribution of backscattered electrons comparison between those for a pure Au target and those calculated in the presence of a 5-nm C-layer on top of the Au surface.





a



b

FIG. 6. Energy distribution of backscattered electrons comparison between those for a pure Al target and those calculated in the presence of a 5-nm C-layer on top of the Al surface.

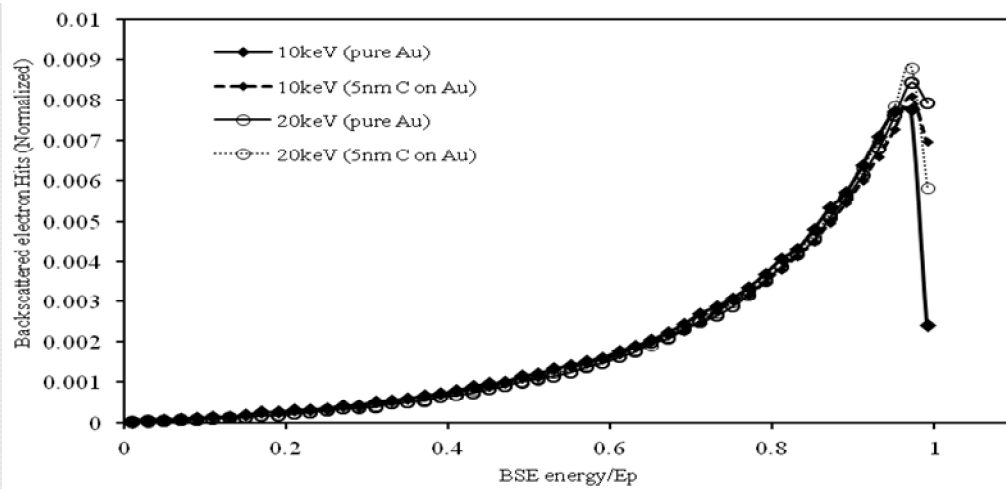


FIG. 7. Energy distribution of backscattered electrons comparison between those for a pure Au target and those calculated in the presence of a 5-nm C-layer on top of the Au surface.

## Conclusion

The presence of contamination on the top of the examined targets affects the backscattering coefficient ( $\eta$ ) as well as the backscattered electron energy distribution. The influence of contamination on the collected BSE spectrum depends on the thickness of the contamination layer and the incident primary electron energy. At low energies,  $E_p \leq 5\text{keV}$ , an increase in BSEs with energies below  $0.70E_p$  and a massive reduction in BSEs with energies above  $0.70E_p$

are observed. Even though the contamination layer has no effect on  $\eta$  values at high  $E_p$ , it has an effect on the BSE energy distribution. As  $E_p$  increases, the shape of the BSE spectrum goes toward the BSE shape of the clean target except for energies above  $0.95E_p$ . These high-energetic backscattered BSEs have a small exit depth, which is filled by the contamination layer (5-nm C top layer). The high energy BSEs are surface-sensitive and can be used to investigate the surface topography.

## References

- [1] Reimer, L., "Scanning Electron Microscopy, Physics of Image Formation and Microanalysis". (Springer, Berlin, Germany, 1985).
- [2] El-Gomati, M.M., Walker, C.G.H., Assa'd, A.M.D. and Zadrazil, M., *Scanning*, 30 (2008) 2.
- [3] Assa'd A.M.D. and El-Gomati M.M., *Scanning Microscopy*, 12 (1998) 185.
- [4] Joy, D.C., *J. of Microsc.*, 147 (1987) 51.
- [5] Jablonski, A., Salva, F. and Powell, C.J., *J. Phys. Chem. Ref. Data*, 33 (2) (2004) 2004
- [6] Walker, C.G.H., Matthew, J.A.D. and El-Gomati, M.M., *Scanning*, 36 (2014) 241
- [7] Yan, H., El-Gomati, M.M., Prutton, M., Wilkinson, D.K. and Chu, D.P., *Scanning*, 20 (1998) 465.
- [8] Star'y, V., *J. Phys. D: Appl. Phys.*, 32 (1999) 1811.
- [9] Dapor, M., Bazzanella, N., Toniutti, L., Miotello, A., Crivellari, M. and Gialanella, S., *Surf. Interface Anal.*, 45 (2013) 677.
- [10] Walker, C.G.H., Luděk, F. and Müllerová, I., *Scanning*, 36 (2016) 802.
- [11] Drouin, D., <http://www.gel.usherbrooke.ca/casino/index.html>, web page.
- [12] Drouin, D., Couture, A.R., Joly, D., Tastet, X., Vincent, A. and Gauvin, R.M., *Scanning*, 29 (2007) 92.
- [13] Mott, N.F. and Massey, H.S.W., "Theory of Atomic Collisions". (Oxford University Press, London, 1965).
- [14] Gauvin, R. and Drouin, D., *Scanning*, 15 (1993) 140.
- [15] Browning, T.Z., Li, J.M., Chui, B., Ye, J., Pease, R.F.W., Czyzewski, Z. and Joy, D.C., *J. Appl. Phys.*, 76 (1994) 2016.
- [16] Murata, K. and Kyser, D.F., *Advances in Electronics and Electron Physics*, 69 (1987) 175.
- [17] Czyzewski, Z., O'Neill MacCallum, D., Romig, A. and Joy D.C., *J. Appl. Phys.*, 68 (1990) 3066.
- [18] Joy, D.C. and Luo, S., *Scanning*, 11 (1989) 180.
- [19] Bethe, H., *Ann. Phys.*, 5 (1930) 325.
- [20] Demers, H., Poirier-Demers, N., Couture, A.R., Joly, D., Guilmain, M., Jonge, N. and Drouin, D., *Scanning*, 33 (2011) 135.
- [21] Assa'd, A.M.D., *Appl. Phys. A*, 124 (2018) 699.
- [22] Kanaya, K. and Okayama, S., *J. Phys. D: Appl. Phys.*, 5 (1972) 43.
- [23] Napchan, E., "Backscattered Electrons in SEM", *Microscopy and Analysis*, (2001) January, 9-11.
- [24] Gineste, T., Belhaj, M., Teyssedre, G. and Puech, J., *App. Surf. Sci.*, 359 (2015) 398.

### Ionic Liquids: Sustainable Media for Nanoparticles

Azeez A. Barzinjy<sup>a,b</sup>, Samir M. Hamad<sup>c,d</sup> and Ashna F. Arkawazi<sup>e</sup>

<sup>a</sup> Department of Physics, College of Education, Salahaddin University, Erbil, Iraq.

<sup>b</sup> Department of Physics Education, Faculty of Education, Ishik University, Erbil, Iraq.

<sup>c</sup> Scientific Research Centre, Cihan University, Erbil, Iraq.

<sup>d</sup> Scientific Research Centre, Soran University, Soran, Erbil, Iraq.

<sup>e</sup> Department of Chemistry, College of Education, University of Garmian, Sulaimani, Iraq.

---

Received on: 3/7/2018;

Accepted on: 23/12/2018

---

**Abstract:** In this paper, an incompressible viscous fluid flow over a flat plate is presented. In the past decade, ionic liquids have attracted great interest both in scientific research world and amongst the most diverse technological and industrial sectors. This fact, together with the growing contribution of the industrial sector, is turning ionic liquids into a key component for the most diverse fields of science, such as nanotechnology, electrochemistry, green chemistry, physics, materials science and engineering, among many others. First, before talking about the ionic liquids' applications, one should answer this question; what are the main properties that make ionic liquids so attractive? In general, ionic liquids are salts formed by very asymmetric and large ions, due to which they have attractive cation-anion forces weaker than those that occur in conventional ionic salts, such as table salt, which causes them to be liquids in a wide range of temperatures, including the ambient temperature in most cases. The term "ionic liquid" is considered a synonym of a "molten salt", although in practice it began to be used when molten salts started to be popular at low temperatures. Indicatively, a compound is usually called a molten salt when the melting temperature is above 100 °C, while an ionic liquid melts at lower temperatures. Due to the growing applications of ionic liquids as engineering fluids, their ability to functionalize or surface-modify materials in the form of nanoparticles has recently been described. Therefore, ionic liquids have been used as solvents for nanoparticle synthesis with a wide variety of sizes and morphologies.

**Keywords:** Ionic Liquids, Nanoparticles, Nanotechnology, Green chemistry, Green Synthesis.

## Introduction

Ionic liquids are salts with low melting points, lower than 100°C. They are composed of an anionic part and a cationic part and due to their great thermal and chemical stability; they can be used in high-temperature processes up to 300°C, since temperatures higher than this cause decomposition. Most of ionic liquids are remaining liquids at temperatures above room temperature, which is the main advantage of these solvents [1]. The main characteristic that

differentiates ionic liquids from molten salts is the wide temperature range in which ionic liquids are liquid compared to traditional salts (Fig. 1).

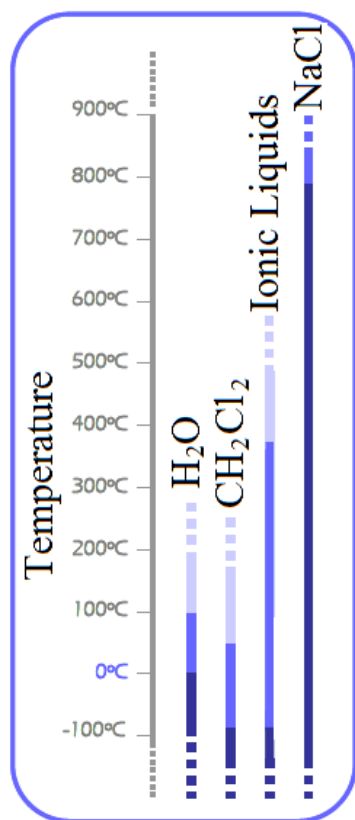


FIG. 1. Comparison of physical states and temperature ranges of different compounds [1].

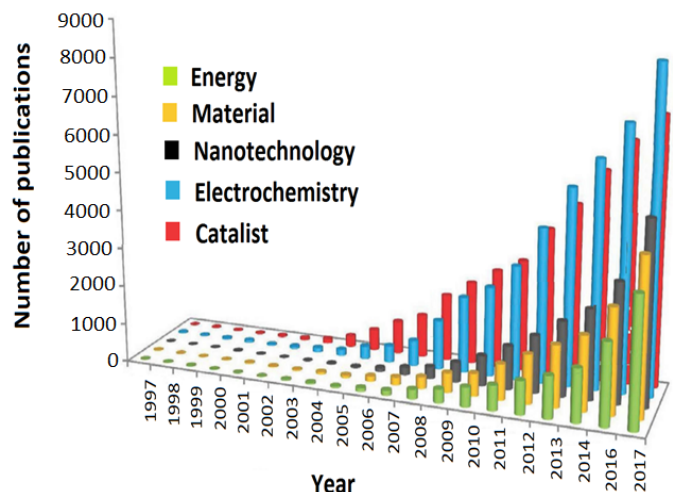


FIG. 2. Number of scientific publications related to ionic liquids in different fields in the period (1997-2017) according to the Institute for Scientific Information (ISI) Web of Science.

However, ionic liquids have a multitude of applications due to possessing many important characteristics. These properties comprise; zero volatility [5], almost zero vapour pressure [6], being simply liquids composed entirely of ions [7], negligible flammability [8], a wide range of potential windows [9], high thermal stability [10], a low melting point [11] and a controlled

miscibility with organic compounds and water [12].

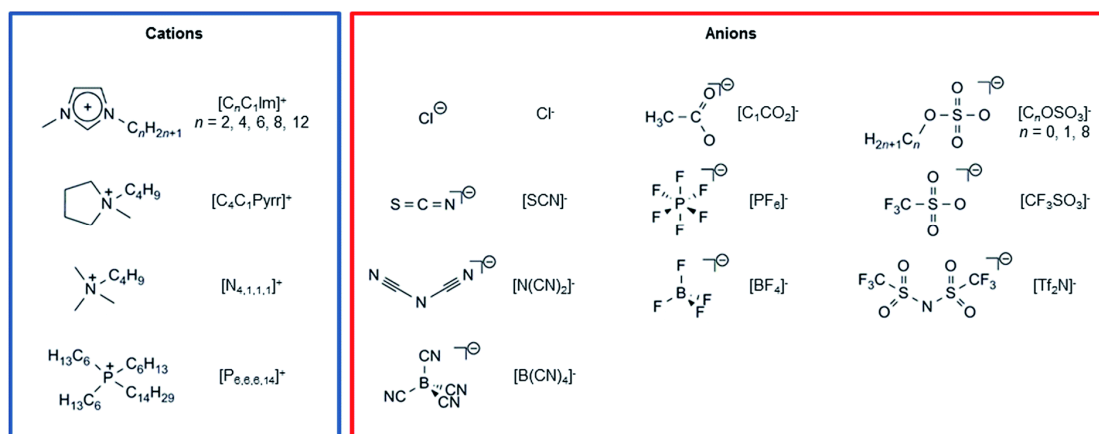
Many of the Ionic liquids are formed by an organic cation and an anion that can be organic or inorganic. Some properties, such as thermal stability and miscibility, are mainly dependent on the anion, while other properties, such as viscosity, surface tension and density, depend on the length of the alkyl group of the cation and/or its shape and symmetry [2].

Due to all combination possibilities of cations and anions, there are a large number of ionic liquids. Thus, ionic liquids offer a wide range of physicochemical properties suitable for different applications. Ionic liquids are considered green liquids of design, because their properties can be adjusted or modified by varying the cation and/or the anion, without generating polluting emissions to the environment [3].

Initially, these materials were developed for their exclusive use in electrochemistry [3], although they have been receiving importance and a particular interest making them present in many fields of sciences [4]. As a representative figure, Fig. 2 shows the spectacular growth in terms of the number of scientific articles on ionic liquids that have been published in the past 20 years.

Due to the possibility of combining the cation; generally organic, voluminous and asymmetric, with various generally inorganic anions although they can also be organic, the term "design solvents" has emerged, since the

illustrates some of the most common ions, anions and cations in the formation of ionic liquids. Since there are many more, the combinations are very numerous due to the fact that their ionic and hybrid organic-inorganic nature as well as ionic liquids possessing unique properties make them interesting for diverse applications [14].



potentially attractive as electrolytes in different electrochemical devices [15].

## Short Historical Review

From the historical perspective, the first material that would fit with the definition of ionic liquid was observed in the middle of the 19<sup>th</sup> century, in a Friedel-Crafts reaction [19], where a liquid phase was obtained, being designated with the name "red oil". Later, research determined that this "red liquid" was an ionic liquid. The first known bibliographical reference in this respect is when Walden [20] in 1914 synthesized ethylammonium nitrate with a melting point of 12 °C [21]. Later, in 1948, the development of ionic liquids formed by chloroaluminium ions. Hurley and Weir [22] discovered that mixing alkylpyridinium chloride with aluminium chloride produces a reaction that yields colourless ionic liquids. This discovery has remained a curiosity for a long time, until its singular properties have become known and electrochemical studies have been initiated. Fig. 4 presents an overall model of an asymmetrical system of ions in the IL structure.

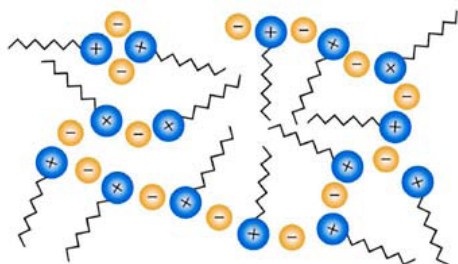


FIG. 4. Reorganized model of an ionic liquid [23].

The real history of ionic liquids began in the US military, with Lowell King, in charge of a research project in piles, to find viable substitutes for the molten salts of  $\text{LiCl/KCl}$ , at that time used as electrolytes [14]. The chloroaluminates were introduced in the field of electrochemistry, since they achieved much lower melting temperatures than expected. In addition, they did not behave as simple binary mixtures. The system they formed and their Lewis acid-base characteristics provided an anion series of the  $\text{Cl}^-$  type;  $[\text{AlCl}_4]^-$ ,  $[\text{Al}_2\text{Cl}_7]^-$  and  $[\text{Al}_2\text{Cl}_{10}]^-$ . For a long period, research and development focused mainly on electrochemical applications [24].

To overwhelm the restrictions of a particular ionic liquid in some areas and feat its greater properties in other areas, combinations of ionic liquids are currently being largely discovered. Ionic liquid mixtures represent a comparatively novel area evolving in the field that has gathered substantial curiosity [25], since they tolerate for extra change of the ionic liquid characteristics for precise requests. The ionic liquids containing the slight part of the mixture can be correspondingly intended to enhance anticipated physical or chemical characteristics. There are numerous requests described for binary ionic liquids as solvents for chemical production and procedures [26], for electrochemical requests such as dye-sensitized solar cells [27, 28], batteries [29, 30] and in chromatography [31].

One can realize that the acid-base chemistry of the components results in a binary ionic liquid material, which is a mixture of two nitrate salts [32]. The specific instance is a glass forming salt with a glass transition temperature of  $2100^\circ\text{C}$ . This ionic liquid is not a one-off curiosity, since there have been many articles and patents for this example alone up to now.

In 1967, a publication by Swain modified the direction of the applications by the use of

benzoate tetra-*n*-hexylammonium as a solvent for kinetic studies. In the 1980s, Hussey and Seddon [33] studied the application of chloroaluminate ionic liquids as polar solvents in the creation of transition metal complexes. At the same time, the first publications appeared where chloraluminates were effective Friedel-Craft catalysts [34]. The main problem with these liquids was their sensitivity to water. In 1990, Michael Zaworotko [35] became able to develop, synthesize and completely characterize salts with new cations, but at the same time being stable anions in water. By this way, the work in the laboratory became easier, with no longer need to work in free moisture atmosphere. These new salts, with anions of the types tetrafluoroborate, hexafluorophosphate, nitrate, sulphate and acetate, proved to be much more stable liquids, at least at low temperatures and although the initial purpose was to use them as electrolytes in piles, they proved to be particularly suitable in other applications [13].

As different studies are carried out in chemical reactions, it is becoming clear that their behaviour is different from that observed in conventional polar and non-polar media. By means of different cations and anions, a large number of compounds can be obtained; their characterization shows the great variety of properties offered by ionic liquids. Nowadays, the catalogue of cations and anions is even bigger, which means that the possibility of creating new ionic liquids is practically unlimited and the applications of ionic liquids are only limited by the imagination of researchers. One way to demonstrate the wide dissemination of these compounds in the scientific field and in the industrial applications is the growing number of publications in this area [14].

## The Role of Ionic Liquids in Green Chemistry

The objective of "Green Chemistry" is to create a cleaner and more sustainable chemistry that does not harm the environment. More specifically, "Green Chemistry" is the design of products or processes that reduce or eliminate the use or production of hazardous substances by offering alternatives with greater environmental compatibility. Along with the use of supercritical fluids, the replacement of traditional volatile organic solvents with non-volatile ionic liquids



as a reaction medium can offer a convenient solution to some of the environmental problems suffered by the current chemical industry, such as the emission of harmful gases, issues associated with the existing aqueous Cr(VI) electroplating solution [36] and the recycling of catalysts [37].

One of the most researched cases is the use of ionic liquids in catalysis, since these cannot only be used as a solvent, but also can act as a catalyst or co-catalyst increasing the speed of the reaction, the yield or changing its selectivity [38]. There are numerous examples and applications of ionic liquids in catalytic reactions, such as the Heck reaction, Diels-Alder reactions, Friedel-Crafts, esterifications or regioselective alkylations as illustrated in several recent reviews [39]. In addition, the solubility of certain gases such as  $H_2$ , CO and  $O_2$  in ILs is generally good, which allows them to participate in reactions such as hydrogenations, carbonylations, hydroformylations and aerobic oxidations.

Another outstanding application within "Green Chemistry" is to replace traditional organic solvents in liquid-liquid extraction processes (Fig. 5). Thus, the data presented by the Robin D. Rogers group reflects that the distribution coefficients for different types of solutes in the ionic liquid system [BMIM][PF<sub>6</sub>] - water are more suitable for practical applications than the classical system 1-octanol- water. These two-phase systems are being actively studied by various groups that intend to develop a new and clean separation technology [40].

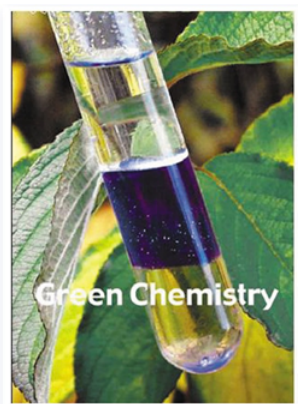


FIG. 5. Green chemistry [40].

Although the applications of ionic liquids have been studied since the 1980s as a means of reaction or catalysis, it was recently when the

first industrial process using ionic liquids was developed. Specifically, the process consists in adding methylimidazole instead of triethylamine to eliminate hydrochloric acid in the production process of dichlorophenylphosphine, improving up to ten times the yield of said reaction thanks to the easy separation of the ionic liquid obtained as a secondary product; Dario [41]. For this reason, the BASF Company has received the prestigious 2004 Innovation Award from the European Chemical News and has gone in history to implement the first chemical process that uses liquids of large-scale ionic [42]. BASF currently offers a process license called BASIL [43] (biphasic acid scavenging utilizing ionic liquids), which can be used in other reactions such as acylations, phosphorylations, sulphonations and silylations (Fig. 6).



FIG. 6. Photograph of a BASIL process reactor. The ionic liquid is separated from the reaction medium allowing the improvement of the reaction yield [43].

As a last application within "Green Chemistry", it is worth highlighting the use of ionic liquids as solvents in reactions catalyzed by enzymes. One of the main advantages that have been identified is that, unlike other polar organic solvents, ionic liquids do not deactivate enzymes, allowing reactions with polar substrates that were previously not possible. In other cases, the use of ionic liquids in biocatalysts offers a greater selectivity, a higher reaction speed and even a greater stability of the enzymes [44].

## Ionic Liquids in Electrochemistry

Ionic liquids present a series of properties (high ionic conductivity, wide range of electrochemical stability) that make their presence in the different branches of electrochemistry more and more consolidated, presenting applications, such as electrolytes in

electrochemical synthesis, solvents in electrodeposition of metals, batteries, super-capacitors, fuel cells, solar cells and devices based on conductive polymers, such as electrochemical sensors, artificial muscles and electro-chromic devices [45].

One of the topics of greatest industrial interest in electrochemistry is that of electrodeposition of metals. As a general rule, the variety of metals that can be electrodeposited in a given medium is limited by the electrochemical stability of said medium. In this sense, the main advantage of the ILs compared to the technologies in aqueous media is their wide range of electrochemical stability [15]. While aqueous solutions have a range of

electrochemical stability of 2 V, the range of electrochemical stability that some ILs have exceeds 4 V depending on the pH of the medium, reaching up to 6V (Fig. 7) [46]. The studies carried out so far have focused on the electrodeposition of metals, such as aluminum, which are too electropositive to be deposited from conventional aqueous solutions. That is, it is necessary to apply a very high potential to the solution in order to achieve the deposition of the metal, producing undesired electrochemical reactions in the aqueous electrolyte. In addition to aluminum, the electrodeposition of lithium, nickel, copper, cadmium, tin, antimony, zinc, silver or semi-conductors, such as germanium and silicon, has also been studied [47].

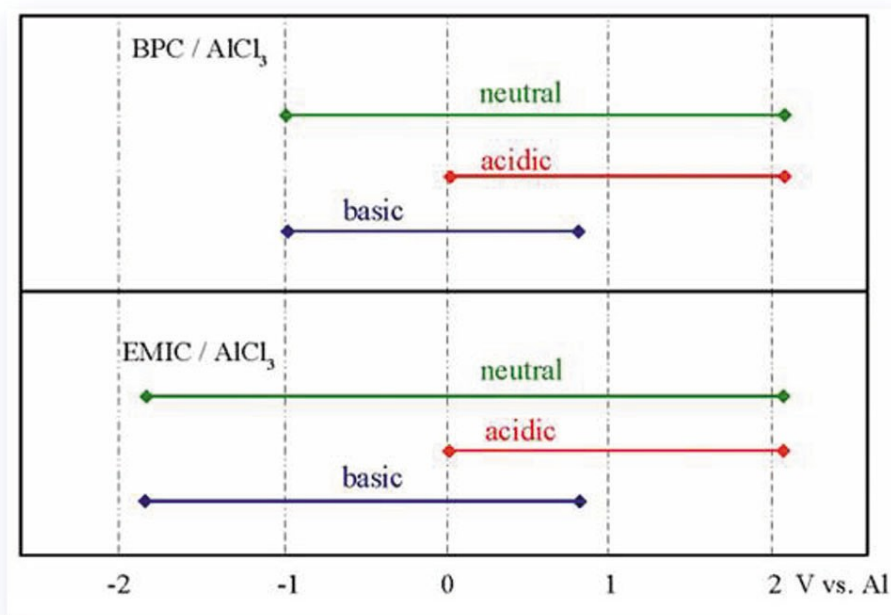


FIG. 7. Electrochemical stability interval for the electrodeposition of aluminum in ionic liquid medium BPC /  $\text{AlCl}_3$  and EMIC /  $\text{AlCl}_3$  [48].

## Nanotechnology

In 1959, Richard Feynman was the first to propose that, at some point, materials could be manufactured with atomic sizes. Feynman stated that: "The principles of physics, as far as I can see, do not speak against the possibility of manoeuvring things atom by atom" [49].

Nanotechnology is the result of the individual manipulation of molecules or atoms with the aim of creating new materials with better properties. It is a relatively new field of research, where structures with dimensions from 1 to 100 nanometers are studied. One nanometer is one trillionth of a meter ( $1 \text{ nm} = 1 \times 10^{-9} \text{ m}$ ) [50]. Fig. 8 shows a comparative diagram between 1 picometer ( $1 \times 10^{-12} \text{ m}$ ) and 1 meter [51].



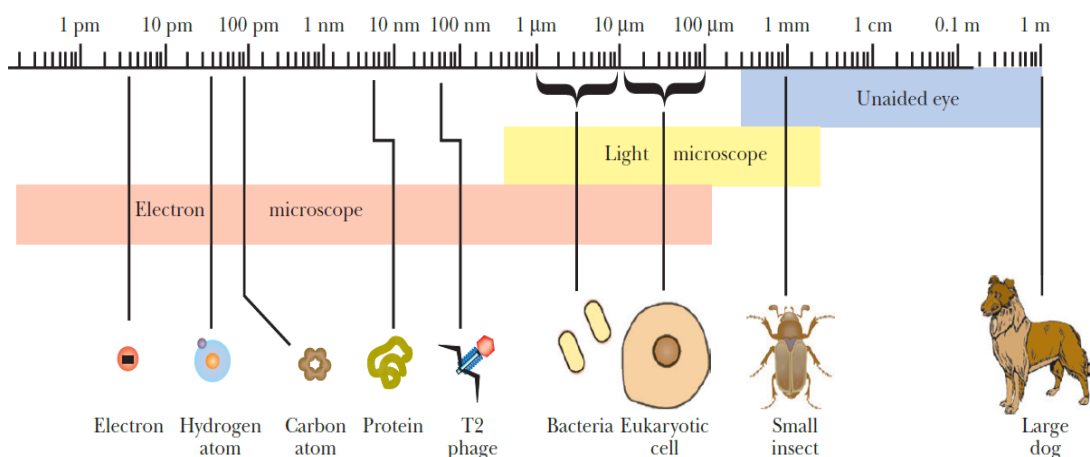


FIG. 8. Size comparison of objects ranging in size from 1 meter to 1 picometer [51].

Nowadays, the study of nanotechnology has been possible in microscopy, biochemistry, physical chemistry, among other sciences, where with the aid of these today it is possible to understand, design, manipulate, characterize and produce nanometric structures. One of the greatest advances in nanotechnology is the production and application of nanoparticles in biological sciences; an instance is its use in antitumor cells [52], pathogens, among others. Some nanomaterials have the characteristic of being antibacterial; for instance, silver, selenium, copper or carbon has shown antimicrobial activity [53].

Nanotechnology is an area of research that, in the past decades, has had great, amazing and

irresistible achievements [54]. It has applications in microscopy and science, such as physics, chemistry, biology, medicine, materials science and engineering [55]. There are currently opportunities to design and produce articles, on a nanometric scale capable of satisfying the needs of this increasingly globalized world. In some areas, the use of nanotechnology has great relevance in energy, electronic and medical industry. The study and development of nanotechnology is so important, because it is the key to solving many of the problems facing the world, such as hunger [56], disease [57], lack of drinking water [58], the need to make better use of energy resources [59], among many others [60] (Fig. 9).

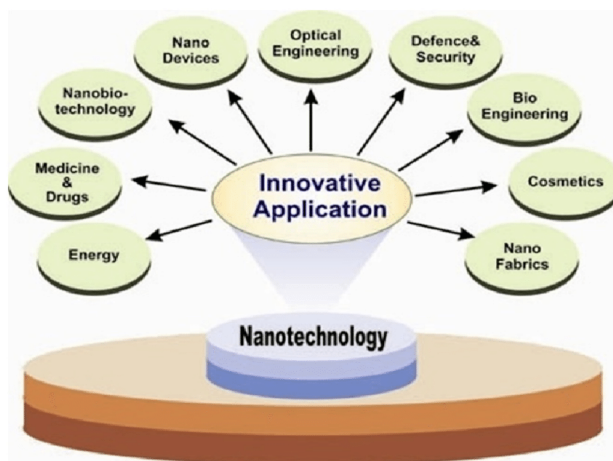


FIG. 9. Numerous uses of nanotechnology [61].

It can be stated that an area that generates a lot of interest and a lot of research is medicine [62], where efforts are aimed at improving quality and life expectancy; some time ago, for example, it was impossible to think that there

would be particles that could directly attack a tumor. At present, this is a reality and there are advances in the treatment of cancer [63], autoimmune [64] or cardiovascular diseases [65].

An alternative of the medical area is the use of nanoparticles as therapeutic agents [66], as well as the coatings with antimicrobial characteristics to prevent the transmission of diseases, spread of infections and bad odours caused by microorganisms [67]. Thus, textile fibres, such as sportswear, underwear or medical textile fibres, such as gauze, bandages or surgical clothing, are today an area to exploit nanotechnology focused on anti-microorganisms [68].

In recent times, science has a revolutionary look at the area of nanotechnology. As the name specifies, the motivation has come from following applied requests, particularly in the fields of electronics and materials science, more willingly than a search for theoretical information. Nanotechnology comprises the separate manipulation of single particles or even atoms. Structure components atom-by-atom or molecule-by-molecule so as to produce materials with different or massively better properties represented possibly the unique aim of nanotechnologists. Nevertheless, the field has extended in a somewhat unclear way and inclined to comprise any structures so small that their investigation or manipulation was intolerable or unfeasible until now. At the nanoscale, quantum effects appear and materials frequently act oddly, related to their bulk properties [51].

## Metallic Nanostructures and Metallic Nanoparticles

Nanotechnology has had a progressive development in recent years, because it describes the creation and exploitation of materials with controlled structural characteristics, with at least one dimension in the nanometer range. Nanotechnology presents a huge potential of applications in different scientific areas and technologies; for this reason, one of its objectives is to obtain nanoparticles of different metallic elements with different shapes and sizes, since they have unique optical [69], electronic [70], magnetic [71] and catalytic [70] properties. It should be noted that, when handling substances, particles and compounds in the nanometric scale, their physical and chemical properties are significantly altered, which creates a completely new perspective for the design of novel materials.

As presented in Fig. 10, the nanostructures possess different shapes. These nanostructures can be spheres, cubes, bi-pyramids, octahedrons, flowers, bars, rices, rods, carrots and wires. Within the ionic liquids, the size of the nanostructures is manageable. For instance, the size of silver nanocubes might be changed from 30 nm to 70 nm through presenting a drop quantity of sulphide or hydrosulphide into reaction-solution or through fluctuating silver forerunners [72]. The dimension of nano-carrots may possibly alter from 120 nm to 250 nm by changing the concentration of forerunners or reaction period.

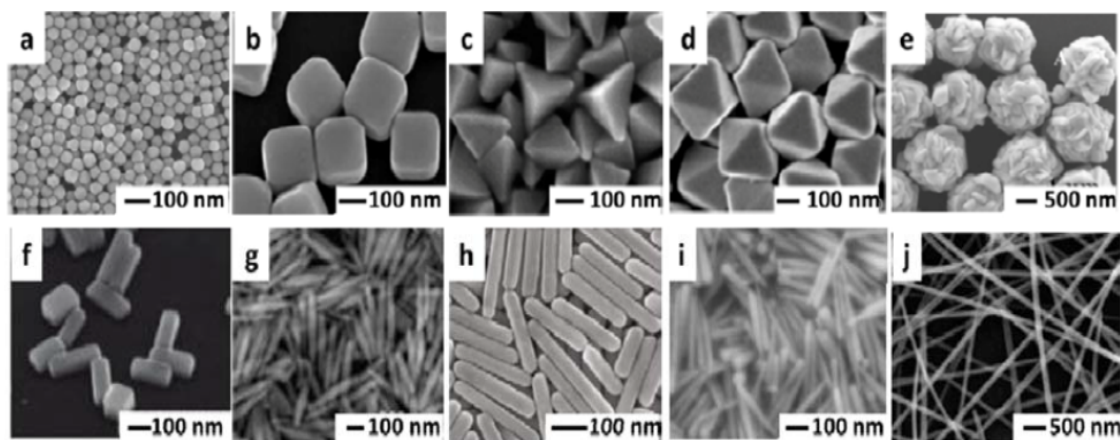


FIG. 10. Altered natures of silver nanostructures. (a) spheres [73], (b) cubes [74], (c) right bi-pyramids [75], (d) octahedrons [76], (e) flowers [77], (f) bars [78], (g) rices [79], (h) rods [80], (i) carrots [81] and (j) wires [82].

However, in the past twenty years, the interest has remarkably increased in nanotechnology, the science that is responsible for studying and generating new synthetic routes for the production of building blocks of different sizes (within the nanometric scale) and investigating their shape, composition, structural surface, load and functionality, or for the construction of self-assembly processes spontaneously directed by defined surface pattern chemistry or lithography; these can form architectures that act in an intelligent function and predict a particular use [83]. For the formation of nanoparticles, one can use the metal salt reduction method with a synthetic reducing agent or with a bioreductor. Another alternative is to use surfactants for their formation. There are also physical techniques, such as laser ablation or reactive vapour deposition, among others; all these techniques are used in a general known method called "bottom-up" method, in which nanostructures are formed atom by atom until you reach materials with nanometric dimensions [84]. Another general method is the well-known one as "top-down" method, where macroscopic materials are fractionated until reaching the nanoscale; within this group of materials we find mechanical polishing and mechanical grinding.

There are different types of nanomaterials which are classified according to the type of material that makes them being divided into: metals, semiconductors and polymers [85]. Some nanoparticles are in the form of dots, tubes, nano-sheets, nano-tubes, nano-discs, spheres, bars and many others [86].

Nanoparticles are currently of great scientific interest due to their wide applications; they are a new type of materials, either based on ceramics, metals, polymers or composite materials (for example: polymer-metal, polymer-ceramic), where at least one of the dimensions of the nanoparticles is in the range of 1 to 100 nm [87]. The nanoparticles retain a large surface area /volume ratio, which allows their use in applications for catalytic materials, drugs or energy storage [88]. Among the most common metallic nanoparticles are those of gold, platinum, palladium and silver these can be synthesized by means of some methods where, in each of them, the morphology of the obtained nanoparticles is checked. There are physical and chemical techniques and among them is the chemical reduction of metallic salts in the

presence of a stabilizing agent, which is a well spread technique [89].

Within metallic nanostructures, the most common and most used to date are nanoparticles, due to the relative ease with which they are obtained and the possibility of controlling their size and shape. A nanoparticle is defined as the smallest unit that can still behave as a complete unit in terms of property and transportation. At least, one of its dimensions lies between 1 and 100 nm. As nanoparticles approach the range of 1 to 10 nm, the effects of size and surface are made more obvious. This has implications that can be manifested in their magnetic properties, in electronic driving, in the melting temperature or chemical reactivity, among others. It is possible to control these properties selectively by modification of size, morphology and composition [90, 91].

These new particles have properties that are improved or completely different from those of their original materials, which open up the possibility of designing systems with specific properties. Many applications of nanoparticles are currently being developed in various fields, such as: image improvement, biological markers, bio-bactericides, solar cells, photonic crystals, among others.

The first object in which metallic nanoparticles were used was the *Lycurgus calice* of the fifteenth century, in Rome. It contained gold nanoparticles [92]. Mayan pigments dating to the eleventh century in the Chichen Itza ruins contain iron and chromium nanoparticles [93]. At the beginning of the sixteenth century, it was known to obscure silver compounds due to light; however, it was not until the nineteenth century when, with the work of Fox-Talbot and Daguerre [94], silver halide was used in the form of nanoparticles in photochemistry and photography [95]. Gold particles have also been used in the melting of glass, better known as "ruby glass" [96].

There are two chief methods for the production of metal nanoparticles: a bottom-up method and a top-down method (Fig. 11) [97]. Bottom-up method contains the creation of a structure; atom by atom, molecule by molecule or by self-assembly. In the top-down method, the suitable preliminary materials are reduced in size by means of physical and chemical procedures [98].

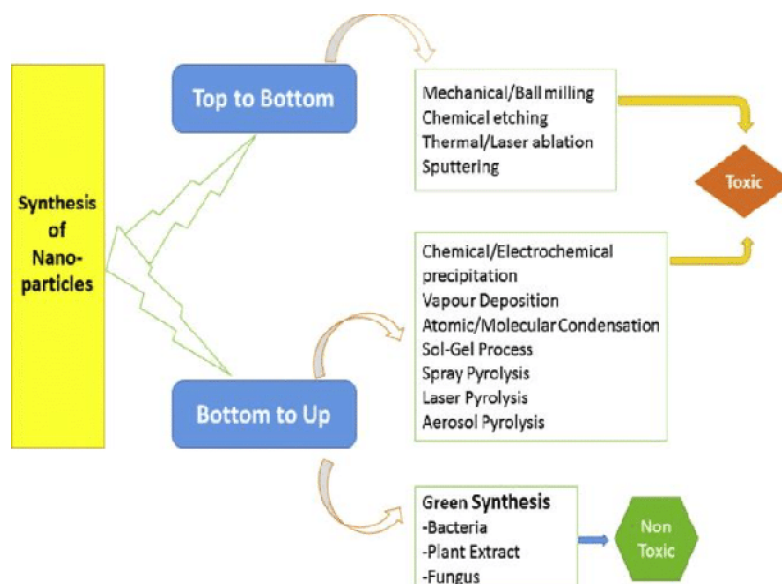


FIG. 11. Dissimilar methods for the production of metallic nanoparticles : (a) Top-bottom and (b) Bottom-up methods [97].

## Ionic and Nanomaterial Liquids

The contribution of ionic liquids to the synthesis of materials and more particularly to that of nanostructures has been gradual during the past decade; however, it is very promising in view of the work [99] having been carried out for the time being. Ionic liquids are a perfect stabilizer system of metallic nanoparticles, which makes them excellent catalysts for very diverse reactions. In addition to the characteristics that were extensively detailed in previous sections, these ionic compounds have the rare property of forming extended systems [100] of hydrogen bonding when they are in a liquid state, which classifies them as "supramolecular solvents" and allows them to provide a certain nanostructural order to some spontaneous reactions (it is an almost essential property in the chemistry of colloids and surfactants).

The term nanotechnology refers to the design, manufacture and use of materials (which receive the generic name of nanomaterials) or devices (nano-devices) of dimensions in the nanometer scale [101]. This range of length ranges from individual atoms and molecules to polymer chains and proteins of considerable length, which makes nanotechnologies a multidisciplinary field of preferential interest for scientific disciplines, such as chemistry, electrochemistry, physics, molecular biology, among others. Perhaps, the clearest and most popular example of nanomaterial with promising

applications is carbon nanotubes. Since their discovery in 1991 by the Japanese Sumio Iijima, carbon nanotubes have received considerable attention due to their extraordinary structural and electronic properties. One of the limitations of nanotubes is that they are strongly entangled with each other in a complex structure that provides them with unique properties, but with difficult processes at the same time [102].

Recently, a group of Japanese researchers has published the possibility of using carbon nanotubes and ILs to form physical gels that can be used in new electronic devices, antistatic materials and electro-conductive inks [103]. The formation of the gels is attributed to interactions of type  $\pi$  - $\pi$  through which nanotubes are surrounded by ionic liquid molecules and form an ordered three-dimensional structure that has physical gel behaviour (Fig. 12). Due to the non-volatility of the ILs, the gels obtained are thermally stable and do not dry or wrinkle even when subjected to vacuum. In a subsequent experiment, these authors used a gel formed by a polymerizable ionic liquid to prepare a highly electro-conductive plastic material. Fukushima *et al.* [103] also explain that, incorporating only 4% by weight of carbon nanotubes, the mechanical properties of the polymer are increased by around 400%, with an electrical conductivity of 0.56 S/cm. On the other hand, several groups are investigating the carbon-IL nanotube pair as electrolyte-electrolyte material, studying the electrochemical behaviour of this particular system and its possible applications [104].



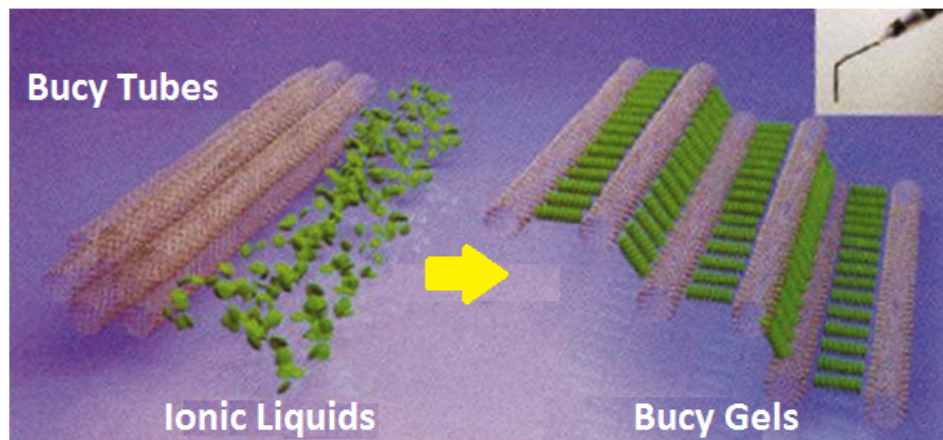


FIG. 12. Representative diagram of the gels obtained using carbon nanotubes and ILs [103].

Another classic example of nanomaterial are metallic nanoparticles that have very particular physico-chemical properties, which makes them interesting in electronic, magnetic, optoelectronic, pharmaceutical, biomedical, cosmetic, energy, sensor or catalytic applications. There are several recent investigations related to ILs and nanoparticles. Thus, Kim *et al.* [105] have developed a new method of synthesizing gold and platinum nanoparticles in one step using new ILs functionalized with thiols. These ILs function as stabilizing agents for the nanoparticles that are obtained with the added attraction that this method gives rise to small particles (2-4 nm) and uniform distributions. Other similar

investigations are related to the formation and stabilization of nanoparticles of other metals, such as iridium, rhodium, ruthenium or  $\text{TiO}_2$ . But, the ILs are not only useful as a means of synthesis of these nanoparticles, since they can also be used to modify the surface of the nanoparticles. Itoh *et al.* [106] have recently published the synthesis and properties of gold nanoparticles modified with ILs based on the imidazolium cation. These authors have proposed the use of gold nanoparticles modified with an IL as an optical sensor for anions, since the presence of certain anions in the medium can induce changes in the colour of the aqueous dispersion of gold nanoparticles (Fig. 13).



FIG. 13. Photograph of dispersion of gold nanoparticles functionalized with an imidazolium LI in the presence of different anions:  $\text{Cl}^-$ ,  $\text{Br}^-$ ,  $\text{BF}_4^-$ ,  $\text{PF}_6^-$  [106].

It can be agreed that room-temperature ionic liquids, such as  $[\text{C}_4\text{mim}]^+ \text{BF}_4^-$ , can be utilized as templates to formulate massive mesoporous silica through the nano-casting method [107]. Also, self-assembly does not depend on amphiphilic interfaces and the attendance of water. It is estimated that the anticipated hydrogen bond stack mechanism with room temperature ionic liquids as templates might open innovative corridors to manufacture mesoporous materials beneath altered circumstances than currently utilized [108].

However, supramolecular structures are big molecules shaped by combination or bonding of smaller molecules. Correspondingly, they go to the nanoscience field as they are frequently likely to improve molecules of an anticipated form or functionality [109]. The prearranged “supramolecular” behaviour of ionic liquids delivers a soft pattern to direct the creation of bimodal porous carbon systems or the development of electrodeposits. Numerous crucial factors, such as: viscosity, polarity, surface tension, hydrogen bonding and over-

coordination with solutes or surfaces, altogether show important roles in moderating class reactivity and mass transportation characteristics leading the origin of nanostructure [110].

Finally, ILs can also be used for transferring metallic nanoparticles from an aqueous phase to an organic phase. The group of Wei *et al.* [111]

have developed a method for transferring gold nanoparticles to different organic solvents including ILs by simple agitation. More recently, CIDETEC has proposed a simple method of capture and transfer of liquid-liquid phase of silver nanoparticles (Fig. 14) [112].

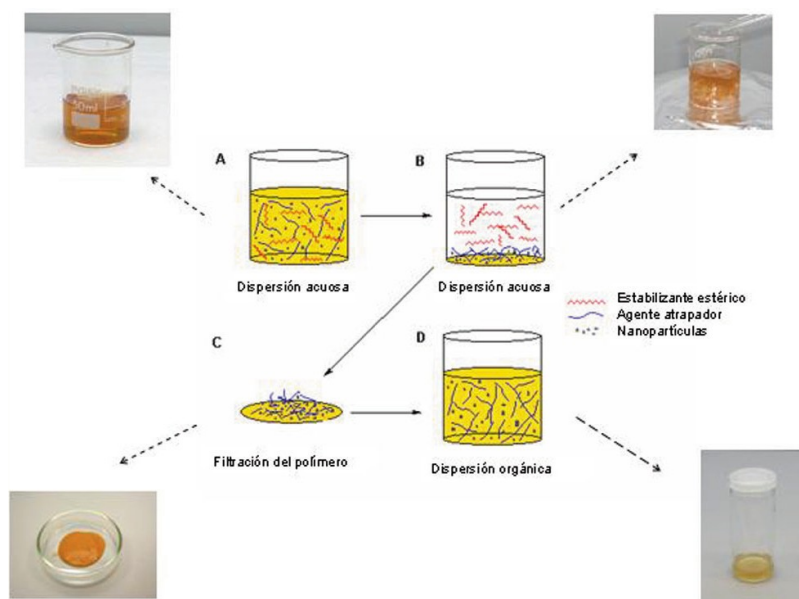


FIG. 14. Phase transfer process of silver nanoparticles using a polymer ionic liquid (PIL) [113].

This new method uses a polymer with a chemical structure similar to an ionic liquid called PIL (polymeric ionic liquid) as a phase transfer vehicle. This PIL precipitates in water by adding certain salts, trapping quantitatively the silver nanoparticles inside it. The polymeric solid can be easily recovered by filtration and subsequently dissolved in different organic solvents. The silver nanoparticles are red dispersed maintaining their initial shape and size [114]. This method not only offers the possibility of keeping the nanoparticles stored in a solid polymer, but also serves to transfer the nanoparticles or other nano-objects from the water to all kinds of organic solvents.

## Nanoparticle Synthesis

In this review article, the authors deliver a summary of typical ionic liquids as exclusive solvents to produce precise nanomaterials comprising shape-organized nanoparticles, electrodeposited films, metal-organic outlines, colloidal gatherings, hierarchically absorbent carbons and DNA or RNA constructions. These

revolutions demonstrate how ionic liquids can achieve manifold roles in leading chemistry and physics at the nanoscale: performing as supramolecular template, metal and carbon source, sacrificial agent and redox agent, altogether in the nonappearance of official steady ligand.

## Electrochemical Approaches

Nano-crystals possessing extraordinary index planes often display events greater than those of the most communal thermodynamically steady, low index; for instance, (111), (100) and even (110) planes because of the attendance of an extraordinary density of atomic stepladders, brackets and twist portion as energetic spots. Unluckily, crystal development rates orthogonal to a high index plane are characteristically quicker; consequently, high index planes are generally reduced throughout nano-crystal growing. Certainly, this leaves a task to manufacture well distinct nano-crystals surrounded by high index surfaces.

Sun et al. have participated extensively to this field in recent times, inventing a forthright electrochemical way to identical  $\sim 200$  nm platinum nano-flowers (Fig. 15) even-handed shrill single crystalline petals through straight electrodeposition on top of a glassy-carbon electrode in chloro-platinic acid comprising reline ionic liquid at  $80^\circ\text{C}$  [115]. The electro-catalytic action of the Pt nano-flowers for

ethanol oxidation in acid solution demonstrated to be approximately twice that of marketable Pt black substance built upon the oxidation current density. Fascinatingly, running the production at other temperatures produced imprecise petals, demonstrating the gentle association among diffusive transference, nucleation and growth in ionic liquids.

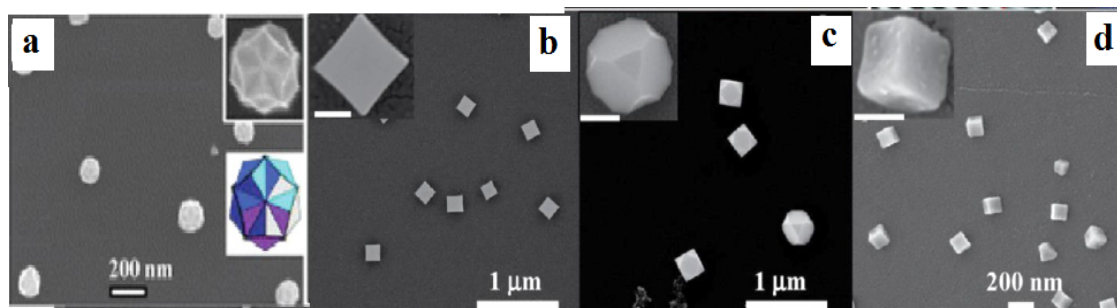


FIG. 15. (a) High amplification SEM image of Pt nano-composites, (b-d) SEM images of Pt nanostructures electrodeposited on glassy carbon at  $80^\circ\text{C}$  for 60 min growth at different combinations of applied square-wave potentials [115].

### Anti-Solvent Approaches

Wong et al. [116] invented an ingenious two-stage anti-solvent approach to 10-nm thick single crystalline mesoporous ZnO nano-sheets by means of firstly liquefying ZnO powders in reline ionic liquid at  $70^\circ\text{C}$  shadowed by relaxed inoculation into a water bath as shown in Fig. 16. Calcination of the recuperated precipitous, which enclosed a combination of wurtzite ZnO and  $\text{Zn}_4\text{CO}_3(\text{OH})_6 \cdot \text{H}_2\text{O}$  segments the latter shaped by cohort of carbonate and hydroxide ions resulting from urea breakdown activated a topotactic conversion connecting combination of vacuums to create superior arbitrarily dispersed holes. The calcined mesoporous ZnO nano-sheets displayed great precise superficial areas and showed approximately as active as profitable  $\text{TiO}_2$  in the photo-catalytic deprivation of methylene blue.

### Wet Chemical Production of Nanostructures

With a convenient room-temperature insignificant reduction of  $\text{HAuCl}_4$  by a selected acid in anhydrous reline ionic liquid, Sun and his group acquired approximately 300-nm polycrystalline gold-star moulded NPs restricted through (331) and adjacent extraordinary index surfaces [117]. The outcome is an outstanding result in that neither kernels nor surfactant additives were necessary. Besides the NPs showing a steady pentagonal regularity, additional star moulded gold NPs of numerous outlets were likewise detected and, through solely regulating the gratified water, additional single morphologies were obtained, comprising snow-flake shape NPs and nano-thorns, as presented in Fig. 17. Moreover, the star-formed NPs verified to be active electro-catalysts, through a 150 mV optimistic change of the start potential for  $\text{H}_2\text{O}_2$  drop and over a 14 folding improvement in drop current density associated with that on a polycrystalline gold electrode, a product qualified to the attendance of high-index surfaces.

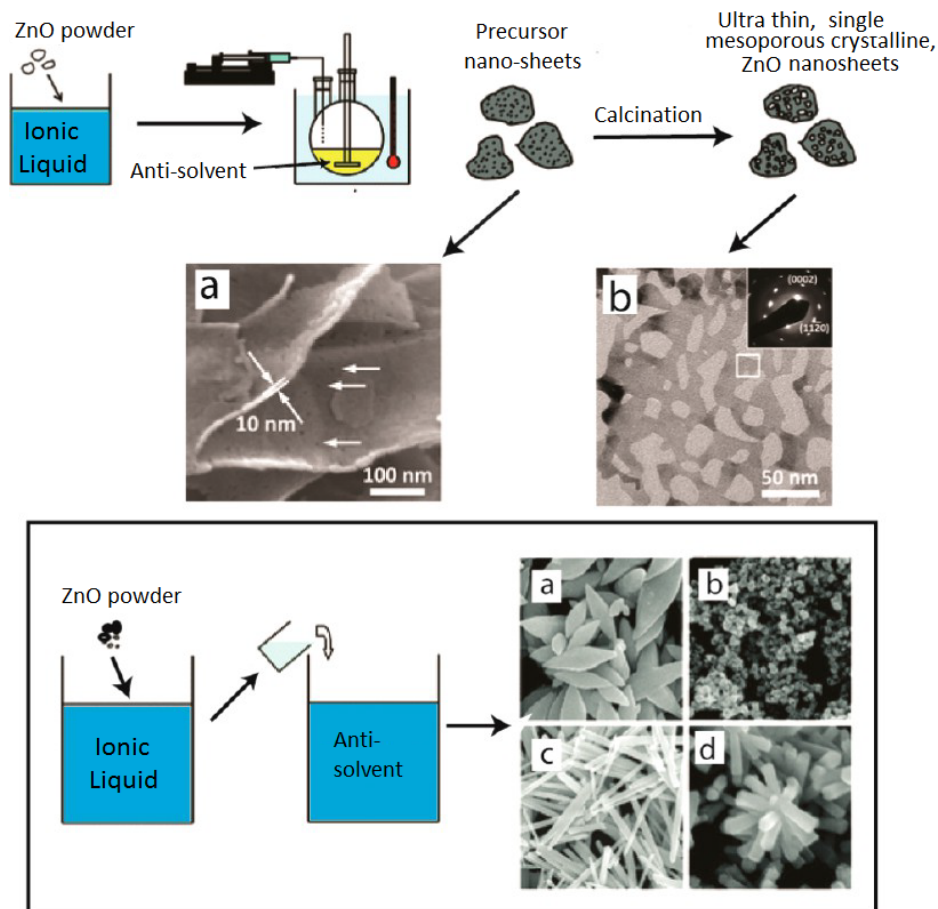


FIG. 16. (Top) An anti-solvent methodology for the production of ZnO nanosheets. (Bottom) Graphical demonstration of the anti-solvent technique for shape-controlled synthesis of varied ZnO nanostructures [118].

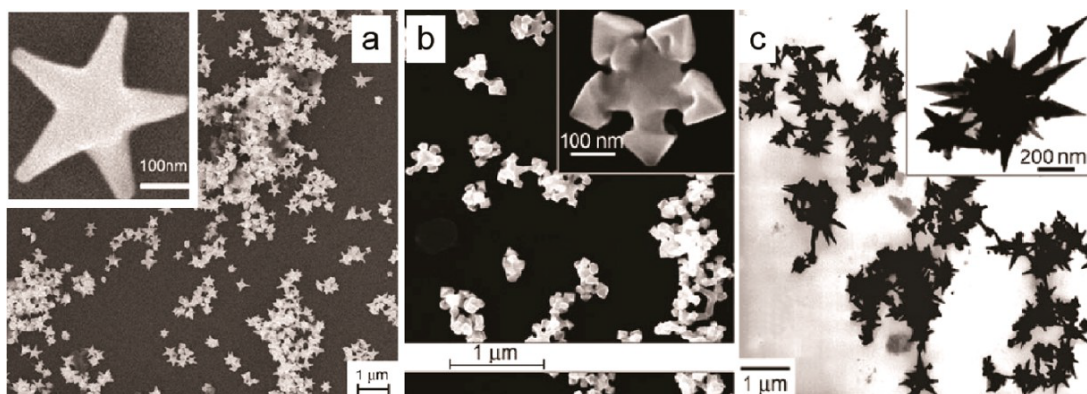


FIG. 17. SEM images of (a) star-shaped and (b) snow-flake-like gold NPs. (c) TEM image of gold nano-thorns [117].



## Toxicity of Ionic Liquids

Up to now, what the authors mentioned regarding the ionic liquids and their roles in nanoparticle preparation is promising. Nevertheless, ionic liquids frequently utilized up to the present time are toxic in nature, which has been verified by numerous toxicological statistics intended at an extensive choice of creatures. However, scientists need to discover innovative approaches to take benefit of the non-volatile nature of ionic liquids not exposed by typical liquid media [119]. Moreover, this feature must also be deliberated when the toxicological concern of ionic liquids is studied. The toxicological investigation of ionic liquids has been always verified; for instance, toxicity bioassessment consuming plants [120] and measurable construction property association modeling [121] have together appeared in the articles. The adaptable nature of ionic liquids once more represents the authority of designer-solvents; specifically, ionic liquids can be intended to be harmless. Through the adjacent partnership between toxicologists and scientists, greener and better-organized ionic liquids can be achieved.

## Conclusions

Nanostructured metals represent an important class of nanomaterials with multiple applications, such as: optics, sensors, catalysts and magnetic recording media, among others. The properties (optical, electronic, magnetic and catalytic) that metallic nanoparticles exhibit have a strong dependence on their shape and size, as well as on the nature of the metal or metals involved.

Ionic liquids and their technological applications constitute an exciting and emerging field of research. Although in the beginning, most of the research was related to their use in

"Green Chemistry", great advances were subsequently made using the ILs in various applications and advanced electrochemical devices. In addition, the use of ILs in the design of nanomaterials is one of the most current and promising fields in nanotechnology due to the very diverse applications of these compounds.

A rapid growth with a great potential can be noticed in metallic nanoparticle synthesis, which potentially leads to generate functional materials. To achieve this objective, it is clear that a multidisciplinary interaction and collaboration between biologists, chemists, physicists and engineers is needed in order to solve this synthesis issue of particles with desired characteristics. This, perhaps, leads to study their properties and their effects on the environment, as well as to explore new applications of the nanostructured metallic materials that are sustainable to be utilized.

Finally, ionic liquids propose incredible chances and open fascinating viewpoints for producing well-arranged nanostructures inside an anhydrous or low containing water medium. The authors accomplish this review article by proposing their views on the progress of the arena, indicating to zones of unblemished and fascinating service which will confidently realize achievement in the upcoming years.

## Acknowledgements

Firstly, the authors would like to thank Almighty Allah for granting them substantial skills, sympathetic skills and the chance to finish this review article efficiently. Without Allah's support, this achievement would not have been probable. They would also like to direct their gratitude to the Soran Research Centre, Salahaddin, Cihan and Ishik University for facility and entrance provision.

## References

- [1] MacFarlane, D.R., Kar, M. and Pringle, J.M., "Fundamentals of Ionic Liquids: From Chemistry to Applications", (Wiley, 2017).
- [2] Han, D. and Row, K.H., *Molecules*, 15 (4) (2010) 2405.
- [3] Rogers, R.D., Seddon, K.R. and Volkov, S., "Green Industrial Applications of Ionic Liquids", (Springer, Netherlands, 2012).
- [4] Kuzmina, O. and Hallett, J., "Application, Purification and Recovery of Ionic Liquids", (Elsevier Science, 2016).
- [5] Ludwig, R. and Kragl, U., *Angewandte Chemie, International Edition*, 46 (35) (2007) 6582.
- [6] Armstrong, J.P. et al., *Physical Chemistry, Chemical Physics*, 9 (8) (2007) 982.

- [7] Lozano, P., "Sustainable Catalysis in Ionic Liquids", (CRC Press, 2018).
- [8] Bermúdez, M.-D. et al., *Molecules*, 14 (8) (2009) 2888.
- [9] Armand, M. et al., Nature Publishing Group, World Scientific, (2011) 129.
- [10] Freemantle, M., "An Introduction to Ionic Liquids", (Royal Society of Chemistry, 2010).
- [11] Ue, M. et al., *Electrochemical and Solid-State Letters*, 5 (6) (2002) A119.
- [12] Gutowski, K.E. et al., *Journal of the American Chemical Society*, 125 (22) (2003) 6632.
- [13] Sowmiah, S. et al., *Molecules*, 14 (9) (2009) 3780.
- [14] Wasserscheid, P. and Welton, T., "Ionic Liquids in Synthesis", (John Wiley and Sons, 2008).
- [15] Armand, M. et al., *Nature Materials*, 8 (8) (2009) 621.
- [16] Berthod, A., Ruiz-Angel, M. and Carda-Broch, S., *Journal of Chromatography A*, 1184 (1-2) (2008) 6.
- [17] Freire, M.G. et al., *Journal of Physical Chemistry B*, 111 (45) (2007) 13082.
- [18] Maton, C., De Vos, N. and Stevens, C.V., *Chemical Society Reviews*, 42 (13) (2013) 5963.
- [19] Earle, M., Seddon, K. and Adams, C., *Chemical Communications*, 19 (1998) 2097.
- [20] Walden, P., *Серия математическая*, 8 (6) (1914) 405.
- [21] Angell, C.A., Ansari, Y. and Zhao, Z., *Faraday Discussions*, 154 (2012) 9.
- [22] Hurley, F.H. and Wier, T.P., *Journal of the Electrochemical Society*, 98 (5) (1951) 207.
- [23] Pernak, J., Rzemieniecki, T. and Materna, K., *Chemik*, 70 (9) (2016) 471.
- [24] Wilkes, J.S., *ECS Transactions*, 3 (35) (2007) 3.
- [25] Chatel, G. et al., *Green Chemistry*, 16 (4) (2014) 2051.
- [26] Lee, S.H. et al., *Journal of Biotechnology*, 133 (4) (2008) 486.
- [27] Lane, G.H. et al., *Electrochimica Acta*, 55 (28) (2010) 8947.
- [28] Wu, J. et al., *Chemical Reviews*, 115 (5) (2015) 2136.
- [29] Taige, M., Hilbert, D. and Schubert, T.J., *Zeitschrift für physikalische Chemie*, 226 (2) (2012) 129.
- [30] Lu, Y. et al., *Angewandte Chemie, International Edition*, 53 (2) (2014) 488.
- [31] Giernoth, R., *Angewandte Chemie, International Edition*, 49 (16) (2010) 2834.
- [32] Plechkova, N.V. and Seddon, K.R., *Chemical Society Reviews*, 37 (1) (2008) 123.
- [33] Scheffler, T.B. et al., *Inorganic Chemistry*, 22 (15) (1983) 2099.
- [34] Boon, J.A. et al., *Journal of Organic Chemistry*, 51 (4) (1986) 480.
- [35] Wilkes, J.S. and Zaworotko, M.J., *Journal of the Chemical Society, Chemical Communications*, 13 (1992) 965.
- [36] Abbott, A.P., et al., *Physical Chemistry Chemical Physics*, 16 (19) (2014) 9047.
- [37] Earle, M.J. et al., *Nature*, 439 (7078) (2006) 831.
- [38] Steinrueck, H.-P. and Wasserscheid, P., *Catalysis Letters*, 145 (1) (2015) 380.
- [39] Zhao, H. and Malhotra, S.V., "Applications of Ionic Liquids in Organic Synthesis". (*Aldrichimica Acta*, 2002).
- [40] Earle, M.J. and Seddon, K.R., *Pure and Applied Chemistry*, 72 (7) (2000) 1391.
- [41] Galán-Cano, F. et al., *Journal of Chromatography A*, 1300 (2013) 134.
- [42] Martins, P.L.G., Braga, A.R. and de Rosso, V.V., *Trends in Food Science and Technology*, 66 (2017) 117.
- [43] Redel, E., Thomann R. and Janiak, C., *Inorganic Chemistry*, 47 (1) (2008) 14.
- [44] Moniruzzaman, M. et al., *Biochemical Engineering Journal*, 48 (3) (2010) 295.
- [45] MacFarlane, D.R. et al., *Energy and Environmental Science*, 7 (1) (2014) 232.
- [46] Yang, Z. and Pan, W., *Enzyme and Microbial Technology*, 37 (1) (2005) 19.

- [47] Endres, F., Abbott, A. and MacFarlane, D., "Electrodeposition from Ionic Liquids", (John Wiley and Sons, 2017).
- [48] Endres, F., Chem. Phys. Chem., 3 (2) (2002) 144.
- [49] Feynman, R.P., There's plenty of room at the bottom: An invitation to enter a new field of physics, in: "Handbook of Nanoscience, Engineering and Technology", 3<sup>rd</sup> Edition, (CRC Press, 2012) 26-35.
- [50] Khan, S.B., Asiri, A.M. and Akhtar, K., "Development and Prospective Applications of Nanoscience and Nanotechnology: Nanomaterials and Their Fascinating Attributes", (Bentham Science Publishers, 2016).
- [51] Clark, D.P. and Pazdernik, N.J., "Biotechnology", (Elsevier Science, 2015).
- [52] Ferrari, M., Nature Reviews: Cancer, 5 (3) (2005) 161.
- [53] Akar, N. et al., Journal of Membrane Science, 437 (2013) 216.
- [54] Rogers, B., Adams, J. and Pennathur, S., "Nanotechnology: Understanding Small Systems", (CRC Press, 2014).
- [55] Machado, M.C. et al., Pediatric Research, 67 (5) (2010) 500.
- [56] Lyons, K., Food First Backgrounder, 16 (1) (2010) 1.
- [57] Ghalandarlaki, N., Alizadeh, A.M. and Ashkani-Esfahani, S., BioMed Research International, (2014).
- [58] Qu, X., Alvarez, P.J. and Li, Q., Water Research, 47 (12) (2013) 3931.
- [59] Roco, M.C., Mirkin, C.A. and Hersam, M.C., Springer Science and Business Media, 1 (2011).
- [60] Allen, J., "What Is the Future of Nanotechnology?", (Reference Point Press, Incorporated, 2016).
- [61] Khan, F.H., Oriental Journal of Chemistry, 29 (4) (2014) 1399.
- [62] Tibbals, H.F., "Medical Nanotechnology and Nanomedicine", (CRC Press, 2017).
- [63] Misra, R., Acharya, S. and Sahoo, S.K., Drug Discovery Today, 15 (19-20) (2010) 842.
- [64] Sahoo, S.K., Dilnawaz, F. and Krishnakumar, S., Drug Discovery Today, 13 (3-4) (2008) 144.
- [65] Godin, B. et al., Trends in Pharmacological Sciences, 31 (5) (2010) 199.
- [66] Zhang, L. et al., Clinical Pharmacology and Therapeutics, 83 (5) (2008) 761.
- [67] Zhang, X. et al., Chemosphere, 82 (4) (2011) 489.
- [68] Li, Y. et al., Toxicology Mechanisms and Methods, 28 (3) (2018) 167.
- [69] Hutter, E. and Fendler, J.H., Advanced Materials, 16 (19) (2004) 1685.
- [70] Sudrik, S.G. et al., Chemistry-A European Journal, 12 (3) (2006) 859.
- [71] Sun, S. et al., Science, 287 (5460) (2000) 1989.
- [72] Zhang, Q. et al., Chemistry-A European Journal, 16 (33) (2010) 10234.
- [73] Liang, H. et al., Journal of Physical Chemistry C, 114 (16) (2010) 7427.
- [74] Im, S.H. et al., Angewandte Chemie, International Edition, 44 (14) (2005) 2154.
- [75] Wiley, B.J. et al., Nano-letters, 6 (4) (2006) 765.
- [76] Tao, A., Sinsermsuksakul, P. and Yang, P., Angewandte Chemie, International Edition, 45 (28) (2006) 4597.
- [77] Liang, H. et al., Advanced Materials, 21 (45) (2009) 4614.
- [78] Wiley, B.J. et al., Nano-letters, 7 (4) (2007) 1032.
- [79] Liang, H. et al., Journal of the American Chemical Society, 131 (17) (2009) 6068.
- [80] Zhang, J., Langille, M.R. and Mirkin, C.A., Nano-letters, 11 (6) (2011) 2495.
- [81] Liang, H. et al., Journal of the American Chemical Society, 135 (26) (2013) 9616.
- [82] Zhang, W. et al., Chemistry of Materials, 20 (5) (2008) 1699.
- [83] Wilson, M. et al., "Nanotechnology: Basic Science and Emerging Technologies", (CRC Press, 2002).

- [84] Klabunde, K.J. and Richards, R., *Nanoscale Materials in Chemistry*, 1035 (2001), Wiley Online Library.
- [85] Liu, W.-T., *Journal of Bioscience and Bioengineering*, 102 (1) (2006) 1.
- [86] Das, I. and Ansari, S.A., "Nanomaterials in Science and Technology", (2009).
- [87] Bhushan, B., "Introduction to Nanotechnology", in: *Springer Handbook of Nanotechnology*, (Springer, 2017), 1-19.
- [88] Naito, M. et al., "Nanoparticle Technology Handbook", (Elsevier Science, 2018).
- [89] Thakkar, K.N., Mhatre, S.S. and Parikh, R.Y., *Nanomedicine: Nanotechnology, Biology and Medicine*, 6 (2) (2010) 257.
- [90] Schubert, U., "Synthesis of Inorganic Materials", (John Wiley and Sons, 2012).
- [91] Xiong, G. et al., *Chemistry of Materials*, 13 (6) (2001) 1943.
- [92] Lee, L., Seddon, G. and Stephens, F., "Stained Glass", (Mitchell Beazley, 1976).
- [93] José-Yacamán, M. et al., *Science*, 273 (5272) (1996) 223.
- [94] Turner, P., "History of Photography", (Hamlyn, 1987).
- [95] Magdassi, S. et al., *Chemistry of Materials*, 15 (11) (2003) 2208.
- [96] Fedlheim, D.L. and Foss, C.A., "Metal Nanoparticles: Synthesis, Characterization and Applications", (CRC Press, 2001).
- [97] Khandel, P. and Shahi, S.K., *Int. J. Nanomater. Biostruct.*, 6 (1) (2016) 1.
- [98] Singhal, G. et al., *Journal of Nanoparticle Research*, 13 (7) (2011) 2981.
- [99] Antonietti, M. et al., *Angewandte Chemie, International Edition*, 43 (38) (2004) 4988.
- [100] Mele, A., Tran, C.D. and De Paoli Lacerda, S.H., *Angewandte Chemie*, 115 (36) (2003) 4500.
- [101] Ratner, M.A. and Ratner, D., "Nanotechnology: A gentle Introduction to the Next Big Idea", (Prentice Hall Professional, 2003).
- [102] Ramsden, J., "Nanotechnology: An Introduction", (Elsevier Science, 2016).
- [103] Fukushima, T. et al., *Science*, 300 (5628) (2003) 2072.
- [104] Barisci, J. et al., *Electrochemistry Communications*, 6 (1) (2004) 22.
- [105] Kim, K.-S., Demberelnyamba, D. and Lee, H., *Langmuir*, 20 (3) (2004) 556.
- [106] Itoh, H., Naka, K. and Chujo, Y., *Journal of the American Chemical Society*, 126 (10) (2004) 3026.
- [107] Zhou, Y., Schattka, J.H. and Antonietti, M., *Nano-letters*, 4 (3) (2004) 477.
- [108] Rubio, J. et al., *Soft Matter*, 7 (22) (2011) 10737.
- [109] Grimme, S. et al., *Organic and Biomolecular Chemistry*, 5 (5) (2007) 741.
- [110] Kang, X. et al., *Journal of the American Chemical Society*, 136 (10) (2014) 3768.
- [111] Wei, G.-T. et al., *Journal of the American Chemical Society*, 126 (16) (2004) 5036.
- [112] Izquierdo, D. et al., *Analytical Chemistry*, 84 (13) (2012) 5723.
- [113] Mecerreyes, D., *Progress in Polymer Science*, 36 (12) (2011) 1629.
- [114] Dupont, J. and Scholten, J.D., *Chemical Society Reviews*, 39 (5) (2010) 1780.
- [115] Wei, L. et al., *Electrochimica Acta*, 76 (2012) 468.
- [116] Dong, J.-Y. et al., *Cryst. Eng. Comm.*, 14 (14) (2012) 4732.
- [117] Dong, J.-Y. et al., *Journal of Physical Chemistry C*, 114 (19) (2010) 8867.
- [118] Liao, H.G. et al., *Angewandte Chemie, International Edition*, 47 (47) (2008) 9100.
- [119] Rogers, R.D., *Nature*, 447 (7147) (2007) 917.
- [120] Couling, D.J. et al., *Green Chemistry*, 8 (1) (2006) 82.
- [121] Zhao, D., Liao, Y. and Zhang, Z., *Clean Soil, Air and Water*, 35 (1) (2007) 42.

### Numerical Testing by a Transfer-Matrix Technique of Simmons' Equation for the Local Current Density in Metal-Vacuum-Metal Junctions

Alexandre Mayer<sup>a</sup>, Marwan S. Mousa<sup>b</sup>, Mark J. Hagmann<sup>c</sup>  
and Richard G. Forbes<sup>d</sup>

<sup>a</sup> Department of Physics, University of Namur, Rue de Bruxelles 61, 5000 Namur, Belgium.

<sup>b</sup> Department of Physics, Mutah University, Al-Karak 61710, Jordan.

<sup>c</sup> Department of Electrical and Computer Engineering, University of Utah, Salt Lake City, Utah, USA.

<sup>d</sup> Advanced Technology Institute, University of Surrey, Guildford GU2 7XH, United Kingdom.

---

Received on: 3/7/2018;

Accepted on: 8/10/2018

---

**Abstract:** We test the consistency with which Simmons' model can predict the local current density obtained for flat metal-vacuum-metal junctions. The image potential energy used in Simmons' original papers had a missing factor of 1/2. Beside this technical issue, Simmons' model relies on a mean-barrier approximation for electron transmission through the potential-energy barrier between the metals. In order to test Simmons' expression for the local current density when the correct image potential energy is included, we compare the results of this expression with those provided by a transfer-matrix technique. We also consider the current densities provided by a numerical integration of the transmission probability obtained with the WKB approximation and Simmons' mean-barrier approximation. The comparison between these different models shows that Simmons' expression for the local current density actually provides results that are in good agreement with those provided by the transfer-matrix technique, for a range of conditions of practical interest. We show that Simmons' model provides good results in the linear and field-emission regimes of current density *versus* voltage plots. It loses its applicability when the top of the potential-energy barrier drops below the Fermi level of the emitting metal.

**Keywords:** Field Electron Emission, Theory, Metal-Vacuum-Metal Junction, Transmission Probability, Mean-Barrier Approximation, Transfer-Matrix Technique.

**PACS:** 85.30.Kk, 79.70.+q, 03.65.Nk.

## I. Introduction

Analytical models are extremely useful for the study of field electron emission. They provide indicative formulae for the emission current achieved with given physical parameters. This enables quantitative understanding of the role of these parameters. Analytical models also support the extraction of useful information from experimental data. They certainly guide the development of

technologies. These analytical models depend however on a series of approximations, typically the WKB (JWKB) approximation for the transmission of electrons through a potential-energy barrier [1–4]. It is therefore natural to question the accuracy of these models.

The accuracy with which the Murphy-Good formulation of Fowler-Nordheim theory [5–8] actually accounts for field electron emission from a flat metal surface was investigated in previous work [9–13]. The approach adopted by Mayer consists of comparing the results of this analytical model with those provided by a transfer-matrix technique [11–14]. This technique provides exact solutions of Schrödinger's equation for this field-emission process. The comparison with the Murphy-Good expression  $J_{\text{MG}} = (\pi k_B T / d) / \sin\left(\frac{\pi k_B T}{d}\right) \times at_F^{-2} \Phi^{-1} F^2 \exp\left[-b v_F \Phi^{\frac{3}{2}} / F\right]$  for the current density obtained with an applied electrostatic field  $F$ , a work function  $\Phi$  and a temperature  $T$  revealed that the results of this analytical model are essentially correct, within a factor of the order 0.5-1. In the Murphy-Good expression,  $a = 1.541434 \times 10^{-6} \text{ A eV V}^{-2}$ ,  $b = 6.830890 \text{ eV}^{-3/2} \text{ V nm}^{-1}$  [10],  $k_B$  is Boltzmann's constant,  $t_F$  and  $v_F$  are particular values of well-known special mathematical functions that account for the image interaction [7, 15],  $d = \hbar e F / (2 t_F \sqrt{2 m \Phi})$  with  $e$  the elementary positive charge and  $m$  the electron mass.  $\hbar$  is Planck's constant  $\hbar/2\pi$ . This study enabled the determination of a correction factor  $\lambda_{\text{MG}}$  to use with the Murphy-Good expression in order to get an exact result [13].

The objective of the present work is to apply the same approach to the analytical model developed by Simmons for the local current density through flat metal-vacuum-metal junctions [16–20]. Simmons' original model is widely cited in the literature. It was however noted that the image potential energy used in the original papers missed out a factor of  $\frac{1}{2}$  [18, 21]. An error in the current density obtained for a triangular barrier in the low-voltage range (Eq. 25 of Ref. 16) was also mentioned [20]. Beside these technical issues, Simmons' original model relies on a mean-barrier approximation for the transmission of electrons through the potential-energy barrier in the junction. It is natural to question this approximation and test the accuracy of the equation proposed by Simmons for the current density obtained in flat metal-vacuum-metal junctions when the correct image potential energy is included. We use for this purpose the

transfer-matrix technique, since it provides exact solutions for this barrier model. This work aims to provide a useful update and a numerical validation of Simmons' model.

This article is organized as follows. In Sec. II, we present the transfer-matrix technique that is used as reference model for the quantum-mechanical simulation of metal-vacuum-metal junctions. In Sec. III, we present the main ideas of Simmons' theory. This presentation essentially focusses on the results that are discussed in this work. In Sec. IV, we compare the results of different models for the current density obtained in flat metal-vacuum-metal junctions. We finally conclude this work in Sec. V.

## II. Modeling of Metal-Vacuum-Metal Junctions by a Transfer-Matrix Technique

The metal-vacuum-metal junction considered in this work is represented in Fig. 1. For this particular example, a static voltage  $V$  of 5 V is applied between the two metals. These metals have a Fermi energy  $\varepsilon_F$  of 10 eV and a common work function  $\Phi$  of 4.5 eV. The gap spacing  $D$  between the two metals is 2 nm. We refer by  $\mu_I$  to the Fermi level of the left-side metal (Region I). The Fermi level of the right-side metal (Region III) is then given by  $\mu_{\text{III}} = \mu_I - eV$ , where  $e$  refers to the elementary positive charge. For convenience, when presenting Simmons' theory, we will use the Fermi level  $\mu_I$  of the left-side metal as reference (zero value) for all potential-energy values discussed in this work. The total electron energy  $E$  will also be defined with respect to  $\mu_I$ . We will only consider positive values for the applied voltage  $V$ , so that the net electron current will always flow from the left to the right. The potential energy in Regions I and III is then given by  $V_I = \mu_I - \varepsilon_F$  and  $V_{\text{III}} = \mu_I - eV - \varepsilon_F$ . The potential energy in the vacuum gap ( $0 \leq z \leq D$ ) is given by  $V(z) = \mu_I + \Phi - eFz + V_{\text{image}}(z)$ , where  $F = V/D$  is the magnitude of the electrostatic field induced by the voltage  $V$ .  $V_{\text{image}}(z)$  refers to the image potential energy that applies to an electron situated between two flat metallic surfaces (see Eq. 7 in Sec. III). This vacuum region is also referred to as Region II.

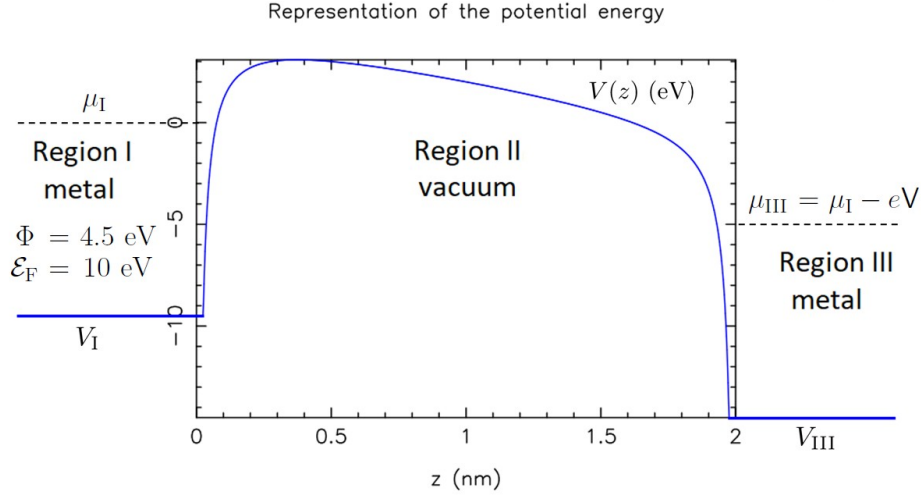


FIG. 1. Potential energy in a metal-vacuum-metal junction. A static voltage  $V$  of 5 V is applied. The gap spacing  $D$  is 2 nm. We take for convenience the Fermi level  $\mu_I$  of the left-side metal as reference for the potential-energy values.

In order to establish scattering solutions in cartesian coordinates, we assume that the wave functions are periodic along the lateral  $x$  and  $y$  directions (these directions are parallel to the flat surface of the two metals). We take a lateral periodicity  $L$  of 10 nm for the wave functions (this value is sufficiently large to make our results independent of  $L$ ). The boundary states in Region I and III are given respectively by:

$$\Psi_{i,j}^{I,\pm}(\vec{r}, t) = e^{i(k_{x,i}x + k_{y,j}y)} e^{\pm i \sqrt{\frac{2m}{\hbar^2}(E - V_I) - k_{x,i}^2 - k_{y,j}^2} z} e^{-iEt/\hbar} \quad \text{and} \quad \Psi_{i,j}^{III,\pm}(\vec{r}, t) = e^{i(k_{x,i}x + k_{y,j}y)} e^{\pm i \sqrt{\frac{2m}{\hbar^2}(E - V_{III}) - k_{x,i}^2 - k_{y,j}^2} z} e^{-iEt/\hbar},$$

where  $i = \sqrt{-1}$  and the  $\pm$  signs refer to the propagation direction of these boundary states relative to the  $z$ -axis.  $E$  is the total electron energy.  $k_{x,i} = i \frac{2\pi}{L}$  and  $k_{y,j} = j \frac{2\pi}{L}$  are the lateral components of the wavevector ( $i$  and  $j$  are two integers also used to enumerate the boundary states).  $E_z = E - \frac{\hbar^2}{2m}(k_{x,i}^2 + k_{y,j}^2)$  corresponds to the normal component of the electron energy.

By using a transfer-matrix technique, we can establish scattering solutions of Schrödinger's equation  $\left[ \frac{\hbar^2}{2m} \Delta + V(\vec{r}) \right] \Psi(\vec{r}, t) = i\hbar \frac{\partial}{\partial t} \Psi(\vec{r}, t)$ . The idea consists of propagating the boundary states  $\Psi_{i,j}^{III,\pm}$  of Region III across the vacuum gap (Region II). Since the potential energy is independent of  $x$  and  $y$ , there is no

coupling between states associated with different values of  $i$  or  $j$  and one can consider the propagation of these states separately. For the propagation of these states, we assume that the potential energy in Region II varies in steps of width  $\Delta z$  along the direction  $z$ . For each integer  $s$  ranging backwards from  $D/\Delta z$  to 1, the potential energy is thus replaced by the constant value  $V_s = \frac{1}{2}[V((s-1)\Delta z) + V(s\Delta z)]$ . The solutions of Schrödinger's equation are then (i) simple plane waves

$$A_s e^{i \sqrt{\frac{2m}{\hbar^2}(E_z - V_s)} z} + B_s e^{-i \sqrt{\frac{2m}{\hbar^2}(E_z - V_s)} z} \quad \text{when} \quad E_z = E - \frac{\hbar^2}{2m}(k_{x,i}^2 + k_{y,j}^2) > V_s, \quad \text{(ii) real exponentials} \quad A_s e^{-\sqrt{\frac{2m}{\hbar^2}(V_s - E_z)} z} +$$

$B_s e^{\sqrt{\frac{2m}{\hbar^2}(V_s - E_z)} z}$  when  $E_z < V_s$  or (iii) linear functions  $A_s + B_s z$  when  $E_z = V_s$ . One can get arbitrarily close to the exact potential-energy barrier by letting  $\Delta z \rightarrow 0$  (we used  $\Delta z = 0.0001$  nm). The propagation of the states  $\Psi_{i,j}^{III,\pm}$  across Region II is then achieved by matching continuity conditions for the wave function  $\Psi$  and its derivative  $\frac{d\Psi}{dz}$  at the boundaries of each step  $\Delta z$ , when going backwards from  $z = D$  to  $z = 0$  [11]. The layer-addition algorithm presented in a previous work should be used to prevent numerical instabilities [22]. The solutions finally obtained for  $z = 0$  are expressed as linear combinations of the boundary states  $\Psi_{i,j}^{I,\pm}$  in Region I.

This procedure leads to the following set of solutions:

$$\Psi_{i,j}^+ \stackrel{z \leq 0}{=} T_{i,j}^{++} \Psi_{i,j}^{I,+} + T_{i,j}^{-+} \Psi_{i,j}^{I,-} \stackrel{z \geq D}{=} \Psi_{i,j}^{III,+}, \quad (1)$$

$$\Psi_{i,j}^- \stackrel{z \leq 0}{=} T_{i,j}^{+-} \Psi_{i,j}^{I,+} + T_{i,j}^{--} \Psi_{i,j}^{I,-} \stackrel{z \geq D}{=} \Psi_{i,j}^{III,-}, \quad (2)$$

where the complex numbers  $T_{i,j}^{\pm\pm}$  correspond to the coefficients of these solutions in Region I.

We can then take linear combinations of these solutions in order to establish scattering solutions that correspond to single incident states  $\Psi_{i,j}^{I,+}$  in Region I or  $\Psi_{i,j}^{III,-}$  in Region III. These solutions will have the form

$$\Psi_{i,j}^+ \stackrel{z \leq 0}{=} \Psi_{i,j}^{I,+} + S_{i,j}^{-+} \Psi_{i,j}^{I,-} \stackrel{z \geq D}{=} S_{i,j}^{++} \Psi_{i,j}^{III,+}, \quad (3)$$

$$\Psi_{i,j}^- \stackrel{z \leq 0}{=} S_{i,j}^{--} \Psi_{i,j}^{I,-} \stackrel{z \geq D}{=} \Psi_{i,j}^{III,-} + S_{i,j}^{+-} \Psi_{i,j}^{III,+}, \quad (4)$$

where the complex numbers  $S_{i,j}^{++}$  and  $S_{i,j}^{--}$  provide respectively the coefficients of the transmitted and reflected states for an incident state  $\Psi_{i,j}^{I,+}$  in Region I. The complex numbers  $S_{i,j}^{--}$  and  $S_{i,j}^{+-}$  provide respectively the coefficients of the transmitted and reflected states for an incident state  $\Psi_{i,j}^{III,-}$  in Region III. These coefficients are given by  $S_{i,j}^{++} = [T_{i,j}^{++}]^{-1}$ ,  $S_{i,j}^{-+} = T_{i,j}^{-+} [T_{i,j}^{++}]^{-1}$ ,  $S_{i,j}^{--} = T_{i,j}^{--} - T_{i,j}^{-+} [T_{i,j}^{++}]^{-1} T_{i,j}^{+-}$  and  $S_{i,j}^{+-} = -[T_{i,j}^{++}]^{-1} T_{i,j}^{+-}$ .<sup>[23]</sup>

These scattering solutions are finally used to compute the local current density  $J$  that flows from Region I to Region III. The idea consists of integrating the contribution of each incident state  $\Psi_{i,j}^{I,+}$  in Region I (this provides the current-density contribution moving to the right) as well as the contribution of each incident state  $\Psi_{i,j}^{III,-}$  in Region III (this provides the current-density contribution moving to the left). The net value of the current density is given by the difference between these two contributions. The detailed expression for the current density  $J$  has been established in previous work [24–26]. It is given formally by:

$$J_{\text{TM}} = \frac{1}{L^2} \frac{2e}{h} \int_{V_I}^{\infty} \sum_{i,j} f_I(E) \frac{v_{\text{III},(i,j)}}{v_{\text{I},(i,j)}} |S_{i,j}^{++}|^2 dE - \frac{1}{L^2} \frac{2e}{h} \int_{V_{\text{III}}}^{\infty} \sum_{i,j} f_{\text{III}}(E) \frac{v_{\text{I},(i,j)}}{v_{\text{III},(i,j)}} |S_{i,j}^{--}|^2 dE, \quad (5)$$

where the summations are restricted to solutions that are propagative both in Region I and Region III. This requires  $E_z = E - \frac{\hbar^2}{2m}(k_{x,i}^2 + k_{y,j}^2) > \max(V_I, V_{\text{III}})$ .

$v_{\text{I},(i,j)} = \frac{\hbar}{m} \sqrt{\frac{2m}{\hbar^2}(E_z - V_I)}$  and  $v_{\text{III},(i,j)} = \frac{\hbar}{m} \sqrt{\frac{2m}{\hbar^2}(E_z - V_{\text{III}})}$  represent the normal component of the electron velocity in Regions I and III.  $\frac{v_{\text{III},(i,j)}}{v_{\text{I},(i,j)}} |S_{i,j}^{++}|^2$  and  $\frac{v_{\text{I},(i,j)}}{v_{\text{III},(i,j)}} |S_{i,j}^{--}|^2$  both represent the transmission probability  $D_{\text{TM}}$  of the potential-energy barrier in Region II, at the normal energy  $E_z$ .  $f_I(E) = 1/\{1 + \exp[(E - \mu_I)/k_B T]\}$  and  $f_{\text{III}}(E) = 1/\{1 + \exp[(E - \mu_{\text{III}})/k_B T]\}$  finally refer to the Fermi distributions in Regions I and III [27].

One can show mathematically that Eq. 5, with  $L \gg 1$ , is equivalent to:

$$J_{\text{TM}} = \int_{\max(V_I, V_{\text{III}})}^{\infty} \Delta N(E_z) D_{\text{TM}}(E_z) dE_z, \quad (6)$$

where the integration is over the normal energy  $E_z$  instead of the total energy  $E$ .  $D_{\text{TM}}(E_z) = \frac{v_{\text{III},(i,j)}}{v_{\text{I},(i,j)}} |S_{i,j}^{++}|^2 = \frac{v_{\text{I},(i,j)}}{v_{\text{III},(i,j)}} |S_{i,j}^{--}|^2$  is the transmission probability of the potential-energy barrier at the normal energy  $E_z$ .  $\Delta N(E_z) = N_I(E_z) - N_{\text{III}}(E_z)$ , with  $N_I(E_z) = \frac{4\pi m e}{h^3} k_B T \ln \left[ 1 + \exp\left(-\frac{E_z - \mu_I}{k_B T}\right) \right]$  and  $N_{\text{III}}(E_z) = \frac{4\pi m e}{h^3} k_B T \ln \left[ 1 + \exp\left(-\frac{E_z - \mu_{\text{III}} + eV}{k_B T}\right) \right]$  represent the incident normal-energy distributions of the two metals. This expression of the local current density is more standard in the field emission community.

For the integration over  $E$  in Eq. 5 or  $E_z$  in Eq. 6, we use a step  $\Delta E$  of 0.01 eV. It was checked that Eq. 5 and Eq. 6 provide identical results. A room temperature  $T$  of 300 K is assumed in this work.

### III. Simmons' Model for the Current Density in Flat Metal-Vacuum-Metal Junctions

We present now the main ideas of Simmons' model for the local current density through a flat metal-vacuum-metal junction (see Fig. 1). This presentation focuses on the results that are actually required for a comparison with the transfer-matrix results.



We keep for consistency the notations introduced in the previous section.

### A. Potential-Energy Barrier

The potential energy in the vacuum gap ( $0 \leq z \leq D$ ) is given by [16]:

$$V(z) = \mu_1 + \Phi - eFz - \frac{1}{2} \frac{e^2}{4\pi\epsilon_0} \left[ \frac{1}{2z} + \sum_{n=1}^{\infty} \left( \frac{nD}{(nD)^2 - z^2} - \frac{1}{nD} \right) \right], \quad (7)$$

where the last term of Eq. 7 accounts for the image potential energy  $V_{\text{image}}(z)$  that applies to an electron situated between two flat metallic surfaces [28]. In Simmons' original papers [16, 17], there is a factor 1/2 missing in the image potential energy. This factor 1/2, which is included for correction in Eq. 7, comes from the self-interaction character of the image potential energy (the image charges follow automatically the displacement of the electron and work must actually only be done on the electron). This technical error was mentioned later by Simmons [18]. It was also pointed out in a paper by Miskovsky et al. [21].

In order to derive analytical expressions for the local current density, Simmons introduces a useful approximation for the image potential energy:  $V_{\text{image}}(z) \cong -1.15\lambda \frac{D^2}{z(D-z)}$  [16]. The potential energy in the vacuum gap can then be approximated by:

$$V(z) = \mu_1 + \Phi - eFz - 1.15\lambda \frac{D^2}{z(D-z)}, \quad (8)$$

where  $\lambda = \frac{e^2}{16\pi\epsilon_0 D}$ . We provide here a corrected expression for  $\lambda$ ; this includes the missing factor  $1/2$ .

### B. Mean-Barrier Approximation for the Transmission Probability

With  $E_z = E - \frac{\hbar^2}{2m}(k_x^2 + k_y^2)$  the normal component of the energy, the probability for an electron to cross the potential-energy barrier in Region II is given, within the simple WKB approximation, [1-4] by:

$$D_{WKB} = \exp \left\{ -\frac{2\sqrt{2m}}{\hbar} \int_{z_1}^{z_2} [V(z) - E_z]^{1/2} dz \right\}, \quad (9)$$

where  $z_1$  and  $z_2$  are the classical turning points of the barrier at the normal energy  $E_z$  (i.e., the solutions of  $V(z_1) = V(z_2) = E_z$  with  $z_1 \leq z_2$ ). Simmons then replaces  $V(z)$  by  $V(z)$

$= \mu_1 + \phi(z)$ , where  $\phi(z) = \Phi - eFz + V_{\text{image}}(z)$  represents the difference between  $V(z)$  and the Fermi level  $\mu_1$  of the left-side metal (this is the metal that actually emits electrons for a positive voltage). He finally proposes a mean-barrier approximation for the transmission probability [16]:

$$D_{\text{Sim}} = \exp \left\{ -\frac{2\sqrt{2m}}{\hbar} \beta \Delta z [\bar{\phi} - (E_z - \mu_1)]^{1/2} \right\}, \quad (10)$$

where  $\Delta z = z_2 - z_1$  represents here the width of the barrier at the Fermi level of the left-side metal (i.e., for  $E_z = \mu_1$ ).  $\bar{\phi} = \frac{1}{z_2 - z_1} \int_{z_1}^{z_2} \phi(z) dz$  represents the mean barrier height above the Fermi level of the left-side metal.  $\beta$  is a correction factor related to the mean-square deviation of  $\phi(z)$  with respect to  $\bar{\phi}$  [16]. For the barrier shown in Eq. 7 (image potential energy included), Simmons recommends using  $\beta = 1$ . The mathematical justification of Eq. 10 can be found in the Appendix of Ref. 16.

### C. Analytical Expression for the Local Current Density

In his original paper [16], Simmons proposes a general formula for the net local current density  $J$  that flows between the two metals of the junction (see Eq. 20 of Ref. 16). The idea consists of integrating the contribution to the current density of each incident state in the two metals (the transmission of these states through the potential-energy barrier is evaluated with Eq. 10). Different analytical approximations were introduced by Simmons to achieve this result (in particular, in Eqs. 15, 16 and 18 that lead to Eq. 20 of Ref. 16; they require  $\frac{2\sqrt{2m}}{\hbar} \beta \Delta z (\bar{\phi} + eV)^{1/2} \gg 1$ ). The temperature-dependence of the current density was established in Ref. 19. The final expression, which accounts for the temperature, is given by:

$$J_{\text{Sim}} = J_0 \times \frac{\pi B k_B T}{\sin(\pi B k_B T)} \times \{ \bar{\phi} \exp(-A \bar{\phi}^{1/2}) - (\bar{\phi} + eV) \exp(-A(\bar{\phi} + eV)^{1/2}) \}, \quad (11)$$

where  $J_0 = \frac{e}{\hbar(2\pi\beta\Delta z)^2}$ ,  $A = \frac{2\sqrt{2m}}{\hbar} \beta \Delta z$  and  $B = \frac{A}{2\bar{\phi}^{1/2}}$ . The term  $J_0 \bar{\phi} \exp(-A \bar{\phi}^{1/2})$  accounts for the current moving to the right. The term  $J_0 (\bar{\phi} + eV) \exp(-A(\bar{\phi} + eV)^{1/2})$  accounts

for the current moving to the left. The temperature-dependence is contained in the factor  $\frac{\pi B k_B T}{\sin(\pi B k_B T)}$  [19, 29]. As mentioned previously, a temperature  $T$  of 300 K is considered in this work.

For a potential-energy barrier approximated by Eq. 8, Simmons provides an approximation for the classical turning points at the Fermi level of the left-side metal [16]. If  $eV < \Phi$ , with  $\Phi$  the local work function, these turning points are given by:

$$\begin{aligned} z_1 &= 1.2\lambda D/\Phi \\ z_2 &= D[1 - 9.2\lambda/(3\Phi + 4\lambda - 2eV)] + z_1 \end{aligned} \quad (12)$$

Otherwise, if  $eV \geq \Phi$ , they are given by:

$$\begin{aligned} z_1 &= 1.2\lambda D/\Phi \\ z_2 &= (\Phi - 5.6\lambda) \left( \frac{D}{eV} \right). \end{aligned} \quad (13)$$

These expressions are calculated with the corrected factor  $\lambda = \frac{e^2 \ln 2}{16\pi\epsilon_0 D}$ . We can then compute the width  $\Delta z = z_2 - z_1$  of the barrier at the Fermi level of the left-side metal as well as the mean barrier height  $\bar{\phi}$  above this Fermi level ( $\bar{\phi}$  represents the mean barrier height, over the range  $\Delta z$ , experienced by an electron tunneling with a normal energy equal to the left-side Fermi level) [16]. The result is given by:

$$\bar{\phi} = \Phi - \frac{eV(z_1 + z_2)}{2D} - \frac{1.15\lambda D}{z_2 - z_1} \ln \left[ \frac{z_2(D - z_1)}{z_1(D - z_2)} \right]. \quad (14)$$

With Simmons' recommendation to use  $\beta = 1$ , we can compute each quantity in Eq. 11. This is the equation we want to test numerically by comparing its predictions with the results of the transfer-matrix technique.  $J_{\text{Sim}}$  depends on the mean-barrier approximation of the transmission probability (Eq. 10), on the analytical approximations introduced by Simmons to establish Eq. 11 and on Eqs. 12, 13 and 14 for  $\Delta z = z_2 - z_1$  and  $\bar{\phi}$ .

## D. Numerical Expressions for the Local Current Density

It is actually possible to integrate numerically the transmission probability  $D_{\text{Sim}}$  provided by Eq. 10. By analogy with the current density  $J_{\text{TM}}$  provided by the transfer-matrix formalism, the current density obtained by the numerical integration of  $D_{\text{Sim}}$  will be given by:

68

$$\begin{aligned} J_{\text{Sim-num}} &= \frac{1}{L^2} \frac{2e}{h} \int_{V_I}^{\infty} \sum_{i,j} f_I(E) D_{\text{Sim}}(E) \\ &\quad - \frac{\hbar^2}{2m} (k_{x,i}^2 + k_{y,j}^2) dE \\ &\quad - \frac{1}{L^2} \frac{2e}{h} \int_{V_{\text{III}}}^{\infty} \sum_{i,j} f_{\text{III}}(E) D_{\text{Sim}}(E) \\ &\quad - \frac{\hbar^2}{2m} (k_{x,i}^2 + k_{y,j}^2) dE \end{aligned} \quad (15)$$

$$= \int_{\max(V_I, V_{\text{III}})}^{\infty} \Delta N(E_z) D_{\text{Sim}}(E_z) dE_z \quad (16)$$

in the standard formulation.  $D_{\text{Sim}}$  is obtained here by a numerical evaluation of Eq. 10 ( $\Delta z = z_2 - z_1$  and  $\bar{\phi}$  are evaluated on the exact barrier given in Eq. 7). The comparison of  $J_{\text{Sim-num}}$  with the results of Eq. 11 will validate the approximations that lead to this analytical expression.

It will also be interesting to consider the current density obtained by a numerical integration of the transmission probability provided by the simple WKB approximation (Eq. 9). The result will be given by:

$$\begin{aligned} J_{\text{WKB}} &= \frac{1}{L^2} \frac{2e}{h} \int_{V_I}^{\infty} \sum_{i,j} f_I(E) D_{\text{WKB}}(E) \\ &\quad - \frac{\hbar^2}{2m} (k_{x,i}^2 + k_{y,j}^2) dE \\ &\quad - \frac{1}{L^2} \frac{2e}{h} \int_{V_{\text{III}}}^{\infty} \sum_{i,j} f_{\text{III}}(E) D_{\text{WKB}}(E) \\ &\quad - \frac{\hbar^2}{2m} (k_{x,i}^2 + k_{y,j}^2) dE \end{aligned} \quad (17)$$

$$= \int_{\max(V_I, V_{\text{III}})}^{\infty} \Delta N(E_z) D_{\text{WKB}}(E_z) dE_z \quad (18)$$

in the standard formulation.  $J_{\text{WKB}}$  will enable a useful comparison with Simmons' theory given the fact that the transmission probability used by Simmons is actually an approximation of the WKB expression.

## IV. Comparison between Different Models for the Local Current Density

We can compare at this point the local current densities provided by the transfer-matrix technique ( $J_{\text{TM}}$  by Eq. 5 or Eq. 6), Simmons' analytical expression ( $J_{\text{Sim}}$  by Eq.

11), a numerical integration of Simmons' formula for the transmission probability ( $J_{\text{Sim-num}}$  by Eq. 16) and a numerical integration of the transmission probability provided by the WKB approximation ( $J_{\text{WKB}}$  by Eq. 18).

In order to understand the different regimes that appear in typical  $J$ - $V$  plots, we will start by showing the  $dJ/dE$  distributions obtained for a few representative cases. This will illustrate the "linear regime" and the "field-emission regime" that are indeed appropriately described by Simmons' equation 11. In the "linear regime", the difference  $\mu_I - \mu_{\text{III}}$  between the Fermi level of the two metals is smaller than the width of the total-energy distribution of the right-flowing and left-flowing contributions to the current. These two contributions tend to cancel out except in an energy window of the order of  $\mu_I - \mu_{\text{III}}$ , which is equal to  $eV$ . In the "field-emission regime", the Fermi level  $\mu_{\text{III}}$  of the right metal is sufficiently far below  $\mu_I$  to make the contribution of the left-flowing current negligible. The diode current is essentially determined by the right-flowing current, which increases rapidly with  $V$ . The "flyover regime" will be beyond the predictive capacities of Simmons' theory. In this regime, the top  $V_{\text{top}}$  of the potential-energy barrier drops below  $\mu_I$ , so that electrons at the Fermi level of the left metal can fly over the top of

this barrier, provided  $E_z = E - \frac{\hbar^2}{2m}(k_x^2 + k_y^2) > V_{\text{top}}$ .

We consider for the moment a gap spacing  $D$  of 2 nm and three representative values of the applied voltage  $V$ : 0.5 V, 5 V and 30 V. The potential-energy distribution  $V(z)$  and the total-energy distribution of the current density  $dJ/dE$  obtained for these values of the applied voltage are represented in Figs. 2, 3 and 4. The  $dJ/dE$  distributions are calculated by the transfer-matrix technique.

With an applied voltage  $V$  of 0.5 V (Fig. 2), the Fermi level  $\mu_{\text{III}} = \mu_I - eV$  of the right-side metal ("Region III") is 0.5 eV below the Fermi level  $\mu_I$  of the left-side metal ("Region I"). The rightwards-moving and leftwards-moving currents in the junction cancel out except in the energy window between  $\mu_{\text{III}}$  and  $\mu_I$  ( $\pm$  a few  $k_B T$ , as a result of the effect of temperature on the electron energy distributions  $f_I(E)$  and  $f_{\text{III}}(E)$ ). The integrated net current density  $J$  that flows from left to right is  $1.5 \times 10^{-6}$  A/cm<sup>2</sup>. We are in the "linear regime" of the  $J$ - $V$  plot. The net current density  $J$  depends indeed essentially on the separation between  $\mu_{\text{III}}$  and  $\mu_I$ , which is equal to  $eV$ . The mean barrier height  $\bar{\phi}$  at the Fermi level is 3.2 eV. Since  $eV \ll \bar{\phi}$ , Eq. 11 will predict a linear  $J$ - $V$  dependence in this regime.

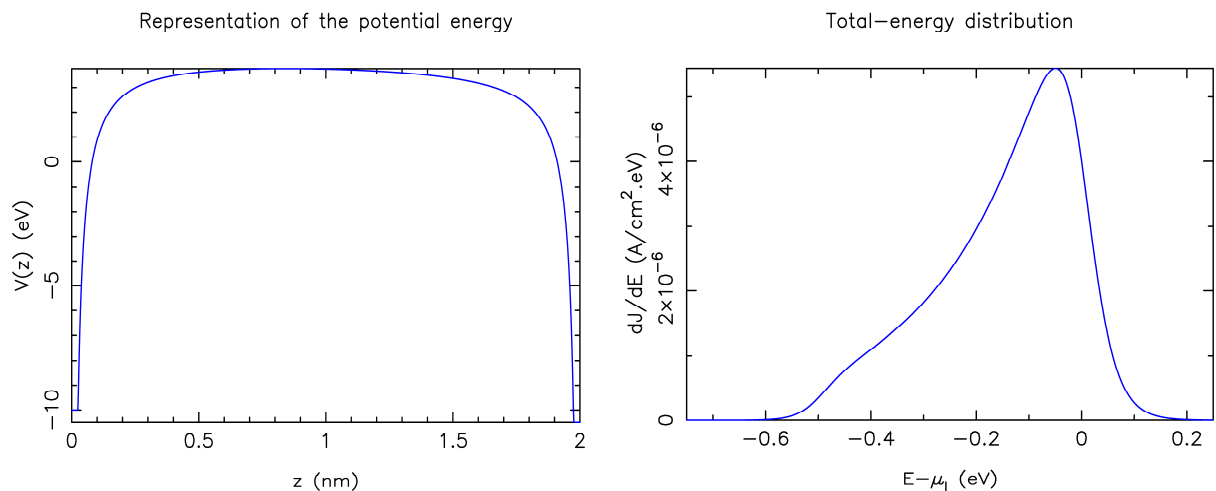


FIG. 2. Potential energy  $V(z)$  (top) and total-energy distribution of the current density  $dJ/dE$  (bottom) for an applied voltage  $V$  of 0.5 V.  $dJ/dE$  is calculated by the transfer-matrix technique. We take for convenience the Fermi level  $\mu_I$  of the left-side metal as reference for the potential-energy values.

With an applied voltage  $V$  of 5 V (Fig. 3), the Fermi level  $\mu_{\text{III}} = \mu_{\text{I}} - eV$  of the right-side metal is 5 eV below the Fermi level  $\mu_{\text{I}}$  of the left-side metal. The net current that flows through the junction is essentially determined by the right-flowing current from the left-side metal ("Region I"). The left-flowing current from the right-side metal ("Region III") only contributes for normal energies 5 eV or more below  $\mu_{\text{I}}$ . Its influence on the net current is negligible. The local current density  $J$  that flows from left to right is 6.2 A/cm<sup>2</sup>. The total-energy

distribution of the local current density  $dJ/dE$  (shown in Fig. 3) is a classical field-emission profile. The electrons that are emitted by the left-side metal cross the potential-energy barrier in the junction by a tunneling process. The local current density  $J$  increases rapidly with  $V$ . We are in the "field-emission regime" of the  $J$ - $V$  plot. The mean barrier height  $\bar{\phi}$  at the Fermi level is 2.6 eV in this case. Since  $eV > \bar{\phi}$ , Eq. 11 will predict a non-linear  $J$ - $V$  dependence.

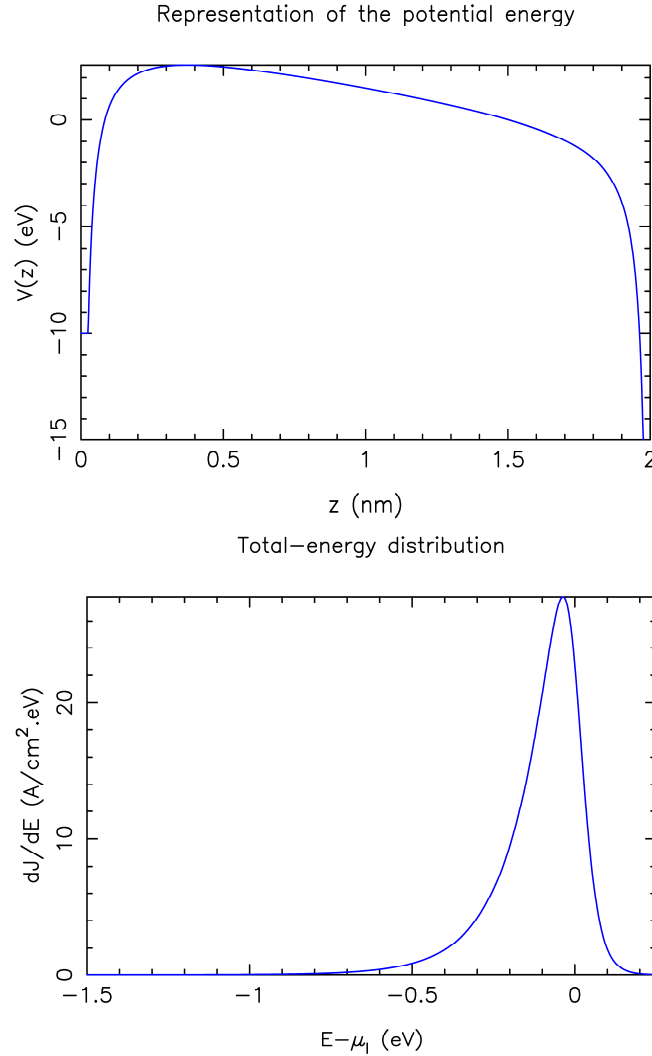


FIG. 3. Potential energy  $V(z)$  (top) and total-energy distribution of the current density  $dJ/dE$  (bottom) for an applied voltage  $V$  of 5 V.  $dJ/dE$  is calculated by the transfer-matrix technique. We take for convenience the Fermi level  $\mu_{\text{I}}$  of the left-side metal as reference for the potential-energy values.

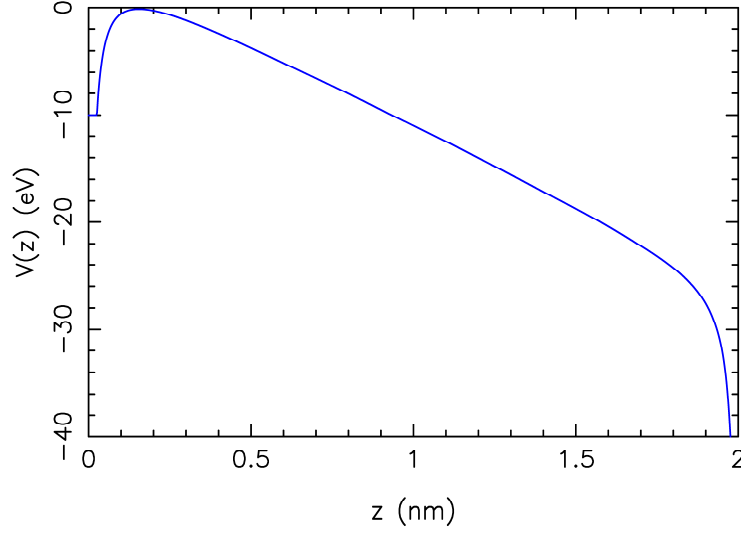
With an applied voltage  $V$  of 30 V (Fig. 4), the top  $V_{\text{top}}$  of the potential-energy barrier drops below the Fermi level  $\mu_{\text{I}}$  of the left-side metal. All incident electrons with a normal energy  $E_z = E - \frac{\hbar^2}{2m}(k_x^2 + k_y^2) > V_{\text{top}}$  can actually cross the junction without

tunneling, although quantum-mechanical reflection effects will occur. There is no classical turning point  $z_1$  or  $z_2$  at the Fermi level  $\mu_{\text{I}}$  of the left-side metal and Simmons' model for the transmission probability  $D_{\text{Sim}}$  and the local current density  $J_{\text{Sim}}$  loses any

applicability. The mean barrier height  $\bar{\phi}$  at the Fermi level can not be calculated in this case, since the turning points  $z_1$  and  $z_2$  are not defined. We are in the “flyover regime” of the  $J$ - $V$  plot. It is probably interesting for future

work to extend Simmons' theory so that it also applies in this regime. It has been shown by Zhang that in the flyover regime, it is necessary to account for space charge effects [30].

Representation of the potential energy



Total-energy distribution

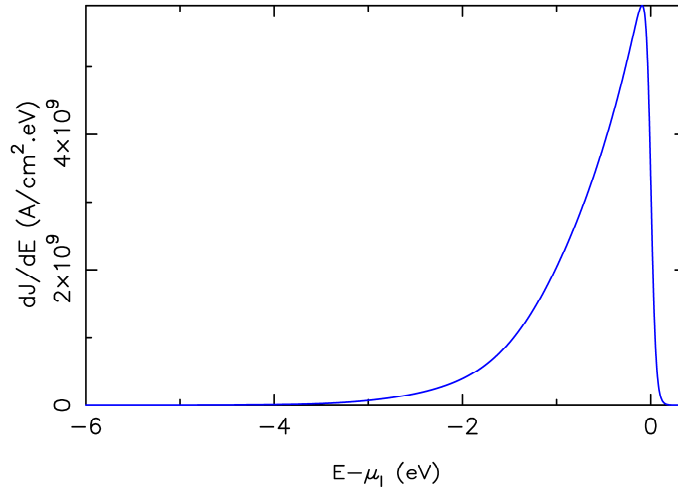


FIG. 4. Potential energy  $V(z)$  (top) and total-energy distribution of the current density  $dJ/dE$  (bottom) for an applied voltage  $V$  of 30 V.  $dJ/dE$  is calculated by the transfer-matrix technique. We take for convenience the Fermi level  $\mu_1$  of the left-side metal as reference for the potential-energy values.

There is also the possibility that at very high current densities, the junction heating will be so great that junction destruction will occur. We are not aware of any work on this effect that is specifically in the context of MVM devices, but for conventional field electron emitters, it is usually thought [31, 32] that heating-related destructive effects will occur for current densities of order  $10^7$  to  $10^8$   $\text{A}/\text{cm}^2$  or higher. The situation can become

very complicated if in reality there are nanoprotusions on the emitting surface that cause local field enhancement, and hence local enhancement of the current density, or if heating due to slightly lower current densities can induce the formation and/or growth of nanoprotusions by means of thermodynamically driven electroformation processes. Detailed examination of these

heating-related issues is beyond the scope of the present work.

The  $J$ - $V$  plot finally obtained for an applied voltage  $V$  that ranges between 0.01 V and 100 V is represented in Fig. 5. The figure represents the local current density  $J_{\text{TM}}$  obtained by the transfer-matrix technique (Eq. 5 or Eq. 6; the results are identical), the current density  $J_{\text{WKB}}$  obtained by a numerical integration of  $D_{\text{WKB}}$  (Eq. 18), the current density  $J_{\text{Sim-num}}$  obtained by a numerical integration of  $D_{\text{Sim}}$  (Eq. 16) and the current density  $J_{\text{Sim}}$  provided by Simmons' analytical model (Eq. 11). These results correspond to a gap spacing  $D$  of 2 nm. The linear, field-emission and flyover regimes are clearly indicated. The results provided by the different models turn out to be in excellent agreement

up to a voltage  $V$  of 10 V.  $J_{\text{Sim-num}}$  deviates progressively from the other models beyond this point. The agreement between  $J_{\text{TM}}$ ,  $J_{\text{WKB}}$  and  $J_{\text{Sim}}$  is remarkable, considering the fact that the current density varies over 19 orders of magnitude for the conditions considered. Simmons' analytical model (Eq. 11) turns out to provide a very good estimate of the current density achieved in the linear and field-emission regimes. Simmons' analytical model however stops working when Eqs. 13 and 14 do not provide  $\bar{\phi} \geq 0$ , which is the case in the flyover regime (the top of the potential-energy barrier drops indeed below the Fermi level  $\mu_1$  of the left-side metal and Eq. 10 for the transmission probability loses any applicability).

Representation of the  $J$ - $V$  data

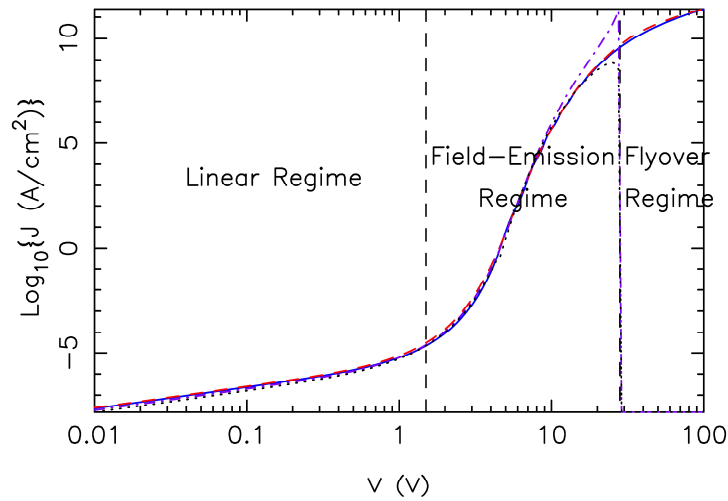


FIG. 5.  $J$ - $V$  plot for a metal-vacuum-metal junction whose gap spacing  $D$  is 2 nm. The four curves correspond to  $J_{\text{TM}}$  (solid),  $J_{\text{WKB}}$  (dashed),  $J_{\text{Sim-num}}$  (dot-dashed) and  $J_{\text{Sim}}$  (dotted). These results correspond to a common work function  $\Phi$  of 4.5 eV, a Fermi energy  $\varepsilon_F$  of 10 eV and a temperature  $T$  of 300 K.

Fig. 6 shows more clearly the differences between the different models. This figure presents the ratios  $J_{\text{WKB}}/J_{\text{TM}}$ ,  $J_{\text{Sim-num}}/J_{\text{TM}}$  and  $J_{\text{Sim}}/J_{\text{TM}}$  between the current densities  $J_{\text{WKB}}$ ,  $J_{\text{Sim-num}}$  and  $J_{\text{Sim}}$  provided by Eqs. 18, 16 and 11 and the transfer-matrix result  $J_{\text{TM}}$  (Eq. 6). The figure shows that  $J_{\text{WKB}}$ ,  $J_{\text{Sim-num}}$  and  $J_{\text{Sim}}$  actually follow the transfer-matrix result  $J_{\text{TM}}$  within a factor of the order 0.5-2 up to an applied voltage  $V$  of 10 V. The current density  $J_{\text{WKB}}$  obtained by a numerical integration of  $D_{\text{WKB}}$  with respect to normal energy (Eq. 18) follows in general the transfer-matrix result more closely. The current density  $J_{\text{Sim}}$  derived

from Simmons' theory still provides very decent results.  $J_{\text{Sim}}$  (Eq. 11) is the analytical expression derived by Simmons (main focus of this article).  $J_{\text{WKB}}$  and  $J_{\text{Sim-num}}$  require a numerical evaluation of the transmission probability (by Eq. 9 or Eq. 10) and a numerical integration of this transmission probability with respect to normal energy to finally obtain the current density. They are presented only for comparison. We note that  $J_{\text{WKB}}$  tends here to overestimate the local current densities. This behavior was already observed with the Schottky-Nordheim barrier that is relevant to field electron emission from

a flat metal, when considering normal energies in the vicinity of the Fermi level of a metal whose physical parameters are the same as those considered at this point ( $\Phi = 4.5$  eV and  $\varepsilon_F = 10$  eV) [11, 12]. As shown in Ref. 13, underestimation of the local current densities by the simple WKB approximation is also possible for smaller values of  $\varepsilon_F$ . We note finally that  $J_{\text{Sim-num}}$  and  $J_{\text{Sim}}$  provide close results up to an applied voltage  $V$  of 10 V. This proves that the approximations that lead to  $J_{\text{Sim}}$  are reasonable up to this point.  $J_{\text{Sim-num}}$ , which is based on a numerical integration of

$D_{\text{Sim}}$ , starts then over-estimating the current density. Simmons' mean-barrier approximation is actually a poor model of the transmission probability when the potential-energy barrier becomes too small (we can indeed have  $E_z - \mu_l > \bar{\phi}$  for values of  $E_z$  that have a non-negligible  $\Delta N(E_z)$ , while in reality  $E_z - \mu_l < \phi(z)$  in the potential-energy barrier). Simmons' analytical expression for the local current density ( $J_{\text{Sim}}$  by Eq. 11) appears to be more robust in these conditions.  $J_{\text{Sim-num}}$  and  $J_{\text{Sim}}$  can not be applied in the flyover regime.

### WKB & Simmons formulas vs Transfer Matrix

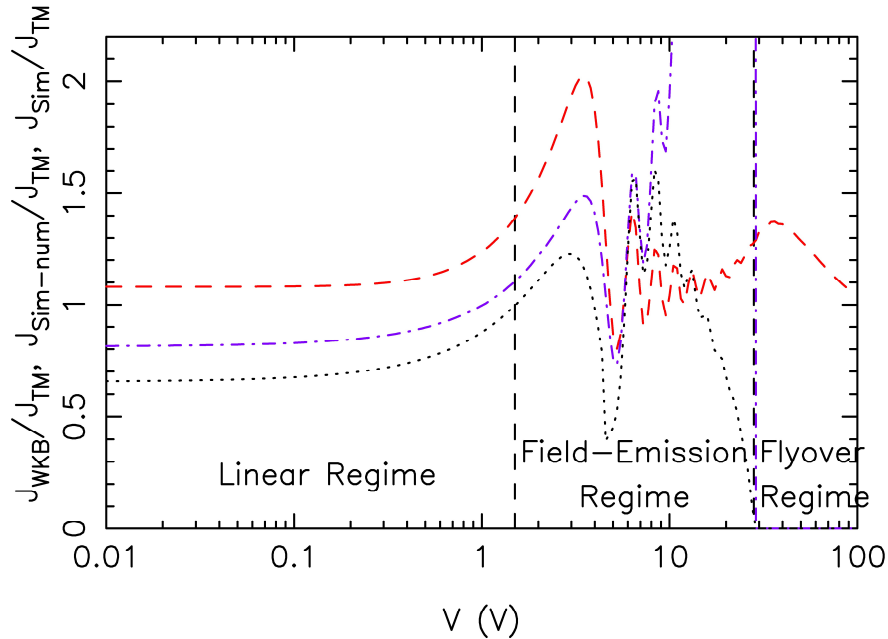


FIG. 6. Ratio  $J_{\text{WKB}}/J_{\text{TM}}$  (dashed),  $J_{\text{Sim-num}}/J_{\text{TM}}$  (dot-dashed) and  $J_{\text{Sim}}/J_{\text{TM}}$  (dotted) for a metal-vacuum-metal junction whose gap spacing  $D$  is 2 nm. These results correspond to a common work function  $\Phi$  of 4.5 eV, a Fermi energy  $\varepsilon_F$  of 10 eV and a temperature  $T$  of 300 K.

We finally provide in Table 1 a more systematic study of the ratio  $J_{\text{Sim}}/J_{\text{TM}}$  between the current density  $J_{\text{Sim}}$  provided by Simmons' analytical model (Eq. 11) and the current density  $J_{\text{TM}}$  provided by the transfer-matrix technique (Eq. 6). These  $J_{\text{Sim}}/J_{\text{TM}}$  ratios are calculated for different values of the gap spacing  $D$ , work function  $\Phi$  and applied voltage  $V$ . The values considered for  $D$  (0.5, 1, 2 and 5 nm),  $\Phi$  (1.5, 2,... 5 eV) and  $V$  (0.01, 0.1, 1 and 10 V) are of practical interest when applying Simmons' theory for the current density in metal-vacuum-metal junctions. The results show that Simmons' analytical expression for the local current density actually provides results that are in good

agreement with those provided by the transfer-matrix technique. The factor  $J_{\text{Sim}}/J_{\text{TM}}$  that expresses the difference between the two models is of the order 0.3-3.7 in most cases. Simmons' model obviously loses its applicability when Eq. 14 for  $\bar{\phi}$  predicts a mean barrier height at the left-side Fermi level  $\bar{\phi} < 0$ . In conditions for which  $\bar{\phi} \geq 0$ , Simmons' analytical expression (Eq. 11) turns out to provide decent estimations of the current density  $J$  that flows in the metal-vacuum-metal junction considered in this work. This justifies the use of Simmons' model for these systems.

TABLE 1. Ratio  $J_{\text{Sim}}/J_{\text{TM}}$  between the local current density  $J_{\text{Sim}}$  provided by Simmons' analytical model and the current density  $J_{\text{TM}}$  provided by the transfer-matrix technique, for different values of the gap spacing  $D$ , the common metal work function  $\Phi$  and the applied voltage  $V$ . The Fermi energy  $\varepsilon_F$  is 10 eV and the temperature  $T$  is 300 K.

$D=0.5$ nm				
$\Phi$ (eV)	$V=0.01$ V	$V=0.1$ V	$V=1$ V	$V=10$ V
1.5	/	/	/	/
2.0	/	/	/	/
2.5	/	/	/	/
3.0	/	/	/	/
3.5	0.362	0.367	0.327	/
4.0	0.470	0.478	0.558	/
4.5	0.481	0.489	0.587	/
5.0	0.462	0.470	0.562	/

$D=1$ nm				
$\Phi$ (eV)	$V=0.01$ V	$V=0.1$ V	$V=1$ V	$V=10$ V
1.5	0.872	0.871	/	/
2.0	1.811	1.898	2.605	/
2.5	1.562	1.630	2.550	/
3.0	1.265	1.312	1.969	/
3.5	1.029	1.062	1.511	/
4.0	0.852	0.876	1.189	0.088
4.5	0.721	0.739	0.964	1.494
5.0	0.622	0.635	0.802	1.993

$D=2$ nm				
$\Phi$ (eV)	$V=0.01$ V	$V=0.1$ V	$V=1$ V	$V=10$ V
1.5	2.781	3.056	3.670	/
2.0	2.137	2.297	3.604	/
2.5	1.594	1.687	2.633	/
3.0	1.218	1.275	1.893	0.961
3.5	0.962	0.999	1.409	1.205
4.0	0.784	0.809	1.092	1.482
4.5	0.656	0.674	0.877	1.259
5.0	0.563	0.576	0.726	1.097

$D=5$ nm				
$\Phi$ (eV)	$V=0.01$ V	$V=0.1$ V	$V=1$ V	$V=10$ V
1.5	1.328	1.411	0.391	/
2.0	1.384	1.500	1.349	0.683
2.5	1.080	1.150	1.362	0.847
3.0	0.851	0.895	1.118	0.814
3.5	0.689	0.717	0.897	0.700
4.0	0.572	0.592	0.731	0.565
4.5	0.487	0.501	0.608	0.434
5.0	0.423	0.434	0.518	0.310



It has been assumed in this modeling paper that both electrodes are smooth, flat and planar. This may not be an adequate modeling approximation and it may be that in some real devices, the electrostatic field near the emitting electrode varies somewhat across the electrode surface. In such cases, the “real average current density” is probably better expressed as  $J_{av} = \alpha_n J_{local}$ , where  $J_{local}$  is the local current density at a typical hot spot and the parameter  $\alpha_n$  (called here the “notional area efficiency”) is a measure of the apparent fraction of the electrode area that is contributing significantly to the current flow. However, there is no good present knowledge of the values of either of these quantities. It is also necessary to be aware that smooth-surface conceptual models disregard the existence of atoms and do not attempt to evaluate the role that atomic-level wave-functions play in the physics of tunneling. In the context of field electron emission [33–35], it is known that these smooth-surface models are unrealistic and that the neglect of atomic-level effects creates uncertainty over the predictions of the smooth-surface models. At present, it is considered that the derivation of accurate atomic-level theory is a very difficult problem, so reliable assessment of the error in the smooth-surface models is not possible at present. However, in the context of field electron emission, our present guess is that the smooth-surface models may over-predict by a factor of up to 100 or more, or under-predict by a factor of up to 10 or more. Recent results obtained by Lepetit are consistent with these estimations [36]. Uncertainties of this general kind will also apply to the Simmons' results and to the results derived in this paper.

## V. Conclusions

We used a transfer-matrix technique to test the consistency with which Simmons' analytical model actually predicts the local current density  $J$  that flows in flat metal-vacuum-metal junctions. Simmons' analytical model relies on a mean-barrier approximation for the transmission probability. This enables the derivation of an analytical expression for the current density. In Simmons' original papers, there is a missing factor of 1/2 in the image potential energy. This factor was included for correction in our presentation of

Simmons' theory. We then compared the current density  $J_{sim}$  provided by this analytical model with the current density  $J_{TM}$  provided by a transfer-matrix technique. We also considered the current densities provided by a numerical integration of the transmission probability obtained with the WKB approximation and Simmons' mean-barrier approximation. The comparison between these different models shows that Simmons' analytical model for the current density provides results that are in good agreement with an exact solution of Schrödinger's equation for a range of conditions of practical interest. The ratio  $J_{sim}/J_{TM}$  used to measure the accuracy of Simmons' model takes values of the order 0.3-3.7 in most cases, for the conditions considered in this work. Simmons' model can obviously only be used when the mean-barrier height at the Fermi level  $\bar{\Phi}$  is positive. This corresponds to the linear and field-emission regimes of  $J$ - $V$  plots. Future work may extend the range of conditions considered for this numerical testing of Simmons' model and seek establishing a correction factor to use with Simmons' equation in order to get more exact results.

## Acknowledgments

Alexandre Mayer is funded by the Fund for Scientific Research (F.R.S.-FNRS) of Belgium. He is member of NaXys, Namur Institute for Complex Systems, University of Namur, Belgium. This research used resources of the “Plateforme Technologique de Calcul Intensif (PTCI)” (<http://www.ptci.unamur.be>) located at the University of Namur, Belgium, which is supported by the F.R.S.-FNRS under the convention No. 2.5020.11. The PTCI is member of the “Consortium des Equipements de Calcul Intensif (CECI)” (<http://www.cec-ihpc.be>).

## References

- [1] Jeffreys, H., Proc. London Math. Soc., s2-23 (1925) 428.
- [2] Wentzel, G., Z. Phys., 38 (1926) 518.
- [3] Kramers, H. A., Z. Phys., 39 (1926) 828.
- [4] Brillouin, L., Compt. Rend., 183 (1926) 24.
- [5] Fowler, R.H. and Nordheim, L., Proc. R. Soc. London Ser. A, 119 (1928) 173.
- [6] Murphy, E.L. and Good, R.H., Phys. Rev., 102 (1956) 1464.
- [7] Good, R.H. and Müller, E.W., “Handbuch der Physik” (Springer Verlag, Berlin, 1956), p176.
- [8] Young, R.D., Phys. Rev., 113 (1959) 110.
- [9] Forbes, R.G., J. Appl. Phys., 103 (2008) 114911.
- [10] Forbes, R.G., J. Vac. Sci. Technol. B, 26 (2008) 788.
- [11] Mayer, A., J. Phys. Condens. Matter, 22 (2010) 175007.
- [12] Mayer, A., J. Vac. Sci. Technol. B, 28 (2010) 758.
- [13] Mayer, A., J. Vac. Sci. Technol. B, 29 (2010) 021803.
- [14] Hagmann, M.J., Int. J. Quantum Chem., 29 (1995) 289.
- [15] Forbes, R.G. and Deane, J.H.B., Proc. R. Soc. A, 463 (2007) 2907.
- [16] Simmons, J.G., J. Appl. Phys., 34 (1963) 1793.
- [17] Simmons, J.G., J. Appl. Phys., 34 (1963) 2581.
- [18] Simmons, J.G., J. Appl. Phys., 35 (1964) 2472.
- [19] Simmons, J.G., J. Appl. Phys., 35 (1964) 2655.
- [20] Matthews, N., Hagmann, M.J. and Mayer, A., J. Appl. Phys., 123 (2018) 136101.
- [21] Miskovsky, N.M., Cutler, P.H., Feuchtwang, T.E. and Lucas, A.A., Appl. Phys. A, 27 (1982) 139.
- [22] Mayer, A. and Vigneron, J.-P., Phys. Rev. E, 59 (1999) 4659.
- [23] One can check indeed that  $\Psi_{i,j}^+ = \hat{\Phi}_{i,j}^+[T_{i,j}^{++}]^{-1}$  and  $\Psi_{i,j}^- = \hat{\Phi}_{i,j}^- - \hat{\Phi}_{i,j}^+[T_{i,j}^{++}]^{-1}T_{i,j}^{+-}$ .
- [24] Mayer, A. and Vigneron, J.-P., Phys. Rev. B, 56 (1997) 12599.
- [25] Mayer, A., Chung, M.S., Weiss, B.L., Miskovsky, N.M. and Cutler, P.H., Phys. Rev. B, 78 (2008) 205404.
- [26] Mayer, A., Chung, M.S., Lerner, P.B., Weiss, B.L., Miskovsky, N.M. and Cutler, P.H., J. Vac. Sci. Technol. B, 30 (2012) 31802.
- [27] The use of factors of the form  $f_I(E)[1-f_{III}(E)]$  and  $f_{III}(E)[1-f_I(E)]$  in the two terms of the current density will provide identical results when the applied voltage  $V$  is static as in this work. For oscillating voltages, the expression 5 must however be used and we consider it therefore as fundamentally more correct.
- [28] For the transfer-matrix calculations, it is the expression 7 that is actually used for  $V(z)$ . The fact that  $V_{\text{image}}(z)$  tends to  $-\infty$  when  $z \rightarrow 0$  or  $z \rightarrow D$  causes convergence issues when solving Schrödinger’s equation by a transfer-matrix approach. The physical reason is related to the existence of bound states in this potential energy. These bound states would be filled in the real device. One can actually question the validity of the image interaction when we are at a few Angströms only to the surface of a metal. A solution to this issue is to cut  $V(z)$  at  $V_I$  when  $z \rightarrow 0$  and at  $V_{III}$  when  $z \rightarrow D$ . This provides the barrier depicted in Fig. 1 in which there is no singularity in the potential energy when crossing the surface of each metal.
- [29] Hrach, R., Czech. J. Phys. B, 18 (1968) 402.
- [30] Zhang, P., Sci. Rep., 5 (2015) 09826.

- [31] Mesyats, G.A., Explosive Electron Emission, (URO Press, Ekaterinburg, 1998).
- [32] Fursey, G., Field Emission in Vacuum Microelectronics, (Kluwer/Plenum, New York, 2005).
- [33] Fowler, R.H. and Guggenheim, E.A., "Statistical Thermodynamics", 2<sup>nd</sup> Ed., (Cambridge Univ. Press, London, 1949).
- [34] Sommerfeld, A., "Thermodynamics and Statistical Mechanics", (Academic Press, New York, 1964).
- [35] Ziman, J.M., "Principles of the Theory of Solids", (Cambridge Univ. Press, London, 1964).
- [36] Lepetit, B., J. Appl. Phys., 122 (2017) 215105.



### Preparation and Preliminary Characterization of Hybrid Alginate – Carrageenan Aerogel: Effect of Gelation Methods

M. Alnaief<sup>a</sup>, B. Mohammad<sup>a</sup>, Mohannad Aljarrah<sup>b</sup> and R. M. Obaidat<sup>c</sup>

<sup>a</sup> *Pharmaceutical and Chemical Engineering Department, Faculty of Applied Medical Sciences, German Jordanian University, Amman, Jordan.*

<sup>b</sup> *Chemical Engineering Department, Faculty of Engineering, Jordan University of Science and Technology, Irbid, Jordan.*

<sup>c</sup> *Department of Pharmaceutical Technology, Faculty of Pharmacy, Jordan University of Science and Technology, Irbid, Jordan.*

---

*Received on: 8/7/2018;*

*Accepted on: 29/10/2018*

---

**Abstract:** Aerogels are a class of nanoporous structured material with a high specific surface area, large porosity and open pore structure. Usually, they are produced by substituting the solvent of a stable gel with air without affecting the 3-D network of the gel. It is possible to engineer the produced material by controlling the precursors, gelling mechanism and drying process. In this work, hybrid aerogel based on alginate and three different types of carrageenan was produced using supercritical fluid technology. CO<sub>2</sub>-induced gelation, as well as GdL-induced gelation, were evaluated for their effect on final textural properties of the produced aerogel. CO<sub>2</sub>-induced gelation method shows enhanced aerogel properties and can be further investigated for the scale-up application. Nevertheless, GdL-induced gelation is easier to perform and produced a smaller specific surface area aerogel if compared with CO<sub>2</sub>-induced gelation method. Hybrid alginate-carrageenan aerogels were produced with high surface area (390-566) m<sup>2</sup>·g<sup>-1</sup> and large pore volume (4.2-6.8) m<sup>3</sup>·g<sup>-1</sup> and with a mesoporous structure (3.2 – 26.8) nm. The produced aerogels have great potential for future biotechnological and pharmaceutical applications.

**Keywords:** Hybrid Aerogel, Alginate, Carrageenan, Supercritical Fluid Extraction, Drug Carrier.

## Introduction

Aerogels are a class of nanoporous materials that are prepared by removing the swelling solvent of a gel without substantially affecting the 3-D network of its structure [1]. The hierarchical structure of aerogels produces many unique properties, such as open pore structure with extremely high porosities (greater than 90%), low thermal conductivity (10-30 W/m·K), very low density (as low as 0.003 g·cm<sup>-3</sup>) and high surface areas (200-1000 m<sup>2</sup>·g<sup>-1</sup>). As a result, aerogels have gained great attention for a various range of applications, such as aeronautics, energy conservation, environmental applications,

food, biomedicines, drug delivery, among many other applications [2–7].

Due to non-toxicity, stability, availability and renewability, natural polysaccharides and their derivatives-based aerogels are gaining more attention for biomedical and pharmaceutical applications. Furthermore, they allow coupling aerogel properties with their biodegradability, biocompatibility and surface functional properties [9, 10].

In addition, the broad portfolio of bio-based polysaccharides allows their use in

pharmaceutical products with different routes of delivery, target organs and/or drug release profiles [5, 6, 11, 12]. Therefore, the drug loading capacity is largely influenced by the chemical structure of the matrix, porosity and surface area of the aerogels. Surface alteration of the gel can hugely play an important role in the release and bioavailability of the entrapped drug, whereas the absorption and release of drugs can be adjusted by matrix synthesis conditions [13].

Polysaccharides are known also as glycans, belonging to the carbohydrates. They are built from mono-saccharides or sugars that are covalently linked together by the glycosidic bond, forming a linear or branched polymeric

chain [14–16]. Alginate is a well-known biopolymer known for its biocompatibility, low toxicity, relatively low cost, stability, availability, renewability and simple gelation methods. It is considered a prominent component for food, textile and paper industries, as well as for pharmaceutical and medical products [17]. Alginate is a negatively charged linear polysaccharide composed of 1,4-linked  $\beta$ -D-mannuronate (M) and 1,4-linked  $\alpha$ -L-guluronate (G) residues. G-blocks of alginate can generate an “egg-box”-like structure hydrogel in contact with divalent cations, such as  $\text{Ca}^{2+}$ ,  $\text{Ba}^{2+}$  and  $\text{Sr}^{2+}$  (Fig. 1) [18].

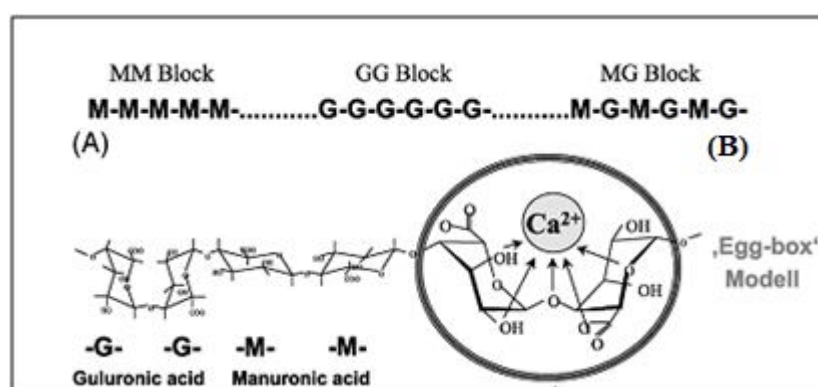


FIG. 1. General alginate, (A) block structure; (B) the formation of the “egg-box” model [14].

On the other hand, carrageenans are a family of seaweed derived polysaccharides composed of alternating  $\alpha$ -(1,3) and  $\beta$ -(1,4) glycosidic links of D-galactose and 3,6-anhydro-L-galactose repeat units. Carrageenan contains high (15 – 40%) sulfate ester contents. There are three major types of carrageenans designated by the Greek letters kappa, iota and lambda, which differ in the degree of galactose unit sulfuration and dehydration. The sulfate groups impart an anionic character and accordingly carrageenans can undergo either thermotropic or ionotropic gelation using cations, such as potassium and calcium ions [19].

Hybrid aerogel has been investigated by different researchers; it is composed of two or more chemically or physically bound components [20–22]. The main advantage of such hybrid components is that they inherit the intrinsic properties of aerogel with enhanced and adjustable mechanical properties, wettability and chemical functionality [23].

The use of  $\text{CO}_2$  as a gelation-inducing method for alginate has been reported previously [21, 24]. The technique has shown some advantages over traditionally used methods [25–27], such as the process allowing to avoid ambient pressure solvent exchange with the possibility of being directly combined with subsequent supercritical drying, in addition, fast depressurization leads to foam like hydrogel [28].

The aim of this study is to develop a hybrid aerogel composed of alginate and different types of carrageenans as the second biopolymer for potential future work in drug delivery. Moreover, this work demonstrates the use of high-pressure  $\text{CO}_2$  as well as the addition of glucono delta-lactone (GdL) to induce cross-linking of the hybrid biopolymers.

This preliminary characterization of hybrid aerogel will form the basis for future work to be carried on and for extending the use of such aerogels into pharmaceutical applications as drug loadings.

## Materials and Methods

### Materials

Sodium alginate,  $\kappa$ -carrageenan,  $\iota$ -carrageenan,  $\lambda$ -carrageenan and calcium carbonate were purchased from Sigma Aldrich. D-(+)-Glucono-delta-Lactone (GdL) was obtained from Guangzhou Fischer Chemical Co. Absolute ethanol was supplied by Solvochem, Holland. Carbon dioxide (CO<sub>2</sub> 99.99%) was provided by the Jordanian Gas Co., Jordan.

All chemicals were used as supplied without any further modification.

### Methods

Fig. 2 shows the general procedure of preparation of aerogel from polysaccharide precursors followed in this work. Firstly, the precursor should be hydrated with deionized water to prepare the needed concentration of the biopolymer. Then, the sol is cross-linked using a chemical or physical cross-linking method to obtain a 3-D network hydrogel structure. After the gel is aged, a stepwise solvent exchange is used to convert the hydrogel into alcogel. Finally, the solvent of the alcogel is removed using supercritical fluid extraction leaving the 3-D nanoporous structure intact.

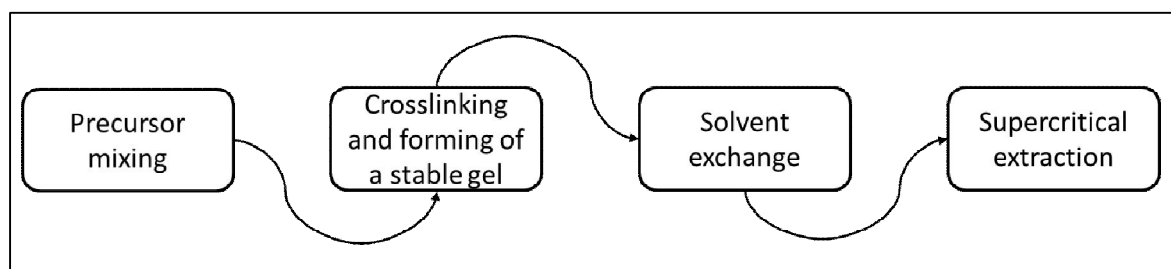


FIG. 2. General procedure of aerogel preparation using polysaccharide precursors.

### Preparation of the Hybrid Aerogel

TABLE 1 shows the prepared samples in this work. Two main process parameters were investigated; namely: (1) carrageenan type and (2) cross-linking method. Other parameters like

CO<sub>2</sub>-induced gelation conditions (temperature, pressure and time), solvent exchange process, biopolymer ratios and biopolymer concentration are still under investigation.

TABLE 1. Sample preparation conditions used in this work.

Sample ID	First polymer	Second polymer	Mixing ratio	Cross-linking method
A1	Alginate 1wt%	Alginate 1 wt %	1:1	CO <sub>2</sub> -induced gelation
L1	Alginate 1wt%	$\lambda$ -carrageenan 1 wt%	1:1	CO <sub>2</sub> -induced gelation
I1	Alginate 1wt%	$\iota$ -carrageenan 1 wt%	1:1	CO <sub>2</sub> -induced gelation
K1	Alginate 1wt%	$\kappa$ -carrageenan 1 wt%	1:1	CO <sub>2</sub> -induced gelation
A2	Alginate 1wt%	Alginate 1 wt %	1:1	GdL
L2	Alginate 1wt%	$\lambda$ -carrageenan 1 wt%	1:1	GdL
I2	Alginate 1wt%	$\iota$ -carrageenan 1 wt%	1:1	GdL
K2	Alginate 1wt%	$\kappa$ -carrageenan 1 wt%	1:1	GdL

The detailed procedure of the hybrid aerogel preparation process is described below.

### Preparation of the Biopolymer Solution

Sodium alginate and three different types of carrageenan solutions (kappa  $\kappa$ , iota  $\iota$  and lambda  $\lambda$  carrageenans) were prepared by dissolving a certain amount of dry biopolymer powder in deionized water to form the needed concentration of the biopolymer solution. The solutions were left under mixing for 24 hours to

ensure complete hydration of the biopolymer. An amount of 0.1825 g CaCO<sub>3</sub> was mixed vigorously with alginate solution for each gram of sodium alginate used in the preparation. The carrageenan solution was then added to the alginate-CaCO<sub>3</sub> suspension to prepare the desired ratio.

### Gelation

Two different procedures were used to induce the release of Ca<sup>+2</sup> and make it available for

cross-linking. The first approach used was CO<sub>2</sub>-induced gelation. The second approach was the addition of GdL to slowly reduce the pH of the hybrid solution to induce cross-linking. In the first one, the mixed suspension of the previous step was transferred to cylindrical moulds and placed in a 1L high-pressure stainless vessel. CO<sub>2</sub> was pumped to the cylinder slowly to obtain a pressure of 50 bar. This condition was kept overnight at room temperature. The second approach is based on the addition of GdL to the alginate/carrageenan mixture to make a molar ratio of 0.5 CaCO<sub>3</sub>:GdL. The resultant suspension was transferred to cylindrical moulds and left overnight to gel.

### Hydrogel to Alcogel

The water phase of the gel was replaced with ethanol following a stepwise solvent exchange process. The solvent exchange steps were: 10, 30, 50, 70, 90, 100, 100 wt%. In each step, equilibrium was allowed over 24 hours.

### Alcogel to Aerogel

The resulting alcogel produced in the previous step was dried using a continuous flow supercritical extraction unit described elsewhere [29]. Briefly, the wet gel was placed in a temperature-controlled 500-ml stainless steel vessel. CO<sub>2</sub> was pumped continuously from the bottom of the vessel at a constant flow of 100 g/min using a high-pressure piston pump. The vessel pressure was controlled using a pneumatic backpressure valve and kept constant at 100 bar. The CO<sub>2</sub>-ethanol phase was driven to a separation vessel. The condition of the separation vessel was kept at about 60 bar and 40 °C to ensure phase separation. The solvent was collected from the bottom, while the ethanol lean CO<sub>2</sub> was recycled to the extraction vessel. The extraction process was performed for over six hours. Fresh CO<sub>2</sub> was introduced several times to the extraction cycle.

### Scanning Electron Microscopy (SEM)

The surface morphology of the samples was obtained using Quanta FEG 450, SEM (FEI, US). Before performing SEM analysis, the samples were placed on stubs and coated with

platinum under vacuum atmosphere using Q150R Rotary-Pumped Sputter Coater/ Carbon Coater (Quorum Technologies, UK).

### Surface Area and Porosity Analysis

The specific surface area and porosity of the prepared particles were determined by Autosorb-1 Series surface area and pore size analyzer, Quantachrome, USA.

## Results and Discussion

Alginate is a natural ionic polysaccharide composed of repeated  $\beta$ -(1–4) linked D-mannuronic acid and  $\alpha$ -L-guluronic acid units. In the presence of divalent cations like Ca<sup>2+</sup> alginate form stable gel [30]. Carrageenan is a natural polysaccharide composed of alternated 1,3-linked  $\beta$ -D galactose and 1,4-linked  $\alpha$ -D-galactose with various degrees of sulfatation. Because of the half ester sulfate, carrageenans are strong anionic and can form gel in the presence of mono-or divalent cations [31]. Hybrid aerogel based on alginate and three different types of carrageenan was prepared following two different procedures. Both procedures are categorized under the internal setting method for the preparation of alginate gel [8, 10, 24, 32, 33]. In this technique, the well-dispersed CaCO<sub>3</sub> in the biopolymer solution will release the Ca<sup>+2</sup> ions upon lowering the pH of the sol phase. After that, the cations will be available for cross-linking and a homogeneous cross-linking will take place.

CO<sub>2</sub> induced gelation method is relatively new and was firstly proposed by Raman et al. as a promising step toward continuous production of alginate-based aerogels [24]. The pH of the sol phase is reduced by forming carbonic acid upon dissolving of CO<sub>2</sub> in the water phase at 50 bar pressure. the extent of carbonic acid formation depends mainly on the system temperature and pressure [34, 35]. The second approach uses GdL (glucono-delta-Lactone), which is the ester of gluconic acid. Upon contact with water, the ester hydrolyzes forming gluconic acid which in turn reduces the pH of the sol phase [36–38].

another biopolymer (566 m<sup>2</sup>/g). Nevertheless, hybrid aerogels have also a relatively high specific surface area compared to alginate alone (390 – 525 m<sup>2</sup>/g). Moreover, all preparation results give a mesoporous structure with a pore size range of 17.2 – 26.8 nm. The pore volume



of the prepared samples was relatively large ( $4.2 - 6.8$ )  $\text{cm}^3 \text{g}^{-1}$ .

It is possible to state that both approaches produced comparable aerogel properties with a slight improvement for the  $\text{CO}_2$ -induced gelation preparations in comparison with GdL preparations. The slight difference can be due to the nature of pH reduction. In  $\text{CO}_2$ -induced gelation, carbon dioxide will continue to dissolve in the water phase and pH will be reduced slowly until equilibrium is reached. This allows a slow release of  $\text{Ca}^{2+}$  ions and the formation of a homogeneous network. Using GdL reduces the pH instantaneously upon addition to the polymer solution and makes the  $\text{Ca}^{2+}$  ions available for cross-linking at once. L1 and L2 preparations contain  $\lambda$ -carrageenan-produced aerogel with the highest specific surface area of 525 and 511  $\text{m}^2/\text{g}$ , respectively. This can be due to the presence of three sulfated groups available for cross-linking with  $\text{Ca}^{2+}$  ions, whereas  $\iota$ -carrageenans contain two sulfated group and  $\kappa$ -carrageenans contain one sulfated group. Nevertheless,  $\kappa$ -carrageenan aerogel preparation shows better specific surface area if compared with  $\iota$ -carrageenan. However, all preparations result in a comparable pore volume and pore size distribution. Raman et al. reported the production of hybrid alginate-based aerogel and other biopolymers, like starch, pectin and carrageenan. The reported specific surface area for  $\lambda$ -carrageenan was 446  $\text{m}^2/\text{g}$  with 2.23  $\text{cm}^3/\text{g}$

as a pore volume. With alginate alone, these values were 586  $\text{m}^2/\text{g}$  and 5.97  $\text{cm}^3/\text{g}$  for specific surface area and pore volume, respectively [24]. Gonçalves et al. proposed alginate-based aerogel microparticles for mucosal drug delivery. In their publication, pH was reduced using acetic acid. Alginate aerogel microparticles were produced with 330  $\text{m}^2/\text{g}$  and 1.7  $\text{cm}^3/\text{g}$  surface area and pore volume, respectively. Further, they produced alginate- $\kappa$ -carrageenan aerogel with 415  $\text{m}^2/\text{g}$  and 3.6  $\text{cm}^3/\text{g}$  for surface area and pore volume, respectively [21]. Robitzer et al. on the other hand reported the preparation of alginate aerogel following the diffusion method, where alginate solution is dropped into  $\text{CaCl}_2$  solution. They reported 495  $\text{m}^2/\text{g}$  and 3.9  $\text{cm}^3/\text{g}$  for surface area and pore volume, respectively. It is possible to say that the method used in this work produces better textural properties of hybrid aerogel in comparison to what is available in the literature. Nevertheless, a complete parametric study of the presented process is needed to understand the significance of each parameter and to develop an optimized process for the production of hybrid aerogel materials. Further, the effect of available functional groups on the hybrid aerogel surface will be further evaluated by testing the adsorption capacity of each preparation for different types of drugs. These two major points will be the subject of our next publication.

TABLE 2. Surface properties of the prepared samples in this study.

Sample ID	Surface area ( $\text{m}^2 \text{cm}^{-3}$ )	Pore volume ( $\text{cm}^3 \text{g}^{-1}$ )	Pore size (nm)
A1	$566 \pm 28$	$6.8 \pm 0.3$	$26.8 \pm 1.3$
L1	$525 \pm 26$	$5.6 \pm 0.2$	$17.2 \pm 2.3$
K1	$503 \pm 25$	$5.5 \pm 0.3$	$21.4 \pm 1.1$
I1	$390 \pm 19$	$5.6 \pm 0.3$	$21.8 \pm 2.1$
A2	$482 \pm 24$	$4.2 \pm 0.2$	$22.5 \pm 1.1$
L2	$511 \pm 25$	$6.5 \pm 0.2$	$17.3 \pm 0.7$
K2	$482 \pm 24$	$5.7 \pm 0.1$	$22.3 \pm 1.1$
I2	$419 \pm 21$	$4.2 \pm 0.1$	$17.1 \pm 0.9$

Fig. 3 shows the SEM images of the samples prepared by the  $\text{CO}_2$ -induced gelation method. Although the textural properties of all prepared samples were comparable, it is possible to differentiate between the samples in terms of the surface structure. Sample A1 shows a more dense and uniform structure in comparison with other samples. Samples L1, K1 and I1 show a more intense fibrous airy structure with

relatively more loose interconnectivity. These textural properties can be explained in light of the preparation procedure; the gelation of all hybrid combinations was based on cross-linking of alginate and the co-gelation of carrageenan. Such a process allows the presence of more voids and less intensity of cross-linking. In addition,  $\text{Ca}^{2+}$  can be used as well for the cross-linking of carrageenans [29, 39, 40].

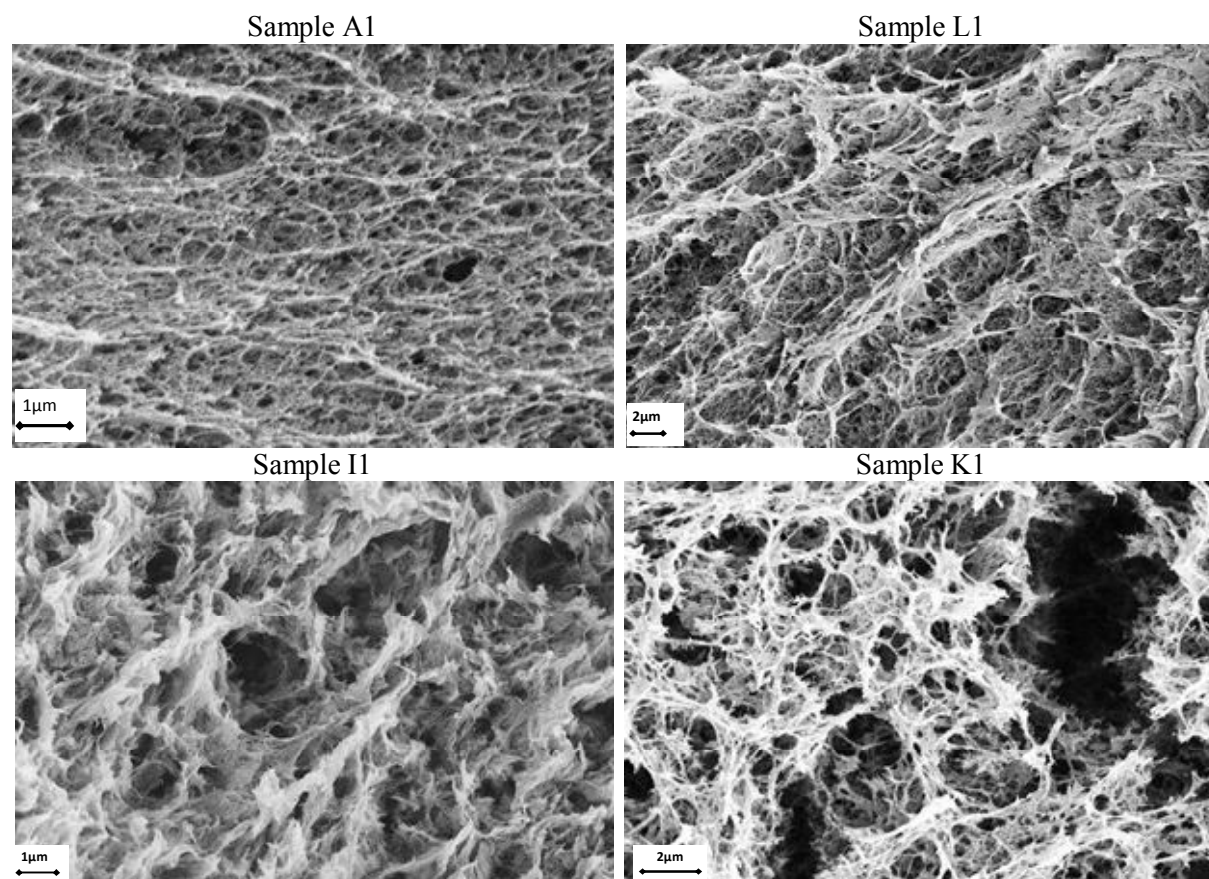


FIG. 3. SEM images of some of the prepared samples in this work.

As can be seen from the results in

TABLE 2 and Fig. 3, nanoporous structured materials based on polysaccharides with a high surface area and accessible pore volume were produced. The produced material can serve as a potential drug carrier [21, 41]. The drug can be loaded into the aerogel structure using supercritical CO<sub>2</sub> or prior to the extraction process during the solvent exchange process [42]. The loading of the drug can be controlled by varying the surface functional group through hybridization with different polysaccharides or different mixing ratios [43].

The drug loading of different active materials on the aerogel structure will be investigated in a future study. The effect of different backbone structures of the prepared aerogels on the release properties of the loaded drugs will be evaluated *in vitro* and *in vivo*.

## Conclusion

Hybrid aerogels based on alginate and three different types of carrageenan were successfully prepared. CO<sub>2</sub>-induced gelation and GdL-induced gelation methods were compared in

terms of the final textural properties of the produced aerogels. Both procedures result in an aerogel with high surface area (390-566) m<sup>2</sup> g<sup>-1</sup> and large pore volume (4.2-6.8) m<sup>3</sup> g<sup>-1</sup> with a mesoporous structure (3.2 – 26.8) nm. CO<sub>2</sub>-induced gelation method shows a slight improvement of aerogel properties in comparison with GdL-induced gelation method. CO<sub>2</sub>-induced gelation is a promising technique that can be scaled up to industrial scale and promote the use of aerogels in industrial applications. The produced hybrid aerogel will be further investigated and proposed as a possible drug carrier for drug delivery applications.

## Acknowledgments

The authors are grateful for the seed fund SAMS 40/2016, Deanship of Graduate Studies and Scientific Research at the German Jordanian University. Dr. Mohammad Alnaief thanks sincerely the DFG Institute for their support under reference: SM 82/11-1, as well as Prof. Smirnova, TUHH, for her time, effort and support.

## References

- [1] Smirnova, I. and Gurikov, P., *J. Supercrit. Fluids*, 134 (2018) 228.
- [2] Akimov, Y.K., *Instrum. Exp. Tech.*, 46 (2003) 287.
- [3] Maleki, H., *Chem. Eng. J.*, 300 (2016) 98.
- [4] Smirnova, I. and Gurikov, P., *Annu. Rev. Chem. Biomol. Eng.*, 8 (2017) 307.
- [5] Obaidat, R.M., Alnaief, M. and Mashaqbeh, H., *AAPS Pharm. Sci. Tech.*, 19 (2018) 2226.
- [6] García-González, C.A., Alnaief, M. and Smirnova, I., *Carbohydr. Polym.*, 86 (2011) 1425.
- [7] Maleki, H., Durães, L., García-González, C.A., del Gaudio, P., Portugal, A. and Mahmoudi, M., *Adv. Colloid Interface Sci.* 236 (2016) 1.
- [8] Alnaief, M., Alzaitoun, M.A., García-González, C.A. and Smirnova, I., *Carbohydr. Polym.*, 84 (2011) 1011.
- [9] Ulker, Z. and Erkey, C., *J. Controlled Release*, 177 (2014) 51.
- [10] Martins, M., Barros, A.A., Quraishi, S., Gurikov, P., Raman, S.P., Smirnova, I., Duarte, A.R.C. and Reis, R.L., *J. Supercrit. Fluids*, 106 (2015) 152.
- [11] García-González, C.A., López-Iglesias, C., Concheiro, A. and Alvarez-Lorenzo, C., in: "Biobased Aerogels Polysacch. Protein-Based Mater.", (The Royal Society of Chemistry, 2018) 295–323.
- [12] Obaidat, R.M., Tashtoush, B.M., Bayan, M.F., Al-Bustami, R.T. and Alnaief, M., *AAPS Pharm. Sci. Tech.*, 16 (2015) 1235.
- [13] Gorle, B.S.K., Smirnova, I. and McHugh, M.A., *J. Supercrit. Fluids*, 48 (2009) 85.
- [14] Dumitriu, S., "Polysacch. Struct. Divers. Funct. Versatility", Ed. Sev. Dumitriu, (2005) 1204.
- [15] Tako, M., *Adv. Biosci. Biotechnol.*, 06 (2015) 22.
- [16] Liu, J., Willför, S. and Xu, C., *Bioact. Carbohydr. Diet. Fibre*, 5 (2015) 31.
- [17] Pawar, S.N. and Edgar, K.J., *Biomaterials* 33 (2012) 3279.
- [18] Lee, K.Y. and Mooney, D.J., *Prog. Polym. Sci.*, 37 (2012) 106.
- [19] Kenar, J.A., in: "Porous Lightweight Compos. Reinf. Fibrous Struct.", Eds. Y. Yang, J. Yu, H. Xu and B. Sun (Springer, Berlin, Heidelberg, 2017), 207–243.
- [20] Veres, P., López-Periago, A.M., Lázár, I., Saurina, J. and Domingo, C., *Int. J. Pharm.*, 496 (2015) 360.
- [21] Gonçalves, V.S.S., Gurikov, P., Poejo, J., Matias, A.A., Heinrich, S., Duarte, C.M.M. and Smirnova, I., *Eur. J. Pharm. Biopharm.*, 107 (2016) 160.
- [22] Wang, R., Shou, D., Lv, O., Kong, Y., Deng, L. and Shen, J., *Int. J. Biol. Macromol.*, 103 (2017) 248.
- [23] Ramadan, H., Ghanem, A. and El-Rassy, H., *Chem. Eng. J.*, 159 (2010) 107.
- [24] Raman, S.P., Gurikov, P. and Smirnova, I., *J. Supercrit. Fluids*, 106 (2015) 23.
- [25] Alnaief, M., "Process Development for Production of Aerogels with Controlled Morphology As Potential Drug Carrier Systems", (Technische Universität Hamburg, 2011).
- [26] Escudero, R.R., Robitzer, M., Di Renzo, F. and Quignard, F., *Carbohydr. Polym.*, 75 (2009) 52.
- [27] Quignard, F., Valentin, R. and Di Renzo, F., *New J. Chem.*, 32 (2008) 1300.
- [28] Quraishi, S., Martins, M., Barros, A.A., Gurikov, P., Raman, S.P., Smirnova, I., Duarte, A.R.C. and Reis, R.L., *J. Supercrit. Fluids*, 105 (2015) 1.
- [29] Alnaief, M., Obaidat, R. and Mashaqbeh, H., *Carbohydr. Polym.*, 180 (2018) 264.
- [30] Aravamudhan, A., Ramos, D.M., Nada, A.A. and Kumbar, S.G., in: "Nat. Synth. Biomed. Polym.", Ed. by S. G. Kumbar, C. T. Laurencin and M. Deng (Elsevier, Oxford, 2014), 67–89.
- [31] Santo, V.E., Frias, A.M., Carida, M., Cancedda, R., Gomes, M.E., Mano, J.F. and Reis, R.L., *Biomacromolecules*, 10 (2009) 1392.

- [32] Silva, C.M., Ribeiro, A.J., Ferreira, D. and Veiga, F., *Eur. J. Pharm. Sci.*, 29 (2006) 148.
- [33] Silva, C.M., Ribeiro, A.J., Figueiredo, I.V., Gonçalves, A.R. and Veiga, F., *Int. J. Pharm.*, 311 (2006) 1.
- [34] Diamond, L.W. and Akinfiev, N.N., *Fluid Phase Equilibria*, 208 (2003) 265.
- [35] Campos, C.E.P.S., Villardi, H.G.D., Pessoa, F.L.P. and Uller, A.M.C., *J. Chem. Eng. Data*, 54 (2009) 2881.
- [36] Agoub, A.A., Giannouli, P. and Morris, E.R., *Carbohydr. Polym.*, 75 (2009) 269.
- [37] Hong, G.P. and Chin, K.B., *Meat Sci.*, 85 (2010) 201.
- [38] Grygorczyk, A. and Corredig, M., *Food Chem.*, 141 (2013) 1716.
- [39] Hermansson, A.-M., Eriksson, E. and Jordansson, E., *Carbohydr. Polym.*, 16 (1991) 297.
- [40] Ikeda, S., Morris, V.J. and Nishinari, K., *Biomacromolecules*, 2 (2001) 1331.
- [41] Gurikov, P. and Smirnova, I., *J. Supercrit. Fluids*, (2017).
- [42] Mehling, T., Smirnova, I., Guenther, U. and Neubert, R.H.H., *J. Non-Cryst. Solids*, 355 (2009) 2472.
- [43] Gonçalves, V.S.S., Gurikov, P., Poejo, J., Matias, A.A., Heinrich, S., Duarte, C.M.M. and Smirnova, I., *Eur. J. Pharm. Biopharm.*, 107 (2016) 160.

### Effect of Relaxation and Cooling Process on Field Electron Emission from Single-Walled Carbon Nanotubes Embedded in Glass

Marwan S. Mousa and Samer I. Daradkeh

*Surface Physics and Materials Technology Lab. Department of Physics, Mutah University, Al-Karak 61710, Jordan.*

---

*Received on: 2/7/2018;*

*Accepted on: 7/3/2019*

---

**Abstract:** Several experiments examined the properties of Field Electron Emission (FEE) from Single-Walled Carbon Nanotubes (SWCNTs), where extensive studies were conducted to improve the emission current density (stability and repeatability) and emission current image concentration. In this study, the effect of relaxation and cooling processes on FEE from SWCNTs embedded in glass has been investigated to keep the ongoing investigation for factors that positively affect the FEE process. It has been found that the relaxation process can ameliorate the FEE, where the “switch-on” phenomenon occurs at lower applied voltage after performing the relaxation process. Also, the saturation region extends down to lower applied voltage values after the relaxation process. In case of the effect of cooling process on FEE, the “switch-on” phenomenon occurs at higher applied voltage values after applying the cooling process. Also, the saturation region extends down to higher applied voltage values and the threshold value has been found to significantly being lowered as the result of the cooling process, where the emission current disappeared at applied voltage values of  $\sim 20$  V. In terms of the effects of the cooling process on emission current images, the emission current image is distributed throughout the screen. Furthermore, it has been experiencing a massive emission current fluctuation after performing the cooling process.

**Keywords:** Field Electron Emission, Single-Walled Carbon Nanotubes, Relaxation and Cooling Processes.

## Introduction

Field electron emission (FEE) is defined as the extraction of free electrons from the surface of a metal caused by an external energy source in the form of an applied electrostatic field [1]. This electrostatic field can bend the potential barrier, so quantum tunneling could take place through the surface potential barrier. Metals are the most commonly used field emitters. However, FEE can take place from metals, semiconductors [2-3], liquids [4] and non-conducting materials [5]. But, the most promising material that could replace metals as a field electron emitter is the Carbon Nanotube (CNT).

The excellent (FEE) features of Carbon Nanotubes (CNTs) have been investigated in

several experiments, which started with Rinzier in 1995 [6] and kept going on till now [7-9]. After MWCNTs have been discovered by Sumio Iijima in 1991 [10], SWCNTs by the same scientist in 1993 [11] and due to their unique properties like high aspect ratio, MWCNTs can lead to a great enhancement of the local electric field near the tip [12]. Also, those are characterized with having long-life time, being less sensitive to operating environment than metallic emitters [13] and the occurrence of field penetration that would lead to reduce the effective work function [14]. The previous properties make CNTs the best candidate to be used as field electron emitters. So, they have been used in many applications in both

technological and industrial fields, like micro- and nano-electronics [15], flat-panel displays [16], radar absorbing coating [17], gas storage and sensors [18]. There are many experimental tests that have been performed to study the effect of several factors on FEE from CNTs, in order to have better understanding of and control the FEE mechanism from CNTs.

The theoretical explanation of FEE has been derived by Fowler and Nordheim in 1928 [19] based on several assumptions, like assuming that the emitter is a smooth flat planar surface, with a uniform external electrostatic field  $F_{ext}$  in a vacuum above the emitter. Atomic structure has been ignored and a Sommerfeld-type free-electron model has been assumed. The electron population taken is to obey Fermi-Dirac statistics and to be in thermodynamic equilibrium at thermodynamic temperature  $T$  [20]. Also, the role of atomic wave-functions in transmission theory has been disregarded. For real-field emitters, these assumptions are unrealistic. So, the theory must be corrected and improved, in order to present a reasonable explanation and prediction of the FEE for new electron emitters, like SWCNTs.

There are research studies that have been carried out to investigate the effect of several factors on the field electron emission, such as the effect of an internally conductive coating on the electron emission from glass tips [21] and the effect of insulating layer on the field electron emission performance of Nano-Apex metallic emitters [22]. The effect of gas adsorption on the field emission of Carbon Nanotubes [23], the effect of aging on field emission lifetime for carbon nanotube cathodes [24], among others, were reported. So, it can be indicated that the field electron emission can be affected by several factors. Our research reported here aims at studying the effect of relaxation and cooling processes. For applying the relaxation process, the emitter is left overnight under high-vacuum conditions after its initial "switch-on" process [22]. The relaxation process has been found to enhance the FEE from SWCNTs. The effect of cooling process on FEE from SWCNTs embedded in micro-glass tip emitters has been investigated. The cooling process can be achieved by adding liquid nitrogen ( $LN_2$ ) inside the specially designed sample holder; thus having the sample at standardized separation close to  $LN_2$ . This kind of emitter has been

manufactured by employing a drawing technique using a glass puller [25], where it has been found that the cooling process affects the threshold values needed for the emission process as well as the distribution of the emission current image over the conductive phosphorus screen.

## Materials and Methodology

In this paper, we will discuss the current-voltage (I-V) characteristics and the related FN plots that have been extracted from the SWCNTs. The material (SWCNTs) in our experiments was produced by catalytic conversion of high-pressure CO over Fe particles (HiPCO) processed at CNI-Huston-Texas, having an average diameter ranging between (1 - 4) nm with a length of (1 - 3)  $\mu\text{m}$ . The emitters were manufactured by employing a drawing technique using glass puller apparatus, that is shown in Fig. 1.



FIG. 1. Actual image of the glass puller apparatus.

The components of the glass puller apparatus were illustrated somewhere else [21]. The SWCNTs were inserted inside the glass tube using mechanical procedures, by pushing the SWCNTs all the way inside the glass tube using a tungsten wire until they reach the tip, then the emitter was positioned inside a Field Emission Microscope (FEM), where the emitter-screen distance of  $\sim 10$  mm is standardized. The glass tube length was about 1 cm. The system was evacuated to a vacuum with a pressure of  $\sim 10^{-8}$  mbar, then the system was baked to  $\sim 170$   $^{\circ}\text{C}$  overnight.



Fig. 2 shows the optical micrographs of (SWCNT-21) and (SWCNT-1) tips, where the SWCNTs are in the broken end of the glass tube opposite to the anode.

Fig. 3 shows the SEM image for (SWCNT-21) and (SWCNT-1), respectively. The tip hole diameter for SWCNT-21 is  $396.5 \mu\text{m}$  and the tip hole diameter for SWCNT-1 is  $246.6 \mu\text{m}$ .

As it has been previously mentioned, the relaxation process can be applied by leaving the emitter for  $\sim 12$  hours under high-vacuum pressure after its initial “switch-on” phenomenon occurs. The cooling process is performed by adding liquid nitrogen inside the sample holder and leaving the system for  $\sim 5$  min, until the cooling process takes effect. Fig. 4 shows how the cooling process can be performed.

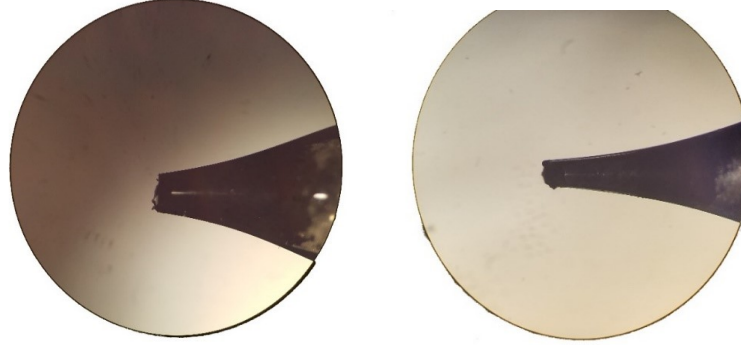


FIG. 2. Optical micrographs of (SWCNT-21) tip and (SWCNT-1) tip at a magnification of 50 times, respectively.

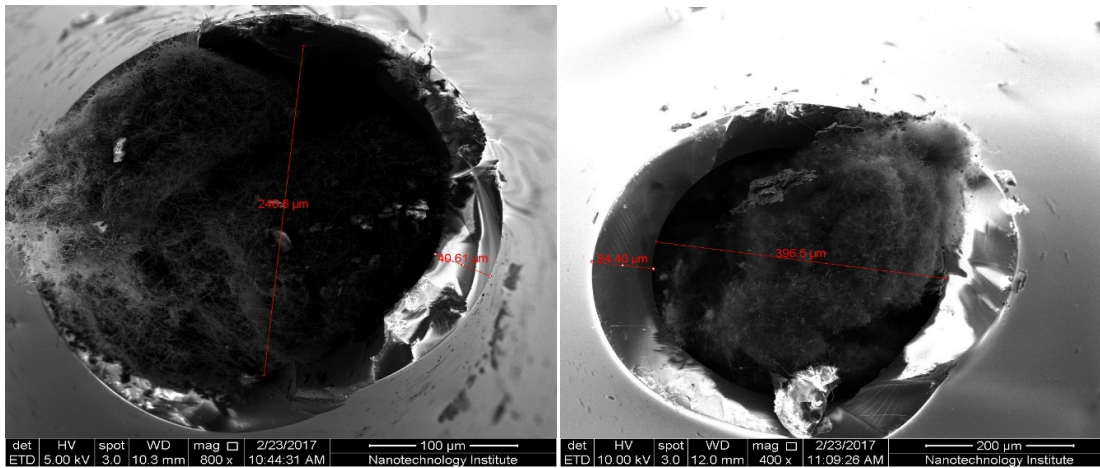


FIG. 3. SEM images of (SWCNT-21) tip at a magnification of 400 times and (SWCNT-1) tip at a magnification of 800 times, respectively.

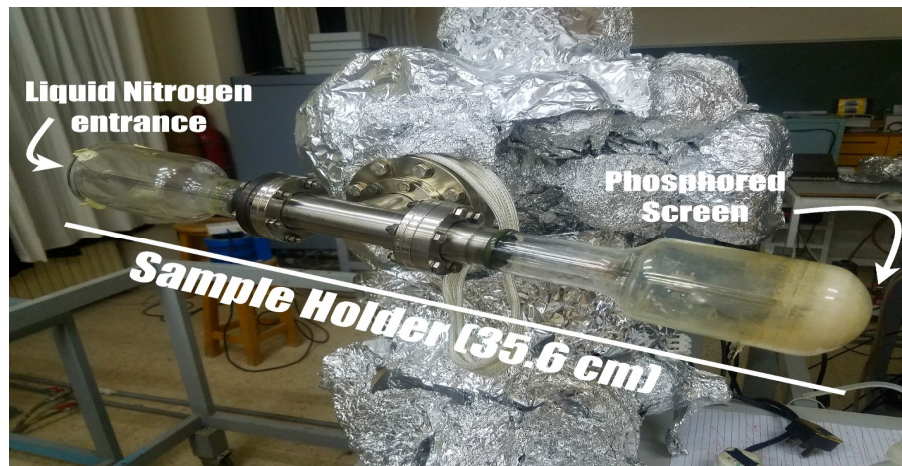


FIG. 4. Actual image of Field Electron Microscopy showing where the liquid nitrogen can be inserted to perform the cooling process.

The testing procedures start with increasing the applied voltage  $V$  slowly until the "switch-on" phenomenon  $V_{SW}$  occurs. At this point, the emission current suddenly increases from nano-ampere range to micro-ampere range. After that, the applied voltage is decreased, so the emission current will fall smoothly to zero. The threshold value  $V_{TH}$  will be measured, which is the lowest applied voltage value, at which the emission current is at its lowest value [26].

## Results and Discussion

The effect of the relaxation process on FEE has been discussed based on the I-V characteristics curve and the FN plot for FEE from SWCNTs-1. Due to the increase of the applied voltage on the (SWCNT-1) tip, the emission current has been initiated with (8 pA), with an applied voltage of (600 V). By further

increasing the voltage, the emission current increased until  $V_{SW}$  was reached; this occurs at (1350 V) producing an emission current of ( $3.7 \times 10^3$  nA). We continued increasing the applied voltage to (1730 V), where the emission current becomes ( $9.5 \times 10^3$  nA). After that, we started to decrease the applied voltage. The saturated region extended down to a voltage value ( $V_{SAT} = 1000$  V), where the emission current value became ( $I_{SAT} = 1.21 \times 10^3$  nA). Emission current vanishes after applied voltage value ( $V_{TH} = 350$  V) was reached, with the emission current becoming ( $I_{TH} = 9.45$  pA). Fig. 5 shows the I-V characteristics with the related FN plot before the relaxation process and the slope of FN plot at low-emission current presented in the FN plot.

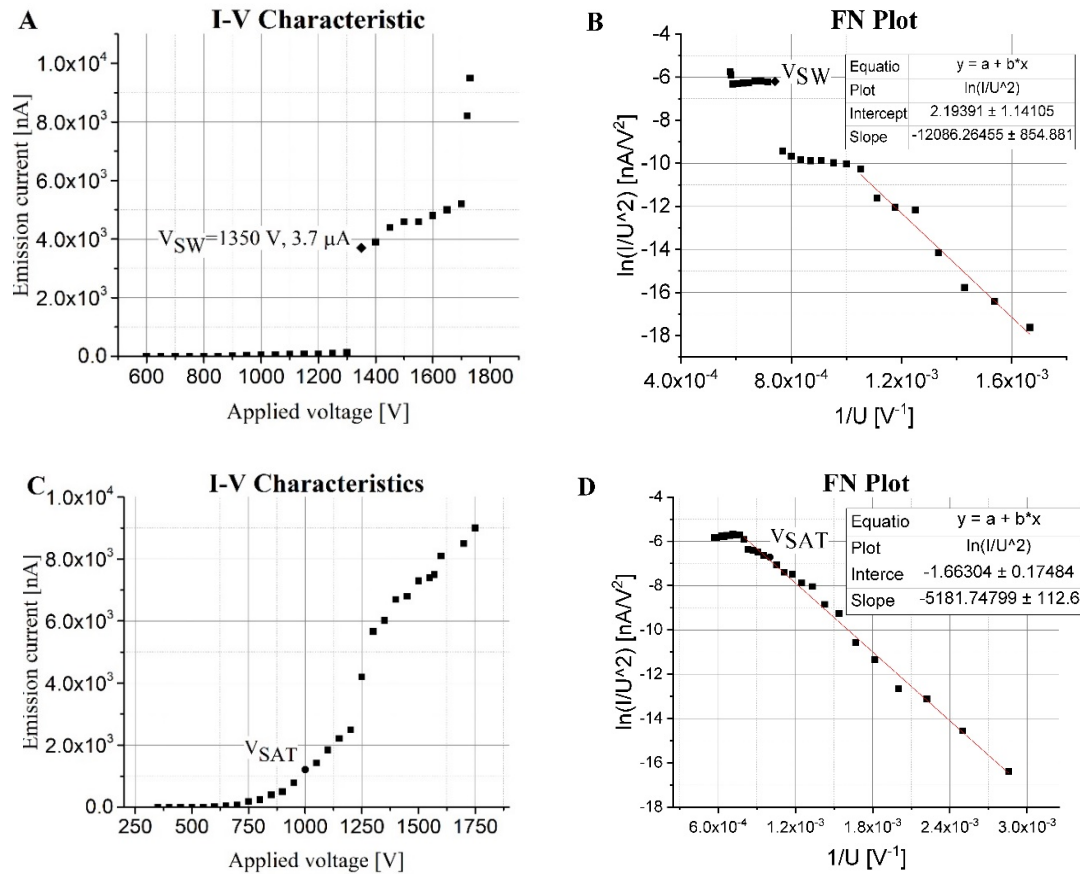


FIG. 5. Before performing the relaxation process on (SWCNT-1). At increasing voltage (A) I-V Characteristics. (B) FN plot. At decreasing voltage (C) I-V Characteristics. (D) FN plot.



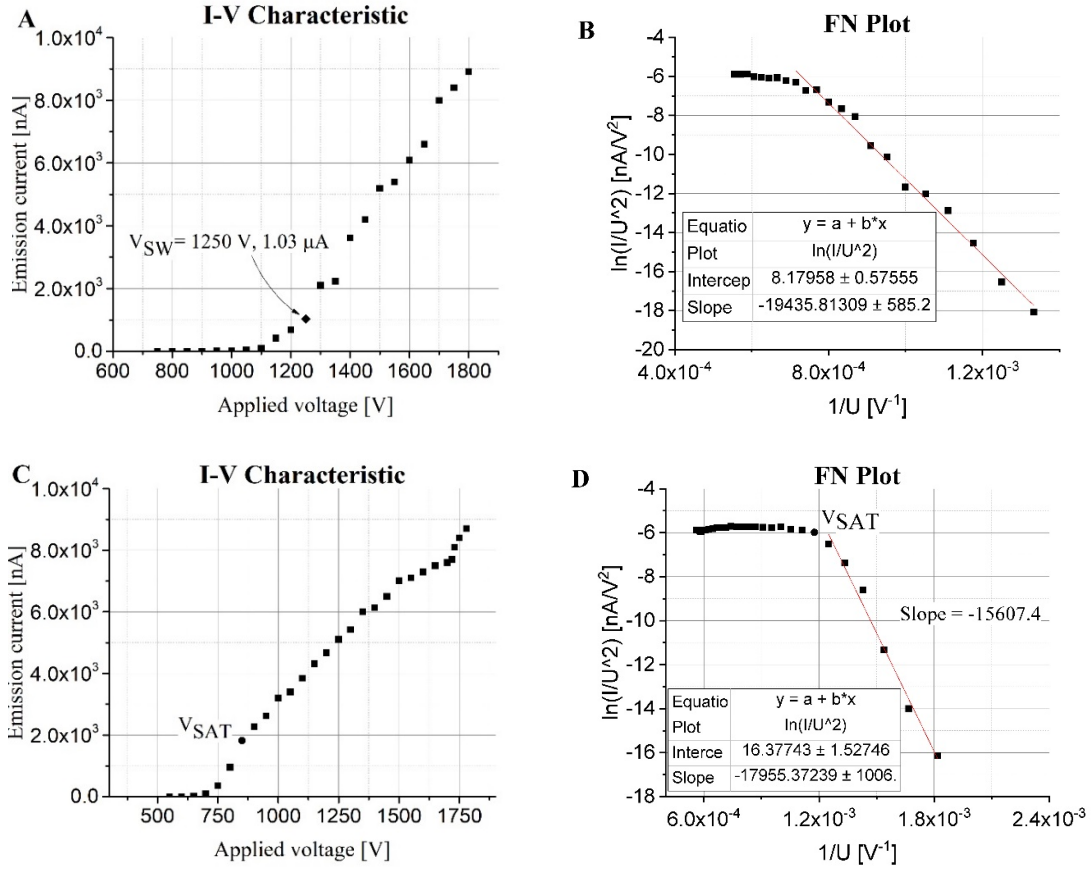


FIG. 6. (SWCNT-1). I-V characteristics and related FN plot after relaxation process. At increasing voltage: (A) I-V Characteristics. (B) FN plot with a slope of -19435.8 Np (at low emission current). At decreasing voltage: (C) I-V Characteristics. (D) FN plot with a slope of -17955.37 Np.

Fig. 5A shows an emission current that suddenly jumps from 137.2 nA at 1300 V to  $3.7 \times 10^3$  nA at 1350 V, which can be attributed to the formation of a new conducting channel. Later on, the system was left for ~12 hours to study the effect of the relaxation process. After applying the relaxation process, a second cycle of increasing and decreasing of applied voltage begun with increasing the applied voltage. This voltage ranges from 750 V up to 1800 V with emission current values ranging from 8 pA up to  $8.92 \times 10^3$  nA as the applied voltage increased. The switch on phenomenon occurs at a voltage

value  $V_{SW} = 1250$  V with an emission current  $I_{SW} = 1.03 \times 10^3$  nA, as seen in Fig. 6A. By decreasing the applied voltage, emission current decreased, but this current remained at micro-ampere range until  $V_{SAT} = 850$  V was reached and the emission current was  $I_{SAT} = 1.82 \times 10^3$  nA, as shown in Fig. 6C. After that point, the emission current decreased to nano-ampere range, until it vanished at ( $V_{TH} = 550$  V,  $I_{TH} = 30$  pA). Fig. 7 shows the emission images before and after the relaxation process.

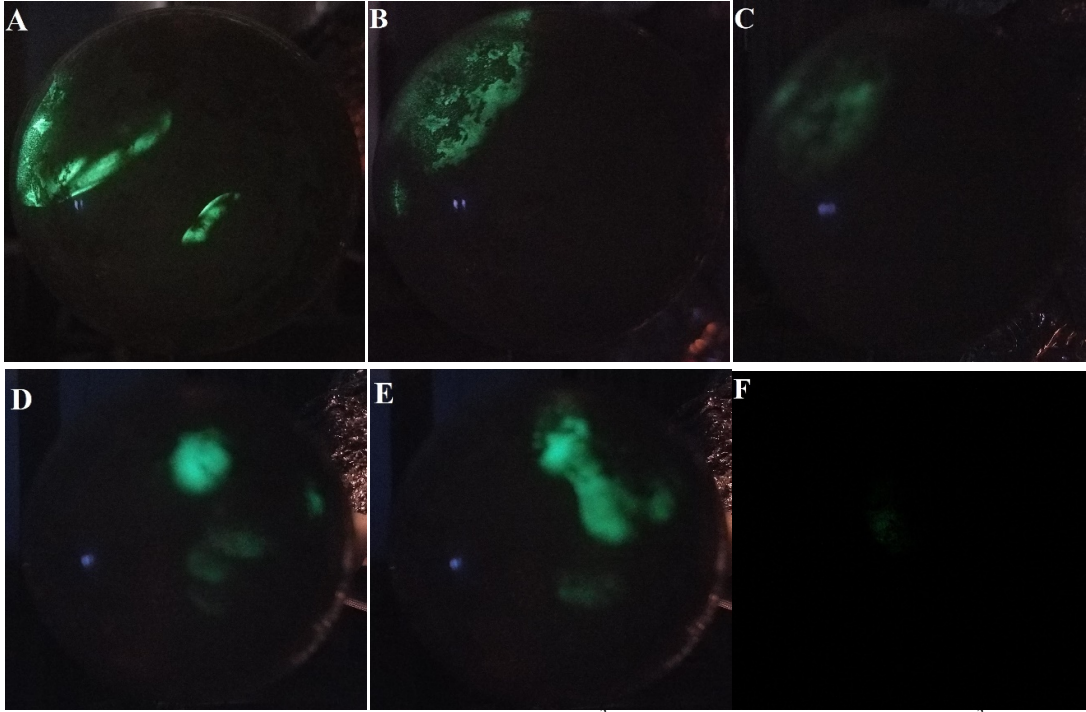


FIG. 7. Before relaxation process: (A)  $V = 1730$  V,  $I = 9.5 \times 10^3$  nA. (B)  $V_{SW} = 1350$  V,  $I_{SW} = 3.7 \times 10^3$  nA. (C)  $V = 1300$  V,  $I = 0.137 \times 10^3$  nA. After relaxation process: (D)  $V = 1800$  V,  $I = 8.92$   $\mu$ A. (E)  $V_{SW} = 1730$  V,  $I_{SW} = 8.1 \times 10^3$  nA. (F)  $V = 1200$  V,  $I = 0.68 \times 10^3$  nA.

The linear behavior that appears at the I-V characteristics in Fig. (6-A and C) can be an indication of the existence of a constant resistance somewhere at the CNT/substrate interface or along the CNT [27], or as an effect of space charge, where it can suppress the FEE from the SWCNT emitter [28].

By comparing Fig. 5 with Fig. 6, it can be noticed that there is an improvement in the shape of plots (both I-V characteristics and FN plots). It is obvious that the relaxation process made the emission current pattern more concentrated based on comparing the emission current pattern before and after the relaxation process as shown in Fig. 6. Figs. (7 A, B and C) represent the emission current images before the relaxation process, where it can be seen from these images that the emission current images are not concentrated. Figs. (7 D, E and F) are the emission current images after the relaxation process and it can be inferred from these figures that the relaxation process affects the emission current images' concentration pattern.

The effect of the cooling process on FEE has been discussed based on the I-V characteristics curve and the FN plot for FEE from SWCNT-21. Cooling process can be achieved by adding liquid nitrogen inside the sample holder and leaving the system for  $\sim 15$  min, so cooling can have its effect on the sample. Before applying the cooling process, the emission current initiated at an applied voltage value of 320 V, where the emission current was 4.2 pA. With slowly increasing of the applied voltage, the emission current gets increased until a sudden jump happens in the emission current, where it is increased from 80.3 nA to  $I_{SW} = 3.05 \times 10^3$  nA, where the applied voltage value was  $V_{SW} = 700$  V. Afterwards, we continued increasing the applied voltage until it reached 1050 V, where the emission current was  $6.2 \times 10^3$  nA. By decreasing the applied voltage, the saturation region extends down to  $V_{SAT} = 450$  V and  $I_{SAT} = 1.1 \times 10^3$  nA. By further decreasing the applied voltage, the emission current decreased until it vanishes at ( $V_{TH} = 140$  V,  $I_{TH} = 4.2$  pA) (see Fig. 8). It should be noted that the slope before the cooling process, during increasing and decreasing the applied voltage, has values of (-5297.5 Np) and (-2347.78 Np), respectively.

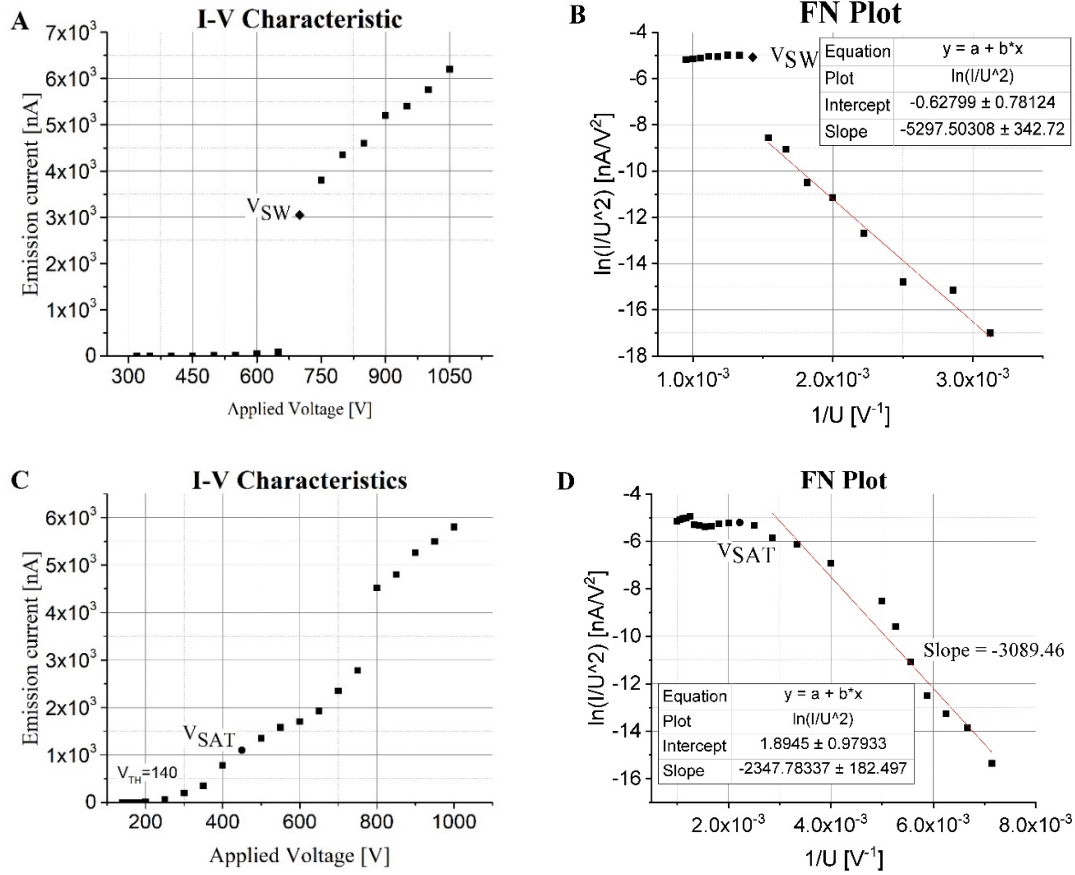


FIG. 8. SWCNT-21 before cooling process with increasing applied voltage. (A) I-V Characteristics. (B) FN plot. When applied voltage decreased (C) I-V Characteristics. (D) FN Plot.

After applying the cooling process, we slowly increased the applied voltage on the tip until the emission current has been initiated at an applied voltage value of (230 V), with an emission current value of (250 pA). “Switch-on” phenomenon appeared at ( $V_{SW} = 1000$  V,  $I_{SW} = 3.6 \times 10^3$  nA). By decreasing the applied voltage, emission current remains in the ( $\mu$ A) range until the applied voltage reached ( $V_{SAT} = 500$  V,  $I_{SAT} = 1.0 \times 10^3$  nA). By further decreasing the applied voltage, the emission current vanishes at ( $V_{TH} = 20$  V), with an emission current value ( $I_{TH} = 50$  pA). Figure (9) shows the I-V Characteristics,

with related FN plots. It can be noticed by comparing the I-V characteristics before and after the cooling process that there is an emission current fluctuation being increased after the cooling process. It can also be noted that from Fig. 10, the emission current pattern gets distributed over the screen as an effect of the cooling process. Figs. (10 A, B and C) show the emission current images before the cooling process, where they are more concentrated than those after the cooling process. Figs. (10 D, E and F) show the emission current images after the cooling process.

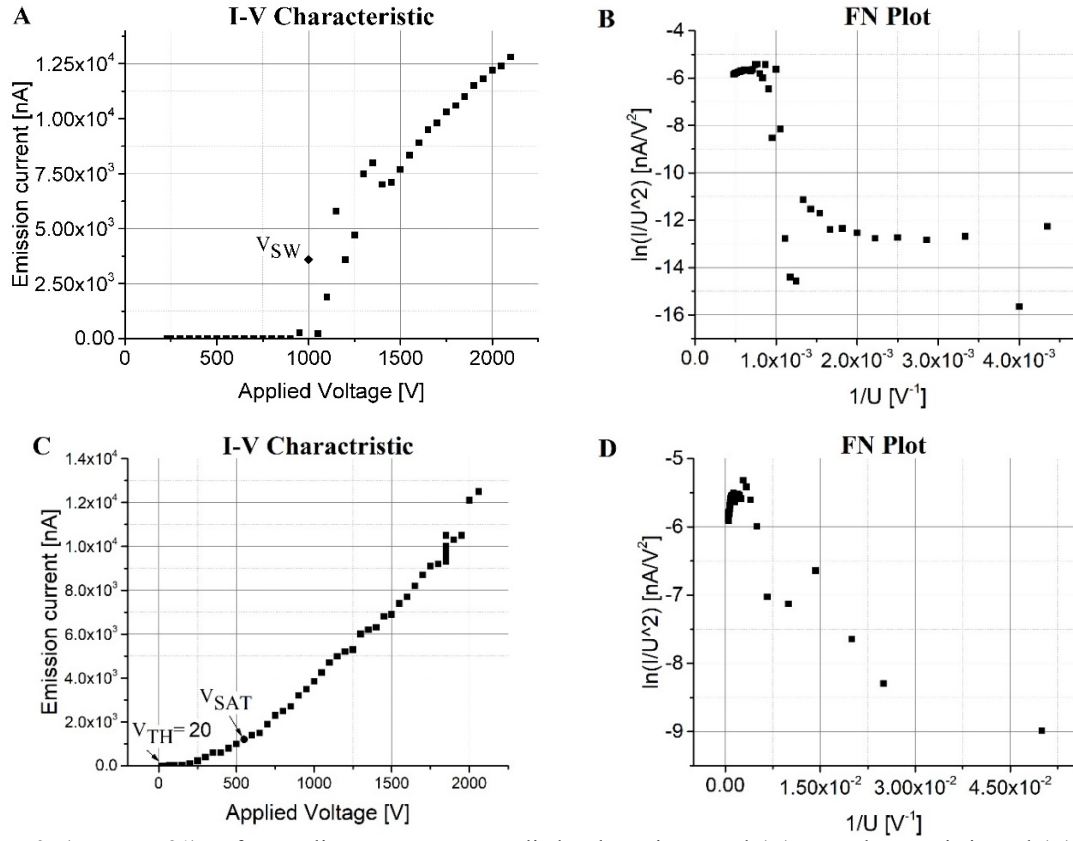


FIG. 9. (SWCNT-21). After cooling process. As applied voltage increased (A) I-V Characteristic and (B) FN plot. As applied voltage decreased (C) I-V Characteristics. (B) FN Plot.

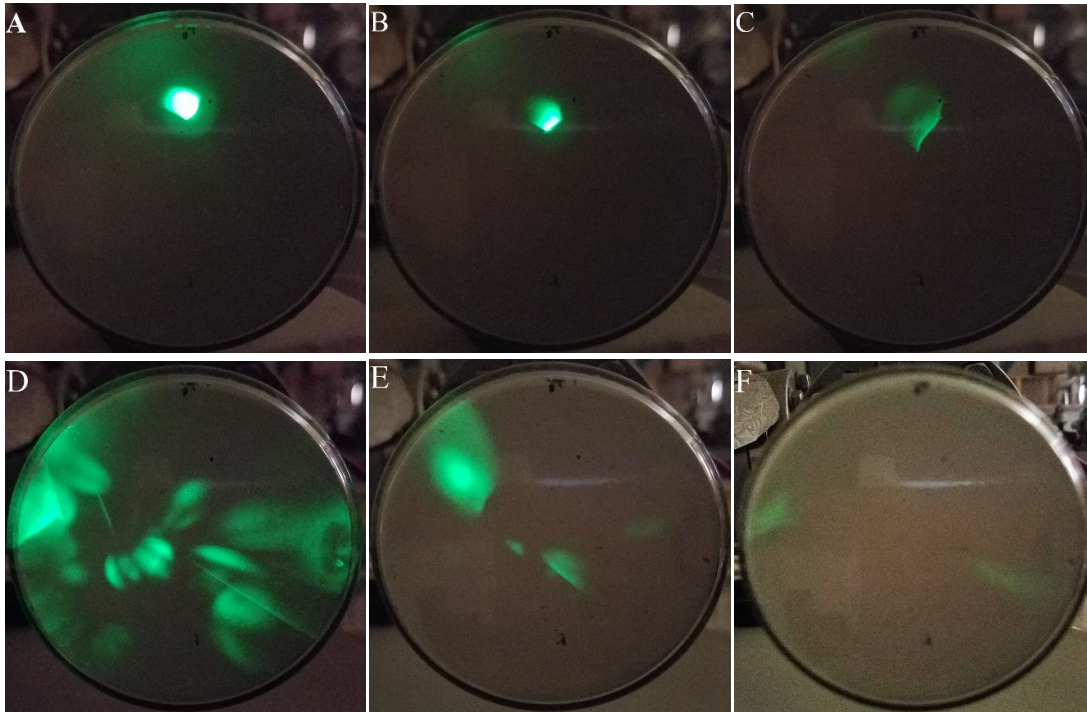


FIG. 10. Before cooling process. (A)  $V = 1050$  V,  $I = 6.2 \times 10^3$  nA. (B)  $V_{SW} = 700$  V,  $I_{SW} = 3.05 \times 10^3$  nA (C)  $V_{SAT} = 450$  V,  $I_{SAT} = 1.1 \times 10^3$  nA. After cooling process. (D)  $V = 1550$  V,  $I = 7.4 \times 10^3$  nA. (E)  $V_{SW} = 1000$  V,  $I_{SW} = 3.6 \times 10^3$  nA. (F)  $V_{SAT} = 500$  V,  $I_{SAT} = 1.0 \times 10^3$  nA.



By comparing Fig. 8 with Fig. 9, it can be noticed that there is an occurrence of emission current fluctuation after performing the cooling process. Additionally, the switch-on phenomenon has occurred at higher voltage values after applying the cooling process. Also, the saturated region extends down to a higher voltage value, but the threshold voltage would have a lower value ( $V_{TH} = 20$  V) after applying cooling process.

## Conclusions

SWCNT emitters have been prepared by employing a drawing method using a glass puller technique. The effects of the relaxation and cooling processes on the FEE have been studied from plotting the I-V characteristics and the FN plots along with the emission current images obtained. The relaxation process has shown to have a significant impact on the FEE, where it

causes a reduction in the applied voltage values required for the “switch-on” phenomenon to take place. Additionally, the saturation region extends down to a lower voltage value and can also enhance the emission current pattern, where it causes it to become more focused and concentrated.

The cooling process affects the FEE mechanism, where  $V_{SW}$  and  $V_{SAT}$  have increased after the cooling process. The most remarkable impact of the cooling process on FEE is the lowering of the  $V_{TH}$  value significantly, which is the lowest applied voltage value that can yield the lowest emission current. Moreover, the cooling process resulted in having the emission current pattern to become non-uniformly distributed over the screen. Also, a constant resistance has been observed at the emitter tip, where this can be indicated from the linear behavior that appears in the I-V plots.

## References

- [1] Parveen, S., Kumar, A., Husain, S. and Husain, M., *Physica B: Condensed Matter*, 505 (2017) 1.
- [2] Stratton, R., *Proceedings of the Physical Society. Section B*, 68 (10) (1955) 746.
- [3] Arkhipov, A.V., Gabdullin, P.G., Gnuchev, N.M., Davydov, S.N., Krel, S.I. and Loginov, B.A., *St. Petersburg Polytechnical University Journal: Physics and Mathematics*, 1 (1) (2015) 47.
- [4] Beams, J.W., *Physical Review*, 44 (10) (1933) 803.
- [5] Vyšinka, M., Vaverka, J., Pavlu, J., Nemecek, Z. and Šafránková, J., *WDS'12 Proceedings of Contributed Papers, Part 2* (2012) 151.
- [6] Rinzler, A.G., Hafner, J.H., Nikolaev, P., Nordlander, P., Colbert, D.T., Smalley, R.E., Lou, L., Kim, S.G. and Tomanek, D., *Science*, 269 (5230) (1995) 1550-3.
- [7] Sun, Y., Shin, D.H., Yun, K.N., Hwang, Y.M., Song, Y., Leti, G., Jeon, S.-G., Kim, J.-I., Saito, Y. and Lee, C.J., *AIP Advances*, 4 (7) (2014) 077110.
- [8] Cheng, Y. and Zhou, O., *Comptes Rendus Physique*, 4 (9) (2003) 1021.
- [9] Hata, K., Takakura, A. and Saito, Y., *Ultramicroscopy*, 95 (2003) 107.
- [10] Iijima, S., *Nature*, 354 (6348) (1991) 56.
- [11] Iijima, S. and Ichihashi, T., *Nature*, 363 (6430) (1993) 603.
- [12] Peng, J., Li, Z., He, C., Deng, S., Xu, N., Zheng, X. and Chen, G., *Physical Review B*, 72 (23) (2005) 235106.
- [13] Dean, K.A. and Chalamala, B.R., *Applied Physics Letters*, 75 (19) (1999) 3017.
- [14] Chen, C.-W., Lee, M.-H. and Clark, S.J., *Applied Surface Science*, 228 (1) (2004) 143.
- [15] Chau, R., Datta, S., Doczy, M., Doyle, B., Jin, B., Kavalieros, J., Majumdar, A., Metz, M. and Radosavljevic, M., *IEEE Transactions on Nanotechnology*, 4 (2) (2005) 153.
- [16] Choi, W.B., Chung, D.S., Kang, J.H., Kim, H.Y., Jin, Y.W., Han, I.T., Lee, Y.H., Jung, J.E., Lee, N.S., Park, G.S. and Kim, J.M., *Applied Physics Letters*, 75 (20) (1999) 3129.
- [17] Lin, H., Zhu, H., Guo, H. and Yu, L., *Materials Research Bulletin*, 43 (10) (2008) 2697.
- [18] Baughman, R.H., Zakhidov, A.A. and de Heer, W.A., *Science*, 297 (5582) (2002) 787.
- [19] Fowler, R.H. and Nordheim, L.W., *Proceedings of the Royal Society of London, Series A: Mathematical, Physical and Engineering Sciences*, 119 (781) (1928) 137.

- [20] Forbes, R., Deane, J., Fischer, A. and Mousa, M., *Jordan J. Phys.*, 8 (3) (2015) 125.
- [21] Mousa, M., *Surface Science*, 246 (1) (1991) 79.
- [22] Al-Qudah, A., Mousa, M. and Fischer, A., *IOP Conference Series: Materials Science and Engineering*, 92 (1) (2015) 012021.
- [23] Kim, C., Choi, Y.S., Lee, S.M., Park, J.T., Kim, B. and Lee, Y.H., *Journal of the American Chemical Society*, 124 (33) (2002) 9906.
- [24] Oki, H., Kinoshita, A., Takikawa, T., Kim, W.S., Murakami, K., Abo, S., Wakaya, F. and Takai, M., *Journal of Vacuum Science & Technology: B - Microelectronics and Nanometer Structures*, 27 (2) (2009).
- [25] Mousa, M.S., Al-Akhras, M.-A. and Daradkeh, S.I., *Jordan J. Phys.*, 11 (1) (2018) 17.
- [26] Latham, R.V. and Mousa, M.S., *Journal of Physics D: Applied Physics*, 19 (4) (1986) 699.
- [27] Minoux, E., Groening, O., Teo, K.B.K., Dalal, S.H., Gangloff, L., Schnell, J.-P., Hudanski, L., Bu, I.Y.Y., Vincent, P., Legagneux, P., Amaratunga, G.A.J. and Milne, W.I., *Nano-Letters*, 5 (11) (2005) 2135.
- [28] Chen, L.F., Song, H., Cao, L.Z., Jiang, H., Li, D.B., Guo, W.G., Liu, X., Zhao, H.F. and Li, Z.M., *Journal of Applied Physics*, 106 (3) (2009) 033703.

## Authors Index

A. A. Barzinjy .....	45
A. M. D. Assa'd.....	37
A. Mayer.....	17, 63
B. Mohammad .....	79
E. S. Bani Ali.....	7
G. R. Spencer .....	1
I. K. Abdullah.....	45
J. Wiedemeier.....	1
M. Aljarrah .....	79
M. Alnaief.....	79
M. J. Hagmann .....	1, 63
M. S. Mousa .....	1,7, 63, 87
Michaël Lobet.....	17
R. G. Forbes .....	63
R. M. Obaidat.....	79
S. I. Daradkeh.....	7, 87
S. M. Hamad. ....	45

## Subject Index

Backscattered Electrons.....	37
Backscattering Coefficient.....	37
Carbon Contamination .....	37
Carrageenan.....	79
CASINO .....	37
Drug Carrier .....	79
Energy Distribution .....	37
Field Electron Emission.....	7, 63, 87
Field-Programmable Gate Array .....	1
Genetic Algorithm.....	17
Gray Codes.....	17
Green chemistry .....	45
Green Synthesis .....	45
Hybrid Aerogel, Alginate.....	79
Ionic Liquids.....	45
Mean-Barrier Approximation .....	63
Metal-Vacuum-Metal Junction .....	63
Metamaterials .....	17
Monte Carlo Model.....	37
MWCNTs .....	7
Nanoparticles.....	45
Nanoscience .....	1
Nanotechnology .....	1, 45
Optical Engineering, Optimization .....	17
Optimization.....	17
Quadratic Approximation .....	17
Relaxation and Cooling Processes.....	87
Scanning Tunneling Microscope.....	1
Single-Walled Carbon Nanotubes .....	87
Supercritical Fluid Extraction.....	79
SWCNTs .....	7
Theory .....	63
Transfer-Matrix Technique .....	63
Transmission Probability.....	63



**المراجع:** يجب طباعة المراجع بأسطر مزدوجة ومرقمة حسب تسلسلها في النص. وتكتب المراجع في النص بين قوسين مربعين. ويتم اعتماد اختصارات الدوريات حسب نظام Wordlist of Scientific Reviewers.

**الجدول:** تعطى الجداول أرقاماً متسلسلة يشار إليها في النص. ويجب طباعة كل جدول على صفحة منفصلة مع عنوان فوق الجدول. أما الحواشي التفسيرية، التي يشار إليها بحرف فوقي، فتكتب أسفل الجدول.

**الرسوم التوضيحية:** يتم ترقيم الأشكال والرسومات والرسومات البيانية (المخططات) والصور، بصورة متسلسلة كما وردت في النص.

تقبل الرسوم التوضيحية المستخرجة من الحاسوب والصور الرقمية ذات النوعية الجيدة بالأبيض والأسود، على أن تكون أصيلة وليست نسخة عنها، وكل منها على ورقة منفصلة ومعرفة برقمها بالمقابل. ويجب تزويد المجلة بالرسومات بحجمها الأصلي بحيث لا تحتاج إلى معالجة لاحقة، وألا تقل الحروف عن الحجم 8 من نوع Times New Roman، وألا تقل سماكة الخطوط عن 0.5 وبكثافة متجانسة. ويجب إزالة جميع الألوان من الرسومات ما عدا تلك التي ستُنشر ملونة. وفي حالة إرسال الرسومات بصورة رقمية، يجب أن تتوافق مع متطلبات الحد الأدنى من التمايز (1200 dpi Resolution) لرسومات الأبيض والأسود الخطية، و 600 dpi للرسومات باللون الرمادي، و 300 dpi للرسومات الملونة. ويجب تخزين جميع ملفات الرسومات على شكل (jpg)، وأن ترسل الرسوم التوضيحية بالحجم الفعلي الذي سيظهر في المجلة. وسواء أرسل المخطوط بالبريد أو عن طريق الشبكة (Online)، يجب إرسال نسخة ورقية أصلية ذات نوعية جيدة للرسومات التوضيحية.

**مواد إضافية:** تشجع المجلة الباحثين على إرفاق جميع المواد الإضافية التي يمكن أن تسهل عملية التحكيم. وتشمل المواد الإضافية أي اشتقاقات رياضية مفصلة لا تظهر في المخطوط.

**المخطوط المنقح (المعدل) والأقراص المدمجة:** بعد قبول البحث للنشر وإجراء جميع التعديلات المطلوبة، فعلى الباحثين تقديم نسخة أصلية ونسخة أخرى مطابقة للأصلية مطبوعة بأسطر مزدوجة، وكذلك تقديم نسخة إلكترونية تحتوي على المخطوط كاملاً مكتوباً على Microsoft Word for Windows 2000 أو ما هو استجد منه. ويجب إرفاق الأشكال الأصلية مع المخطوط النهائي المعدل حتى لو تم تقديم الأشكال إلكترونياً. وتخزن جميع ملفات الرسومات على شكل (jpg)، وتقدم جميع الرسومات التوضيحية بالحجم الحقيقي الذي ستظهر به في المجلة. ويجب إرفاق قائمة ببرامج الحاسوب التي استعملت في كتابة النص، وأسماء الملفات على قرص مدمج، حيث يعلم القرص بالاسم الأخير للباحث، وبالرقم المرجعي للمخطوط للمراسلة، وعنوان المقالة، والتاريخ. ويحفظ في مغلف واقٍ.



#### حقوق الطبع

يُشكّل تقديم مخطوط البحث للمجلة اعترافاً صريحاً من الباحثين بأن مخطوط البحث لم يُنشر ولم يُقدّم للنشر لدى أي جهة أخرى كانت وبأي صيغة ورقية أو إلكترونية أو غيرها. ويشتترط على الباحثين ملء أنموذج ينص على نقل حقوق الطبع لتصبح ملكاً لجامعة اليرموك قبل الموافقة على نشر المخطوط. ويقوم رئيس التحرير بتزويد الباحثين بأنموذج نقل حقوق الطبع مع النسخة المرسلة للتتقيق. كما ويُمنع إعادة إنتاج أي جزء من الأعمال المنشورة في المجلة من دون إذن خطي مُسبق من رئيس التحرير.

#### إخلاء المسؤولية

إن ما ورد في هذه المجلة يعبر عن آراء المؤلفين، ولا يعكس بالضرورة آراء هيئة التحرير أو الجامعة أو سياسة اللجنة العليا للبحث العلمي أو وزارة التعليم العالي والبحث العلمي. ولا يتحمل ناشر المجلة أي تبعات مادية أو معنوية أو مسؤوليات عن استعمال المعلومات المنشورة في المجلة أو سوء استعمالها.

**الفهرسة:** المجلة مفهرسة في:

 <b>ULRICHSWEB™</b> GLOBAL SERIALS DIRECTORY	<b>Emerging Sources Citation Index (ESCI)</b>	
--	---	---

## معلومات عامة

المجلة الأردنية للفيزياء هي مجلة بحوث علمية عالمية متخصصة مُحكمة تصدر بدعم من صندوق دعم البحث العلمي، وزارة التعليم العالي والبحث العلمي، عمان، الأردن. وتقوم بنشر المجلة عمادة البحث العلمي والدراسات العليا في جامعة اليرموك، إربد، الأردن. وتُنشر البحوث العلمية الأصلية، إضافة إلى المراسلات القصيرة Short Communications، والملاحظات الفنية Technical Notes، والمقالات الخاصة Feature Articles، ومقالات المراجعة Review Articles، في مجالات الفيزياء النظرية والتجريبية، باللغتين العربية والإنجليزية.

## تقديم مخطوط البحث

تقدم البحوث عن طريق إرسالها إلى البريد الإلكتروني : [jjp@yu.edu.jo](mailto:jjp@yu.edu.jo)

تقديم المخطوطات إلكترونياً: اتبع التعليمات في موقع المجلة على الشبكة العنكبوتية.

ويجري تحكيم البحوث الأصلية والمراسلات القصيرة والملاحظات الفنية من جانب مُحكمين اثنين في الأقل من ذوي الاختصاص والخبرة. وتُشجّع المجلة الباحثين على اقتراح أسماء المحكمين. أما نشر المقالات الخاصة في المجالات الفيزيائية النشطة، فيتم بدعوة من هيئة التحرير، ويُشار إليها كذلك عند النشر. ويُطلب من كاتب المقال الخاص تقديم تقرير واضح يتسم بالدقة والإيجاز عن مجال البحث تمهيداً للمقال. وتُنشر المجلة أيضاً مقالات المراجعة في الحقول الفيزيائية النشطة سريعة التغير، وتشجّع كاتبي مقالات المراجعة أو مُستكثبيها على إرسال مقترح من صفحتين إلى رئيس التحرير. ويُرفق مع البحث المكتوب باللغة العربية ملخص (Abstract) وكلمات دالة (Keywords) باللغة الإنجليزية.

## ترتيب مخطوط البحث

يجب أن تتم طباعة مخطوط البحث ببنط 12 نوعه Times New Roman، ويسطر مزدوج، على وجه واحد من ورق A4 (21.6 × 27.9 سم) مع حواشي 3.71 سم، باستخدام معالج كلمات ميكروسوفت وورد 2000 أو ما استُجد منه. ويجري تنظيم أجزاء المخطوط وفق الترتيب التالي: صفحة العنوان، الملخص، رموز التصنيف (PACS)، المقدمة، طرق البحث، النتائج، المناقشة، الخلاصة، الشكر والاعتراف، المراجع، الجداول، قائمة بدليل الأشكال والصور والإيضاحات، ثم الأشكال والصور والإيضاحات. وتُكتب العناوين الرئيسية بخط غامق، بينما تُكتب العناوين الفرعية بخط مائل.

**صفحة العنوان:** وتشمل عنوان المقالة، أسماء الباحثين الكاملة وعناوين العمل كاملة. ويكتب الباحث المسؤول عن المراسلات اسمه مشاراً إليه بنجمة، والبريد الإلكتروني الخاص به. ويجب أن يكون عنوان المقالة موجزاً وواضحاً ومعبراً عن فحوى (محتوى) المخطوط، وذلك لأهمية هذا العنوان لأغراض استرجاع المعلومات.

**الملخص:** المطلوب كتابة فقرة واحدة لا تزيد على مائتي كلمة، موضحة هدف البحث، والمنهج المتبع فيه والنتائج وأهم ما توصل إليه الباحثون.

**الكلمات الدالة:** يجب أن يلي الملخص قائمة من 4-6 كلمات دالة تعبر عن المحتوى الدقيق للمخطوط لأغراض الفهرسة.

**PACS:** يجب إرفاق الرموز التصنيفية، وهي متوافرة في الموقع <http://www.aip.org/pacs/pacs06/pacs06-toc.html>.

**المقدمة:** يجب أن توضّح الهدف من الدراسة وعلاقتها بالأعمال السابقة في المجال، لا أن تكون مراجعة مكثفة لما نشر (لا تزيد المقدمة عن صفحة ونصف الصفحة مطبوعة).

**طرائق البحث (التجريبية / النظرية):** يجب أن تكون هذه الطرائق موضحة بتفصيل كاف لإتاحة إعادة إجرائها بكفاءة، ولكن باختصار مناسب، حتى لا تكون تكراراً للطرائق المنشورة سابقاً.

**النتائج:** يستحسن عرض النتائج على صورة جداول وأشكال حيثما أمكن، مع شرح قليل في النص ومن دون مناقشة تفصيلية.

**المناقشة:** يجب أن تكون موجزة وتركز على تفسير النتائج.

**الاستنتاج:** يجب أن يكون وصفاً موجزاً لأهم ما توصلت إليه الدراسة ولا يزيد عن صفحة مطبوعة واحدة.

**الشكر والاعتراف:** الشكر والإشارة إلى مصدر المنح والدعم المالي يكتبان في فقرة واحدة تسبق المراجع مباشرة.



# Jordan Journal of PHYSICS

An International Peer-Reviewed Research Journal issued by the  
Support of the Scientific Research Support Fund

Published by the Deanship of Research & Graduate Studies, Yarmouk University, Irbid, Jordan

Name: ..... الأسم:  
Specialty:..... التخصص:  
Address: ..... العنوان:  
P.O. Box:..... صندوق البريد:  
City & Postal Code: ..... المدينة/الرمز البريدي:  
Country: ..... الدولة:  
Phone: ..... رقم الهاتف:  
Fax No:..... رقم الفاكس:  
E-mail:..... البريد الإلكتروني:  
No. of Subscription: ..... عدد الاشتراكات:  
Method of Payment: ..... طريقة الدفع:  
Amount Enclosed:..... المبلغ المرفق:  
Signature: ..... التوقيع:

Cheques should be paid to Deanship of Research and Graduate Studies - Yarmouk University.

I would like to subscribe to the Journal  
For

- ☐ One Year  
☐ Two Years  
☐ Three Years

## One Year Subscription Rates

	Inside Jordan	Outside Jordan
Individuals	JD 8	€ 40
Students	JD 4	€ 20
Institutions	JD 12	€ 60

## Correspondence

### Subscriptions and Sales:

**Prof. Ibrahim O. Abu Al-Jarayesh**  
Deanship of Research and Graduate Studies  
Yarmouk University  
Irbid – Jordan  
**Telephone:** 00 962 2 711111 Ext. 2075  
**Fax No.:** 00 962 2 7211121





جامعة اليرموك



المملكة الأردنية الهاشمية

# المجلة الأردنية للفيزياء

مجلة بحوث علمية عالمية متخصصة محكمة  
تصدر بدعم من صندوق دعم البحث العلمي

عدد خاص

المجلة الأردنية  
**للفيزياء**  
مجلة بحوث علمية عالمية محكمة

المجلد (12)، العدد (1)، نيسان 2019م / شعبان 1440هـ

المجلة الأردنية للفيزياء: مجلة علمية عالمية متخصصة محكمة تصدر بدعم من صندوق دعم البحث العلمي، عمان، الأردن، وتصدر عن  
عمادة البحث العلمي والدراسات العليا، جامعة اليرموك، إربد، الأردن.

رئيس التحرير:

ابراهيم عثمان أبو الجرايش  
قسم الفيزياء، جامعة اليرموك، إربد، الأردن.  
[ijaraysh@yu.edu.jo](mailto:ijaraysh@yu.edu.jo)

هيئة التحرير:

ضياء الدين محمود عرفة  
قسم الفيزياء، الجامعة الأردنية، عمان، الأردن.  
[darafah@ju.edu.jo](mailto:darafah@ju.edu.jo)

نبيل يوسف أيوب  
رئيس الجامعة الأمريكية في مادبا، مادبا، الأردن.  
[nabil.ayoub@gju.edu.jo](mailto:nabil.ayoub@gju.edu.jo)

جميل محمود خليفة  
قسم الفيزياء، الجامعة الأردنية، عمان، الأردن.  
[jkalifa@ju.edu.jo](mailto:jkalifa@ju.edu.jo)

سامي حسين محمود  
قسم الفيزياء، الجامعة الأردنية، عمان، الأردن.  
[s.mahmood@ju.edu.jo](mailto:s.mahmood@ju.edu.jo)

نهاد عبدالرؤوف يوسف  
قسم الفيزياء، جامعة اليرموك، عمان، الأردن.  
[nihadyusuf@yu.edu.jo](mailto:nihadyusuf@yu.edu.jo)

مروان سليمان موسى  
قسم الفيزياء، جامعة مؤتة، الكرك، الأردن.  
[mmousa@mutah.edu.jo](mailto:mmousa@mutah.edu.jo)

أكرم عبد المجيد الروسان  
قسم الفيزياء التطبيقية، جامعة العلوم والتكنولوجيا الأردنية، إربد، الأردن.  
[akram@just.edu.jo](mailto:akram@just.edu.jo)

محمد خالد الصغير  
قسم الفيزياء، الجامعة الهاشمية، الزرقاء، الأردن.  
[msugh@hu.edu.jo](mailto:msugh@hu.edu.jo)

سكرتير التحرير: مجدي الشناق

ترسل البحوث إلى العنوان التالي:

الأستاذ الدكتور إبراهيم عثمان أبو الجرايش  
رئيس تحرير المجلة الأردنية للفيزياء  
عمادة البحث العلمي والدراسات العليا، جامعة اليرموك  
إربد، الأردن

هاتف 00 962 2 7211111 فرعي 2075

E-mail: [jjp@yu.edu.jo](mailto:jjp@yu.edu.jo) Website: <http://Journals.yu.edu.jo/jjp>